Université de Montréal

Méthodes multiphysiques et multimodales d'imagerie biomédicale d'élastographie

par

Guillaume Flé

Département de pharmacologie et physiologie

Institut de génie biomédical

Faculté de médecine

Thèse présentée en vue de l'obtention du grade de

Philosophiæ Doctor (Ph.D.)

en Génie Biomédical

12 mai 2023

© Guillaume Flé, 2023

Université de Montréal

Cette thèse intitulée

Méthodes multiphysiques et multimodales d'imagerie biomédicale d'élastographie

présentée par

Guillaume Flé

a été évaluée par un jury composé des personnes suivantes :

Frédéric Leblond
(président-rapporteur)

Guy Cloutier
(directeur de recherche)

Patrick Vermette
(membre du jury)

Jonathan Vappou
(examinateur externe)

Gerardo Ferbeyre
(représentant du doyen des ESP)

Résumé

L'imagerie biomédicale d'élastographie, visant à cartographier les propriétés mécaniques des tissus mous, est explorée à travers des approches multiphysiques et multimodales regroupant la microscopie optique d'une part et l'imagerie par résonance magnétique associée à la stimulation électrique d'autre part. Tout d'abord, une méthode de génération d'ondes élastiques, nécessaires aux expériences d'élastographie par résonance magnétique (ERM), suivant une approche de stimulation *in situ* est présentée. Cette dernière repose sur l'induction de forces de Lorentz, sources de mouvement, dans un matériau soumis à une stimulation électrique et exposé au champ magnétique d'un système d'imagerie par résonance magnétique (IRM). Un dispositif expérimental d'ERM par force de Lorentz est proposé et testé avec des fantômes de gélatine de différentes rigidités. Le champ ondulatoire mesuré est démontré provenir de la force de Lorentz établie au sein des échantillons et a permis la reconstruction d'images de rigidité au moyen d'un algorithme d'inversion habituellement appliqué au traitement de données cliniques. La faible amplitude des déplacements capturés suggère toutefois que les déformations induites seraient difficilement mesurables par ERM dans des conditions de stimulation électrique sûres. Si cette caractéristique questionne la faisabilité de l'ERM par force de Lorentz, elle ouvre la voie à l'application simultanée de l'ERM conventionnelle et de la stimulation électrique dans une même région d'intérêt, permettant l'analyse de la réponse biomécanique de tissus biologiques à une stimulation électrique. Cet aspect est abordé à travers une étude numérique de stimulation transcrânienne par courant alternatif associée à l'ERM dans un modèle 3D de cerveau de souris. L'impact des forces de Lorentz, inhérentes à cette combinaison, sur les reconstructions de viscoélasticité est étudié via un algorithme

d'inversion non-linéaire par sous-zones. Un volet d'imagerie de la conductivité ohmique par résonance magnétique est incorporé aux simulations de façon à approximer la distribution de courant électrique induit par stimulation. L'union de ces différentes approches pourrait être pertinente dans le cadre de la caractérisation du cerveau et révéler davantage de mécanismes physiologiques ensemble qu'individuellement.

Dans un second temps, l'évaluation de la viscoélasticité des tissus biologiques est abordée à l'échelle de la cellule grâce à la micro-élastographie optique. Cette approche repose également sur la génération, la mesure et l'analyse d'ondes élastiques harmoniques dans le milieu sondé et est appliquée à des ovocytes de souris d'un diamètre avoisinant 85 µm. Les déformations locales sont mesurées dans le plan des images expérimentales acquises à une fréquence de 200 kHz et sont traitées par un modèle de déplacements 3D exploitant la symétrie planaire des ovocytes imagés. La reconstruction de cartes de viscoélasticité est assurée par l'algorithme itératif d'inversion non-linéaire par sous-zones, emprunté à l'élastographie par résonance magnétique. Les images de module de stockage produites démontrent un niveau de précision supérieur aux images obtenues par inversion directe, sur la base de différentiabilité des structures internes de l'ovocyte. La génération inédite d'images du module de perte dans de telles cellules et la robustesse de l'ensemble de cette approche sont des indicateurs encourageant d'une éventuelle applicabilité future aux procédures de fécondation *in vitro*.

Mots clés : Élastographie, Imagerie par résonance magnétique, Microscopie optique, Tomographie d'impédance électrique

Abstract

Biomedical elastography imaging, aiming at mapping the mechanical properties of soft tissues, is explored through multiphysical and multimodal approaches combining optical microscopy on one hand and magnetic resonance imaging associated with electrical stimulation on the other hand. First, a method for generating elastic waves, necessary for magnetic resonance elastography (MRE) experiments, following an *in situ* actuation approach is presented. The latter is based on the induction of Lorentz forces, sources of motion, in a material subjected to an electrical stimulation and exposed to the magnetic field of a magnetic resonance imaging (MRI) system. An experimental set-up for Lorentz force MRE is proposed and tested with gelatin phantoms of different stiffness. The measured wave field is shown to originate from the Lorentz force established within the samples and allowed the reconstruction of stiffness images using an inversion algorithm typically applied to clinical data processing. The small amplitude of the captured displacements, however, suggests that the induced deformations would be difficult to measure by MRE under safe electrical stimulation conditions. If this characteristic questions the feasibility of Lorentz force MRE, it opens the way to the simultaneous application of conventional MRE and electrical stimulation in the same region of interest, allowing the analysis of the biomechanical response of biological tissues to electrical stimulation. This aspect is addressed through a numerical study of transcranial alternating current stimulation associated with MRE in a 3D mouse brain model. The impact of Lorentz forces, inherent to this combination, on viscoelasticity reconstructions is studied via a nonlinear subzone inversion algorithm. A magnetic resonance imaging component of the ohmic conductivity is incorporated into the simulations in

order to approximate the electrical current distribution induced by stimulation. The union of these different approaches could be relevant for the characterization of the brain and may reveal more physiological mechanisms together than individually.

In a second step, the evaluation of the viscoelasticity of biological tissues is approached at the cell level using optical microelastography. This approach is also based on the generation, measurement and analysis of harmonic elastic waves in the probed medium and is applied to mouse oocytes with a diameter of about 85 µm. Local deformations are measured in the plane of the experimental images acquired at a frequency of 200 kHz and are processed by a 3D displacement model exploiting the planar symmetry of the imaged oocytes. Viscoelasticity maps are reconstructed using the iterative subzone nonlinear inversion algorithm borrowed from magnetic resonance elastography. The storage modulus images produced demonstrate a higher level of accuracy than images obtained by direct inversion, based on the differentiability of the internal structures of the oocyte. The novel generation of loss modulus images in such cells and the robustness of the overall approach are encouraging indicators of potential future applicability to *in vitro* fertilization procedures.

Key words : Elastography, Magnetic Resonance Imaging, Optical Microscopy, Electrical Impedance Tomography

Table des matières

Liste des tableaux

Table des figures

plane is set at the center of the oocyte. A high-speed camera captures images of the oocyte being pulsed by the actuation micropipette. **b.** Images acquired with the camera at a 200 kHz frame rate during harmonic actuation are processed with an optical-flow method to estimate in-plane displacements (u and v). A full-field displacement data set (u, v, and w) is approximated using a 3D oocyte geometry-based model. The procedure is described in the Methods section. 131

20 **Viscoelasticity reconstructions performed on simulated displacement data.** Panels **a** and **b** represent the two experiment-based shear modulus distributions used in simulations, $\mu_1 = 2.5 \times \mu_{\text{exp}}$ and $\mu_2 = \mu_{\text{exp}}$, where μ_{exp} refers to the average distribution observed in experiments (see the Methods section for details). The individual domains in μ_{exp} were set to $\mu_{\text{exp,nucleolus}} = 768 + i268$ Pa, $\mu_{\text{exp,nucleus}} = 615 + i217$ Pa, $\mu_{\text{exp,cytoplam}} = 444 + i147$ Pa, and $\mu_{\text{exp,zp}} = 202 + i68$ Pa. For each simulation, the wavelength and isotropic 30-µm subzone are indicated in the first column of both panels by the sine curve in the spherical oocyte domain and the red square, respectively. For each panel, the second and third columns represent, respectively, the true and reconstructed distributions using the approximated full-field displacements. 132

21 **Storage and loss modulus reconstructions in 21 mouse oocytes. a.** Anatomical image of a representative mouse oocyte and corresponding segmented regions. **b.** Average values of storage modulus reconstructions performed on 21 oocytes. All reconstructions converged to stable distributions ($\mu_{r,fc}$). **c.** Average values of fully converged loss modulus reconstructions (13 out of 21) in the five segmented regions ($\mu_{r,fc}$). **d.** Average values of partially converged loss modulus reconstructions (8 out of 21) in the five segmented regions ($\mu_{r,pc}$). **e.** Representative oocyte for which both the storage and loss modulus reconstructions were complete. Images show the oocyte and corresponding segmented regions,

Liste des sigles et des abréviations

IRM (*MRI*)	Imagerie par résonance magnétique (*Magnetic Resonance Imaging*)	**TIE (*EIT*)**	Tomographie d'impédance électrique (*Electrical Impedance Tomography*)
TIERM (*MREIT*)	Tomographie d'impédance électrique par résonance magnétique (*Magnetic Resonance Electrical Impedance Tomography*)	**ERM (*MRE*)**	Élastographie par résonance magnétique (*Magnetic Resonance Elastography*)
US	Ultrasonographie	**OCT**	Optical Coherence Tomography (*Tomographie par cohérence optique*)
FUSE	Focused Ultrasound Elastography (*Élastographie par ultrasons focalisés*)	**OCE**	Optical Coherence Elastography (*Élastographie par cohérence optique*)
MDEV	Multi-Frequency Dual Elasto Visco Inversion (*Double inversion visco-élastique multifréquence*)	**LFE**	Local Frequency Estimation (*Estimation locale de la fréquence*)
HMDI	Heterogeneous Multifrequency Direct Inversion (*Inversion directe multifréquence hétérogène*)	**NLI**	Nonlinear Inversion (*Inversion nonlinéaire*)
tACS	Transcranial Alternating Current Stimulation (*Stimulation transcrânienne par courant alternatif*)	**NIBS**	Noninvasive Brain Stimulation (*Stimulation non-invasive du cerveau*)
TV	Total Variation (*Variation totale*)	**SP**	Soft Prior Regularization (*Régularisation à partir d'information spatiale préalable*)
CG	Conjugate Gradient (*Gradient conjugué*)	**MEG**	Motion Encoding Gradient (*Gradient d'encodage de phase*)
TMS	Transcranial Magnetic Stimulation (*Stimulation magnétique transcrânienne*)	**TES**	Transcranial Electrical Stimulation (*Stimulation électrique transcrânienne*)

ICSI Intracytoplasmic Sperm Injection (*Injection intracytoplasmique de sperme*)

AFM Atomic Force Microscopy (*Microscopie par force atomique*)

Remerciements

Les travaux décrits au cours des pages suivantes ont bénéficié de différentes contributions que je tiens à saluer ici. Tout d'abord, merci à Guy Cloutier, directeur du LBUM, de m'avoir donné carte blanche et laissé poursuivre des projets éloignés des thématiques du laboratoire. C'était risqué et loin d'être gagné. Merci également pour sa confiance et patience face aux nombreuses difficultés que j'ai rencontrées, et en particulier de m'avoir encouragé à prendre du recul lorsque nécessaire. Et finalement, pas d'argent, pas de doctorat : merci d'en avoir assuré le financement.

À Guillaume Gilbert, merci de m'avoir ouvert les portes de la salle D pour les expériences d'ERM. Surtout, merci d'avoir constamment répondu présent, week-ends et jours fériés, pour tester de nouveaux dispositifs expérimentaux. Merci également à Stéphane Bedwani de m'avoir dépanné et imprimé en 3D mes modèles de porte-fantômes.

À Greg FitzHarris et Gaudeline Rémillard-Labrosse, merci de m'avoir accueilli comme un prince dans leur équipe et d'avoir mis leur laboratoire à disposition pour les travaux de micro-élastographie. Je ne pouvais pas espérer de meilleures conditions.

Bien sûr, je remercie chaleureusement Eli Van Houten pour son soutien et sa bienveillance. Je lui suis reconnaissant de m'avoir tendu la main dès l'examen prédoctoral et de s'être investi depuis. Merci également d'avoir été disponible pour répondre patiemment à mes questions ou simplement discuter d'aspects plus généraux, scientifiques ou non. C'était, et c'est toujours, un plaisir. Finalement, l'aboutissement du doctorat doit beaucoup à la méthode NLI, c'est une grande chance d'y avoir eu accès. Merci de l'avoir mise à ma disposition et de m'avoir formé à son utilisation.

Aux membres du comité, Frédéric Leblond, Patrick Vermette, Jonathan Vappou et Gerardo Ferbeyre, merci d'avoir accepté d'évaluer ces travaux.

Le cheminement de doctorat s'est fait en bonne compagnie et je tiens à remercier tous les collègues et amis de m'avoir supporté maugréer pendant la traversée. Je pense en particulier à Mercedes, Matthias, Anne-Sophie et Nico, vos présence et soutien ont été précieux. Je pense également à Guillaume B., ses gâteaux, Boris, Pedro, Marie Vroum-Vroum (joyeux anniversaire !), Samuel, Jennifer, Arnaud, Marie-Hélène, François, Louise, Norio et Loyda, merci d'avoir maintenu la bonne humeur à bord. Un grand merci à Marie J. et son enthousiasme pour faire du 11ème un espace agréable, mais surtout, merci de toujours bien me rappeler que mes repas ont l'air dégoutants. Bonne continuation à Sajad, Iman, Ladan et Hari ! À bientôt sur la route de l'élasto. Aux anciens membres du laboratoire et de l'étage, Julia Germaine Faurie, Élise, Marc, Manish et Marie M., c'était un plaisir ! J'adresse un remerciement particulier à Pol, *Doc' Tape*, dont les travaux ont inspiré mes projets de recherche, mais dont la rencontre a été paradoxalement fortuite. J'ai davantage découvert un ami qu'un collaborateur et garde un bon souvenir de la réparation au scotch et de l'art du recyclage.

Merci à Sophie, Flora et Marc pour les encouragements et d'avoir suivi mes trajectoires et dérives depuis la France, à Marine pour les nombreuses discussions et sorties, et aux Upplads d'être fidèles au poste.

J'ai une pensée ici pour Françoise et Denise, qui, j'en suis sûr, ont pu suivre la fin de cette histoire d'une manière ou d'une autre.

Ce chapitre et les suivants n'auraient pas abouti sans le soutien inconditionnel de mes parents, Carmen et Denis, ici ou ailleurs, de jour comme de nuit. Merci de m'avoir encouragé à suivre mon chemin, même de l'autre côté de l'océan. Je me réjouis de le parcourir en sens inverse et de penser aux visites annuelles au passé.

Je dédie ces dernières lignes à Agathe qui m'a supporté, accompagné, réconforté, ramassé, encouragé, remis sur pied et j'en passe. Merci d'être là et de toujours trouver les mots justes. Merci d'avoir été patiente et compréhensive face aux imprévus et reports. Et surtout, merci de transformer chaque jour le banal en spécial.

Introduction

La palpation manuelle de la peau et des organes superficiels est une pratique diagnostique exercée depuis des siècles et permet de distinguer des régions de rigidités différentes. La détection d'un contraste de dureté inhabituel dans la zone palpée est un indicateur d'une pathologie éventuelle et requiert une attention particulière. Bien qu'essentiels, les examens manuels demeurent qualitatifs et sont pratiqués dans le cadre d'approches diagnostiques et thérapeutiques préliminaires. Le développement croissant des systèmes d'imagerie médicale au cours des trente dernières années a favorisé l'extension de l'auscultation manuelle à la caractérisation quantitative et visuelle des propriétés physiques des tissus, en surface et en profondeur. La technique d'*élastographie* a ainsi permis de cartographier la rigidité de nombreux milieux, de l'échelle microscopique de la cellule individuelle à l'échelle macroscopique du cerveau humain en passant par le foie, les muscles et les parois artérielles.

Une expérience d'élastographie peut être résumée en trois étapes. Une contrainte mécanique est tout d'abord imposée au milieu étudié, la réponse de ce dernier est imagée puis quantifiée sous la forme de petites déformations locales, lesquelles sont finalement analysées par le biais de la résolution d'un problème inverse aboutissant à la cartographie de propriétés mécaniques dans la région imagée. Lorsque la contrainte est dynamique, les ondes acoustiques induites et leurs caractéristiques reflètent le comportement mécanique du milieu de propagation : plus le matériau est mou, plus la vitesse de propagation est faible et plus la longueur d'onde est petite. L'élastographie, quasi-statique ou dynamique, est aujourd'hui intégrée aux échographes et systèmes d'imagerie par résonance magnétique (IRM) de certains centres hospitaliers et conserve une dynamique croissante soutenue par les activités de

recherche liées à l'amélioration des équipements et des algorithmes de traitement d'images, et à la caractérisation mécanique de différents tissus.

Les projets de recherche décrits au cours des chapitres suivants approchent l'imagerie de propriétés mécaniques des solides mous sous un angle multimodal et multiphysique à travers des expériences d'élastographie harmonique par résonance magnétique (ERM, ou MRE pour *magnetic resonance elastography*) et de micro-élastographie optique (MEO, ou OME pour *optical microelastography*). Cette dernière est en partie abordée par le prisme de l'ERM dont les développements au cours des deux dernières décennies ont bénéficié à la méthode de MEO, mise au point en 2017. La reconstruction de cartes de viscoélasticité à partir d'images d'ERM ou de MEO est notamment assurée par le biais d'une même méthode de résolution du problème inverse, initialement développée dans le cadre de l'ERM. Par ailleurs, une approche d'ERM combinée avec la stimulation électrique est également exposée et incorpore un volet d'imagerie des propriétés électriques des tissus biologiques à travers la méthode de tomographie d'impédance électrique par résonance magnétique (TIERM, ou MREIT pour *magnetic resonance electrical impedance tomography*). Les objectifs de ces travaux sont :

1) proposer un protocole combinant l'ERM, la stimulation électrique et la modélisation des courants induits dans une même région d'intérêt visant à permettre l'évaluation locale de la réponse biomécanique des tissus soumis à une telle stimulation,

2) contribuer au développement de la micro-élastographie optique à travers la cartographie du module de cisaillement complexe d'ovocytes de souris.

Ces deux aspects s'ancrent dans des dynamiques de recherche contemporaines et constituent des axes de développement nouveaux ou peu étudiés. Les principes de l'élastographie et des méthodes principales de reconstruction de cartes de propriétés mécaniques sont présentés dans le **Chapitre 1** où une attention particulière est portée à l'élastographie par résonance magnétique. Une revue des différentes techniques d'élastographie par onde de cisaillement est proposée dans l'article *Viscoelasticity imaging of biological tissues and single cells using shear wave propagation, Frontiers In Physics, 2021, 9 :66-103* [**13**] exposé en annexe.

Elastographie par résonance magnétique et stimulation électrique

La combinaison de l'ERM et de la neurostimulation appliquée à la souris, récemment présentée par Patz *et al.* [**14**], a permis de localiser l'activité neuronale à travers l'imagerie des propriétés biomécaniques du cerveau où des variations locales de rigidité indiquent les ensembles de neurones activés par stimulation. Dans cette configuration expérimentale, la région stimulée électriquement (patte arrière) est distincte de la région imagée par ERM (cerveau), si bien que les forces volumiques de Lorentz induites par l'interaction entre le champ magnétique du système IRM et le courant délivré par stimulation peuvent être négligées. Lorsque ces régions concordent, de telles forces volumiques sont présentes dans le champ de mesure et introduisent un terme de source d'onde élastique dans l'équation du mouvement caractéristique d'une expérience d'élastographie. Deux questions se posent alors :

1) ces ondes mécaniques peuvent-elles être mesurées et utilisées en élastographie ?

2) quel est leur impact sur la résolution du problème inverse, habituellement traité à partir d'une formulation sans source ?

Grasland-Mongrain *et al.* [**15, 16**] se sont intéressés à l'imagerie ultrasonore d'ondes élastiques générées par force de Lorentz au moyen d'un aimant et de dispositifs de stimulation électrique et magnétique, et ont produit des champs de déplacements dans différentes configurations expérimentales. L'observation antérieure de tels champs ondulatoires par ERM a été présentée par Basford *et al.* [**17**] où des fantômes conducteurs, soumis à des pulsations électriques par le biais d'électrodes, sont immergés dans le champ magnétique d'un système IRM. La source des ondes imagées par ERM n'a toutefois pas été validée dans la mesure où les électrodes, en plus du fantôme parcouru par une densité de courant, sont susceptibles d'être à l'origine de vibrations observées. Les premiers travaux présentés dans le présent document s'articulent autour de cette thématique et tentent de répondre à la première question ci-dessus avec la conception d'un montage d'ERM favorisant l'isolation de la source de mouvement (forces volumiques de Lorentz), la génération et la mesure de champs ondulatoires

d'amplitude suffisante pour la reconstruction de cartes de rigidité. Ce dernier aspect n'a, à notre connaissance, pas été traité dans le cadre de l'élastographie. Les résultats, décrits dans l'article présenté au **Chapitre 2** et intitulé *Lorentz force induced shear waves for magnetic resonance elastography applications, Scientific Reports, 2021, 11(1), 12785*, indiquent que l'intensité des forces volumiques de Lorentz nécessaire à une mesure d'élastographie de qualité serait difficilement atteignable dans des conditions de stimulation électrique sûres. En revanche, cette particularité suggère que l'ERM traditionnelle pourrait être combinée à la stimulation électrique, de façon similaire à Patz *et al.* [**14**], et en outre cibler une même région d'intérêt, ouvrant ainsi la voie à la caractérisation de la réponse biomécanique du cerveau liée à sa stimulation non-invasive. L'approche combinée de la stimulation non-invasive du cerveau (NIBS, pour *non-invasive brain stimulation*) et de l'imagerie biomécanique par IRM encourage également la cartographie de ses propriétés électriques, permettant la modélisation de la propagation des courants induits par stimulation et par conséquent l'identification des régions stimulées. La tomographie d'impédance électrique par résonance magnétique assure ce pan de l'expérience et peut théoriquement être ajoutée à d'éventuels protocoles de NIBS + ERM. Le traitement de cet aspect et de la deuxième question ci-dessus est amorcé à l'aide de simulations numériques dans un modèle 3D de cerveau de souris décrit dans l'article présenté au **Chapitre 4** et intitulé *Imaging the electro-mechanical properties of the mouse brain during transcranial electrical stimulation : numerical simulations* (prêt à soumettre), où sont évalués la distribution de la conductivité électrique et l'impact des forces volumiques de Lorentz sur la reconstruction de cartes de viscoélasticité via une méthode d'inversion non-linéaire et un modèle mécanique exempt de terme de source.

Micro-élastographie optique d'ovocytes de souris

La mise en évidence de liens entre la mécano-biologie et la fonction cellulaire a initié de nombreuses recherches visant à caractériser la biomécanique des cellules et son rôle [**18, 19**]. Différentes méthodes, adaptées aux petites dimensions et à la fragilité des tissus cellulaires, ont été présentées et ont permis d'établir des mesures globales de rigidité et de viscosité [**20**].

À ce titre, l'identification non-destructive des propriétés mécaniques des domaines cellulaires internes est difficilement réalisable à travers les techniques rhéologiques décrites dans la littérature. En élastographie, des images de distribution de propriétés mécaniques sont produites et permettent d'évaluer la contribution des différents domaines internes imagés. Toutefois, l'induction contrôlée et la mesure d'ondes élastiques présente un degré de difficulté croissant avec la réduction de la taille de l'objet étudié. En particulier, le recours à des fréquences d'oscillations bien supérieures à la gamme de fréquences caractéristiques de l'élastographie macroscopique peut être anticipé de façon à induire un champ ondulatoire de longueur d'onde adaptée aux dimensions de la cellule. Grasland-Mongrain *et al.* ont récemment abordé cette difficulté et ont proposé la micro-élastographie optique permettant la génération et l'imagerie de champs de déplacements dans des ovocytes de souris d'un diamètre avoisinant 85 µm avec une résolution temporelle et spatiale de l'ordre de la milliseconde et du micromètre, respectivement [**2**]. Des mesures de corrélation spatiotemporelles opérées sur ces images de déplacements ont ensuite abouti à la cartographie pixel-par-pixel de la longueur d'onde et des cartes de rigidité ont finalement été produites sous l'hypothèse de la mesure d'ondes de cisaillement. Cette approche inédite ouvre la voie à l'étude biomécanique, résolue spatialement, de mécanismes cellulaires à des échelles de temps et de distance jusqu'alors inexplorées.

Récemment, Yanez *et al.* ont démontré que le devenir d'un ovocyte après fécondation *in vitro* peut être prédit à partir des propriétés mécaniques de ce dernier [**21**]. En particulier, la mesure de la viscoélasticité des embryons résultant a permis de distinguer les cellules les plus viables des moins viables avec plus de précision qu'une caractérisation purement élastique. L'application de la MEO à la description viscoélastique d'ovocytes est alors toute indiquée mais introduit néanmoins deux obstacles importants :

1) la composante visqueuse, responsable d'effets de faible amplitude de courbure du champ de déplacements et d'atténuation, est difficile à reconstruire en élastographie,

2) le champ ondulatoire mesuré est composé, en toute hypothèse, de contributions autres que des ondes de cisaillement uniquement.

Ces deux aspects sont discutés dans l'article présenté au **Chapitre 5** et intitulé *Imaging the subcellular viscoelastic properties of mouse oocytes, PNAS, 2023, 120(21), e2213836120.*

Chapitre 1

Élastographie

Les travaux de recherche présentés dans ce document s'articulent autour de l'élastographie harmonique. Les principes généraux regroupant des sollicitations quasi-statiques et dynamiques applicables à différentes modalités d'imagerie sont exposés dans la section 1.1 de ce chapitre. La section 1.2 porte une attention particulière aux méthodes de reconstruction d'images de viscoélasticité isotropique utilisées en élastographie par résonance magnétique harmonique (ERM). La méthode d'estimation locale de la fréquence (LFE pour *local frequency estimation*), utilisée dans les travaux constituant l'article 1, y est présentée. La section 1.3 est consacrée à la méthode d'inversion non-linéaire (NLI pour *nonlinear inversion*) par sous-zones, employée dans les travaux décrits par les articles 2 et 3.

1.1. Principes de l'élastographie

L'imagerie de la rigidité des tissus biologiques a longuement été motivée par la palpation manuelle de la peau et des organes superficiels. La détection au toucher d'une région de texture différente de celle de son milieu environnant demeure une approche diagnostique essentielle exercée par les médecins et les patients. L'imagerie complémente cette pratique par sa capacité à délimiter une région d'intérêt et à en mesurer quantitativement les propriétés mécaniques, souvent sensibles à une évolution pathologique. L'élastographie consiste ainsi à produire des cartes de viscoélasticité du tissu imagé, caractérisée par la réponse du milieu à une déformation imposée. La sollicitation du tissu par l'application d'une contrainte

mécanique est donc nécessaire de manière à en mesurer et interpréter la réponse sous forme de dissipation d'énergie et de résistance mécanique. La nature de la contrainte appliquée détermine le type d'élastographie, *i.e.*, quasi-statique ou dynamique.

1.1.1. Élastographie quasi-statique

Cette approche vise à cartographier la déformation interne du tissu résultant de l'application d'une contrainte externe et à en extraire un taux de déformation en % ou un module d'élasticité en pascal (Pa). La quantification de la déformation est obtenue par corrélation des images de texture acquises avant et pendant la sollicitation. Lorsque la contrainte est connue, la relation contrainte-déformation permet l'extraction d'une distribution absolue des paramètres mécaniques. Le manque d'information sur la contrainte imposée permet toutefois une reconstruction relative des propriétés.

La première description de l'élastographie quasi-statique, présentée par Ophir *et al.* en 1991 [**22**], repose sur l'application d'une compression imagée par ultrasonographie (US). Cette contrainte est souvent exercée dans une direction parallèle au plan d'imagerie ce qui limite la sensibilité de la mesure à des déformations proches de la sonde d'acquisition. L'ultrasonographie et la tomographie par cohérence optique (OCT) en sont des exemples avec des profondeurs d'interrogation de quelques centimètres et quelques millimètres, respectivement. L'élastographie quasi-statique ultrasonore a notamment été employée dans le cadre de la mesure de la déformation locale du cœur [**23, 24, 25, 26**] et de la détection de plaque carotidienne [**27, 28, 29**]. Dans une moindre mesure, l'élastographie quasi-statique par OCT a permis la mesure de la rigidité de microstructures [**30, 31**] et de parois vasculaires [**32, 33**]. L'IRM a également permis la mise en œuvre de l'élastographie quasi-statique [**34, 35, 36, 37**].

1.1.2. Élastographie dynamique

Les premières estimations de rigidité *in vivo* à partir de la mesure de déplacements temporels ont été publiées par Krouskop *et al.* en 1987, où des vibrations générées par une

pulsation en surface sont suivies par un système Doppler ultrasonore [**38**]. Une extension de cette approche à l'imagerie par effet Doppler a permis à Lerner *et al.* [**39**] et Parker *et al.* [**40**] de produire des images de rigidité par ultrasons. Cette approche de *sonoélasticité* est à l'origine de l'élastographie contemporaine.

Deux régimes d'excitation temporelle sont principalement adoptés en élastographie dynamique : transitoire et harmonique. Dans les deux cas, la contrainte peut être appliquée à la surface du tissu, comme en élastographie quasi-statique, ou générée à l'intérieur par le biais d'une force distribuée dans le milieu et suffisamment intense dans la zone ciblée pour engendrer une déformation. L'élastographie par ultrasons focalisés (FUSE) supporte ces deux régimes et consiste à concentrer en un point choisi l'énergie mécanique transmise au tissu par le biais d'une sonde ultrasonore. La dilatation et contraction subséquente du matériau au point focal génère une onde élastique dont la propagation est suivie par échographie sous forme d'une série de cartes temporelles de déplacements locaux. L'excitation est transitoire dans le cas d'une impulsion ultrasonore unique, ou harmonique dans le cas d'une excitation régulière répétée à une fréquence donnée. Les déplacements peuvent également être produits à la surface du tissu par un dispositif impulsionnel ou vibratoire et être mesurés, comme en FUSE, par échographie. Cette approche vibratoire est privilégiée en élastographie IRM, présentée en 1995 par Muthupillai *et al.* [**41**], où des déplacements harmoniques sont générés par une oscillation guidée de la surface du milieu et se propagent à travers la région d'intérêt. Quelques résultats d'activation transitoire à travers la génération de déplacements par ultrasons focalisés ont été présentés en MRE [**42, 43, 44**]. Cependant, la faible résolution temporelle de l'IRM par rapport à l'US complexifie le suivi de la propagation de l'onde élastique en temps réel. L'application d'une contrainte harmonique, synchronisée avec la séquence IRM d'acquisition d'image, est par conséquent principalement utilisée en MRE.

L'imagerie optique a encouragé la transposition de l'élastographie dynamique à des échelles difficilement accessibles à l'US et l'IRM, tant spatialement que temporellement. Notamment, l'élastographie par cohérence optique (OCE), initialement présentée par Jacques *et al.* [**45**] et Schmitt [**46**] en 1998, a permis de cartographier la rigidité de la cornée, tout

d'abord globalement puis à différentes profondeurs séparées de quelques dizaines de microns, ouvrant ainsi une voie d'application clinique en ophtalmologie [**11, 47, 48, 49, 50, 51, 52**]. D'autres exemples d'application de l'OCE ont été publiés avec l'imagerie de rigidité intravasculaire [**53, 54**] et du cerveau de souris *ex vivo* [**55, 56**]. L'élastographie photo-acoustique, présentée en 2011 par Gao *et al.* [**57**], offre des possibilités d'imagerie encourageantes démontrées *ex vivo* dans le cadre d'endoscopie [**58**] et de cirrhose du foie [**59, 60**], et *in vivo* avec la caractérisation mécanique des vaisseaux sanguins dans le doigt humain [**60**].

En 2017, Grasland-Mongrain *et al.* [**2**] ont proposé la micro-élastographie optique à travers la cartographie non-invasive et ultra-rapide de la rigidité de cellules individuelles à une résolution de l'ordre de 500 nanomètres. Cette approche par microscopie en champ clair repose sur l'imagerie de la réponse d'une cellule à l'application d'une vibration haute fréquence ($\sim$ 15 kHz) à sa surface. La vibration générée par un cristal piézoélectrique est transmise à la cellule par le biais d'une micropipette. Les microdéformations induites dans le milieu par la perturbation harmonique externe sont simultanément capturées par une caméra CMOS (*Complementary Metal–Oxide–Semiconductor*) à des fréquences de l'ordre de 200 kHz puis quantifiées sous forme de déplacements par corrélation d'images. Les cartes de déplacements sont ensuite converties en cartes de rigidité par la résolution d'un problème inverse défini par la modélisation mécanique de la cellule.

1.2. Reconstruction d'images de viscoélasticité en ERM

En élastographie, les cartes de déplacements ou de déformations du tissu constituent l'observation nécessaire à la reconstruction de cartes de propriétés mécaniques. Un problème inverse est alors formulé à partir d'un problème direct décrivant la réponse du matériau à la sollicitation. Bien que les principes physiques sous-jacents soient indépendants des modalités d'imagerie, la modélisation mécanique est souvent abordée selon les caractéristiques particulières de la technique de détection utilisée (dimension et (an)isotropie de la résolution de l'image principalement). En MRE, les déplacements peuvent être mesurés le long des trois

axes de l'espace dans plusieurs plans successifs, permettant ainsi l'intégration de jeux de données 3D complets à la modélisation mécanique et formulation du problème inverse.

L'équation de Navier dans le domaine fréquentiel décrit la réponse d'un solide hétérogène, viscoélastique et isotrope à une contrainte harmonique :

$$\nabla \cdot (\mu \nabla \mathbf{u}) + \nabla \left((\lambda + \mu) \nabla \cdot \mathbf{u} \right) = -\rho \omega^2 \mathbf{u} \tag{1}$$

où $\mathbf{u}$ (m) est le champ de déplacements complexes dans les trois directions de l'espace, μ (Pa) est le module de cisaillement, λ (Pa) est le premier coefficient de Lamé, ρ (kg.m^{-3}) est la densité du matériau et ω (rad.s^{-1}) est la pulsation de la contrainte. De multiples stratégies ont été proposées afin d'extraire des cartes de module de cisaillement à partir de ce modèle et des déplacements mesurés. Les méthodes de reconstruction les plus rencontrées en MRE sont présentées dans cette section.

1.2.1. Approches directes

Les approches directes consistent à reformuler l'équation (1) au moyen d'une série d'hypothèses de telle manière que le module de cisaillement devienne l'unique inconnue à estimer. Dans le cas de déplacements volumiques dans un matériau localement homogène, la séparation du champ de déplacement total $\mathbf{u}$ en deux champs de compression $\mathbf{u}_c = \nabla \phi$ et de cisaillement $\mathbf{u}_s = \nabla \times \boldsymbol{\psi}$, où ϕ et $\boldsymbol{\psi}$ sont des potentiels de Helmholtz, permet d'établir deux équations de propagation indépendantes reliant les champs ϕ et $\boldsymbol{\psi}$ aux propriétés mécaniques du matériau :

$$\mu \Delta \boldsymbol{\psi} = -\rho \omega^2 \boldsymbol{\psi}, \tag{2}$$

$$(\lambda + 2\mu) \Delta \phi = -\rho \omega^2 \phi. \tag{3}$$

Dans ces conditions, l'équation (2) permet l'évaluation directe de μ à partir du rotationnel du champ de déplacements mesuré $\mathbf{u}$. Cette approche, mise en pratique en MRE par Sinkus *et al.* [**61**], requiert la détection d'un champ de déplacements complet et 3D, et le calcul de dérivées spatiales du 3$^{\text{ème}}$ ordre.

Lorsque le solide est viscoélastique et que la contrainte appliquée au milieu est harmonique, le module de cisaillement et les déplacements formulés dans le domaine fréquentiel sont à valeurs complexes. La viscoélasticité du matériau peut alors être évaluée grâce aux parties réelle et imaginaire du module de cisaillement $\mu = \mu_r + i\mu_i$, aussi appelées modules de stockage (μ_r) et de perte (μ_i). Le module de stockage représente l'énergie que le solide peut emmagasiner sous forme de déformation élastique et le module de perte représente l'énergie dissipée dans le milieu. Par exemple, la viscoélasticité du cerveau humain [**62, 63, 64**] et de souris [**65**], du foie [**66, 67**], du sein [**68**] et de la prostate *ex vivo* [**69**] a été évaluée par le biais de cette décomposition en champs de rotationnel et divergence nuls.

Une approche par éléments finis d'inversion directe de l'équation de Navier, localement homogène et compressible, a été présentée par Fovargue *et al.* [**70**]. Celle-ci consiste à limiter l'impact du champ de compression sans recourir au rotationnel à travers l'élimination du terme de pression via l'utilisation de fonctions de forme à divergence nulle. La suppression de la composante $\mathbf{u}_c$ du champ total $\mathbf{u}$ a également été abordée dans l'espace des fréquences spatiales par le filtrage des composantes centrales autour de $(k_x, k_y, k_z) = 0$, ou par l'hypothèse d'un champ ondulatoire de pur cisaillement où $\mathbf{u} = \mathbf{u}_s$. Ces approches, présentées par Oliphant *et al.* [**71**] et Manduca *et al.* [**72, 73**], permettent d'éviter le calcul du rotationnel et l'acquisition de toutes les composantes de mouvement nécessaires. La viscoélasticité du foie [**74, 75**], de cerveaux humains [**74, 76, 77, 78, 79**] et de souris [**80**] a été caractérisée à travers ces méthodes. Quelles que soient les simplifications apportées, l'inversion directe d'équations de type Helmholtz nécessite l'évaluation du ratio entre des mesures bruitées et l'opérateur Laplacien appliqué à ces mesures. Cette manipulation dans des régions de faibles déformations les rend particulièrement sensibles au bruit et déstabilise le processus d'inversion.

Une approche multifréquence, nommée *Multi-Frequency Dual Elasto Visco Inversion* (MDEV), a été proposée par Hirsch *et al.* afin de limiter ces difficultés et consiste à opérer l'inversion sur une somme pondérée des images de déplacements à différentes fréquences [**81**]. L'hypothèse d'une faible dispersion du module de cisaillement permet d'obtenir un duo

unique de cartes de la norme du module de cisaillement complexe $|\mu|$ et de sa phase angulaire Φ à partir de signaux multifréquences. Ceux-ci sont donnés par :

$$|\mu| = \rho \frac{\sum_{j=1}^{3} \sum_{k=1}^{N} \omega_k^2 |u_j^* (\omega_k)|}{\sum_{j=1}^{3} \sum_{k=1}^{N} |\Delta u_j^* (\omega_k)|}, \tag{4}$$

$$\Phi = \arccos \left(- \frac{\sum_{j=1}^{3} \sum_{k=1}^{N} \left[\Delta u_j^{'} (\omega_k) \, u_j^{'} (\omega_k) + \Delta u_j^{''} (\omega_k) \, u_j^{''} (\omega_k) \right]}{\sum_{j=1}^{3} \sum_{k=1}^{N} |\Delta u_j^* (\omega_k)| \, |u_j^* (\omega_k)|} \right), \tag{5}$$

où N est le nombre de fréquences d'oscillations, j = (1,2,3) représente la composante du rotationnel du mouvement complexe, u_j^*, et $u_j^{'} = \Re \left\{ u_j^* \right\}$ et $u_j^{''} = \Im \left\{ u_j^* \right\}$. Cette méthode a notamment été employée pour la caractérisation de la viscoélasticité du cerveau [**82**], du foie et de la prostate [**82, 81**]. Dans la continuité des reconstructions multifréquences, le calcul contraignant du Laplacien des déplacements a été contourné par Tzschätzsch *et al.* avec la méthode k-MDEV où le nombre d'onde d'un champ de déplacement décomposé en une somme d'ondes planes est reconstruit [**83**]. Les cartes de vitesses d'ondes de cisaillement obtenues présentent des contrastes manifestes et identifiables aux structures anatomiques sous-jacentes, notamment dans la zone abdominale [**83, 84, 85**], le cerveau humain [**84, 86**] et de souris [**87**]. Les parties réelle $k^{'}$ et imaginaire $k^{''}$ du nombre d'onde sont données par :

$$k_j^{'} = \left\| \nabla \frac{u_j}{|u_j|} \right\|, \tag{6}$$

et :

$$k_j^{''} = \frac{||\nabla |u_j|||}{|u_j|}. \tag{7}$$

Des cartes spatiales de vitesse c et d'atténuation a de l'onde de cisaillement sont alors produites à partir des expressions suivantes :

$$c = \left(\frac{\sum_{i,j,n} \frac{k_j^{'}(\omega_i, \vartheta_n)}{\omega_i} w_j (\omega_i, \vartheta_n)}{\sum_{i,j,n} w_j (\omega_i, \vartheta_n)} \right)^{-1}, \tag{8}$$

$$a = \left(\frac{\sum_{i,j,n} \frac{2\pi k_j^{''}(\omega_i, \vartheta_n)}{\omega_i} w_j (\omega_i, \vartheta_n)}{\sum_{i,j,n} w_j (\omega_i, \vartheta_n)} \right)^{-1}, \tag{9}$$

où i indique la fréquence angulaire d'oscillation, j indique la composante du mouvement, n indique la direction de l'onde plane et w_j est un poids spatial donné par $w_j(\omega_i, \vartheta_n) = |u_j(\omega_i, \vartheta_n)|^4$. La caractérisation biomécanique via l'évaluation du nombre d'onde est une voie empruntée depuis les débuts de l'élastographie par résonance magnétique, notamment à travers la LFE (*Local Frequency Estimation*), présentée par Westin *et al.* [**88**] et Knutsson *et al.* [**89**] et initialement appliquée à la MRE par Muthupillai *et al.* [**41**]. Cette méthode opère dans l'espace des fréquences spatiales (k_x, k_y, k_z) et ne requiert pas l'estimation de dérivée spatiale des déplacements. Le nombre d'onde local k_0' du champ ondulatoire est évalué par le biais de filtres notés $\tilde{\mathcal{H}}_1$ et $\tilde{\mathcal{H}}_2$ appliqués aux images de déplacements $\tilde{\mathbf{u}} = \mathcal{F}(\mathbf{u})$, où $\mathcal{F}$ dénote la transformée de Fourier spatiale, à travers la relation :

$$\frac{\mathcal{F}^{-1}\left(\tilde{u}_i \cdot \tilde{\mathcal{H}}_2\right)}{\mathcal{F}^{-1}\left(\tilde{u}_i \cdot \tilde{\mathcal{H}}_1\right)} = k_0^{'}. \tag{10}$$

Les filtres $\tilde{\mathcal{H}}_1$ et $\tilde{\mathcal{H}}_2$ sont reliés par :

$$\tilde{\mathcal{H}}_2(k', \vartheta; k_C) = k^{'} \cdot \tilde{\mathcal{H}}_1\left(k^{'}, \vartheta; k_C\right) = k_C \cdot \sqrt{2}\tilde{\mathcal{H}}_1\left(k^{'}, \vartheta, 2k_C\right), \tag{11}$$

où k_C est la fréquence centrale du filtre défini par :

$$\tilde{\mathcal{H}}_1\left(k^{'}, \vartheta; k_C\right) = R_C(k') \cdot \sum_{m=1}^{N_d} D_m(\vartheta), \tag{12}$$

où N_d est le nombre de dimensions spatiales, $R_C(k')$ est la partie radiale du filtre dont l'indice C indique la fréquence centrale et D_m est un filtre directionnel dans la direction ϑ par rapport à chaque dimension m. La partie radiale $R_C(k')$ est donnée par :

$$R_C(k') = \exp\left(-\frac{2}{2\ln 2}\ln^2\left(\frac{k^{'}}{k_C}\right)\right), \tag{13}$$

Le filtre D_m est donné par :

$$D_m(\vartheta) = \begin{cases} \left(\hat{\mathbf{k}}' \cdot \hat{\mathbf{n}}_m\right)^2 & \text{si } \left(\hat{\mathbf{k}}' \cdot \hat{\mathbf{n}}_m\right) > 0, \\ 0 & \text{sinon.} \end{cases} \tag{14}$$

La figure 1.a résume les étapes principales suivies par l'algorithme LFE. Les figures 1.b, 1.c et 1.d présentent respectivement un exemple de la partie radiale d'un filtre lognormal (Eq. 13), d'un filtre directionnel le long de l'axe vertical (Eq. 14) et du produit des deux (Eq. 12).

① $\mathbf{u}(\mathbf{x}) = \begin{bmatrix} u_1 \\ u_2 \\ u_3 \end{bmatrix}(\mathbf{x}) \longrightarrow \tilde{u}_i(\mathbf{k}) = \mathcal{F}_{2D}(u_i(\mathbf{x}))$

② Filtre lognormal $\tilde{\mathcal{H}}_1$

③ $\dfrac{\mathcal{F}^{-1}\left(\tilde{u}_i \cdot \tilde{\mathcal{H}}_1(k', \vartheta; 2k_C)\right)}{\mathcal{F}^{-1}\left(\tilde{u}_i \cdot \tilde{\mathcal{H}}_1(k', \vartheta; k_C)\right)} = \dfrac{k'_0}{k_C\sqrt{2}}.$

(a) Étapes principales de l'algorithme LFE

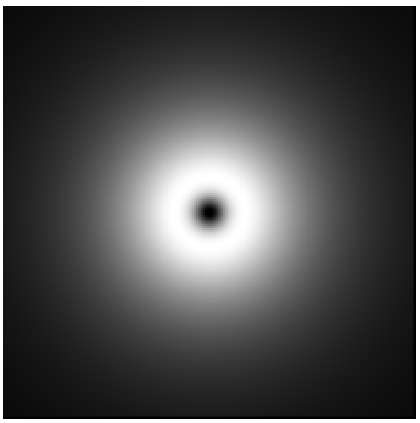

(b) Partie radiale du filtre lognormal (Eq. 13)

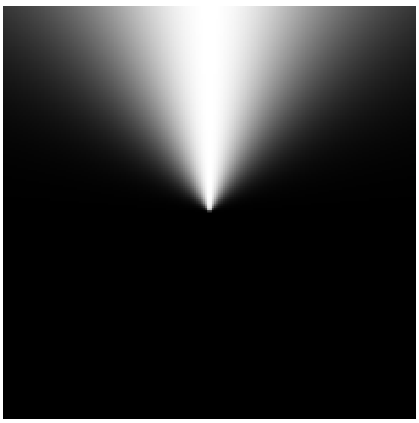

(c) Filtre directionnel (Eq. 14)

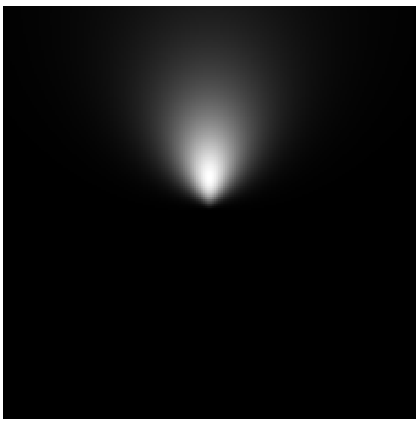

(d) Produit de la partie radiale et angulaire (Eq. 12)

Figure 1 – Résumé de l'algorithme LFE et exemples des fonctions utilisées

Braun *et al.* [**90**] et McGee *et al.* [**91**] ont décrit l'utilisation de LFE avec d'autres types de filtres. Le nombre d'onde du champ ondulatoire estimé est relié à la vitesse de l'onde qu'il caractérise par $c = \lambda f$ où λ est la longueur d'onde et f est la fréquence temporelle. Cette approche est équivalente à l'inversion de l'équation de Helmholtz dans un solide élastique, *i.e.*, sans amortissement, localement homogène et isotrope [**92**]. LFE a été employée dans tout type d'expérience d'élastographie. Le poumon [**93**], le foie [**94**], la prostate [**95**], le cerveau [**96, 97**], le cœur [**98**] et des fantômes [**99**] en sont quelques exemples. Lorsque la vitesse c

du champ ondulatoire est cartographiée, la (visco)élasticité du matériau est caractérisée par la rigidité de cisaillement (*shear stiffness*) définie par $\mu_S = \rho c^2$. Pour un matériau viscoélastique, $\mu_S = 2\left|\mu\right|^2 / \left(\mu_r + \left|\mu\right|\right)$. Pour un matériau purement élastique, $\mu_S = \mu_r$. Si la rigidité de cisaillement μ_S et la vitesse c peuvent être identifiées à partir du module de cisaillement complexe, l'opération inverse nécessite la caractérisation de l'atténuation du champ de déplacements dans le milieu, souvent considérée par le biais d'un modèle rhéologique et d'une décomposition du champ de déplacements en ondes planes (voir équation (9)).

Bien que l'élastographie soit fondée sur la détection d'hétérogénéité structurelle, l'hypothèse d'homogénéité locale est souvent invoquée et permet de négliger la variation spatiale locale des propriétés mécaniques et d'extraire les variables μ et λ des opérateurs différentiels de l'équation (1). Quelques exceptions ont été présentées, notamment par Barnhill *et al.* [**100**] avec la méthode *Heterogeneous Multifrequency Direct Inversion* (HMDI). Celle-ci suppose que la divergence des déplacements et la dispersion du module de cisaillement aux fréquences imposées sont négligeables. Des déplacements induits à plusieurs fréquences sont tout d'abord mesurés afin de surdéterminer le module de cisaillement, puis un système global d'équations hétérogènes du mouvement à chaque fréquence est défini, où le gradient des propriétés mécaniques est conservé dans la matrice des coefficients. Les reconstructions obtenues présentent davantage de contraste que MDEV mais demeurent quantitativement similaires. Sánchez *et al.* [**101**] ont également proposé une approche où l'hétérogénéité de la distribution des propriétés mécaniques est maintenue dans l'équation du mouvement. Cette méthode consiste à formuler la reconstruction du module de cisaillement comme un problème de minimisation où $\mu = \operatorname{argmin}\left\{\left|\nabla\mu\right|^2\right\}$, et où μ est contraint de vérifier l'équation du mouvement (exempte du terme de compression).

Le traitement spécifique des ondes de compression dans les milieux quasi-incompressibles, outre le filtrage des basses fréquences spatiales, a également été abordé par des formulations directes du problème inverse en éléments finis. Honarvar *et al.* [**102**] ont notamment publié une formulation faible de l'équation de Navier hétérogène à laquelle l'opérateur rotationnel a été appliqué afin d'éliminer le champ de compression. Par ailleurs, une formulation mixte

déplacements-pression du problème direct a été employée par Honarvar *et al.* [**103, 104**] dans laquelle le champ de déplacements $\mathbf{u}$ et le terme de pression $p = -K\nabla \cdot \mathbf{u}$ sont les inconnues du problème, où K (Pa) est le module de compressibilité isostatique. Cette formulation évite le verrouillage numérique lorsque le matériau se rapproche de l'incompressibilité et est conservée à l'établissement du problème inverse où μ et p sont les inconnues à reconstruire [**105**].

Dans un autre contexte, l'élastographie passive, issue de l'ultrasonographie et décrite par Catheline *et al.* [**106**], permet d'estimer les longueurs d'ondes des vibrations naturellement présentes dans le corps, sans activation externe. Cette méthode repose sur le concept de retournement temporel exposé par Fink en 1992 [**107**] et consiste à identifier les maxima de corrélation entre deux champs de déplacements temporels, l'un dans la direction des temps croissants et l'autre dans la direction des temps décroissants. La fonction de corrélation est donnée par le produit de convolution :

$$\Psi^{TR}(\mathbf{r}, -t) = u_m(\mathbf{r}_0, -t) \underset{t}{\otimes} u_m(\mathbf{r}, t), \tag{15}$$

où u_m est la m$^{\text{ème}}$ composante du mouvement mesuré. La carte des maxima de corrélation indique la position des sources virtuelles, ou tâches focales, vers lesquelles le champ ondulatoire se rétro-propagerait dans une expérience de retournement temporel. La taille de ces sources virtuelles est contrainte par le critère de Rayleigh imposant une taille minimum de la tâche focale environ égale à la demi-longueur d'onde du champ ondulatoire. Une carte de longueurs d'onde peut ainsi être extraite de l'information portée par la fonction de corrélation, et être convertie en carte de vitesses c. L'approche d'élastographie passive par retournement temporel requiert que le champ ondulatoire mesuré vérifie l'équation de propagation d'onde dans un solide purement élastique (*i.e.* sans atténuation), localement homogène et isotrope. L'équation d'onde est donnée par :

$$\Delta\Phi - \frac{1}{c^2}\frac{\partial^2\Phi}{\partial t^2} = 0, \tag{16}$$

où Φ est un champ vectoriel se propageant. Par conséquent, la mesure expérimentale Φ peut être représentée sous la forme de cartes de déplacements u_m, de taux de déformation $\varepsilon_{m,n}$ ou de vitesses particulaires v_m, chacune de ces quantités étant caractérisée par une vitesse de propagation c. Toutefois, la conversion de cartes de vitesses en cartes de rigidités n'est possible que si le champ ondulatoire évalué est un champ de cisaillement. En pratique, une alternative à la mesure de la taille de la tâche focale consiste à approximer la longueur d'onde à partir des champs de déplacements et du taux de déformation retournés temporellement. Ce dernier est exprimé de façon similaire à l'équation (15) :

$$\xi^{TR}(\mathbf{r}, -t) = \varepsilon_{m,n}(\mathbf{r}_0, -t) \underset{t}{\otimes} \varepsilon_{m,n}(\mathbf{r}, t), \tag{17}$$

Le nombre d'onde k peut ensuite être obtenu par hypothèse d'ondes planes grâce à la notation complexe $\varepsilon_{m,n} = ik_n u_m$. Suite à cette hypothèse, l'équation (17) évaluée à $t = 0$ et $\mathbf{r} = \mathbf{r}_0$ s'écrit :

$$\xi_0^{TR} \approx -k^2 \Psi_0^{TR}, \tag{18}$$

où :

$$\begin{cases} \Psi_0^{TR} = \Psi^{TR}(\mathbf{r}_0, t_0), \\ \xi_0^{TR} = \xi^{TR}(\mathbf{r}_0, t_0). \end{cases} \tag{19}$$

Le nombre d'onde k est alors donné par :

$$k = \frac{2\pi}{\lambda} \approx \sqrt{-\frac{\xi_0^{TR}}{\Psi_0^{TR}}}. \tag{20}$$

Cette approche d'élastographie passive a principalement été employée en ultrasonographie [**108, 109, 110**]. Quelques exceptions ont toutefois été présentées, notamment par Zorgani *et al.* [**111**] en MRE et Grasland-Mongrain *et al.* [**2**] en micro-élastographie optique.

1.2.2. Approches indirectes

Par opposition aux approches directes où les distributions des propriétés mécaniques $\boldsymbol{\theta}$ sont obtenues par manipulation du champ de déplacements mesuré $\mathbf{u}_m$, les approches itératives consistent à identifier $\boldsymbol{\theta}$ à partir de simulations numériques de champs de déplacements

$\mathbf{u}_s = f(\boldsymbol{\theta})$ dans le tissu imagé au moyen d'un modèle mécanique. La reconstruction s'opère par des modifications successives de $\boldsymbol{\theta}$ grâce à l'évaluation de l'écart entre les déplacements mesurés et les déplacements simulés. La distribution $\boldsymbol{\theta}$ à l'itération $j+1$, notée $\boldsymbol{\theta}_{j+1}$, est une mise à jour de $\boldsymbol{\theta}_j$, modifiée de manière à réduire cet écart. Les simulations numériques de $\mathbf{u}_s$ sont assurées par la discrétisation du modèle mécanique dans un domaine défini par la géométrie du tissu. La mise à jour de la distribution $\boldsymbol{\theta}_j$ à chaque itération j est obtenue par la minimisation d'une fonction objectif définie en fonction de l'écart entre $\mathbf{u}_m$ et $\mathbf{u}_s$. Dans le modèle viscoélastique décrit par l'équation (1), $\boldsymbol{\theta}$ peut représenter le module de cisaillement μ, le coefficient de Lamé λ (ou le module de compressibilité K) et/ou la masse volumique ρ du matériau. Les procédures d'inversions itératives sont numériquement plus complexes que celles d'inversions directes, souvent mal conditionnées, mais assurent une plus grande fidélité du modèle mécanique aux conditions expérimentales et une meilleure tolérance au bruit de mesure. Des exemples de processus d'inversion non-linéaire en élastographie sont donnés par Kallel et Bertrand en ultrasonographie [**112**], Oberai *et al.* [**113**] et Samani *et al.* [**114**] en MRE quasi-statique, et Honarvar *et al.* [**103**] et Van Houten *et al.* [**115**] en MRE harmonique. Le problème inverse formulé à partir des équations tri-dimensionnelles des modèles continus et harmoniques de viscoélasticité, impliquant les parties réelles et imaginaires des trois composantes de mouvements, représente un coût calculatoire important. La taille du problème a été réduite par Honarvar *et al.* en 2012 [**103**] grâce à une représentation parcimonieuse des propriétés $\boldsymbol{\theta}$ dans l'espace des cosinus discrets, diminuant ainsi le nombre d'inconnues à reconstruire. Une approche différente, appelée *Overlapping Subzone Nonlinear Inversion*, a été proposée en 1999 par Van Houten *et al.* [**116**] où les propriétés sont reconstruites séparément dans des fractions du domaine total, appelées sous-zones, puis combinées pour former une image globale. Depuis, cette approche a bénéficié de nombreux développements visant à stabiliser la reconstruction et à inclure davantage de modèles mécaniques.

1.3. Inversion non-linéaire par sous-zones (NLI)

1.3.1. Présentation générale

La méthode d'inversion non-linéaire par sous-zones est formulée suivant une procédure d'optimisation de distribution des propriétés mécaniques étant donné une mesure expérimentale de déplacements dans les trois directions de l'espace. La fonction objectif représentant l'écart entre les déplacements mesurés $\mathbf{u}_m$ et les déplacements simulés par éléments finis $\mathbf{u}_s$, selon une distribution de propriété $\boldsymbol{\theta}$ et un modèle mécanique, est définie par :

$$\Phi = \frac{1}{2} \left(\mathbf{u}_s \left(\boldsymbol{\theta} \right) - \mathbf{u}_m \right)^H \left(\mathbf{u}_s \left(\boldsymbol{\theta} \right) - \mathbf{u}_m \right). \tag{21}$$

La minimisation itérative de Φ est opérée dans des sous-zones individuelles Ω_z traitées indépendamment les unes des autres. La distribution globale des propriétés, $\boldsymbol{\theta}_\Omega$, est alors donnée par une combinaison d'un ensemble de minimisations individuelles de Φ à l'échelle de chaque sous-zone, notée Φ_{Ω_z}, [**116, 117**] :

$$\boldsymbol{\theta}_\Omega = \sum_{z=1}^{Nz} \underset{\boldsymbol{\theta}_{\Omega_z}}{\operatorname{argmin}} \left(\Phi_{\Omega_z} \right), \tag{22}$$

où N_z est le nombre de sous-zones et $\boldsymbol{\theta}_{\Omega_z}$ est la distribution identifiée dans la sous-zone z. Les sous-zones sont des quadrilatères et sont générées aléatoirement dans le domaine total au début de chaque itération globale. Leur taille et taux de recouvrement sont prescrits par l'utilisateur et sont spécifiques au problème étudié. L'utilisation récurrente de NLI au cours de la dernière décennie a permis d'étalonner ces paramètres dans le cadre de l'élastographie du cerveau [**118**].

La minimisation exprimée par (22) génère une distribution de propriété $\boldsymbol{\theta}_\Omega$ sans information préalable de l'utilisateur. La seule contrainte imposée à $\boldsymbol{\theta}_{\Omega_z}$ est de minimiser l'équation (21) pour chaque sous-zone. La reconstruction peut toutefois être influencée par l'ajout de termes de régularisation à la fonction objectif de manière à favoriser un comportement spécifique de la distribution reconstruite. Deux types de régularisation incorporés à l'algorithme

NLI ont principalement été employés : la minimisation de la variation totale (TV) et la régularisation à partir d'information spatiale préalable, *Soft Prior Regularization* (SP) [**119**]. La régularisation TV pénalise le gradient des propriétés en en limitant la variation locale. La régularisation SP permet d'inclure une information préalable sur la structure du domaine imagé à travers une segmentation en régions distinctes et promeut une distribution homogène dans chacune des régions identifiées, sans pour autant en pénaliser le gradient aux frontières. La fonction objectif définie dans chaque sous-zone et comprenant les termes de régularisation TV et SP est donnée par :

$$\begin{aligned}\Phi\left(\boldsymbol{\theta}\right) = & \frac{1}{2}\left(\mathbf{u}_s\left(\boldsymbol{\theta}\right) - \mathbf{u}_m\right)^H \left(\mathbf{u}_s\left(\boldsymbol{\theta}\right) - \mathbf{u}_m\right) \\ & + \iiint_{\Omega_z} \left(\alpha_{TV}\sqrt{\nabla\boldsymbol{\theta}^H \nabla\boldsymbol{\theta}}\right) dV \\ & + \alpha_{SP}\boldsymbol{\theta}^T \left[\mathbf{L}\right]^T \left[\mathbf{L}\right]\boldsymbol{\theta},\end{aligned} \tag{23}$$

où les indices Ω_z ont été abandonnés pour alléger le texte. La quantité de régularisation à appliquer est ajustable grâce aux paramètres α_{TV} pour la régularisation TV et α_{SP} pour la régularisation SP. Le vecteur $\nabla\boldsymbol{\theta}$ est le gradient de la propriété $\boldsymbol{\theta}$. La matrice $\mathbf{L}$ décrit la connexion entre les points du domaine et leur appartenance à chaque région ségmentée par l'utilisateur [**119, 120, 121**]. Il est important de rappeler que la minimisation s'opère à l'échelle de la sous-zone, si bien que des régions homogènes réparties à travers plusieurs sous-zones sont malgré tout traitées indépendamment dans leur zone d'appartenance.

1.3.2. Modèle mécanique

La discrétisation en éléments finis mise en oeuvre dans NLI permet la description de matériaux complexes à travers des modèles mécaniques généraux. Les solides décrits au cours des chapitres suivants sont modélisés comme des matériaux hétérogènes, viscoélastiques, quasi-incompressibles et isotropes, soumis à une excitation harmonique de pulsation ω. Une formulation mixte impliquant les variables de déplacements et de pression est introduite de manière à éviter le verrouillage numérique lorsque $\nabla\cdot\mathbf{u}$ tend vers 0 [**105**]. Le problème direct

aux conditions limites est donné par [**122**] :

$$\begin{cases} \nabla \cdot (\mu \nabla \mathbf{u}) + \nabla (\mu \nabla \cdot \mathbf{u} - p) = -\rho \omega^2 \mathbf{u} & \text{in } \Omega, \\ Ktr(\boldsymbol{\varepsilon}) = -p & \text{dans } \Omega, \\ \mathbf{u} = \mathbf{u}_0 & \text{sur } \Gamma_u, \\ \mathbf{n} \cdot \boldsymbol{\sigma}_E = \mathbf{f}_0 & \text{sur } \Gamma_\sigma, \end{cases} \tag{24}$$

où Ω est le domaine représentant le matériau, Γ_u et Γ_σ sont les frontières du domaine Ω, $\mathbf{u}$ est le champ de déplacements à valeurs complexes, μ est le module de cisaillement complexe, p est le champ de pression, ρ est la densité, K est le module de compressibilité défini par $K = (2\mu + 3\lambda)/3$, ε est le tenseur des déformations, $\mathbf{u}_0$ est le vecteur des déplacements imposés aux frontières Γ_u, $\mathbf{f}_0$ est le vecteur des forces de traction exercées dans la direction $\mathbf{n}$ normale à la surface Γ_σ et σ_E est le tenseur des contraintes exercées sur le solide.

1.3.3. Ajustement itératif des distributions des propriétés

L'écart entre les déplacements mesurés et les déplacements simulés défini par l'équation (21) est une mesure de l'erreur de l'identification au cours du processus de reconstruction. Chaque itération consiste donc à identifier une direction dans laquelle chercher une nouvelle distribution des propriétés de telle sorte que l'erreur de reconstruction décroit. Cette étape à l'itération $i+1$ est représentée par :

$$\boldsymbol{\theta}_{i+1} = \boldsymbol{\theta}_i + \alpha_i \mathbf{p}_i, \tag{25}$$

où $\mathbf{p}_i$ est la "direction de recherche" appelée direction de descente et α_i représente la distance à parcourir dans la direction $\mathbf{p}_i$ garantissant une mise à jour suffisamment satisfaisante des propriétés. L'identification de α_i et $\mathbf{p}_i$ constitue un problème d'optimisation numérique dont la résolution peut être abordée selon différentes approches. La méthode du gradient conjugué a été utilisée dans les travaux des articles 2 et 3 et est présentée dans le paragraphe suivant. La suite de cette section repose sur la description de l'algorithme NLI formulée par

McGarry (thèse) [**117**] et sur le contenu des références Tan *et al.* [**122**], Martins et Ning [**1**], et Shewchuk [**123**]. Les notations définies dans McGarry [**117**] sont conservées ici.

1.3.3.1. *Direction de descente par la méthode des Gradients Conjugués (CG)*

La méthode des Gradients Conjugués repose sur l'observation qu'une direction de croissance certaine vers le maximum de la fonction Φ est fournie par son gradient $\nabla\Phi$, pointant dans la direction de croissance la plus rapide. Une direction de descente $\mathbf{p}$ vers le minimum de Φ peut alors être obtenue dans la direction opposée de son gradient, *i.e.*, $-\nabla\Phi$. Toutefois, l'unique référence au gradient de Φ comme direction de descente peut aboutir à une récurrence des directions de recherche de minimum. La méthode des Gradients Conjugués permet d'identifier une direction de descente en prenant en compte les directions de descentes précédentes et impose que les directions successives soient conjuguées. La direction $\mathbf{p}$ à l'itération i est donnée par :

$$\mathbf{p}_i = -\nabla\Phi_i + \beta_i \mathbf{p}_{i-1}, \tag{26}$$

où β_i peut être obtenu par la formule de Polak–Ribière :

$$\beta_i = \frac{\nabla\Phi_i^H \left(\nabla\Phi_i - \nabla\Phi_{i-1}\right)}{\nabla\Phi_{i-1}^H \nabla\Phi_{i-1}}. \tag{27}$$

Une contrainte sur le signe de β_i garantit que la direction $\mathbf{p}_i$ ainsi obtenue est une direction de descente : $\beta_i \leftarrow \max(0, \beta_i)$.

Le calcul du gradient de la fonction objectif, nécessaire à l'identification d'une direction de descente, est abordé selon la nature du problème d'optimisation. Différentes approches sont présentées dans Nocédal et Wright [**124**] et Martins et Ning [**1**]. À première vue, l'évaluation de la variation de la fonction objectif Φ au voisinage $\pm\delta\boldsymbol{\theta}_i$ d'une propriété $\boldsymbol{\theta}_i$ est coûteuse dans la mesure où elle requiert la résolution du problème aux conditions limites $\mathbf{u}_s = f\left(\boldsymbol{\theta}_i \pm \delta\boldsymbol{\theta}_i\right)$ pour chaque perturbation $\boldsymbol{\theta}_i \pm \delta\boldsymbol{\theta}_i$. Dans le cadre du problème viscoélastique et de NLI, le gradient $\nabla\Phi$ est calculé par la méthode de l'état adjoint décrite par Oberai, Barbone et collègues [**113, 125, 126, 127, 128**] et est mise en oeuvre dans l'algorithme NLI par McGarry [**117**] et Tan *et al.* [**122**]. La méthode de l'état adjoint permet le calcul de $\nabla\Phi$

pour l'ensemble des propriétés à reconstruire à partir de deux résolutions du problème direct, donné par :

$$\mathbf{A}\left(\boldsymbol{\theta}\right)\mathbf{u}_s = \mathbf{f}, \tag{28}$$

où $\mathbf{A}\left(\boldsymbol{\theta}\right)$ est la matrice de rigidité et $\mathbf{f}$ un vecteur de contrainte. La dérivée de Φ par rapport à la propriété θ_t, où t représente la $t^{\text{ème}}$ propriété mécanique θ_t, est donnée par :

$$\frac{\partial \Phi}{\partial \theta_t} = \mathbf{u}_a^T \frac{\partial \mathbf{A}}{\partial \theta_t} \mathbf{u}_s, \tag{29}$$

où $\mathbf{u}_s$ est la solution du problème direct formulé par l'équation 28 à partir de la distribution actuelle des propriétés $\boldsymbol{\theta}_i$ et $\mathbf{u}_a$ est la solution de ce même problème direct où le vecteur de contrainte $\mathbf{f}$ est cette fois remplacé par le vecteur d'erreur sur les déplacements $(\mathbf{u}_s\left(\boldsymbol{\theta}_i\right) - \mathbf{u}_m)$.

Le gradient de la fonction objectif, $\nabla\Phi$, et la direction de descente à l'itération précédente, $\mathbf{p}_{i-1}$, permettent de générer la direction de descente à l'itération actuelle à partir de l'équation 26. Par ailleurs, McGarry [**117**] décrit une méthode de calibrage des directions de descente dans le but de diminuer leur sensibilité aux différences d'amplitudes entre les types de propriétés $\boldsymbol{\theta}_t$ ($\mu, K,$ et ρ par exemple) et de limiter l'impact des distributions de propriétés mécaniques n'assurant pas de progression suffisante vers le minimum de la fonction objectif. La direction de descente calibrée pour l'identification de la propriété mécanique $\boldsymbol{\theta}_t$ est donnée par :

$$\mathbf{p}_t^s\left(k\right) = \delta_\mu \frac{\sum|\boldsymbol{\mu}|}{\sum|\mathbf{p}_\mu|} \cdot \frac{|\mathbf{J}_g|_\mu}{|\mathbf{J}_g|_t} \cdot \frac{|\nabla\Phi|_t}{|\nabla\Phi|_\mu} \mathbf{p}_t\left(k\right), \tag{30}$$

où δ_μ est un changement relatif imposé au module de cisaillement μ, $\mathbf{p}_\mu$ est la direction de descente pour l'identification de μ et $|\mathbf{J}_g|_t$ est donné par $|\mathbf{J}_g|_t = \sqrt{\frac{\partial \mathbf{u}^H}{\partial \theta_t}\frac{\partial \mathbf{u}}{\partial \theta_t}}$.

1.3.3.2. *Recherche linéaire du pas dans la direction de descente*

Les méthodes de descente orientent la recherche du minimum de la fonction objectif dans une direction donnée $\mathbf{p}$. Il reste alors à déterminer la distance α à parcourir dans cette direction de manière à assurer une diminution satisfaisante de l'erreur Φ. La détermination du paramètre α constitue l'étape de recherche linéaire du pas dans la direction de descente

et consiste à identifier la racine de la dérivée du profil de $\Phi(\boldsymbol{\theta}+\alpha\mathbf{p})$ dans la direction $\mathbf{p}$. Par "diminution satisfaisante", il est entendu que la réduction de l'erreur n'a pas besoin d'être optimale pour assurer une convergence globale finale. La recherche intensive d'une réduction optimale de l'erreur le long de $\mathbf{p}$ à chaque itération globale présente peu d'intérêt lorsque la direction de descente est amenée à évoluer, en particulier au début du processus d'inversion. Une réduction partielle, progressive et relativement moins coûteuse de l'erreur à travers un grand nombre d'itérations globales est préférée à une réduction optimale et coûteuse sur un nombre plus faible d'itérations globales. Deux méthodes de recherche linéaire du pas de descente sont incorporées dans l'algorithme NLI et décrites dans McGarry [**117**]. La première méthode est une méthode Sécante et approxime le profil de la fonction objectif dans la direction $\mathbf{p}$ avec une parabole exprimée par un développement de Taylor d'ordre deux de Φ au voisinage de $\boldsymbol{\theta}$:

$$\Phi(\boldsymbol{\theta}+\alpha\mathbf{p}) \approx \Phi(\boldsymbol{\theta}) + \alpha\left[\frac{\partial}{\partial\alpha}(\Phi(\boldsymbol{\theta}))\right] + \frac{\alpha^2}{2}\left[\frac{\partial^2}{\partial\alpha^2}(\Phi(\boldsymbol{\theta}))\right], \tag{31}$$

où $\partial_\alpha \Phi(\boldsymbol{\theta}+\alpha\mathbf{p})|_{\alpha=0} = \mathfrak{Re}\left\{\mathbf{p}^H\nabla\Phi(\boldsymbol{\theta}+\alpha\mathbf{p})\right\}\Big|_{\alpha=0} = \mathfrak{Re}\left\{\mathbf{p}^H\nabla\Phi(\boldsymbol{\theta})\right\}$. La méthode Sécante contourne l'évaluation de la matrice Hessienne avec une approximation de la dérivée du deuxième ordre par une différence finie de dérivées du premier ordre évaluée entre deux points proches :

$$\frac{\partial^2}{\partial\alpha^2}(\Phi(\boldsymbol{\theta})) \approx \frac{\mathfrak{Re}\left\{\mathbf{p}^H\nabla\Phi(\boldsymbol{\theta}+\delta_\alpha\mathbf{p})\right\} - \mathfrak{Re}\left\{\mathbf{p}^H\nabla\Phi(\boldsymbol{\theta})\right\}}{\delta_\alpha}, \tag{32}$$

où $\delta\alpha$ est la distance entre les deux points d'évaluation. L'équation de la fonction objectif approximée est alors donnée par :

$$\Phi(\boldsymbol{\theta}+\alpha\mathbf{p}) \approx \Phi(\boldsymbol{\theta}) + \alpha\mathfrak{Re}\left\{\mathbf{p}^H\nabla\Phi(\boldsymbol{\theta})\right\} + \frac{\alpha^2}{2}\frac{\mathfrak{Re}\left\{\mathbf{p}^H\nabla\Phi(\boldsymbol{\theta}+\delta_\alpha\mathbf{p})\right\} - \mathfrak{Re}\left\{\mathbf{p}^H\nabla\Phi(\boldsymbol{\theta})\right\}}{\delta_\alpha}. \tag{33}$$

Un point stationnaire est obtenu par la résolution de $\partial_\alpha\Phi = 0$:

$$\frac{\partial}{\partial\alpha}\Phi(\boldsymbol{\theta}+\alpha\mathbf{p}) \approx \mathfrak{Re}\left\{\mathbf{p}^H\nabla\Phi(\boldsymbol{\theta})\right\} + \alpha\frac{\mathfrak{Re}\left\{\mathbf{p}^H\nabla\Phi(\boldsymbol{\theta}+\delta_\alpha\mathbf{p})\right\} - \mathfrak{Re}\left\{\mathbf{p}^H\nabla\Phi(\boldsymbol{\theta})\right\}}{\delta_\alpha} = 0. \tag{34}$$

La réécriture de (34) permet d'obtenir α :

$$\alpha = -\delta_\alpha \frac{\mathfrak{Re}\left\{\mathbf{p}^H \nabla\Phi\left(\boldsymbol{\theta}\right)\right\}}{\mathfrak{Re}\left\{\mathbf{p}^H \nabla\Phi\left(\boldsymbol{\theta}+\delta_\alpha \mathbf{p}\right)\right\} - \mathfrak{Re}\left\{\mathbf{p}^H \nabla\Phi\left(\boldsymbol{\theta}\right)\right\}}. \tag{35}$$

La valeur de δ_α peut être choisie afin de réutiliser le gradient de Φ, calculé à l'itération i, lors de l'évaluation de la différence finie (Eq. 32) à l'itération $i+1$:

$$\delta\alpha_{i+1} = -\alpha_i, \tag{36}$$

et :

$$\alpha_{i+1} = -\delta_{\alpha_{i+1}} \frac{\mathfrak{Re}\left\{\mathbf{p}^H \nabla\Phi\left(\boldsymbol{\theta}\right)\right\}}{\mathfrak{Re}\left\{\mathbf{p}^H \nabla\Phi\left(\boldsymbol{\theta}+\delta_\alpha \mathbf{p}\right)\right\} - \mathfrak{Re}\left\{\mathbf{p}^H \nabla\Phi\left(\boldsymbol{\theta}\right)\right\}}. \tag{37}$$

L'algorithme de recherche linéaire par la méthode Sécante itère jusqu'à ce que la limite d'itération fixée par l'utilisateur soit atteinte ou jusqu'à ce que l'amplitude de mise à jour de la propriété $||\alpha\mathbf{p}||$ devienne inférieure à une tolérance également fixée par l'utilisateur. Un petit nombre d'itérations assure une sélection inexacte mais rapide d'un pas de descente dans la mesure où peu d'évaluations du gradient de Φ, *i.e.*, peu de résolutions du problème directe, sont nécessaires. Toutefois, le point stationnaire identifié par l'équation 34 peut être un maximum ou un minimum et dépend du signe de la dérivée seconde $\partial^2_{\alpha,\alpha}\Phi\left(\boldsymbol{\theta}+\alpha\mathbf{p}\right)$. Si la courbure est négative, l'algorithme identifie un pas de croissance et non un pas de descente. Un garde-fou incorporé à l'algorithme NLI permet dans ce cas d'identifier un pas de descente, à un coût calculatoire cependant plus élevé, grâce aux conditions de Wolfe qui imposent à la fonction objectif une décroissance suffisante et le choix d'un pas suffisamment élevé dans la direction de descente. Les deux paragraphes suivants reposent sur la section 2.3.3 de McGarry [**117**] et la discussion du chapitre 4 de Martins et Ning [**1**].

La condition de décroissance suffisante (i) requiert que la fonction objectif à l'itération $i+1$, $\Phi\left(\boldsymbol{\theta}_{i+1}\right)$, soit inférieure à la fonction objectif à l'itération précédente i, $\Phi\left(\boldsymbol{\theta}_i\right)$, et majorée par une ligne de niveau donnée par $y\left(\alpha\right) = \Phi\left(\boldsymbol{\theta}_i\right) + \mu_1\alpha\mathfrak{Re}\left\{\mathbf{p}^H\nabla\Phi\left(\boldsymbol{\theta}_i\right)\right\}$:

$$\Phi\left(\boldsymbol{\theta}_{i+1}\right) \leqslant \Phi\left(\boldsymbol{\theta}_i\right) + \mu_1\alpha\mathfrak{Re}\left\{\mathbf{p}^H\nabla\Phi\left(\boldsymbol{\theta}_i\right)\right\}, \tag{38}$$

où $\Phi(\boldsymbol{\theta}_{i+1}) = \Phi(\boldsymbol{\theta}_i + \alpha\mathbf{p})$. La valeur négative de $\mathfrak{Re}\{\nabla\Phi(\boldsymbol{\theta}_i)\}$ assure que la ligne $y(\alpha)$ est décroissante. La pente de décroissance est imposée par le choix de μ_1 tel que $0 < \mu_1 \leqslant 1$. Dans le cas où α est choisi en dehors de ce domaine de validité, $\Phi(\boldsymbol{\theta}_{i+1})$ est de nouveau évaluée à partir d'une fraction $\rho < 1$ de la valeur de α initialement choisie : $\alpha_{nouveau} = \rho\alpha_{initial}$. Il s'agit d'une méthode de retour sur trace appliquée jusqu'à ce que la condition de décroissance suffisante (Eq. 38) soit satisfaite. Cette approche garantit une identification du pas de descente mais nécessite autant d'évaluation de Φ, *i.e.*, de résolution du problème directe, que de fois où un $\alpha_{nouveau}$ est sélectionné. La condition de décroissance suffisante est illustrée à la Fig. 2.a.

La condition de taille de pas suffisante (ii) requiert que la fonction objectif à l'itération suivante soit minorée par une seconde ligne de niveau de façon à empêcher le choix de pas trop faibles conduisant à une réduction marginale de l'erreur. Cette condition est donnée par :

$$\Phi(\boldsymbol{\theta}_{i+1}) \geqslant \Phi(\boldsymbol{\theta}_i) + \mu_2\alpha\mathfrak{Re}\left\{\mathbf{p}^H\nabla\Phi(\boldsymbol{\theta}_i)\right\}, \tag{39}$$

où $\mu_1 < \mu_2 < 1$. Une fois que α satisfait la condition de décroissance suffisante (i), la condition de taille de pas suffisante (ii) est évaluée et les limites supérieure et inférieure de α sont ajustées de façon à identifier une gamme de taille de pas satisfaisant les conditions (i) et (ii). La condition de taille de pas suffisante est illustrée à la Fig. 2.b.

La condition de courbure suffisante (iii) impose une caractéristique supplémentaire, non utilisée dans NLI mais tout de même présentée ici, sur le choix de α et requiert que la pente de $\Phi(\boldsymbol{\theta}_{i+1})$ le long de $\mathbf{p}$ soit une fraction de la pente de $\Phi(\boldsymbol{\theta}_i)$ le long de $\mathbf{p}$. La comparaison de la pente de Φ en deux points différents, $\boldsymbol{\theta}_i$ et $\boldsymbol{\theta}_{i+1}$, constitue une évaluation de courbure. Cette condition est donnée par :

$$\left|\mathfrak{Re}\left\{\mathbf{p}^H\nabla\Phi(\boldsymbol{\theta}_{i+1})\right\}\right| \leqslant \mu_2\left|\mathfrak{Re}\left\{\mathbf{p}^H\nabla\Phi(\boldsymbol{\theta}_{i+1})\right\}\right|. \tag{40}$$

Pour des valeurs de μ_2 suffisamment petites, l'inégalité 40 assure l'exclusion des valeurs de α ne produisant pas de diminution suffisante de la pente de Φ le long de $\mathbf{p}$. Dans le cas où la condition donnée par Eq. 38 est satisfaite et celle donnée par Eq. 40 non-satisfaite, la valeur

de α est augmentée jusqu'à ce que Eq. 40 soit satisfaite. Cette contrainte revient à restreindre la gamme de valeurs de α valides identifiées par la condition de décroissance minimum. Une relation entre la pente de décroissance suffisante imposée par μ_1 et la courbure suffisante imposée par μ_2 est donnée par :

$$0 < \mu_1 < \mu_2 < 1 \tag{41}$$

Cette inégalité assure que les valeurs de α satisfaisant une condition satisfont également l'autre condition. La condition de courbure suffisante est illustrée à la Fig. 2.c.

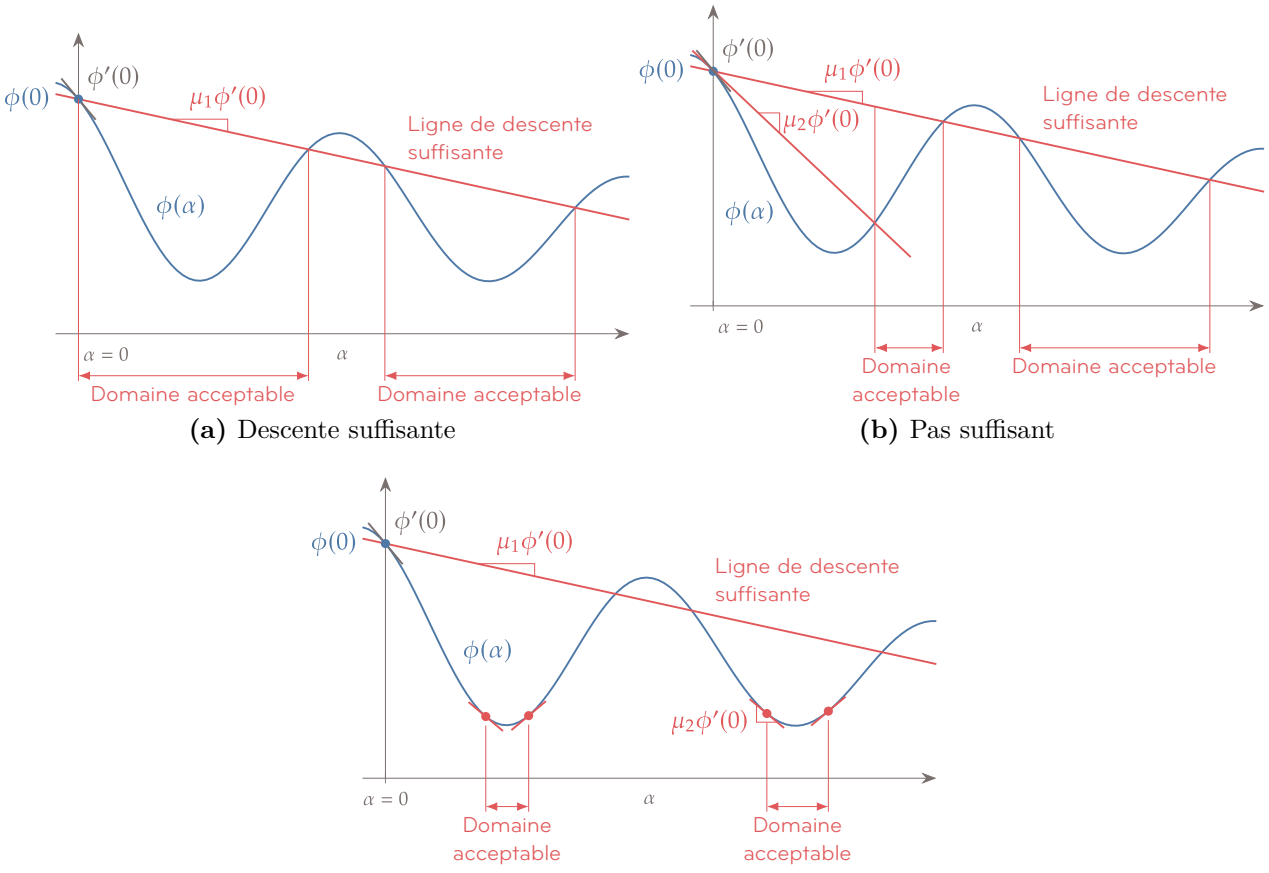

(a) Descente suffisante

(b) Pas suffisant

(c) Courbure suffisante

Figure 2 – Conditions de Wolfe. Graphiques extraits et modifiés à partir de Martins et Ning [**1**]

Une fois identifiés, la direction de descente $\mathbf{p}$ et le pas α génèrent une mise à jour de la distribution des propriétés $\boldsymbol{\theta}$. Ce processus est répété jusqu'à ce que le nombre total d'itérations globales imposé par l'utilisateur soit atteint, ou jusqu'à ce que la variation des

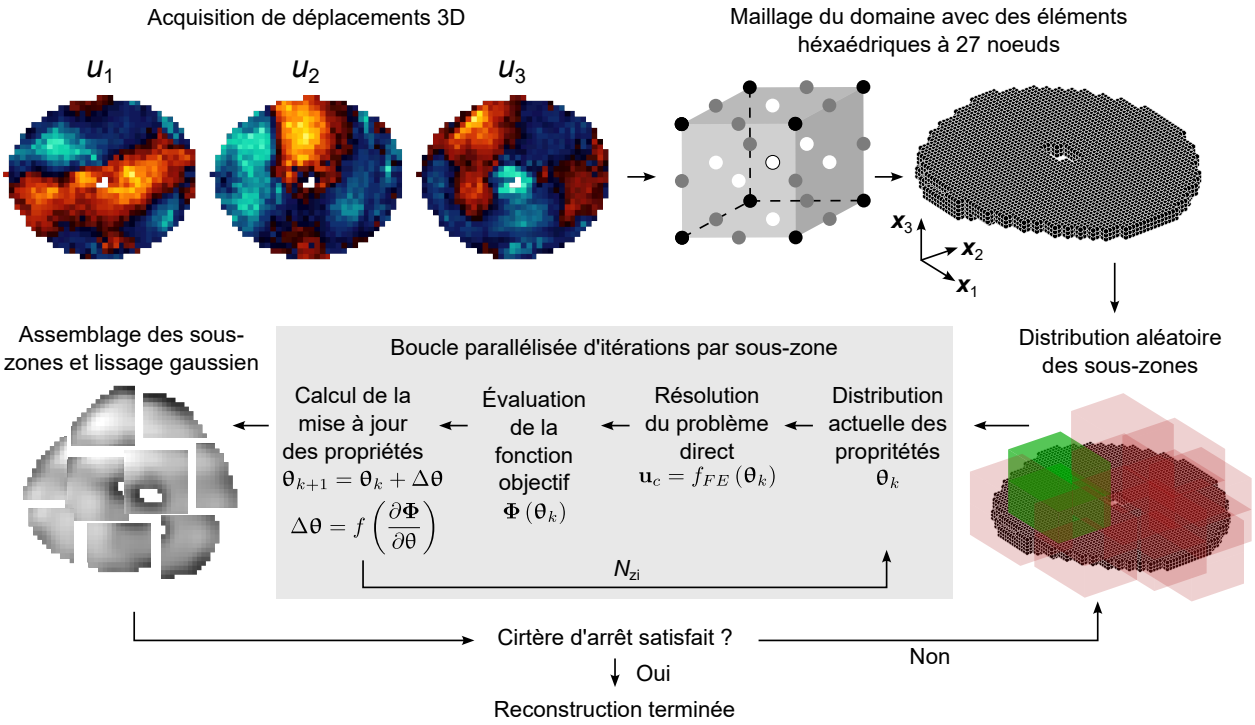

Figure 3 – Résumé du fonctionnement de l'algorithme NLI

mises à jour entre deux itérations successives soit inférieure à une tolérance choisie par l'utilisateur.

La figure 3 illustre le fonctionnement de l'algorithme NLI à partir de cartes de déplacements mesurées dans un volume le long des trois directions de l'espace au cours d'une acquisition d'élastographie par résonance magnétique.

1.4. Conclusion du chapitre

Un état des lieux des méthodes de reconstruction des propriétés mécaniques utilisées en élastographie par résonance magnétique a été présenté, incluant la LFE et l'algorithme NLI. L'utilisation de la LFE dans ce projet de doctorat est rapportée dans l'article 1 et celle de l'algorithme NLI dans les articles 2 et 3.

Chapitre 2

Lorentz force induced shear waves for magnetic resonance elastography applications

Ce chapitre repose sur l'article intitulé "Lorentz force induced shear waves for magnetic resonance elastography applications" publié en 2021 dans le journal *Scientific Reports* par Guillaume Flé, Guillaume Gilbert, Pol Grasland-Mongrain et Guy Cloutier.

Avant propos

La technique d'ERM par force de Lorentz proposée et décrite dans ce chapitre s'inscrit dans le cadre d'une acquisition d'élastographie par résonance magnétique concomitante à une stimulation électrique. Cette étude expérimentale est motivée par la propriété d'amortissement des tissus biologiques, principalement responsable de l'atténuation des ondes de cisaillement dans une région d'intérêt et de la limite de l'application de l'ERM à des fréquences de vibration rarement supérieures à 60 Hz. Une solution naturelle à cette difficulté consiste à induire des vibrations d'amplitudes plus élevées à la surface du tissu dans l'optique d'en compenser l'atténuation jusqu'à la région d'intérêt, sans toutefois pouvoir garantir que celle-ci soit suffisamment illuminée. L'alternative proposée dans ce chapitre vise à générer des sources d'ondes mécaniques *in situ* dans le but, à terme, de réduire la distance que l'onde a à parcourir entre la zone où elle est émise et la zone d'intérêt, de façon à en limiter l'atténuation par des trajets plus courts. Ces sources d'ondes mécaniques sont des forces

volumiques de Lorentz résultant du couplage champ magnétique - courant de stimulation électrique dans le tube du système de résonance magnétique. En particulier sont évalués l'intensité des courants nécessaires à la génération d'ondes mécaniques mesurables par ERM ainsi que l'impact de ces sources volumiques sur la reconstruction de propriétés élastiques par la méthode d'inversion directe LFE, reposant sur la description d'un solide purement élastique, localement homogène et isotrope.

Contributions des auteurs

Guillaume Flé : proposition du projet, reproduction de travaux antérieurs, conception assistée par ordinateur du porte fantôme, acquisition des données expérimentales, programmation et test d'algorithmes d'inversion directe, conception des simulations numériques, rédaction et révision de l'article.

Guillaume Gilbert : pilotage du système IRM, inversion LFE par *MRE/Wave* du système d'imagerie et révision de l'article.

Pol Grasland-Mongrain : contribution aux expériences ultrasonores préliminaires, révision de l'article.

Guy Cloutier : direction générale, financement et révision de l'article.

Résumé

Les propriétés mécaniques quantitatives des tissus biologiques peuvent être cartographiées à l'aide de la technique d'élastographie par ondes de cisaillement. Cette technologie a démontré un potentiel important dans divers organes mais présente une limite due à l'atténuation de ces ondes élastiques dans les tissus biologiques. Cette diminution inhérente d'amplitude dans la direction de propagation pourrait être contournée par une stimulation des tissus plus près des régions d'intérêt en utilisant d'autres techniques de sollicitation mécanique. La présente étude examine la possibilité d'une application en élastographie par résonance magnétique de génération d'ondes de cisaillement par forces de Lorentz dans des

fantômes imitant les propriétés mécaniques des tissus biologiques. Dans cette optique, un courant électrique, délivré aux fantômes, est combiné au champ magnétique d'un scanner IRM clinique. La méthode d'estimation de la fréquence locale est utilisée pour évaluer la valeur réelle du module de cisaillement des fantômes testés à partir des déplacements induits par force de Lorentz. La simulation des expériences par éléments finis démontre un comportement du champ ondulatoire cohérent avec les mesures mais présente des longueurs d'onde plus élevées. Les résultats exposés suggèrent qu'une technique d'élastographie par résonance magnétique basée sur la force de Lorentz pourrait être envisagée dans le but de produire des sources *in situ* d'ondes de cisaillement.
Mots clés : Élastographie par résonance magnétique, force de Lorentz, stimulation électrique, ondes élastiques

Abstract

Quantitative mechanical properties of biological tissues can be mapped using the shear wave elastography technique. This technology has demonstrated a great potential in various organs but shows a limit due to wave attenuation in biological tissues. An option to overcome the inherent loss in shear wave magnitude along the propagation pathway may be to stimulate tissues closer to regions of interest using alternative motion generation techniques. The present study investigated the feasibility of generating shear waves by applying a Lorentz force directly to tissue mimicking samples for magnetic resonance elastography applications. This was done by combining an electrical current with the strong magnetic field of a clinical MRI scanner. The Local Frequency Estimation method was used to assess the real value of the shear modulus of tested phantoms from Lorentz force induced motion. Finite element modeling of reported experiments showed a consistent behavior but featured wavelengths larger than measured ones. Results suggest the feasibility of a magnetic resonance elastography technique based on the Lorentz force to produce an *in situ* shear wave source.

Key words: Magnetic resonance elastography, Lorentz force, electrical stimulation, elastic waves

2.1. Introduction

Stiffness difference between healthy and abnormal biological tissues has long been put to use in the form of manual palpation to diagnose potential diseases. Although helpful to roughly estimate tissue stiffness, more precise and quantitative stiffness assessments can be reached using modern techniques such as shear wave elastography imaging [**129, 130, 131, 132**]. This method relies on the propagation of shear waves of which the speed is proportional to the square root of the shear modulus of the medium [**133**] in linearly elastic, homogeneous, isotropic and infinite solids. Shear wave elastography requires to (1) induce shear waves within the sample, (2) track local displacements propagating as a shear wave, and (3) compute mechanical parameters from displacement images. Although some imaging techniques have been proposed to track shear waves, such as optical coherence tomography [**134**] or a high speed camera [**2**], main imaging methods for elastography remain ultrasound [**135**] and magnetic resonance imaging (MRI) [**41**]. In MRI, computation of viscoelastic parameters has been performed with different algorithms, such as local frequency estimation (LFE) [**136**], algebraic inversion of the equation of wave propagation [**71, 72, 61**], identification methods using finite elements [**116**], and temporal cross-correlation [**109, 111**].

In terms of shear wave generation, external actuators placed on the surface of the imaged tissue are mostly used in magnetic resonance elastography (MRE). In such cases, elastic waves propagate, and attenuate, from the surface to the region of interest while being tracked by the scanner. Pneumatic actuators have been widely used in MRE and have shown versatility through applications to liver [**137**], brain [**138**], heart [**139**], and lung [**93**]. In this system, air pulses are generated by an active driver outside the MR room and routed through a plastic tube to a passive transducer attached to the patient. The setup is simple and handles well mono-frequency waveforms in the range of $\sim$ 40 Hz to $\sim$ 110 Hz. However, the uncontrolled acoustic response of pulsed air along the connection tube may render multi-frequency MRE

difficult. Alternatively, a rigid rod has been attached directly to the pulsing active driver on one end and to a pad tied to the patient on the other end, which allowed for multi-frequency MRE [**75, 74, 140**]. Other successful surface actuation apparatus have been reported, such as piezoelectric [**141**] and Lorentz coil drivers [**66**] where the magnetic field of the MR scanner and the current injected in the coil combine to generate vibrations. So far, the presented solutions to produce displacement fields have in common the decrease of motion deflection as the driving frequency increases. This feature along with the inherent damping behavior of viscoelastic tissues limit *in vivo* applications to low frequencies. To circumvent this limitation, mechanical devices relying on the centrifugal force have been presented, such as the "gravitational transducer" [**142**]. This system is made of a mass rotating about an axis of which the spinning frequency is driven by a motor outside the MR room. The centrifugal force exhibited in this type of actuator allows to increase the vibration amplitude by increasing the rotation frequency. This is an elegant solution to elicit displacement fields of sufficient amplitude at high frequencies within a reasonable distance from the surface actuator. However, challenges may remain at deep locations due to attenuation.

Instead of attempting to produce motion fields likely to reach the region of interest from the surface, an alternative may be to vibrate tissues closer to the targeted area thus shortening the propagation pathway and reducing the related wave damping. Ultrasound radiation pressure sources have been presented in that regard [**42**] but carry practical implementation difficulties in the context of MR imaging. Intrinsic MRE, consisting in capitalizing on the natural pulsation of arteries as a motion source, requires no external actuator and has shown great potential at heartbeat frequencies [**111, 143, 144, 145**]. Alternatively, the Lorentz force has been proposed for direct application of a motion (as opposed to Lorentz coils) to tissue mimicking phantoms by Grasland-Mongrain *et al.* [**15, 146**]. They showed the possibility of producing shear waves within a conductive medium using the Lorentz force produced by a permanent portable magnet and external electrodes or a magnetic stimulation device, and an ultrasonic scanner for detection [**15, 146, 147**].

Here, we hypothesized that a similar configuration could be used as a remote mechanism for shear wave induction in MRE by taking advantage of the strong magnetic field of MR scanners. Mechanical displacements of electromagnetic origin have been observed in soft solids using MRI [**17**] but to our knowledge, no study has reported the use of the Lorentz force to produce *in situ* displacements in the context of MR elastography. In the present work, we propose to evaluate the feasibility of generating and detecting shear waves from a Lorentz force source within tissue mimicking samples. A specific MR compatible experimental setup was designed to isolate the Lorentz force contribution of the measured displacement field. Finally, preliminary conclusions on stiffness reconstructions from Lorentz force induced motion using the well-established LFE method are reported.

2.2. Method

The proposed method consists in producing a Lorentz force density in tissue mimicking gels (phantoms) which in turn induces shear waves that are recorded using an MR clinical system and processed to retrieve elasticity information. The expression of the Lorentz force density ($N.m^{-3}$) is given by:

$$\mathbf{f} = \mathbf{J} \times \mathbf{B}, \tag{42}$$

where $\mathbf{J}$ is the current density ($A..m^{-2}$) and $\mathbf{B}$ the magnetic field (T) [**148**]. Here, the strong homogeneous magnetic field of the MR scanner and externally applied currents were used to produce the Lorentz force.

2.2.1. Experimental setup

In all the experiments reported in the present manuscript, agar phantoms were poured into a 3D printed mould and crossed by an electrical current $\mathbf{J}$ and a magnetic field $\mathbf{B}$ (Fig. 4). Details about the different phantoms used are given in the paragraphs below and in Table 1. Saline baths (20%w) were designed on the two sides of the phantom holder to make the electrical contact between the phantom and external electrodes. This permitted to avoid mechanical contacts between electrodes and the phantom, thus allowing to isolate

the Lorentz force density as the source of motion (*i.e.*, avoid artefact movements). The electrical current was brought by means of electrodes (copper wires) plunged into the saline. Wires were placed parallel to the static magnetic field direction from the end of the bore to the phantom holder, and maintained fixed from above the phantom holder to the saline baths. Special care was taken to avoid mechanical contacts between wires and the rest of the setup to eliminate other movement artefacts. The phantom was placed in a 32-channel receive-only head coil in the bore of a 3 T MRI scanner (Achieva TX, Philips Healthcare, Best, Netherlands). The coil was positioned at the bore isocentre to minimise eddy currents and to facilitate the reproducibility of experiments. The phantom was oriented along the magnetic field (z axis, red arrow in Fig. 4a) and the current was mainly flowing along the y axis (green arrow in Fig. 4a) between the two electrodes so that the magnetic field and the current were perpendicular. The induced Lorentz force was oscillating along the x axis (black arrow in Fig. 4a) at the frequency of the current. A motion field was then produced with in-plane components parallel and perpendicular to the Lorentz force, *i.e.* along x and z axes. The electrical current was provided by a waveform generator (Agilent, 33250A 80 MHz), amplified (Brüel & Kjaer, power amplifier type 2706) and routed through a 2-Ω shunt resistance in series with the phantom and the generator. Two sinusoidal waveforms of 60 Hz and 90 Hz were successively used in the experiments.

Table 1 – Phantom properties

Experiment #	**Phantom**	**Agar (w %)**	**Saline (salt w % in volume water)**
1	A	0.4	10
2	B	0.5	0.9
	C	0.7	0.9
	D	0.8	0.9
	E	1	0.9

2.2.2. MRI acquisitions

For actuation and motion detection, current delivery to the phantom was synchronised with the motion encoding gradients (MEGs) of a 2D gradient echo sequence tailored to

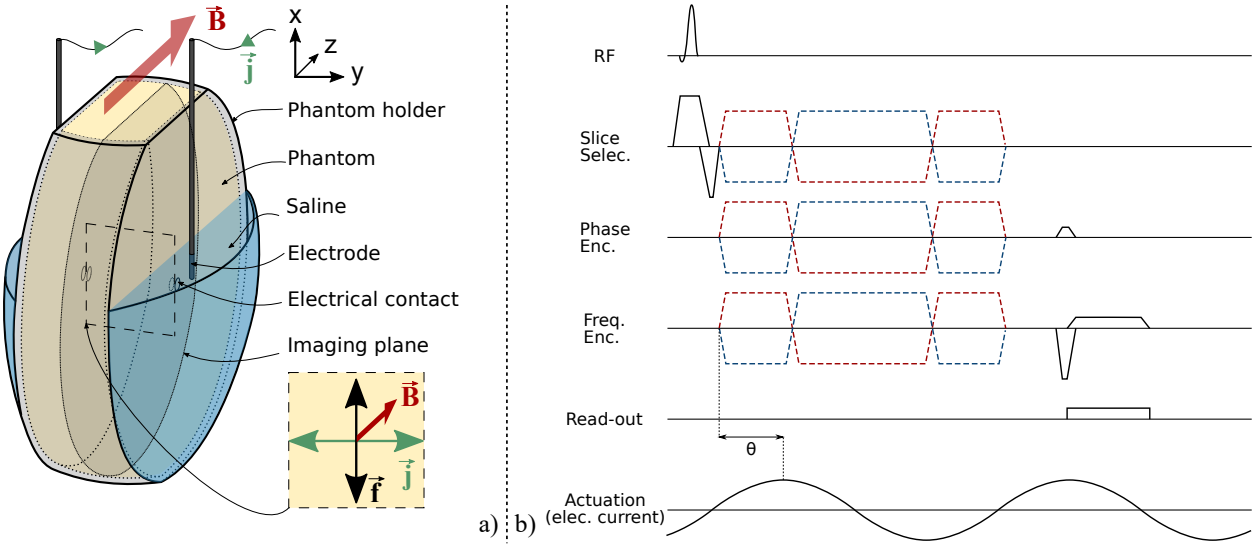

Figure 4 – a. Experimental setup. The dimensions of the phantom were $13 \times 3 \times 14$ cm^3 along the x, y, and z axes, respectively. $\mathbf{B}$ is the static magnetic field along the z axis produced by the MRI system. $\mathbf{J}$ is the harmonic current density applied to the phantom using external electrodes plunged into the saline baths and with a main oscillating direction along the y axis. $\mathbf{f}$ is the Lorentz force density produced within the phantom from the combination of $\mathbf{B}$ and $\mathbf{J}$, and with a main oscillating direction along the x axis. For clarity, the main directions of $\mathbf{J}$ and $\mathbf{f}$ are represented and zoomed in the dashed cross-section. In the first experiment, electrical currents of 60 Hz and 90 Hz frequencies and of 137.5 mA peak-to-peak intensity were used. Phantom A was homogeneous and doped with NaCl to be electrically conductive. See Table 1 for phantom contents and Fig. 8 for details of the second experiment. **b.** MRE pulse sequence diagram. MEGs of opposite polarities are indicated by the red and blue dashed lines. θ represents the phase offset between actuation and MEGs. MEGs along different directions (slice selection, phase encoding, and read-out) are successively activated in separate acquisitions.

elastography experiments [**149**] (Fig. 4b). The current generator was triggered by the MR scanner at the beginning of the MRE pulse sequence, in the same way as with other standard mechanical transducers. The phase accumulation experienced by spins undergoing harmonic actuation is given by:

$$\Phi = \int_0^\tau \gamma \mathbf{G}\left(t\right) \cdot \mathbf{u}\left(\mathbf{r}_0, t\right) \, \mathrm{d}t, \tag{43}$$

where γ (rad.s^{-1}.T^{-1}) is the sample's gyromagnetic ratio, τ (s) the period of actuation, and $\mathbf{G}$ (T.m^{-1}) the motion encoding gradient amplitude. Generated motion was encoded along three orthogonal directions (anterior–posterior, right-left, foot-head). Parameters of the elastography sequence were: repetition time TR = 50 and 56 ms (adjusted to match a

multiple of the shear wave vibration period), echo time TE = 15 and 20 ms, spatial resolution = 1.25 mm × 1.25 mm, slice thickness = 5 mm, elastography phases = 4, amplitude of the motion encoding gradients = 31 $mT.m^{-1}$ (highest value available to ensure maximum detection in the furthest regions from the motion source), and motion encoding over one cycle.

For displacement field measurements, two phase images were successively acquired with MEGs of opposite polarities. The second phase image was then subtracted from the first one using the exponential form of the complex MR signal to eliminate potential static phase offsets, thus producing a single phase difference image free of unwanted constant background. During the acquisition (whole TR) of both phase images, the generator was continuously delivering the same oscillating electrical current. The induced phase offset due to current injection in the phantom was then the same in these images and was consequently cancelled out in the phase difference operation. Additionally, receive coils were syntonised to the Larmor frequency of hydrogen's proton and consequently show a low sensitivity to the low-frequency currents used in our study. To compute displacement maps from phase difference images, the encoding coefficient $|\xi|$ in ($rad.m^{-1}$) was computed using $|\xi| = \left|\frac{\gamma G_0(\sin(\pi f\tau))-2\sin\left(\frac{1}{2}\pi f\tau\right)}{\pi f}\right|$, which approximates first moment nulling gradients and where γ ($rad.s^{-1}.T^{-1}$) is the sample's gyromagnetic ratio, τ (s) and G_0 ($T.m^{-1}$) are the period and the amplitude of the MEG respectively, and f (Hz) is the excitation frequency [**150**].

2.2.3. Inverse problem and data processing

Once shear waves were produced and detected, the next step consisted in generating maps of viscoelastic parameters. The forward problem relating harmonic displacements to tissue mechanical properties is described by the Navier's equation:

$$\nabla \cdot (\mu \nabla \mathbf{u}) + \nabla \left((\lambda + \mu) \nabla \cdot \mathbf{u} \right) = -\rho \omega^2 \mathbf{u}, \tag{44}$$

where ρ is the material's density ($kg.m^{-3}$), ω the motion angular velocity ($rad.s^{-1}$), $\mathbf{u}$ the motion field (m), λ ($N.m^{-2}$) the first Lamé coefficient [**151**] and $\mu = \mu_r + i\mu_i$ ($N.m^{-2}$) the

complex shear modulus. In agar and agar-doped phantoms, the real part of the complex shear modulus (storage modulus) was shown to considerably dominate the imaginary part (loss modulus) [**152, 153**]. The LFE, which ignores the loss modulus, was then chosen to retrieve first elasticity information from Lorentz force induced displacements in agar phantoms, given its availability and wide use in the MRE community. The LFE reconstructions could allow validating the working hypothesis to show the possibility of implementing the Lorentz force MRE method on a clinical scanner. Additionally, the LFE is known to be more robust against noise than other direct methods involving the estimation of second or higher order derivatives [**71, 61**].

The LFE consists in applying pairs of filters to the selected harmonic of the displacement data in the k-space. These filters are called log-normal quadrature filters and are generally centered on frequencies separated by one octave [**89**]. The ratio of displacements processed by each filter of one pair is equal to the local wave number. As the actuation frequency ω is known (*i.e.*, electrical current frequency), the wave number k can then be related to the local real value of the shear modulus in (N.m^{-2}) using $\mu_r = \rho \left(\frac{\omega}{k}\right)^2$, where $\mu_r = \mathfrak{Re}\{\mu\}$. This is equivalent to solving the Helmholtz equation $\mu_r \Delta \mathbf{u} = -\rho\omega^2 \mathbf{u}$, which is a simplified version of the Navier's equation under the assumptions of tissue incompressibility, local homogeneity, and no shear wave attenuation. Shear modulus maps computed from displacements along the actuation direction (x axis) are reported in this study.

Prior to inversion, phase images were automatically unwrapped using a software embedded in the scanner (Resoundant Inc., Rochester, MN). Shear modulus images were then filtered to remove outliers using the *smoothn* Matlab function [**154, 155**]. For displacement display (Fig. 6), a separate phase unwrapping procedure was used [**156, 157, 158**].

2.2.4. Experiment 1

To demonstrate the proposed method, two experimental conditions were designed, both consisting in generating shear waves in tissue mimicking gels. The first one intended to show the feasibility of generating shear waves with the Lorentz force under favourable conditions

(*i.e.*, an electrically conductive, soft, and homogeneous phantom, termed phantom A in Table 1), and to observe them with the MRI scanner. Two sinusoidal electrical currents of 137.5 mA peak-to-peak with frequencies of 60 Hz and 90 Hz were respectively used. Such intensity is 69 times as large as values reported in electrical stimulation (ES) protocols performed on humans ($i_{ES} = 2$ mA peak-to-peak) [**159**]. Results are shown Fig. 6.

2.2.5. Experiment 2

The purpose of the second experiment was to show that Lorentz force induced shear waves could be used to distinguish regions with different mechanical properties within the same heterogeneous structure using phantoms with different mechanical properties (termed B, C, D, and E in Table 1), and a less conductive medium corresponding to physiological conditions. To create the heterogeneous structure, phantom B was poured on top of phantom C in one phantom holder (Figs. 4a and 8a), and phantom D was poured on top of phantom E in another phantom holder (Figs. 4a and 8a). Sinusoidal currents of 62.22 mA peak-to-peak at frequencies of 60 Hz and 90 Hz were used, which corresponds to $33 \times i_{ES}$.

2.2.6. Simulations

A finite element physical model corresponding to the first experiment using phantom A was designed with Comsol 5.5 (COMSOL LiveLink with Matlab, Inc., Palo Alto, CA) to assess the displacement patterns obtained from a convolution of point-like sources, and to compare with experimental data. Simulations consisted in two steps, first computing the Lorentz force density distribution within the phantom, and second computing the wave field resulting from this Lorentz force density source term. To compute the Lorentz force density distribution, the following boundary value problem was solved using the electric current

module:

$$\begin{cases} \nabla \cdot (\sigma \nabla V) = 0 & \text{in the phantom,} \\ I = \int_{\varepsilon^+} \sigma \dfrac{\partial V}{\partial \mathbf{n}} ds = -\int_{\varepsilon^-} \sigma \dfrac{\partial V}{\partial \mathbf{n}} ds, \qquad \nabla V \times \mathbf{n} = 0 & \text{on electrical contacts,} \\ \sigma \dfrac{\partial V}{\partial \mathbf{n}} = 0 & \text{on phantom walls,} \end{cases} \tag{45}$$

where V is the electric potential (V), σ the electrical conductivity (S.m^{-1}), I the electrical current (A), S the surface areas (m^2) of the electrical contact, and $\mathbf{n}$ is a unit vector perpendicular to the outer boundary. The externally applied electrical current I was modeled perpendicular to the phantom at the electrical contact location (Fig. 4a). The intensity and frequency of the current were the same as in the first experiment (60 Hz and 90 Hz, peak-to- peak amplitude of 137.5 mA). The phantom conductivity was homogeneous and set to 1 S.m^{-1} as it impacts neither the current density distribution within the phantom nor its intensity, which are governed by the boundary conditions in this model. From the electric potential distribution V, the current density was computed using Ohm's law: $\mathbf{J} = -\sigma \nabla V$. The Lorentz force density distribution in the phantom (Fig. 5) was then computed using Eq. 42:

$$\mathbf{f} = \begin{pmatrix} J_x \\ J_y \\ J_z \end{pmatrix} \times \begin{pmatrix} B_x \\ B_y \\ B_z \end{pmatrix} = \begin{pmatrix} J_x \\ J_y \\ J_z \end{pmatrix} \times \begin{pmatrix} 0 \\ 0 \\ B_z \end{pmatrix}, \tag{46}$$

where $|\mathbf{B}| = B_z = 3$ T is the magnetic field produced by the MR scanner.

To compute the displacement field resulting from the Lorentz force density distribution in the phantom, the following boundary value problem was solved using the solid mechanics module:

$$\begin{cases} \nabla \cdot (\mu \nabla \mathbf{u}) + \nabla (\mu \nabla \cdot \mathbf{u} - p) + \mathbf{f} = -\rho \omega^2 \mathbf{u} & \text{in the phantom,} \\ Ktr(\boldsymbol{\varepsilon}) = -p & \text{in the phantom,} \\ \mathbf{u} = \mathbf{u}_0 & \text{on phantom holder's walls,} \end{cases} \tag{47}$$

where $\mathbf{u}$ is the displacement field (m), ρ is the material's density (kg.m^{-3}), ω is the pulsation (rad.s^{-1}), μ is the complex shear modulus (N.m^{-2}), K is the bulk modulus (N.m^{-2}), p is the pressure field (Pa), $\boldsymbol{\varepsilon}$ is the strain tensor, and $\mathbf{f}$ is the Lorentz force density (N.m^{-3}). The bulk modulus was set to 2.2 GPa (water). Although the approximation of no shear wave attenuation remains reasonable for agar phantoms in the calculation of the solution to the inverse problem, such approximation has large consequences on the calculated solution to the forward problem. The definition of a loss modulus was thus found necessary to account for the slight damping behavior of the phantom.

To fix the loss modulus μ_i, the reported trend of the relationship between storage and loss moduli in agar phantoms was used. As aforementioned, the storage modulus was shown to dominate the loss modulus in agar and agar-doped phantoms. More specifically, around an order of magnitude difference can be observed between these two parameters [**152, 153**]. The storage moduli at both frequencies were then fixed from the shear modulus distributions in Fig. 7, and the loss moduli were fixed from the above-mentioned $\mu_i - \mu_r$ relationship. However, given the uncertainty on the phantom's exact mechanical properties (variability in maps of Fig. 7 for μ_r and approximated μ_i), the forward problem was solved multiple times using different sets of complex shear moduli. In the first simulation, μ_r values at both frequencies were set to the mean values of the shear modulus distributions in Fig. 7: $\mu_{r,\,60\text{ Hz}} = 1546$ Pa and $\mu_{r,\,90\text{ Hz}} = 1768$ Pa. Loss moduli μ_i were set to 1/10th of the storage moduli: $\mu_{i,\,60\text{ Hz}} = 155$ Pa and $\mu_{i,\,90\text{ Hz}} = 177$ Pa. Results are shown in Fig. 6. In the second and third simulations, the same μ_r values were used and μ_i values were varied and successively set to 1/5th and 1/20th of μ_r values. In the fourth and fifth simulations, μ_r values were changed towards the lower values in the shear modulus distributions in Fig. 7, and μ_i were set to 1/10th of μ_r in each case. Results are shown in Fig. 6. All combinations of μ_r and μ_i parameters are gathered in Table 2. This iterative framework intended to show that, despite uncertainties on the phantom's exact mechanical characteristics, different possible storage and loss moduli do impact the shear wave propagation patterns and their

wavelengths but do not question the Lorentz force density origin of the produced motion fields, which is what the simulation was meant to highlight.

Regarding the geometry, side boundaries (phantom holder's walls) were fixed while the upper boundary was left free to mimic the configuration of Fig. 4. Both calculations (electric potential and displacement field) were performed in the frequency domain. Complex displacements in the imaged plane were then extracted and Fourier transformed into the time domain, aligned with the experimental displacement data, and Fourier transformed back into the frequency domain for display of the real and imaginary parts in Fig. 6. Mesh adaptations were performed to allow refinements where the gradients of solutions were high. No mesh dependence was observed in final results.

Table 2 – Complex shear moduli $\mu = \mu_r + i\mu_i$ (Pa) used in the simulations.

Simulation #	**Frequency**	
	60 Hz	**90 Hz**
1	$1546 + i155$	$1768 + i177$
2	$1546 + i310$	$1768 + i354$
3	$1546 + i78$	$1768 + i89$
4	$1200 + i120$	$1500 + i150$
5	$1000 + i100$	$1300 + i130$

2.3. Results and discussion

2.3.1. Experiment 1 and simulations

Figure 5 shows the distribution of the Lorentz force density along the x, y, and z axes in the imaging plane. A significant contribution along the x axis was observed while contributions along the y and z axes were found negligible. This behavior is consistent given the expression of the Lorentz force density (vector cross-product) and main directions of current density (along y axis) and magnetic field (along z axis).

Figure 6 displays the experimentally measured displacement fields along the three directions of space and the simulated ones computed from the Lorentz force density distribution. The storage moduli used to characterize the phantom in these simulations were obtained

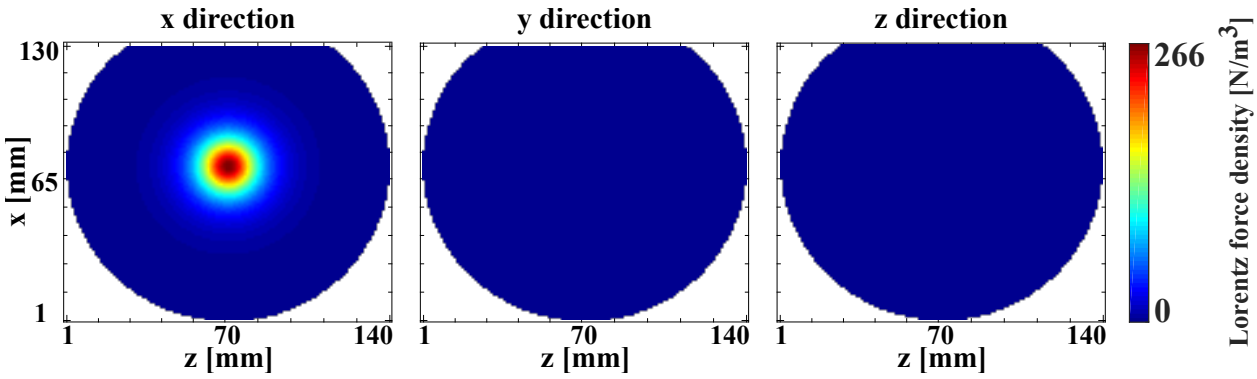

Figure 5 – Simulated Lorentz force density maps in phantom A of the first experiment. Maps are located in the imaging plane of Fig. 4. The applied current was 137.5 mA peak-to-peak at a frequency of 90 Hz. A significant Lorentz force component is observed along the x axis, but it is negligible along the y and z axes.

from the mean values of the shear modulus distributions displayed in Fig. 7. The loss moduli were approximated to 1/10th of the storage moduli. Figure 6 shows the line profiles of the polarized displacement fields along the propagation directions for each tested combination of μ_r and μ_i (Table 2).

In Fig. 6, the experimental displacement patterns along x and z allow for clear identification of the shear wave source, *i.e.*, where the Lorentz force density is the highest (Fig. 5), namely between electrical contacts within the saline bath-phantom structure (Fig. 4a). No other shear wave origin could be observed, indicating the absence of movement artefacts. Experimental and simulated displacement fields show similar patterns. They both present a monopole-like arrangement along the x axis and a dipole mode along the z axis, at both frequencies. These patterns correspond to the shear mode described by the Green's function solution to the inhomogeneous Navier's equation [**160**]. However, no clear pattern could be identified along the y axis in experimental data where the motion amplitude was very low resulting in measurement errors (broad areas with negative-only or positive-only displacement values).

Simulated displacements along the y axis show maximum amplitudes on the order of 10 nm, which cannot be measured with the MR scanner. Although presenting the same modes and propagation directions as experimental data, simulated displacement fields feature wavelengths larger than measured ones, which suggests a mismatch in the definition of the

material properties in the simulations rather than an underlying modeling issue. The storage moduli were assigned based on experimental estimations, which implies that the storage shear modulus distribution from the LFE inversion was overestimated. The line profiles along propagation directions for possible complex shear modulus values present the same behavior around the center of the line, which matches the distribution of the Lorentz force density, regardless of the mechanical parameters used. The side lobes towards opposite edges have, however, their own individual behavior. All simulated configurations provided maximum displacement amplitudes larger than the measured ones. This suggests that the experimental displacement amplitudes may have been underestimated, which would be consistent with their low values close to the reported detection limit of a few hundreds of nanometers in MRE [**41**].

Potential global under evaluation of displacement amplitudes have theoretically no impact on the LFE reconstruction, which does not depend on the displacement amplitude but on the wavelength estimation so long as enough signal-to-noise ratio is available. Qualitatively, the noticeable change in wavelength between measurements at 60 Hz and 90 Hz further confirms the wave field dependence on the frequency of the Lorentz force density. The impact of current intensity on the displacement field was also observed in other experiments where the current intensity was varied. With a current at 60 Hz and 113 mA peak-to-peak, the mean norm of the displacement field calculated over the whole field of view was 0.14 μm. This value accordingly dropped to 0.07 μm when the current was lowered by a factor of 2. The same conclusion was drawn at 90 Hz with the displacement mean norm decreasing from 0.08 μm to 0.06 μm (ratio of 1.2) when the current was lowered from 149 mA peak-to-peak to 113 mA peak-to-peak (ratio of 1.3).

Figure 7 shows the shear storage modulus distributions obtained with the LFE inversion performed on x displacements. The LFE relies on the evaluation of the wave number in motion field images making it particularly sensitive to reflections off boundaries and wave interferences, which result in apparent larger or smaller wavelengths and consequently higher or lower shear moduli even in homogeneous tissues. This is assumed to be the case at

60 Hz and 90 Hz where regions with higher and lower values respectively formed semi-circle branches on the left- and right-hand sides. These arcs of circles are consistent with the wave front geometries of the experimental x displacements shown in Fig. 6. At the center of both frequency maps, higher shear moduli correspond to regions where the assumption of a body force free solid underlying the derivation of the elastic Helmholtz equation is no longer valid due to the presence of the Lorentz force density (Fig. 5). The presence of the Lorentz force density translates into overestimated shear moduli to compensate for the inertia term. The mean values over the entire field of views are $\mu_{r,\ 60\ \mathrm{Hz}} = 1546 \pm 383$ Pa and $\mu_{r,\ 90\ \mathrm{Hz}} = 1768 \pm 440$ Pa.

2.3.2. Experiment 2

Figure 8 displays results of the second experimental condition consisting in generating shear waves using the Lorentz force in phantoms with different mechanical properties. The shear modulus maps were generated from x displacements, as in Fig. 7, for the evaluation of the impact of the Lorentz force density on reconstruction (the Lorentz force density pulses along the x axis). Phantom names corresponding to upper and lower parts of the phantom compartments are indicated in red in upper and lower right corners of shear modulus maps. Despite the higher electrical resistance due to lower salt content in those phantoms, currents with sufficient intensities 62 mA peak-to-peak could be applied to conduct these measurements with sufficient signal-to-noise ratios.

The separation between the two phantom layers is clearly visible on all shear modulus maps. However, the distribution within each layer shows a significant variance, especially in the phantom E. No major difference was measured between phantoms C and D at both frequencies despite the difference in agar concentration. The dotted line shows the separation between the two compartments where the shear modulus mean values and standard deviations were calculated. The dashed circle in the middle represents the extent to which the Lorentz force varied from its maximum magnitude (centre of the circle) to 1/10th of this maximum (edge of the circle). No impact of the Lorentz force could be observed in this

circle as opposed to the centre of shear modulus maps in Fig. 7. This may be explained by the spatial coincidence of the Lorentz force distribution and the stiffness discontinuity. The LFE was reported to lack sensitivity at the boundary between media of different stiffness [**150**] because of the spatial extent of the filters and the assumption of local homogeneity. This leads to estimated stiffness values to be inaccurate within a certain distance to media boundary.

Another impact of the Lorentz force on the resolution of the inverse problem may appear in the coupling of the shear (divergence free) and pressure (curl free) fields near the source, as opposed to the far field where shear and pressure waves travel at different speeds [**4**]. The pressure field was also shown in Ref. [**61**] to introduce a DC component into the displacement field produced by external surface actuators (*i.e.*, no body force and no coupling of shear and pressure fields). Applying the curl operator to the Navier's equation allows to isolate the contribution of the shear field at the cost of noise enhancement due to third-order derivatives [**61**]. As aforementioned, the presence of a body force in the field of view of the imaged tissue theoretically leads to overestimated mechanical parameters where the source is. Additional mapping of the motion source distribution may then be necessary to correct for the overestimation. In other reported cases where body forces (other than Lorentz forces) are present, such as supersonic shear imaging [**4**], conventional methods to discard the body force term in the Navier's equation consist in selecting displacement data after the shear wave source was switched off or selecting ROIs far from the source. Chatelin *et al.* [**161**] have developed a method to solve the inverse problem while taking body forces into account in the context of high intensity focused ultrasound. It allows to estimate optimal stiffness values through a minimisation process between experimental displacements and simulated displacements using Green's formalism. Such technique may provide the potential of including body forces in the calculation of the solution to the inverse problem in Lorentz force MR elastography.

Direct inversion techniques based on the Helmholtz equation conceptually allow for the addition of a source term in the formulation of the forward problem, but still rely on a local

homogeneity assumption and high order derivatives. Identification techniques [**116, 162**] have shown good performance on brain MRE and involve the complete formulation of the viscoelastic forward problem, thus allowing for the addition of a source term. The gradient of mechanical parameters across the imaged domain is also taken into account. Additionally, such methods have been successful in configurations where the motion source, as in our case, is present in the field of view; that is in intrinsic MRE where the displacement field is produced by arteries pulsing within the imaged domain [**143, 145**].

In Lorentz force MRE, mapping the Lorentz force density distribution can be achieved using magnetic resonance electrical impedance tomography (MR-EIT), which allows to measure electrical current densities and conductivities of electrically inhomogeneous media [**163**]. Current *in vivo* techniques of MR-EIT resort to sets of electrodes attached to the tissue of interest [**164**]. Then, electric pulses are delivered to the tissue while being imaged, which presents many similarities with Lorentz force MRE. Additionally, MR-EIT is, like MRE, a phase contrast MR technique, which in turn may be combined using the Lorentz force as a tool for dual electrical–mechanical property mapping.

2.4. Limitations

The present study investigated the feasibility of generating shear waves using a Lorentz force produced in the imaged phantom from the combination of the MR magnetic field and electrical stimulation. Despite successful generation and detection of motion fields, limitations are severalfold. In terms of MR sequence, phase difference images were output by the scanner but no access to raw data was possible, which limited detailed investigation of phase image pre-processing steps. Comparison of displacement fields measured with different fully accessible MR sequences using the same experimental setup would be necessary for quantitative assessment of Lorentz force MRE efficiency and to identify any MR sequence related variability. On the reconstruction end, the LFE performed well at producing images with clear delineations of global heterogeneous structures, which is key in medical imaging but showed significant variance within homogeneous structures in Fig. 8, and artefacts due to

wave reflection and interference in Fig. 7. This makes further mechanical testing and cross-comparisons of shear modulus estimates using standard actuation systems meaningless at this stage. Particularly, accurate evaluation of the impact of the source term on the retrieved properties should be addressed in full development by comparing Lorentz force MRE to other MRE procedures, as those listed in the previous paragraphs, which is beyond the scope of the presented study. Finally, the main limitation is the amplitude of the electrical current that is for now around 30 times above the human security threshold (2 mA peak-to-peak in humans). Nevertheless, future studies should focus on implementing our method on pre-clinical MR scanners with higher magnetic fields and stronger encoding gradients, which would allow reducing significantly the intensity of the current necessary to have robust displacement maps. For specific human applications, implementation on 7 T or higher gradient scanners might be envisaged.

2.5. Conclusion

In summary, this study demonstrated the feasibility of generating shear waves using the Lorentz force, producing stiffness maps from the displacement field, and reporting on potential impacts of the Lorentz force density on the reconstruction process. Overall, acquisitions were performed at two frequencies over three different phantom types implying removing and inserting phantom holders back into the experimental setup for each experimental condition. The consistent results obtained through multiple acquisitions indicate the robustness and reproducibility of the method. Despite significant variance in the shear modulus maps in Fig. 8, clear delineation of the two layers were observed, which is essential in medical imaging.

The LFE reconstructions could allow validating the working hypothesis to show the possibility of implementing the Lorentz force MRE method on a clinical scanner. This experimental condition using phantoms doped with physiological salt concentrations suggest that this method could be used for in vivo applications in MR elastography provided current intensities lower than 2 mA, as in transcranial alternative current stimulation (tACS)

experiments [**165, 166**]. This currently seems far from clinical applications but shows an interesting potential for preclinical studies where scanners with higher magnetic fields are available, thus producing a higher Lorentz force density for a given current value. Specific human applications on 7 T or higher magnetic field scanners might also be possible in the future.

Lowering the current intensity may also be reached by increasing other imaging parameters such as the motion encoding gradient amplitude (for instance to 285 $mT.m^{-1}$) [**167**], the number of averaging over identical acquisitions repeated successively (to increase the signal-to-noise ratio), the number of MEG cycles (provided a suitable trade-off with the echo-time. Latitude thus remains to improve motion detection and reduce the current intensity. In terms of spatial selectivity, recent tACS results have shown that optimal electrode positioning on the scalp along with multi-frequency current application allow for delivering current to targeted deep regions into the brain [**168**]. Such current sequence design may be helpful in conceptualising Lorentz force MR brain elastography thus circumventing the low penetration of shear waves at high frequencies in conventional MR elastography due to significant attenuation. It may also provide the advantage of *in situ* localized vibrations to reduce diffraction artefacts by the skull when using an external vibration source.

As introduced above, a main advantage compared with conventional MR elastography is the fact that no external actuator is required thus excluding complex wave coupling between the external body and the imaged organ. The possibility of varying the shear wave frequency by a simple change in current frequency is another advantage. Eventually, Lorentz force MR elastography may be further developed as a remote mean to generate shear waves, notably with electric stimulation devices instead of electrodes, as in Ref. [**146**]. At present, a framework involving tests of other MR sequences along with other reconstruction methods is currently being designed and may help sharpen the proposed technique. This will allow for quantitative characterization of the measured displacement fields using various encoding schemes and quantitative assessment of the impact of the Lorentz force density on the reconstructed mechanical parameter maps. The inclusion of MR-EIT protocols to Lorentz force

MRE is also under development in an attempt to provide an original human or preclinical tool for assessment of both mechanical and electrical properties.

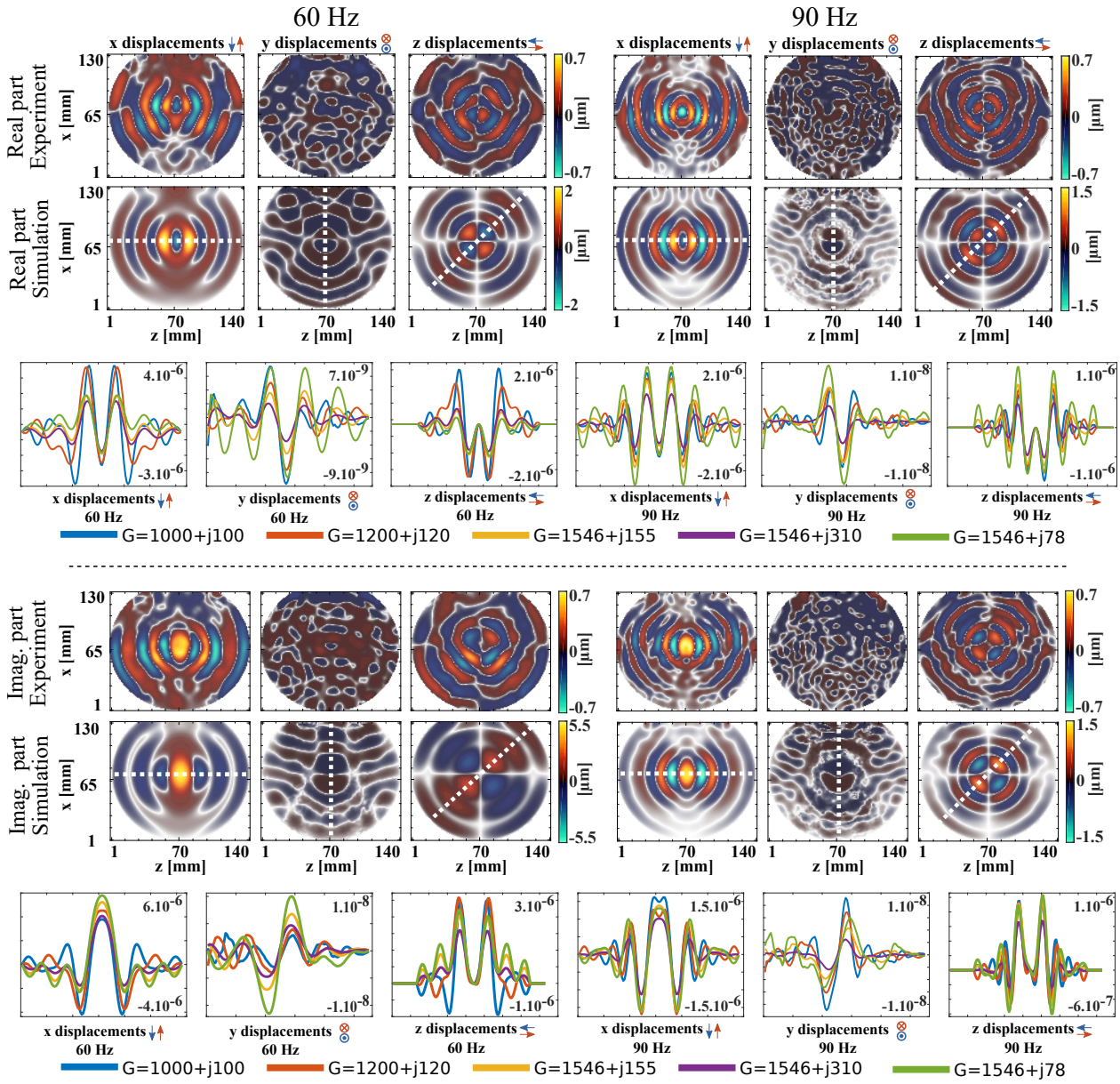

Figure 6 – First experiment: Real and imaginary parts of the experimental and simulated complex displacement fields in phantom A along x, y, and z directions in the MR slice. The origin of elastic waves clearly appears at the centre of displacement maps. Images were acquired (experiment) and extracted (simulation) in the greyed-out sagittal plane located at the centre of the phantom, as indicated in Fig. 4 ("imaging plane" label). Two electrical currents were used with frequencies of 60 Hz and 90 Hz, and an intensity of 137.5 mA peak-to-peak in both experiment and simulation. The complex shear moduli used to obtain the displayed simulated displacement maps were: $\mu_{\,60\text{ Hz}} = 1546 + i155$ Pa and $\mu_{\,90\text{ Hz}} = 1768 + i177$ Pa. Line profiles of the real and imaginary parts of displacements along the propagation directions (dashed white line) are plotted for each combination of storage and loss moduli described in Table 2. This figure intended to show that diffraction patterns characteristic of a body force actuation could be observed where the Lorentz force was peaking, regardless of the complex shear moduli.

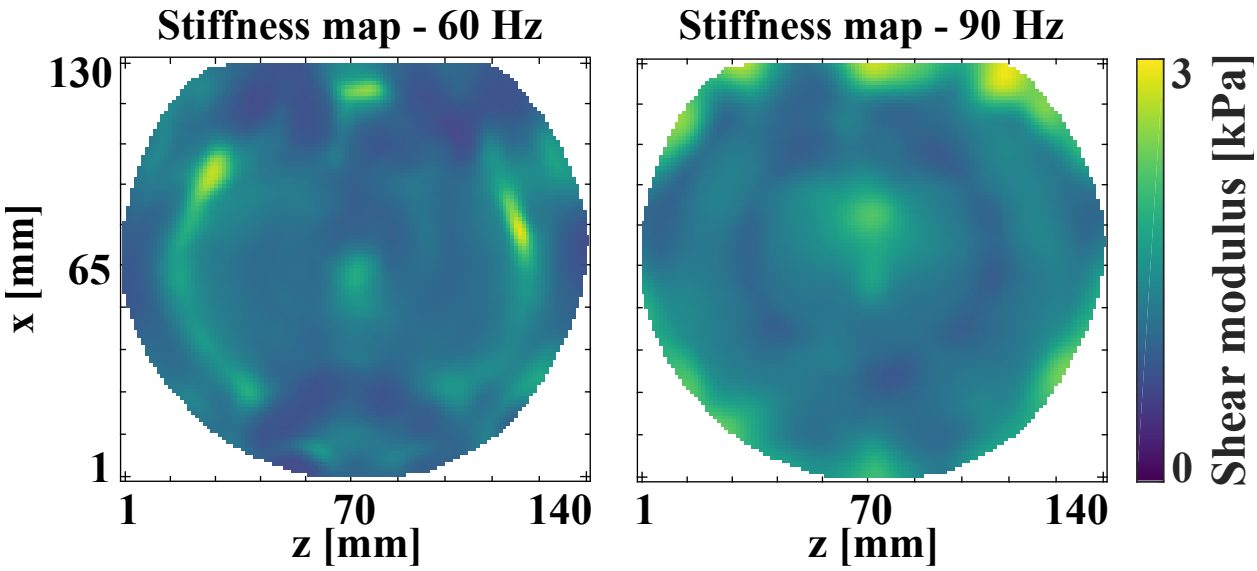

Figure 7 – This figure shows reconstructions of stiffness distributions using the LFE inversion method applied to displacement data from the first experiment. Phantom A was homogeneous and displacements along the x axis were processed. The harmonic currents applied had a frequency of 60 Hz and 90 Hz and an intensity of 137.5 mA peak-to-peak. Local maxima are assumed to be due to LFE limitations arising from the presence of the Lorentz force and wave reflections off boundaries. Images were acquired in the imaged plane indicated in Fig. 4a. The mean values over the entire field of views are $\mu_{r,\ 60\ \mathrm{Hz}} = 1546 \pm 383$ Pa and $\mu_{r,\ 90\ \mathrm{Hz}} = 1768 \pm 440$ Pa.

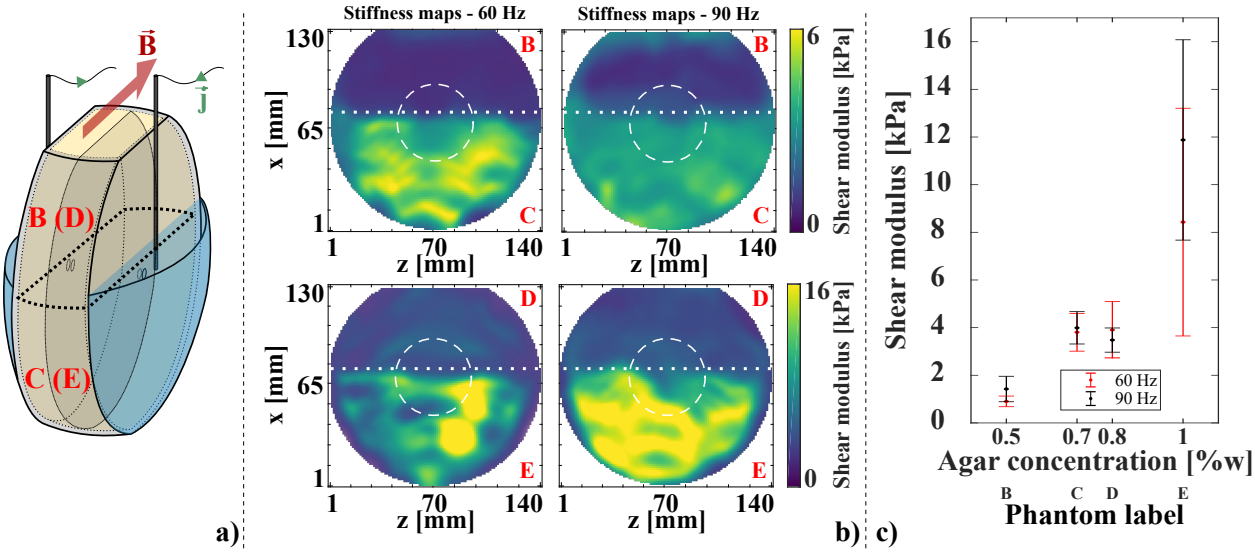

Figure 8 – Second experiment. **a.** Phantoms arrangement: B (D) on top of C (E). Phantom separation is indicated by the thick black dashed line. The greyed-out sagittal plane is the acquisition plane. **b.** Stiffness maps from harmonic actuations at 60 Hz and 90 Hz with a current intensity of 62 mA peak-to-peak in phantoms B, C, D, and E. Mean values and standard deviations were calculated in compartments separated by the dotted line. The dashed circle indicates the region where the magnitude of the Lorentz force density drops from its maximum value to 1/10th of this maximum. **c.** Mean shear storage moduli in phantoms B, C, D, and E. Error bars correspond to standard deviations. The separation between lower and higher parts of phantoms on stiffness maps, which corresponds to higher and lower agar concentrations, respectively, is clearly visible in panel b.

Chapitre 3

Tomographie d'impédance électrique par résonance magnétique

La combinaison de l'élastographie par résonance magnétique et de la stimulation électrique décrite au chapitre précédent a permis d'induire des forces volumiques de Lorentz, sources d'ondes de cisaillement dans des fantômes d'agar conducteurs. Les résultats présentés suggèrent que l'intensité des courants de stimulation électriques garantissant des champs ondulatoires d'amplitudes mesurables par ERM serait, à l'heure actuelle, trop élevée pour envisager une application *in vivo* au moyen de systèmes d'IRM cliniques 3 T. Cependant, une procédure de cartographie des propriétés mécaniques et électriques au cours d'une même session d'imagerie par résonance magnétique pourrait être envisagée et constituerait une base de caractérisation électromécanique des tissus biologiques. Des acquisitions combinées d'ERM extrinsèque et de tomographie d'impédance électrique par résonance magnétique permettraient cette double caractérisation.

Ce chapitre présente les bases de la tomographie d'impédance électrique par résonance magnétique (TIERM ou MREIT pour *magnetic resonance electrical impedance tomography*) et une approche de reconstruction de la conductivité électrique des tissus à partir des données de densité de flux magnétique acquises par une séquence dédiée d'IRM. La mise en oeuvre préliminaire d'une procédure expérimentale de mesure de distributions de densité de flux magnétique dans un fantôme d'agar conducteur est également présentée.

Les expériences d'élastographie par force de Lorentz présentées dans le chapitre 2 reposent sur l'utilisation de fantômes d'agar de conductivité homogène. Dans ce cas, les conditions d'injection et de propagation du courant aux frontières permettent de déterminer une distribution unique de densité de courant, $\mathbf{J} = (J_x, J_y, J_z)$ (A.m^{-2}) et de force de Lorentz, $\mathbf{f}_L$ (N.m^{-3}), quelle que soit la valeur de la conductivité ohmique du milieu $\sigma\,(x, y, z) = \sigma_0$ (S.m^{-1}). Les tissus biologiques présentent toutefois des distributions de conductivité hétérogènes dont la reconstruction devient nécessaire à la cartographie de la distribution du courant induit par stimulation. Cette reconstruction est notamment permise en IRM par la méthode de TIERM. Celle-ci repose sur l'acquisition d'images de résonance magnétique d'un tissu soumis à une stimulation électrique basse fréquence (< 1 kHz). La densité de courant générée dans le milieu, déterminée par sa conductivité électrique et les conditions aux limites, perturbe la phase du signal de résonance magnétique, laquelle peut être convertie en densité de flux magnétique $\mathbf{B} = (B_x, B_y, B_z)$. En pratique, seule la composante B_z parallèle au champ principal $\mathbf{B}_0 = ||\mathbf{B}_0||\,\mathbf{e}_z$ du scanner IRM est mesurable. La distribution de conductivité électrique dans le tissu imagé est alors reconstruite à partir de la formulation d'un problème direct reliant $\mathbf{J}$ et σ d'une part et d'un problème inverse reliant B_z, $\mathbf{J}$ et σ d'autre part. Les propriétés électromagnétiques des tissus sont résumées dans le tableau 3. En TIERM, la basse fréquence du courant électrique injecté permet de négliger la permittivité diélectrique du tissu, *i.e.*, $\kappa \approx \sigma$. Par ailleurs, sa perméabilité magnétique μ est supposée être proche de celle du vide, *i.e.*, $\mu \approx \mu_0$.

3.1. Théorie générale

3.1.1. Problème direct

La loi de Biot-Savart, la loi d'Ohm et les équations de Maxwell établissent le cadre théorique d'une expérience de TIERM. La loi de Biot-Savart décrit la densité de flux magnétique $\mathbf{B}$ (T) générée par une densité de courant continu $\mathbf{J}$ distribuée dans un milieu Ω de

Tableau 3 – Propriétés électromagnétiques des tissus

	Symbole	Nom	Description
Propriétés électriques	χ_e	Susceptibilité diélectrique (-)	Caractérise la polarisation $\mathbf{P}$ du matériau sous l'effet d'un champ électrique externe $\mathbf{E}$, *i.e.*, la capacité des dipôles à pivoter dans le milieu. $\mathbf{P} = \epsilon_0 \chi_e \mathbf{E}$[a] .
	ϵ	Permittivité diélectrique (F.m^{-1})	Caractérise la densité de flux électrique $\mathbf{D}$ résultant de la polarisation du matériau sous l'effet d'un champ électrique externe. $\epsilon = \epsilon_0 (1 + \chi_E)$ et $\mathbf{D} = \epsilon_0 \mathbf{E} + \mathbf{P} = \epsilon_0 (1 + \chi_E) \mathbf{E} = \epsilon \mathbf{E}$.
	σ	Conductivité électrique (S.m^{-1})	Caractérise la capacité d'un matériau à conduire une charge électrique.
	κ	Admittivité (S.m^{-1})	$\kappa = \sigma + i\omega\epsilon$.
	ρ	Densité de charge (C.m^{-3})	Densité totale de charge $\rho = \rho_{\text{liées}} + \rho_{\text{libres}}$ où les charges liées résultent de la polarisation du matériau et peuvent se déplacer localement tandis que les charges libres peuvent traverser le milieu.
Propriétés magnétiques	χ_m	Susceptibilité magnétique (-)	Caractérise la magnétisation $\mathbf{M}$ du matériau sous l'effet d'un champ magnétique externe $\mathbf{H}$. $\mathbf{M} = \mu_0 \chi_m \mathbf{H}$[b].
	μ	Perméabilité magnétique (H.m^{-1})	Caractérise la densité de flux magnétique $\mathbf{B}$ résultant de la magnétisation du matériau sous l'effet d'un champ magnétique externe. $\mu = \mu_0 (1 + \chi_m)$ et $\mathbf{B} = \mu_0 \mathbf{H} + \mathbf{M} = \mu_0 (1 + \chi_m) \mathbf{H} = \mu \mathbf{H}$.

[a] ϵ_0 est la constante de susceptibilité diélectrique du vide définie par $\epsilon_0 = 8.85 \times 10^{-12}$ F.m^{-1}
[b] μ_0 est la constante de perméabilité magnétique du vide définie par $\mu_0 = 4\pi \times 10^{-7}$ H.m^{-1}

conductivité ohmique $\sigma\,(x,y,z)$:

$$\mathbf{B}\,(\mathbf{r}) = \frac{\mu_0}{4\pi} \iiint_{\Omega} \frac{\mathbf{J}\,(\mathbf{r}') \times (\mathbf{r} - \mathbf{r}')}{|\mathbf{r} - \mathbf{r}'|^3}\, d\mathbf{r}' + \mathbf{B}_{ext}\,(\mathbf{r})\,, \tag{48}$$

où $\mathbf{B}_{ext}$ est la densité de flux magnétique induite dans le domaine Ω par des courants extérieurs à Ω. La composante selon l'axe z de la densité de flux magnétique est alors définie uniquement en fonction des composantes x et y de la densité de courant électrique, *i.e.*, J_x et J_y :

$$B_z\,(\mathbf{r}) = \frac{\mu_0}{4\pi} \iiint_{\Omega} \frac{J_x\,(\mathbf{r}')\,(y - y') - J_y\,(\mathbf{r}')\,(x - x')}{|\mathbf{r} - \mathbf{r}'|^3}\, d\mathbf{r}' + B_{z,ext}\,(\mathbf{r})\,. \tag{49}$$

La densité de courant électrique $\mathbf{J}$ dans le tissu est déterminée en fonction de la conductivité σ par loi d'Ohm :

$$\mathbf{J} = \sigma\mathbf{E} = -\sigma\nabla V, \tag{50}$$

où V est le potentiel électrique (V).

Finalement, les équations de Maxwell décrivant les interactions entre champs électrique $\mathbf{E}$ et magnétique $\mathbf{H} = \mathbf{B}/\mu_0$ sont incorporées. En dehors du cadre d'expérience de TIERM, celles-ci permettent notamment de caractériser la propagation de la lumière et sa vitesse, établissent les relations d'induction entre champs électrique et magnétique et mènent à la formulation de la conservation de la charge électrique. Les équations de Maxwell se présentent sous différentes formes selon les propriétés électromagnétiques et temporelles du problème étudié et sont présentées dans le tableau 4. Les champs soulignés sont à valeur réelle et indiquent une dépendance temporelle et les champs non-soulignés sont à valeur complexe et indiquent un régime harmonique.

Tableau 4 – Équations de Maxwell

Formulation générale			**Dans le vide**			**Harmonique**		
$\nabla\cdot\underline{\mathbf{E}} = \rho/\epsilon$	(51)		$\nabla\cdot\underline{\mathbf{E}} = 0$	(52)		$\nabla\cdot\mathbf{E} = \rho/\epsilon$	(53)	
$\nabla\cdot\underline{\mathbf{B}} = 0$	(54)		$\nabla\cdot\underline{\mathbf{B}} = 0$	(55)		$\nabla\cdot\mathbf{B} = 0$	(56)	
$\nabla\times\underline{\mathbf{E}} = -\frac{\partial}{\partial t}\underline{\mathbf{B}}$	(57)		$\nabla\times\underline{\mathbf{E}} = -\frac{\partial}{\partial t}\underline{\mathbf{B}}$	(58)		$\nabla\times\mathbf{E} = -i\omega\mathbf{B}$	(59)	
$\nabla\times\underline{\mathbf{H}} = \underline{\mathbf{J}} + \frac{\partial}{\partial t}\epsilon\underline{\mathbf{E}}$	(60)		$\nabla\times\underline{\mathbf{H}} = \frac{\partial}{\partial t}\epsilon\underline{\mathbf{E}}$	(61)		$\nabla\times\mathbf{H} = \mathbf{J} + i\omega\epsilon\mathbf{E}$	(62)	

En tomographie d'impédance électrique, le courant continu injecté dans le tissu permet de négliger la dépendance temporelle/fréquentielle des équations de Maxwell et de considérer le problème aux conditions limites suivant :

$$\begin{cases} \nabla\cdot\mathbf{J} = 0 = \nabla\cdot\mathbf{B}, & \mathbf{J} = \dfrac{1}{\mu_0}\nabla\times\mathbf{B} \quad \text{dans } \Omega, \\ \mathbf{J} = \sigma\mathbf{E}, & \nabla\times\mathbf{E} = 0 \quad \text{dans } \Omega, \\ I = -\displaystyle\int_{\varepsilon^+}\mathbf{J}\cdot\mathbf{n}\,ds = \int_{\varepsilon^-}\mathbf{J}\cdot\mathbf{n}\,ds, & \mathbf{J}\times\mathbf{n} = 0 \quad \text{sur } \varepsilon^+\bigcup\varepsilon^- \\ \mathbf{J}\cdot\mathbf{n} = 0 & \text{sur } \partial\Omega\backslash\overline{\varepsilon^+\bigcup\varepsilon^-}. \end{cases} \tag{63}$$

Le problème direct donné par Eq. 63 décrit une expérience de TIERM au cours de laquelle un courant électrique est injecté dans Ω par les biais d'électrodes ε^+ et ε^-.

3.1.2. Problème inverse

La reconstruction de la conductivité électrique en TIERM a notamment été proposée avec l'algorithme B_z harmonique [**169, 170**]. Cette approche repose sur la reconstruction itérative de la conductivité à partir de la courbure de B_z, $\nabla^2 B_z$, et à travers le développement suivant. L'équation 56 de conservation de flux et le rotationnel de l'équation 62 de Maxwell-Ampère avec $\omega = 0$ donnent :

$$\begin{aligned} \nabla \times \nabla \times \mathbf{H} &= \nabla (\nabla \cdot \mathbf{H}) - \nabla^2 \mathbf{H} = \nabla \times \mathbf{J}, \\ &= -\nabla^2 \mathbf{H}, \\ \Leftrightarrow -\nabla^2 \mathbf{H} &= \nabla \times \mathbf{J}. \end{aligned} \tag{64}$$

L'identité vectorielle $\nabla \times (\mathbf{\Psi A}) = \mathbf{\Psi} \nabla \times \mathbf{A} + \nabla \mathbf{\Psi} \times \mathbf{A}$ et la loi d'Ohm permettent d'écrire :

$$\nabla \times \mathbf{J} = \nabla \times (\sigma \mathbf{E}) = \nabla \sigma \times \mathbf{E}. \tag{65}$$

L'équation 64 peut alors se réécrire :

$$\nabla^2 \mathbf{H} = \nabla \sigma \times \nabla V = \nabla^2 \mathbf{B} \frac{1}{\mu_0}. \tag{66}$$

La composante selon $\mathbf{e_z}$ de $\nabla^2 \mathbf{B}$ est donc donnée par :

$$\frac{1}{\mu_0} \nabla^2 B_z = \frac{\partial \sigma}{\partial x} \frac{\partial V}{\partial y} - \frac{\partial \sigma}{\partial y} \frac{\partial V}{\partial x}. \tag{67}$$

L'équation 67 est la relation constitutive de l'algorithme B_z harmonique. L'acquisition de N_e images de $B_{z,e}$, où $e = 1, \cdots, N_e$, dans un tissu successivement soumis à N_e injections de

courants linéairement indépendants, permet de reformuler l'équation 67 :

$$\underbrace{\begin{bmatrix} \frac{\partial V_1}{\partial y} & -\frac{\partial V_1}{\partial x} \\ \vdots & \vdots \\ \frac{\partial V_{N_e}}{\partial y} & -\frac{\partial V_{N_e}}{\partial x} \end{bmatrix}}_{\mathbf{U}, \text{ de (63)}} \underbrace{\begin{Bmatrix} \frac{\partial \sigma}{\partial x} \\ \\ \frac{\partial \sigma}{\partial y} \end{Bmatrix}}_{\mathbf{s}, \text{ inconnues}} = \frac{1}{\mu_0} \underbrace{\begin{Bmatrix} \nabla^2 B_{z,1} \\ \vdots \\ \nabla^2 B_{z,N_e} \end{Bmatrix}}_{\mathbf{b}, \text{ mesure}}. \tag{68}$$

La reconstruction itérative consiste en une résolution successive de la formule suivante :

$$\mathbf{U}_k \mathbf{s}_{k+1} = \mathbf{b}, \tag{69}$$

où $\mathbf{s_{k+1}}$ est donné par :

$$\mathbf{s}_{k+1} = \left(\mathbf{U}_k^T \mathbf{U}_k + \frac{\lambda}{|\mathbf{U}_k^T \mathbf{U}_k|} \mathbf{I}_{Ne} \right) \mathbf{U}_k^T \mathbf{b}, \tag{70}$$

où $\mathbf{I}_{Ne}$ est la matrice identité de taille $N_e \times N_e$ et λ est un paramètre de régularisation. Finalement, la conductivité σ_{k+1} est obtenue par la résolution de l'équation de Poisson suivante :

$$\begin{cases} \tilde{\nabla}^2 \sigma_{k+1} = \tilde{\nabla} \cdot \mathbf{s}_{k+1} & \text{dans } \Omega_t, \\ \\ \sigma_{k+1} \;=\; \sigma_0 & \text{sur } \partial\Omega_t. \end{cases} \tag{71}$$

L'opérateur $\tilde{\nabla}$ indique des dérivées dans le plan de l'image Ω_t et σ_0 est la conductivité aux frontières du domaine dans l'image, $\partial\Omega_t$. Une revue détaillée du fonctionnement de l'algorithme B_z harmonique et d'autres méthodes de reconstruction d'image de conductivité électrique par TIERM sont présentées dans Seo et Woo [**171, 172**] et Seo *et al.* [**173**]. En particulier, les auteurs rapportent trois observations essentielles :

1. Si σ est une solution de l'équation de Biot-Savart (Eq. 49), $\alpha\sigma$ en est également une solution pour tout $\alpha > 0$. La connaissance préalable de la conductivité dans une partie du domaine imagé ou la mesure du potentiel V en deux points aux frontières permet d'écarter le facteur d'échelle. Des valeurs de conductivités locales peuvent être préalablement établies aux frontières du domaine grâce à l'utilisation d'un gel de contact électrode-tissu de conductivité connue.

2. La densité de flux magnétique B_z est insensible aux contrastes de conductivité dans la direction perpendiculaire aux lignes équipotentielles, c'est à dire, dans la direction de ∇V (identique à celle de $\mathbf{J}$).

3. B_z est sensible aux contrastes de conductivité dans la direction tangentielle aux lignes équipotentielles, c'est à dire, dans une direction perpendiculaire à ∇V (*i.e.*, perpendiculaire à $\mathbf{J}$).

Le 3$^{\text{ème}}$ point est décliné en trois situations :

3.1. Si $\nabla^2 B_z > 0$ au point $\mathbf{r_0}$, σ augmente dans la direction $\mathbf{J}(\mathbf{r_0}) \times \mathbf{e_z}$

3.2. Si $\nabla^2 B_z < 0$ au point $\mathbf{r_0}$, σ diminue dans la direction $\mathbf{J}(\mathbf{r_0}) \times \mathbf{e_z}$

3.3. Si $\nabla^2 B_z = 0$ au point $\mathbf{r_0}$, σ ne varie pas dans la direction $\mathbf{J}(\mathbf{r_0}) \times \mathbf{e_z}$

Ces propriétés de sensibilités directionnelles imposent l'injection d'au moins deux courants dans des directions perpendiculaires entre elles. En pratique, deux paires d'électrodes, $\left(\varepsilon_1^+, \varepsilon_1^-\right)$ et $\left(\varepsilon_2^+, \varepsilon_2^-\right)$, sont positionnées autour du domaine imagé de façon à maximiser l'aire formée par $(\mathbf{J}_1 \times \mathbf{J}_2) \cdot \mathbf{e_z}$.

3.2. Dispositif expérimental

Un dispositif expérimental a été mis en place dans l'optique de conduire une expérience simple de TIERM avec un scanner IRM 3 T (Achieva TX, Philips Healthcare, Best, Netherlands). Les 5 éléments principaux sont :

— conception d'un fantôme et de son support incluant les électrodes et connecteurs

— programmation du signal électrique à délivrer au fantôme et synchronisé avec la séquence d'acquisition IRM

— programmation de la séquence IRM (assurée par Dr. Guillaume Gilbert)

— programmation de l'algorithme B_z harmonique

La géométrie du fantôme et de son support est représentée Fig. 9 et est inspirée des expériences standard de TIERM (voir par exemple [**174**]). Le profil du signal électrique a été

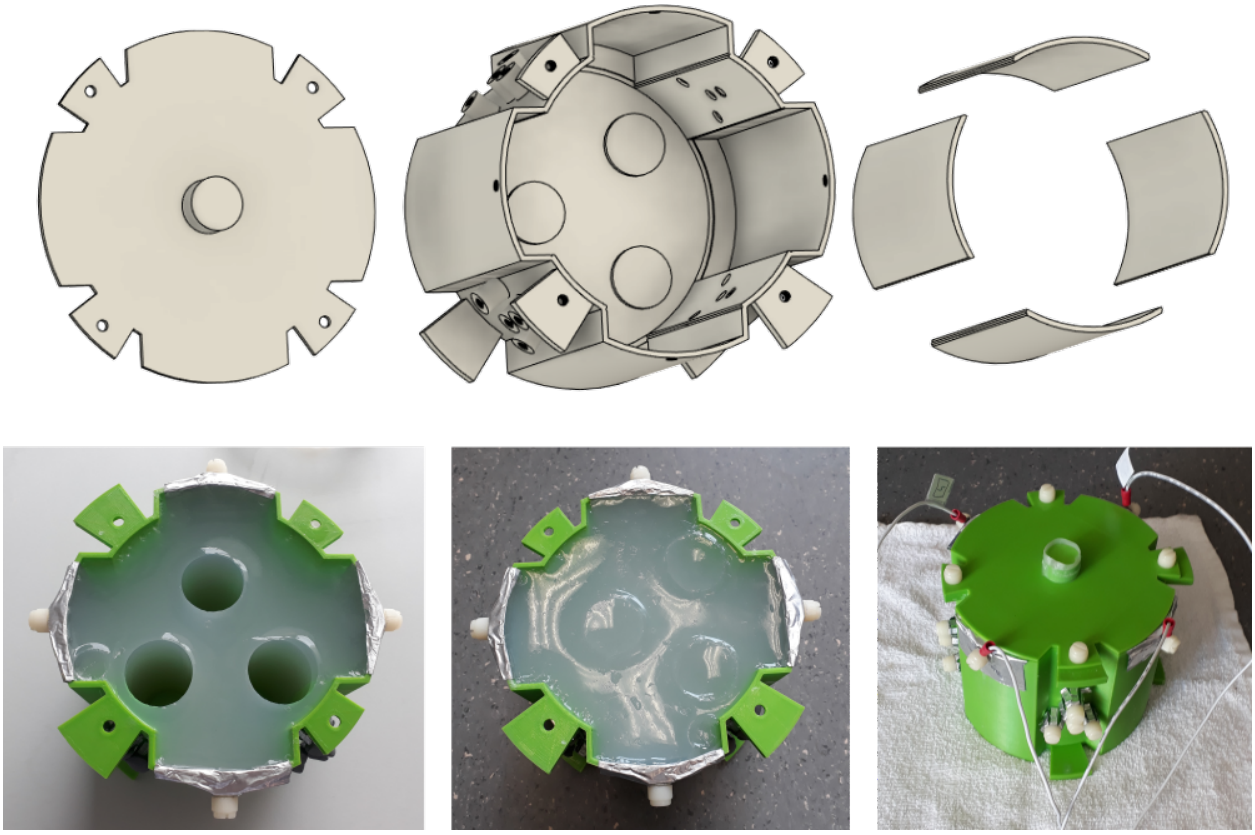

Figure 9 – Fantôme de TIERM et son support. La première ligne représente une vue éclatée du support avant impression. La deuxième ligne représente l'objet imprimé et le fantôme avec inclusions.

conçu sur Matlab et exporté vers un générateur d'onde Keysight 33500B (Keysight Technologies, Santa Rosa, Californie, États-Unis).

La Fig. 10 représente le signal intégré au générateur d'onde. Les deux segments correspondent aux deux régimes de polarités opposées utilisés avec la séquence IRM décrite plus bas. Un signal de déclenchement "TTL" est envoyé à la séquence IRM au début de chaque segment (voir également la Fig. 11). Le signal électrique est ensuite amplifié par un amplificateur (Brüel & Kjær, type 2706).

La Fig. 11 présente la séquence IRM d'écho de spin utilisée pour produire les images de densité de flux magnétique. Des récepteurs "TTL" ont été ajoutés pour assurer la synchronisation de la séquence avec le générateur de courant. La chronologie est la suivante : temps d'injection $T_C = 13.6$ ms, temps de répétition $T_R = 800$ ms, temps d'écho $T_E = 25$ ms.

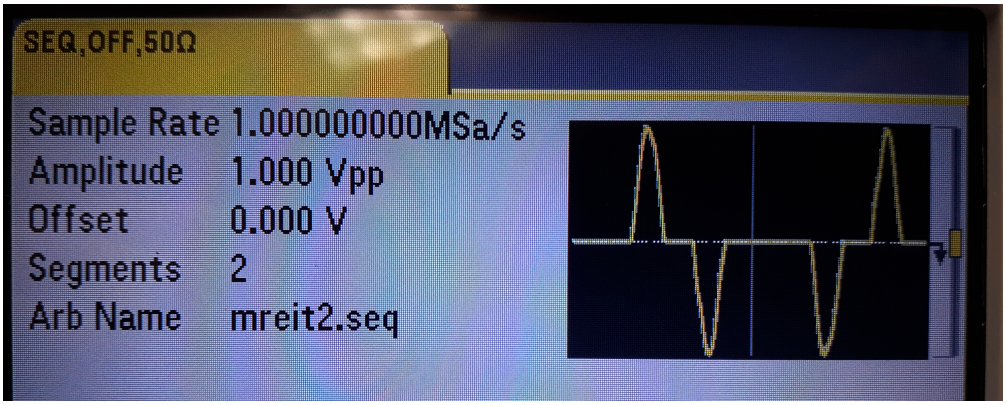

Figure 10 – Forme du signal électrique de TIERM.

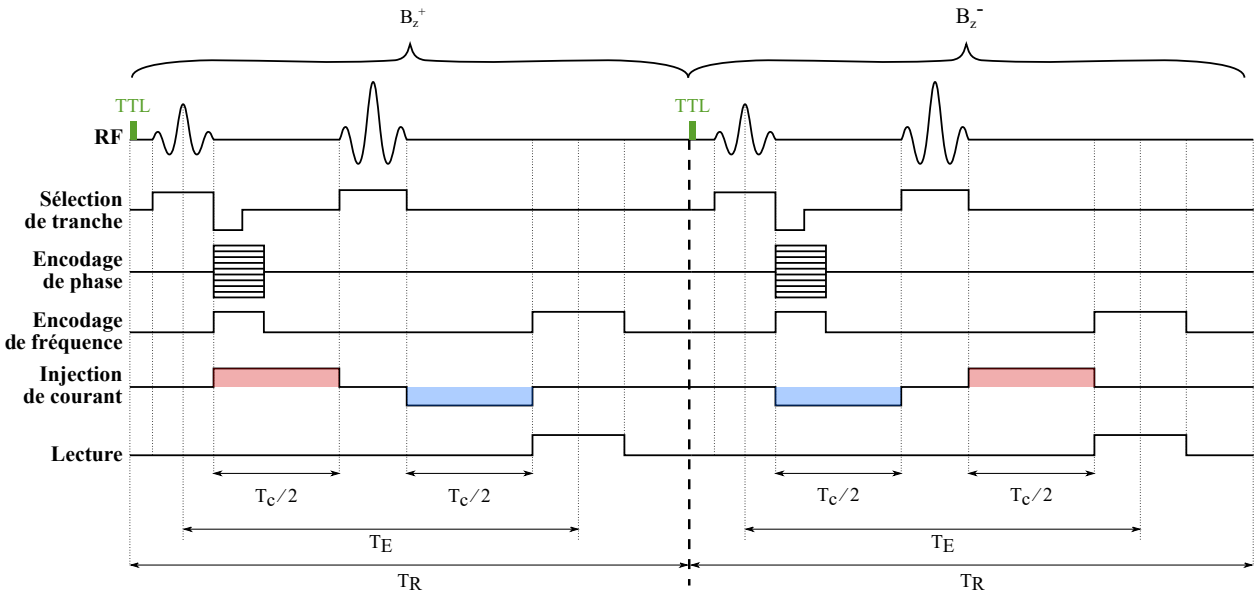

Figure 11 – Séquence IRM d'écho de spin à laquelle des déclencheurs "TTL" ont été ajoutés.

Le signal correspondant à une image de résonance magnétique est donné par :

$$M^{\pm}(x,y) = \rho(x,y)\, e^{i\delta(x,y)} e^{\pm i\gamma B_z(x,y) T_C}, \tag{72}$$

où l'exposant $\pm$ représente les deux polarités d'injection de courant, δ est un déphasage statique, ρ est l'amplitude du signal de résonance magnétique et $\gamma = 26.75 \times 10^7$ rad.s^{-1}.T^{-1} est le rapport gyromagnétique de l'hydrogène. Le déphasage causé par B_z s'écrit :

$$\Psi(x,y) = \arg\left(\frac{M^+(x,y)}{M^-(x,y)}\right) = 2\gamma B_z(x,y)\, T_C \tag{73}$$

L'acquisition de deux images correspondant à des courants de polarités opposées permet de supprimer l'artéfact systématique δ par le biais de la relation 73. La densité de flux magnétique B_z est alors donnée par :

$$B_z(x,y) = \frac{\Psi(x,y)}{2\gamma T_C} \tag{74}$$

La Fig. 12 représente une cartographie de B_z obtenue à partir de la méthode présentée ci-dessus. Les contours rouge et bleu symbolisent la paire d'électrode active pendant l'acquisition. Pour compléter ces expériences préliminaires, une deuxième injection de courant devrait être assurée à travers la deuxième paire d'électrode, assurant la stabilité de la reconstruction de la conductivité.

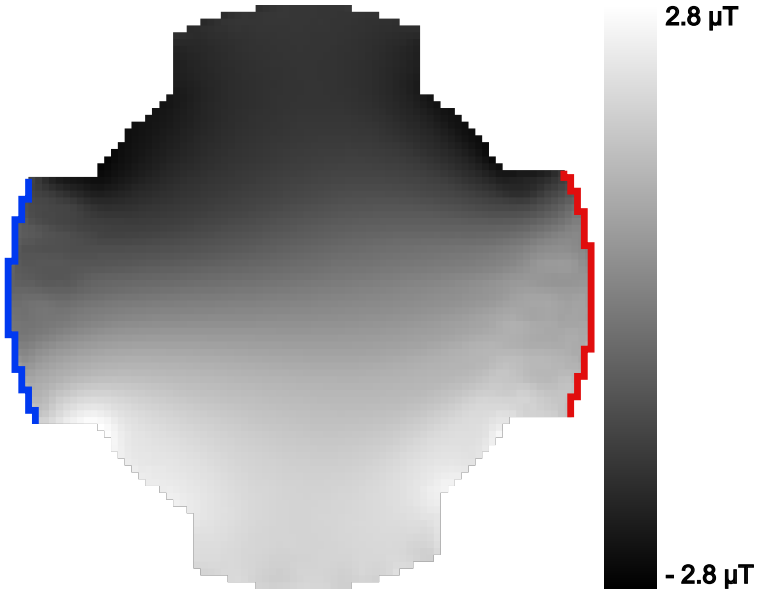

Figure 12 – Carte de densité de flux magnétique B_z.

3.3. Conclusion

Des expériences préliminaires de tomographie d'impédance électrique par résonance magnétique sur fantôme ont été conduites à travers la conception d'un dispositif expérimental standard à 4 électrodes. Des images de densité de flux magnétique dans des coupes d'un fantôme conducteur ont été obtenues par la modification d'une séquence simple d'écho de spin.

Les temps d'acquisitions pourront être réduits par l'imagerie de coupes successives amorcée avant l'écoulement complet de chaque TR associé, lorsque la séquence devient inactive. Par ailleurs, les similarités entre les séquences à contraste de phase d'ERM et de TIERM, du point de vue de l'encodage de la quantité d'intérêt et de la synchronisation du système d'IRM avec la sollicitation externe, pourraient également être mises à profit dans le cadre d'une double caractérisation électrique et mécanique des biotissus par résonance magnétique. La reconstruction de distributions de conductivité électrique à partir de l'algorithme B_z harmonique est présentée dans le chapitre suivant à l'aide de simulations numériques dans un modèle 3D de cerveau de souris.

Chapitre 4

Imaging the electro-mechanical properties of the mouse brain during transcranial electrical stimulation : numerical simulations

Ce chapitre repose sur l'article intitulé "Imaging the electro-mechanical properties of the mouse brain during transcranial electrical stimulation : numerical simulations" prêt à soumettre par Guillaume Flé, Elijah Van Houten, Guillaume Gilbert et Guy Cloutier.

Avant propos

Bien que la méthode d'ERM par force de Lorentz ne soit à priori pas applicable cliniquement pour des raisons de sécurité liées à l'utilisation de courants électriques trop élevés, cette approche peut être reconsidérée d'un point de vue pré-clinique à des échelles spatiales plus faibles. En particulier, les champs électriques établis au cours d'une stimulation électrique sont sensibles aux dimensions spatiales et atteignent des ampleurs supérieures de deux ordres de grandeur dans un cerveau de souris en comparaison au cerveau humain, moyennant une même intensité de stimulation [**175**]. Les questions relatives à l'amplitude de la force de Lorentz et à celle des ondes de cisaillement émises se posent alors de nouveau dans une optique d'application aux petits animaux avec des systèmes d'IRM à hauts champs magnétiques. Cette problématique est abordée ici par le biais de simulations numériques dans un

modèle de tête de souris. Trois thématiques particulières ont motivé ces travaux. La première est relative à la faisabilité de l'ERM par force de Lorentz à l'échelle du cerveau de souris. La seconde est relative à l'utilisation d'une méthode itérative de reconstruction d'images de viscoélasticité reposant sur une description générale du mouvement dans un solide viscoélastique, hétérogène, isotrope et exempt de forces volumiques. La troisième ajoute aux aspects liés à l'élastographie un volet de tomographie d'impédance électrique par résonance magnétique, pertinent lorsqu'un dispositif regroupant la stimulation électrique et l'imagerie par résonance magnétique est mis en place. L'évaluation *in silico* du protocole proposé est une étape valable de développement technologique, préalablement à tout test expérimental étant donné les coûts et difficultés pratiques associés à la procédure décrite dans ce chapitre.

Contributions des auteurs

Guillaume Flé : proposition du projet, conception des simulations numériques, programmation de l'algorithme Bz harmonique, rédaction et révision de l'article.

Elijah Van Houten : mise à disposition de l'algorithme NLI, révision de l'article.

Guillaume Gilbert : participation aux expériences de résonance magnétique préliminaires, révision de l'article.

Guy Cloutier : direction générale, financement et révision de l'article.

Résumé

De récents progrès en imagerie de l'activité fonctionnelle du cerveau ont suggéré que des interactions complexes entre ses propriétés mécaniques et l'activité neuronale se manifestent au cours de procédures de neurostimulation. En particulier, des variations locales de la rigidité du cerveau de souris, mesurées par élastographie par résonance magnétique (ERM), ont été corrélées avec l'activation induite par stimulation électrique et ont permis l'identification visuelle de la région sensible à partir d'images d'élasticité. Lorsque les protocoles de stimulation électrique et d'ERM sont conduits simultanément, le courant électrique administré se

couple au champ magnétique du système IRM et produit des forces volumiques de Lorentz. Ces forces sont distribuées relativement au positionnement des électrodes, dépendent de la conductivité électrique des tissus, et induisent des ondes mécaniques élastiques interférant avec le champ d'ondes mécaniques générées par l'oscillateur externe de l'ERM. Dans cette étude, nous avons modélisé un protocole d'imagerie combinant l'ERM et la tomographie d'impédance électrique par résonance magnétique (TIERM), permettant la caractérisation respective de la viscoélasticité et la conductivité électrique du cerveau de souris, notamment au cours d'une procédure de stimulation électrique transcrânienne. En particulier, nous avons simulé une expérience concomitante d'ERM et de stimulation transcrânienne à courant alternatif (tACS) et étudié l'impact des forces volumiques de Lorentz induites par la tACS sur les images de propriétés mécaniques reconstruites via une méthode d'inversion non-linéaire par sous-zones. Des données synthétiques d'ERM ont été générées dans un modèle réaliste de tête de souris et ont été analysées dans le cadre de trois situations spécifiques : ERM standard, ERM standard + tACS, et tACS uniquement. L'expérience numérique de TIERM a été abordée par la simulation de la distribution de la densité du flux magnétique résultant des faibles courants continus spécifiques à ce protocole, et les cartes de conductivité électrique ont été obtenues par l'analyse de la courbure spatiale de la densité du flux magnétique. Les résultats montrent que les forces volumiques de Lorentz produites par des courants d'intensité physiologiquement acceptable induisent des ondes élastiques d'amplitudes trop faibles pour être détectées par IRM, même avec des systèmes de 11 Tesla. Dans l'éventualité où ces déplacements pourraient être imagés avec précision, l'absence de forces volumiques dans la formulation du problème inverse se traduit par d'importantes erreurs de reconstruction. La TIERM pourrait contribuer à compléter cette approche par la cartographie de la distribution de la conductivité électrique, et par extension celle de la distribution des forces de Lorentz. Les déplacements mesurés au cours d'une session d'ERM et de tACS combinées montrent que la contribution du transducteur externe d'ERM domine celle de la force de Lorentz, ce qui a permis une reconstruction précise d'images de viscoélasticité à partir du champ d'ondes acoustiques total. Cette approche multiphysique peut être transposée à l'imagerie

du cerveau humain et peut offrir plus de possibilités pour la caractérisation des fonctions cérébrales ensemble qu'isolément.

Mots clés : ERM, TIERM, tACS, Éléments finis, Simulation, Problème inverse

Abstract

Recent advances in brain functional activity mapping have suggested that complex interactions between neuronal activity and brain mechanical properties manifest during neurostimulation. Notably, local stiffness variations in the mouse brain, measured with magnetic resonance elastography (MRE), have been correlated with the electric stimulation induced brain activation, and have allowed visual identification of the responsive region from elasticity images. When electrical stimulation and MRE are performed simultaneously, the administered electric current couples with the strong magnetic field of the MR scanner to produce Lorentz body forces. Those body forces are dependent on electrode positioning and tissue electrical conductivity, and induce mechanical elastic waves that interfere with the mechanical wave field generated by the MRE actuation system. Here, we modeled an imaging protocol combining MRE and magnetic resonance electrical impedance tomography (MREIT), allowing characterizing respectively the mouse brain viscoelasticity and electrical conductivity during transcranial electrical stimulation. In particular, we simulated a concomitant MRE - transcranial alternating current stimulation (tACS) experiment and investigated the impact of tACS induced Lorentz body forces on the reconstructed mechanical property images using a specialized subzone non-linear inversion approach. Synthetic MRE data were generated in a realistic mouse head model and three situations were analyzed: standard MRE, standard MRE + tACS, and tACS only. The numerical experiment of MREIT was addressed by simulating the magnetic flux density distribution resulting from the MREIT-specific low intensity direct currents applied to the mouse scalp, and electric conductivity maps were recovered through the analysis of the magnetic flux density's spatial curvature. Results suggest that the small amplitude of the Lorentz force induced elastic waves would be too weak to be detected when small-amplitude currents compatible with

safety limits are used, even with 11 Tesla MR systems. In the unlikely situation where those waves would be accurately sampled, reconstructions showed important errors due to the absence of body forces in the current formulation of the inverse problem, which MREIT might help provide through the mapping of the electric conductivity distribution. In the alternative combined MRE - tACS session, MRE actuation-induced displacements dominated the Lorentz force contribution, which permitted an accurate recovery of viscoelasticity images from the total acoustic wave field. This multi-physics approach has potential for translation to human brain imaging, and may provide more possibilities for the characterization of brain function together than in isolation.

Key words: MRE, MREIT, tACS, Finite Elements, Simulation, Inverse Problem

4.1. Introduction

Psychiatric and neurological diseases as well as the neuronal mechanisms related to behavior and cognition have been increasingly studied in research through non-invasive brain stimulation (NIBS). NIBS consists in activating specific areas of the brain by applying a weak electric current to targeted regions of the head. Since the early stage of NIBS, an important field of investigation has been the relationship between brain function and behavior. As such, different experimental strategies have been designed to explore individual's responses to the electric stimulus and assess the physiological impact of the stimulation site in the brain on vision [**176**], audition [**177**], motor [**178, 179, 180**], somatosensation [**181**], language [**182, 183**], attention [**184, 185**], memory [**186, 187**], reasoning [**188, 189**], decision making [**190, 191, 192**], and social behavior [**193, 194, 195**], as reviewed by Polania *et al.* [**179**]. Parallel to shaping the brain function, recent studies have suggested that NIBS may also pertain to treatments of neurological disorders. For instance, changes of cognitive functions in patients with Alzheimer's disease following a NIBS session support the idea that neuroplasticity may be modulated to reduce symptoms [**196, 197, 198, 199, 200**]. Similarly, NIBS was also found to enhance motor functions in cases of Parkinson's disease, for which no cure currently exists [**201, 202, 203, 204, 205**].

The main two categories of techniques used to electrically stimulate the brain are transcranial magnetic stimulation (TMS) and transcranial electric stimulation (TES) [**179**]. TMS stimulates a localized brain region via a remote coil supplied with short electric pulses. In turn, the induced time-varying magnetic field elicits an electric current in the adjoining conductive brain region. The temporal profile of the stimulation can be shaped by applying a single or multiple pulses at adjustable repetition rates. This technique allows a more accurate spatial selection of the targeted area than TES but has a lower penetration depth which restricts the stimulation site to cortical regions. TES consists in applying the current directly to the scalp through one or more pairs of electrodes. Three variants of TES have been introduced and are based on different electric current types: transcranial direct current stimulation (tDCS), transcranial alternative current stimulation (tACS), and transcranial random noise stimulation (tRNS). In all cases, the size and location of affected brain areas essentially depends on electrode design and positioning [**206**], which are primarily effective for cortical stimulation as the electric field disperses in deeper areas. Nevertheless, sub-cortical regions could be reached in mice using a time-interference based tACS method [**207**]. Constructive electric field interferences were produced by introducing a small frequency difference between the applied electric signals allowing recruiting deep neurons without stimulating the surrounding area. Finally, transcranial focused ultrasounds have been presented as an emerging technique that complements TES and TMS by its higher spatial resolution and ability to target the deep brain [**208**].

Overall, published NIBS guidelines have underlined the importance of combining neuroimaging and computational modeling to accurately characterize current flux patterns, identify affected brain structures, and optimize NIBS protocols [**179**]. As such, conductivity imaging becomes crucial for modeling realistic brain electrical properties. Recent work on magnetic resonance electrical impedance tomography (MREIT), which is based on the analysis of the magnetic flux density induced in the imaged tissue as an electric flux passes, has aimed at providing reliable estimates of the ohmic conductivity distribution and electric flux patterns in the brain [**209, 210, 211, 212**]. While electric property characterization

and computational modeling do not supersede physiological validation, they are seen as tools that may help further understand the brain's response to NIBS and identify areas that might have been unintentionally activated along the current pathway.

In addition to NIBS techniques, recent advances related to neuronal activity mapping have suggested that complex couplings between the functional activity of the brain and its mechanical properties may be of use in neuroscience. The biomechanics of the brain could notably be inferred non-invasively with magnetic resonance elastography (MRE) [**118**], where mechanical parameters are reconstructed from the analysis of mechanical elastic waves that develop in the head owing to intrinsic (cardiac pulsation) or extrinsic (mechanical actuator) motion sources. Extrinsic MRE of the mouse brain has notably allowed measuring stiffness variations in the thalamus during the electrical stimulation of the hind paw, which suggests that elasticity images may be used to identify active neuron sets [**14**]. In humans, intrinsic MRE has been used to measure reductions and increases in different regions of the visual cortex during visual stimulation [**213**]. Similar MRE studies have been conducted to investigate the structure-function relationship in the brain through the analysis of the correlation between specific features in biomechanical parameter images and the specific tasks (motor or cognitive) participants were asked to perform in the protocol. For instance, memory performance was found to relate to tissue biomechanics in the subfields of the hippocampus (shear stiffness [**214**]), damping ratio [**215, 216, 217**]). Motor function performances have also been investigated and were found to correlate with damping ratio variations in the hippocampus for aerobic exercise tasks [**217**] and with global brain shear stiffness variations for dynamic balance related tasks [**218**].

The different approaches to brain activity mapping mentioned above, through NIBS and examination of biomechanical changes, suggest that a dual mechanical-electrical MR-based characterization procedure may be of interest for monitoring the effects of the electrical stimulation of the brain. Here, we propose to combine transcranial electric stimulation, mechanical, and electrical imaging of the mouse brain, with MRE and MREIT, respectively, via computational modeling and numerical simulations. Specifically, the electric current

density that develops in the conductive brain couples with the strong magnetic field of the MRI system to generate Lorentz force densities in the tissue. Thus, we also investigate the impact of the presence of Lorentz force-induced motion in the elastography images on the mechanical property reconstruction procedure, which usually relies on a body-force free physical model.

4.2. Methods

4.2.1. Mouse head model

Simulations were conducted in a mouse head model constructed from open-access mouse scans and consisting of five anatomical structures: skin/subcutaneous tissue, skull, cerebrospinal fluid (CSF), brain white and grey matters. Head contours were segmented from the Digimouse atlas [**219**], the skull from [**220**], and white and grey matter domains from [**221**]. Individual segments were then registered to the Digimouse coordinate system and the CSF was represented by the space between the brain and the skull. Handling of mouse scans and domain registration were performed using the medical image processing application ITK-SNAP [**222**] and exported in NiFTI format to Matlab (Matlab R2019b, The Mathworks, Massachusetts, USA) for segment-based material physical property definition (see sections 4.2.2 and 4.2.4 for details). The final mouse head model had a resolution of 120 μm^3 and is shown in Figure 13.a.

4.2.2. MREIT

A typical brain MREIT experiment consists in inducing a low-amplitude direct electric current density $\mathbf{J}(\mathbf{r})$ in the head and measuring the resulting magnetic flux density's z component $B_z(\mathbf{r})$ with MRI. The internal current density is generated by delivering an external current to the scalp through surface electrodes operated by a waveform generator synchronized with the MRI pulse sequence. Four electrodes are usually used and placed to ensure a suitable current coverage as well as generate at least two linearly independent current distributions in the imaged domain. The Biot-Savart law relates the tomographic direct

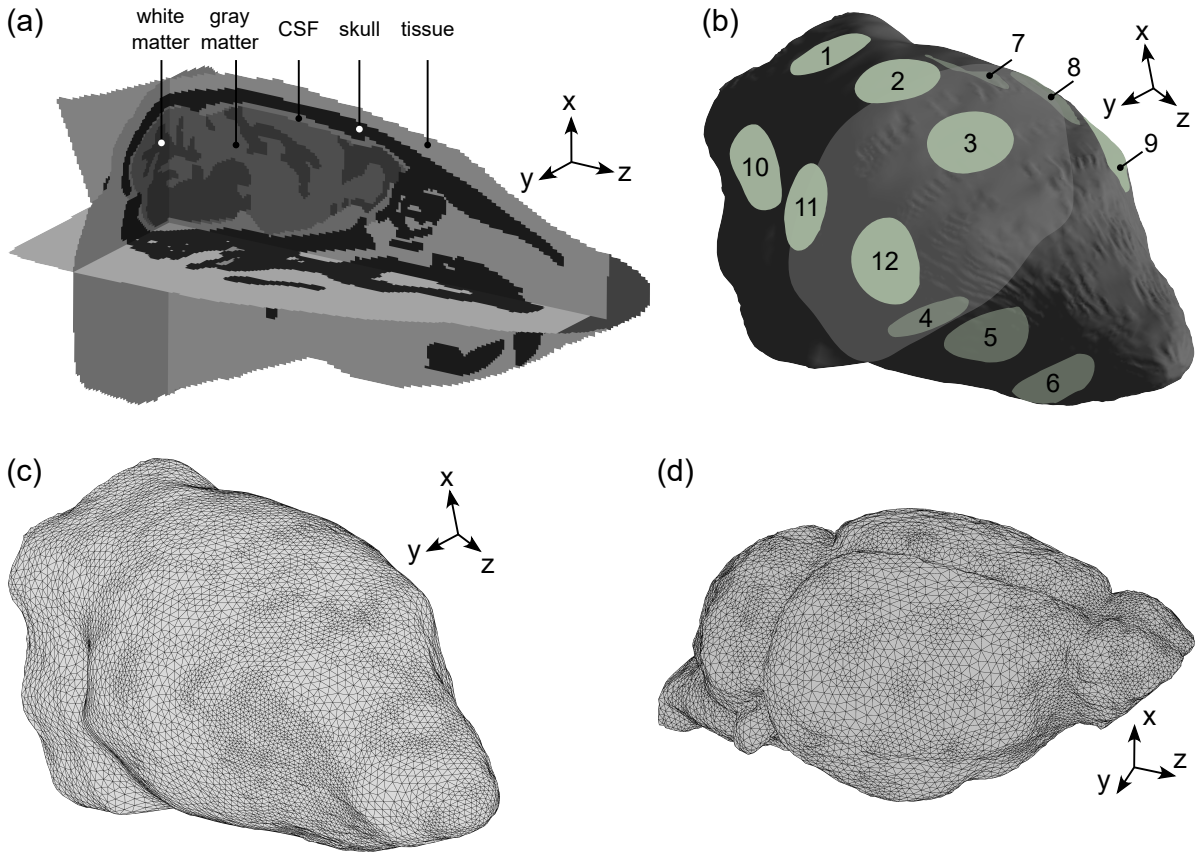

Figure 13 – Mouse head geometry and meshes. **a.** The model was made of five structural domains: skin/subcutaneous tissue, skull, CSF, brain white and grey matters. The z axis was modeled along the direction of the MR scanner's magnetic field (foot-head direction), the x and y axes were parallel to the antero-posterior and left-right directions, respectively. **b.** External view of the mouse head domain where surface electrodes were modeled by 12 2-mm radius circles organized into groups. Group 1: (1,2,3), group 2: (7,8,9), group 3: (4,5,6), group 4: (10,11,12). **c.** External view of the mouse head mesh used to simulate electric current porpagation (MREIT and tACS). **d.** External view of the mouse brain mesh used to simulate the propagation of mechanical elastic waves (MRE).

current density in the imaged slices to the induced magnetic flux density's z component:

$$B_z(\mathbf{r}) = \frac{\mu_0}{4\pi} \iiint_{\Omega} \frac{J_x(\mathbf{r}')(y-y') - J_y(\mathbf{r}')(x-x')}{|\mathbf{r}-\mathbf{r}'|^3} d\mathbf{r}', \tag{75}$$

where μ_0 is the magnetic permeability of the free space, which is assumed to be the same as that of the material. The volume integral in Eq. 75 can be expressed as a convolution in the physical space [**223, 209**]:

$$B_z(\mathbf{r}) = \mu_0 (G_y * J_x - G_x * J_y)(\mathbf{r}), \tag{76}$$

where $G_i = \frac{1}{4\pi}\frac{x_i}{|\mathbf{r}|^3}$, and as a product in the k-space:

$$B_z(\mathbf{r}) = \mu_0 \mathcal{F}^{-1}\left\{\mathcal{F}\left\{G_y\right\} \cdot \mathcal{F}\left\{J_x\right\} - \mathcal{F}\left\{G_x\right\} \cdot \mathcal{F}\left\{J_y\right\}\right\}(\mathbf{r}), \tag{77}$$

where $\mathcal{F}$ denotes the Fourier transform. The k-space formulation allows a faster evaluation of $B_z(\mathbf{r})$ from current densities than the evaluation of the volume integral. The current density distribution is given by Ohm's law:

$$\mathbf{J} = \sigma\mathbf{E} = -\sigma\nabla V, \tag{78}$$

where σ is the electric conductivity and V is the electric potential, solution to following boundary value problem:

$$\begin{cases} \nabla \cdot (\sigma \nabla V) = 0 & \text{in } \Omega, \\ I = \int_{\varepsilon^+} \sigma \dfrac{\partial V}{\partial \mathbf{n}} ds = -\int_{\varepsilon^-} \sigma \dfrac{\partial V}{\partial \mathbf{n}} ds, \qquad \nabla V \times \mathbf{n} = 0 & \text{on } \varepsilon^+ \bigcup \varepsilon^-, \\ \sigma \dfrac{\partial V}{\partial \mathbf{n}} = 0 & \text{on } \partial\Omega \backslash \overline{\varepsilon^+ \bigcup \varepsilon^-}, \end{cases} \tag{79}$$

where $\partial\Omega$ represents the surface bounding the computational domain Ω, ε^+ and ε^- represent the load and grounded electrodes, and $\mathbf{n}$ is the unit vector normal to $\partial\Omega$. Current densities in MREIT experiments were simulated in the whole mouse head by solving the forward problem described by Eq. 79 using the electric current module of Comsol Multiphysics with Matlab Livelink (Comsol Inc. Stockholm, Sweden). The induced magnetic flux density was then computed with Matlab via Eq. 77. The computational domain was defined in Comsol by lofting the mouse head transverse (x,y) contours along the z axis. Internal domains were modeled by distributing material properties across the geometry. Electric conductivity values were set to 0.465 S.m^{-1} in the skin, 0.01 S.m^{-1} in the skull, 1.654 S.m^{-1} in the CSF, 0.126 S.m^{-1} in the white matter, and 0.275 S.m^{-1} in the gray matter [**175**]. Relative permittivity and permeability were defined globally and set to a homogeneous value of 1. Then, a set of 12 2-mm radius circular surface electrodes was designed using Comsol's CAD tools. Electrodes were organized into four groups of three units evenly spaced along the z axis on opposing sides of the mouse scalp, and placed to cover to whole brain region. An external view of the mouse

head domain with the electrodes is shown in Fig. 13.b. The computational mesh, shown in Fig. 13.c, contained 1283014 tetrahedral elements with minimum and maximum target sizes of 2.4×10^{-4} m and 5.0×10^{-4} m, respectively. Current and magnetic flux densities were computed for six MREIT numerical experiments, where different combinations of electrode groups were used. Each experiment involved one electrode group for current delivery (1 mA in total) and one grounded electrode group. The six combinations were (group 1, group 3), (group 2, group 4), (group 4, group 1), (group 3, group 4), (group 2, group 3), and (group 2, group 1), where the first group of each couple indicates the loading electrodes and the second group the grounded electrodes.

The inverse problem of MREIT was solved using the *iterative harmonic* B_z method [**169, 224**]. This technique is based on the observations that B_z is sensitive to conductivity contrasts in directions perpendicular to the tomographic current densities and insensitive in parallel directions. For direct currents, the magnetic flux density, the conductivity of the medium, and the electric potential are related through [**225**]:

$$\nabla^2 \mathbf{B} = \mu_0 \nabla\sigma \times \nabla V. \tag{80}$$

The z component of Eq. 80 is then given by:

$$\nabla^2 B_z = \mu_0 \left(\frac{\partial\sigma}{\partial x}\frac{\partial V}{\partial y} - \frac{\partial\sigma}{\partial y}\frac{\partial V}{\partial x} \right). \tag{81}$$

Considering the six MREIT experiments, Eq. 81 can be expressed in matrix form as:

$$\underbrace{\begin{bmatrix} \frac{\partial V_1}{\partial y} & -\frac{\partial V_1}{\partial x} \\ \vdots & \vdots \\ \frac{\partial V_6}{\partial y} & -\frac{\partial V_6}{\partial x} \end{bmatrix}}_{\mathbf{U}} \underbrace{\begin{Bmatrix} \frac{\partial\sigma}{\partial x} \\ \frac{\partial\sigma}{\partial y} \end{Bmatrix}}_{\mathbf{s}} = \frac{1}{\mu_0} \underbrace{\begin{Bmatrix} \nabla^2 B_{z,1} \\ \vdots \\ \nabla^2 B_{z,6} \end{Bmatrix}}_{\mathbf{b}}. \tag{82}$$

The following iterative reconstruction procedure is defined from Eq. 82:

$$\mathbf{U}_k \mathbf{s}_{k+1} = \mathbf{b}, \tag{83}$$

which allows evaluating the x and y components of the conductivity gradient. The actual conductivity distribution is finally recovered through the following Poisson's equation [**169**]:

$$\begin{cases} \tilde{\nabla}^2 \sigma_{k+1} = \tilde{\nabla} \cdot \mathbf{s}_{k+1} & \text{in } \Omega_t, \\ \sigma_{k+1} = \sigma_e & \text{on } \partial\Omega_t, \end{cases} \tag{84}$$

where $\tilde{\nabla}$ indicates 2D in-plane derivatives in the slice Ω_t and σ_e represents the conductivity on the external boundary of the domain. The harmonic B_z method uses an initial conductivity distribution σ_0 to start the reconstruction procedure and evaluate the $\mathbf{U}$ matrix in Eq. 82. A homogeneous distribution $\sigma_0 = \sigma_e = 0.465$ S.m^{-1} was used and corresponded to the conductivity on the boundary of the head domain, which was assumed to be experimentally measurable. The inversion was conducted over ten iterations. For meshing, size constraints were imposed to enforce refinement in specific regions. Target sizes were set to 2.4×10^{-4} m for elements in the vicinity of expected material discontinuities, based on simulated B_z data, and to 1.0×10^{-3} m for elements away from material discontinuities, where low B_z variations were observed. The mesh contained 940023 tetrahedral elements.

4.2.3. tACS

For tACS simulations, the same mouse head model as in the MREIT forward model was used. Two numerical experiments were conducted using two two-electrode combinations. This time, electrodes were used in isolation rather than in groups and the combinations were (electrode 2, electrode 11) and (electrode 11, electrode 5), where the first member of each electrode pair indicates the loading electrode and the second member the grounded electrode. Electrode 2 was placed above the cortex, electrode 11 was facing the caudate putamen, and electrode 5 was on the neck, opposing electrode 11. Electrode combinations were chosen with the aim of generating Lorentz body forces of maximum amplitude. This was achieved by selecting loading and grounded electrodes with the same z coordinate, thus resulting in current densities with main directions lying in (x,y) planes and producing Lorentz force densities, $\mathbf{f}_L$, with main directions perpendicular to both the current density, $\mathbf{J}$, and the MR

scanner's magnetic flux density, $\mathbf{B}_0$, according to:

$$\mathbf{f}_L = \mathbf{J} \times \mathbf{B}_0. \tag{85}$$

The alternating current frequency was set to 900 Hz. This specific value was chosen to match a typical actuation frequency in mouse brain MRE experiments [**226**], which allowed evaluating the impact of tACS induced motion, through Lorentz forces, on the MRE reconstruction procedure. Electric conductivities were the same as in the MREIT simulations and were assumed frequency independent in the investigated frequency range [**227**].

4.2.4. MRE

In MRE, the mechanical properties of soft solids are reconstructed from the analysis of mechanical elastic waves induced in the imaged tissue and tracked with MRI [**228**]. Those elastic waves are low frequency (up to about 100 Hz in humans and to about 1.5 kHz in mice) and are induced by external actuators or are naturally present in the body from heart pulsations. Assuming that soft brain tissues are heterogeneous, viscoelastic, nearly incompressible, and isotropic materials, the response of the tissue undergoing a harmonic actuation at an angular frequency ω is described by the following equation of motion with displacement variables:

$$\begin{cases} \nabla \cdot (\mu \nabla \mathbf{u}) + \nabla (\mu \nabla \cdot \mathbf{u} - p) + \mathbf{f}_b = -\rho \omega^2 \mathbf{u} & \text{in } \Omega, \\ Ktr(\boldsymbol{\varepsilon}) = -p & \text{in } \Omega, \\ \mathbf{u} = \mathbf{u}_e & \text{on } \Gamma_u, \\ \mathbf{n} \cdot \boldsymbol{\sigma}_e = \mathbf{f}_e & \text{on } \Gamma_\sigma, \end{cases} \tag{86}$$

where Ω is the brain domain, $\mathbf{u} = [u, v, w]^T$ is the complex displacement vector (m), μ is the complex shear modulus (Pa), p is the pressure field (Pa), ρ is the mass density (kg.m^{-3}), ω is the actuation angular frequency (rad.s^{-1}), $\mathbf{f}_b$ represents the body force density in the domain (N.m^{-3}), K is the bulk modulus (Pa), $\boldsymbol{\varepsilon}$ is the strain tensor, $\mathbf{u}_0$ is the displacement vector on the domain's boundary Γ_u, $\boldsymbol{\sigma}_e$ is the stress tensor, $\mathbf{n}$ is the unit vector normal to the surface

boundary Γ_σ, and $\mathbf{f}_e$ is the traction force vector. In standard MRE experiments, the scanned tissue is usually free of body forces and the corresponding $\mathbf{f}_b$ term in Eq. 86 is neglected in the formulation of the elastography inverse problem for mechanical property recovery. This does not apply when MRE and tACS are conducted simultaneously as Lorentz force densities develop in the brain, as described by Eq. 85.

The solid mechanics module of Comsol Multiphysics was used to conduct MRE simulations in the brain domain of the head model detailed in section 4.2.1 to investigate the impact of Lorentz forces on the elastography measurement and reconstruction procedures. First, an STL-format brain mesh was generated with Matlab using the iso2mesh toolbox [**229, 230**] and imported in Comsol to create the geometry object. Then, internal domains were modeled by distributing the mechanical properties across the brain geometry. Shear modulus values were set to $5397 + i1836$ Pa in the white matter and $4997 + i1426$ Pa in the grey matter domains [**226**]. A homogeneous density and incompressible bulk modulus were defined and set to 1000 kg.m^{-3} and 2.2×10^9 Pa [**231**], respectively. A heterogeneous mesh was generated with mesh size gradients to resolve the material discontinuities. A target size of 2.2×10^{-4} m at material boundaries and an overall maximum size of 3.0×10^{-4} m were imposed. An external view of the final mesh, containing 400888 tetrahedral elements, is shown in Fig. 13.d. In a first simulation type, a displacement field was simulated in the brain from the application of Dirichlet boundary conditions (5.0×10^{-6} m displacements along the x axis) to mimic a typical mouse brain MRE experiment, free of body forces [**232**]. In a second simulation type, Lorentz force induced displacement fields were simulated from the tACS current distributions described in the section 4.2.3 along with an 11-T magnetic flux density oriented along the z axis of the scanner. The Lorentz force density distributions corresponding to the two two-electrode configurations of section 4.2.3 were computed according to Eq. 85 with $||\mathbf{B}_0|| = 11$ T. In Eq. 86, this translates to $\mathbf{f}_b = \mathbf{f}_L$. In both simulation types, the actuation frequency (through prescribed displacements or Lorentz forces) was 900 Hz [**226**].

The inverse problem of elastography was addressed using a specialized non-linear inversion (NLI) technique [**116, 233**]. NLI identifies mechanical property distributions, the shear modulus in the present work, that is a best-fit of the measured displacements $\mathbf{u}_m$ through Eq. 86, with $\mathbf{f}_b = 0$. Finite element solutions of this equation, $\mathbf{u}_c$, are computed using sets of shear modulus distributions, successively enhanced with property updates across 100 global iterations in order to minimize the mismatch between $\mathbf{u}_c$ and $\mathbf{u}_m$ through the following objective function:

$$\Phi = \frac{1}{2} \left(\mathbf{u}_c \left(\boldsymbol{\theta} \right) - \mathbf{u}_m \right)^H \left(\mathbf{u}_c \left(\boldsymbol{\theta} \right) - \mathbf{u}_m \right), \tag{87}$$

where $\boldsymbol{\theta}$ is the vector containing the inferred mechanical properties and H is the complex-conjugate transpose. The most likely approximation of the true shear modulus is the distribution that minimizes the objective function. The particularity of this NLI formulation is the decomposition of the total imaged domain into overlapping *subzones* processed individually and in parallel. Thus, the inverse problem consisting in identifying relevant property updates is solved at the subzone level, which mitigates the computational cost associated to the 3D problem. In this numerical study, the measured displacements $\mathbf{u}_m$ were the displacements simulated with Comsol in the mouse head model. In the inverse problem, the solution to the boundary value system in Eq. 86 (with $\mathbf{f}_b = 0$) was computed on a 27-node hexahedral finite-element mesh. Displacement and property meshes had the same resolution of 120 μm^3. Subzones had an isotropic size of 1.3 mm with a 20% overlap. Property updates in each subzone were computed using the conjugate gradient method (CG) and a global property distribution in the total domain was generated by assembling the subzones at the end of each global iteration. Gaussian smoothing was applied to the property distribution at the subzone assembly step in order to stabilize the reconstruction process. The initial shear modulus distribution used to start the reconstruction process was set to $6000 + i2000$ Pa.

Three displacement data types were processed with NLI. First, the body force free displacement field resulting from prescribed displacements on boundaries and mimicking standard extrinsic MRE. Second, the superposition of the Lorentz force induced displacements and the body force free displacements, mimicking simultaneous extrinsic MRE and tACS

experiments. Third, Lorentz force induced displacements alone, mimicking a tACS experiment.

4.3. Results

The distributions of the tACS-induced Lorentz body forces, simulated by solving Eqs. 79 and 85 in the two two-electrode configurations, are displayed in Fig. 14.

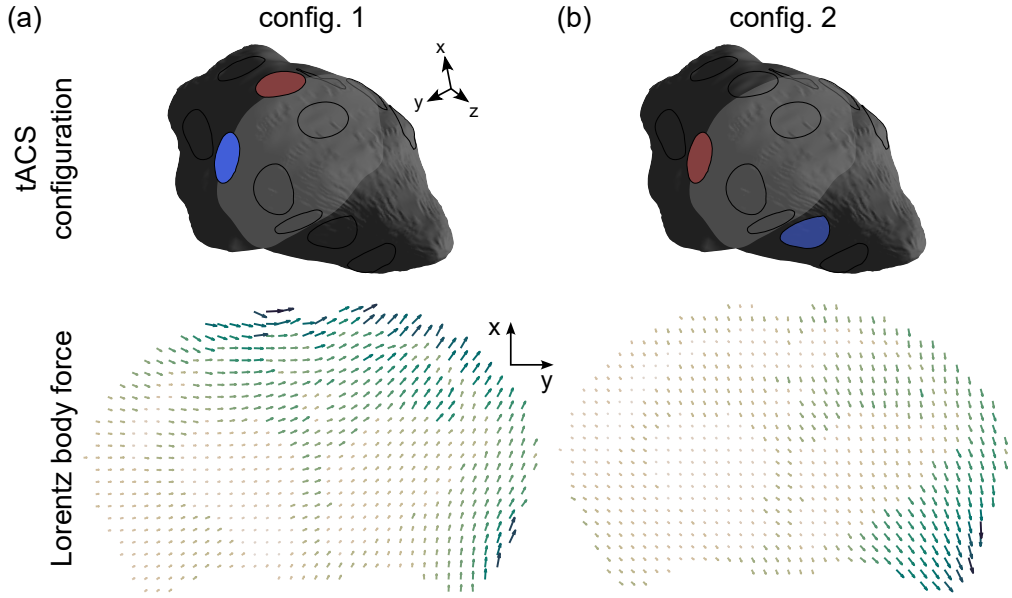

Figure 14 – Lorentz force density distributions in a representative slice of the brain corresponding to the two two-electrode tACS configurations. The arrows' lengths are proportional to the amplitude of the body force. In each panel, the minimum and maximum force strengths were respectively: **a.** 11.5 $N.m^{-3}$and 137.9 $N.m^{-3}$. **b.** 9.2 $N.m^{-3}$and 106.1 $N.m^{-3}$.

The real part of the finite element displacement fields, solution to Eq. 86 for the three MRE simulations, *i.e.* MRE, MRE+tACS, and tACS, are presented in Fig 15.

Figure 16 shows complex shear moduli reconstructed with NLI using each of the displacement fields presented in Fig. 15.

The magnetic flux density generated by each of the six MREIT direct currents and computed using the k-space formulation of the Biot-Savart law, given by Eq. 77, is shown in Fig. 17.

Finally, the electric conductivity reconstructed using the harmonic B_z algorithm is shown in Fig. 18.

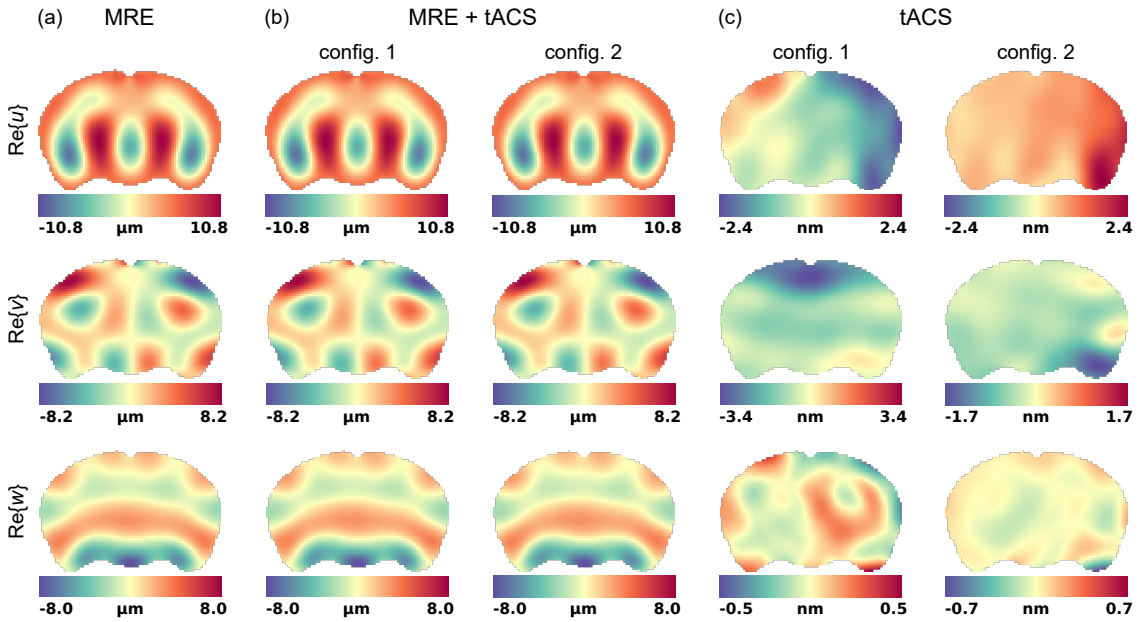

Figure 15 – Motion fields in a representative slice of the mouse brain model. Displacements were evaluated in three experiment mimicking situations: **a.** standard extrinsic MRE, **b.** simultaneous extrinsic MRE and tACS using two electrode configurations ((2,11) and (11,5)), and **c.** tACS only using the same two electrode configurations.

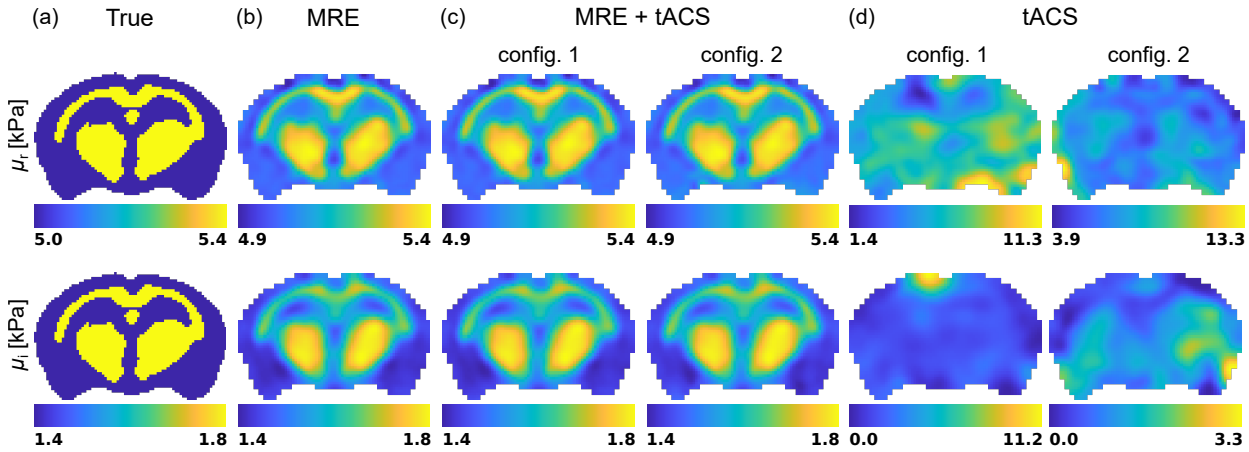

Figure 16 – Shear modulus reconstructions in a representative slice of the brain model obtained with the subzone NLI method applied in the three experiment mimicking situations: **a.** standard extrinsic MRE (displacements from Dirichlet boundary conditions only), **b.** simultaneous extrinsic MRE and tACS (displacements from Dirichlet boundary conditions and body forces), and **c.** tACS only (displacements from body forces only).

4.4. Discussion

Simulations of an MR protocol combining transcranial electric stimulation and successive evaluations of the mouse brain's mechanical and electrical properties through MRE and

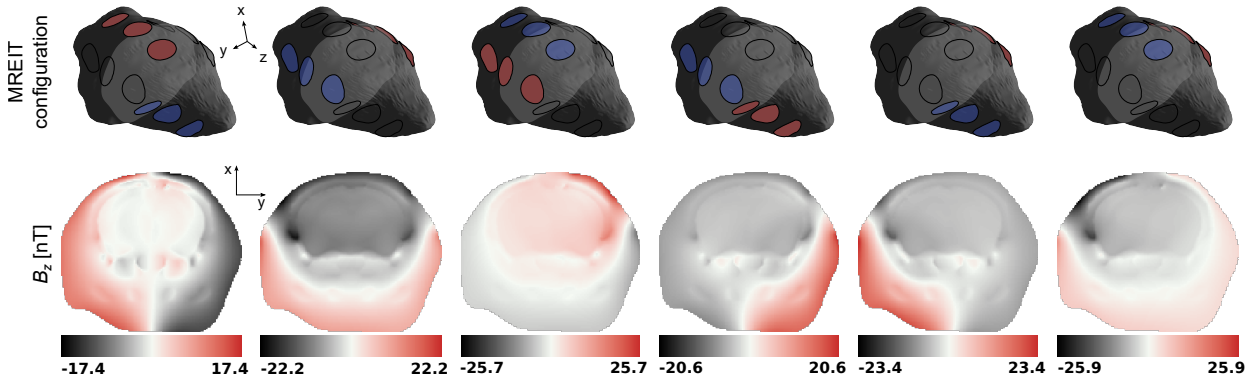

Figure 17 – Magnetic flux density B_z in a representative slice of the mouse head model for the 6 electrode group configurations in the MREIT numerical experiment. The representative slice is represented in light gray in the mouse head diagrams.

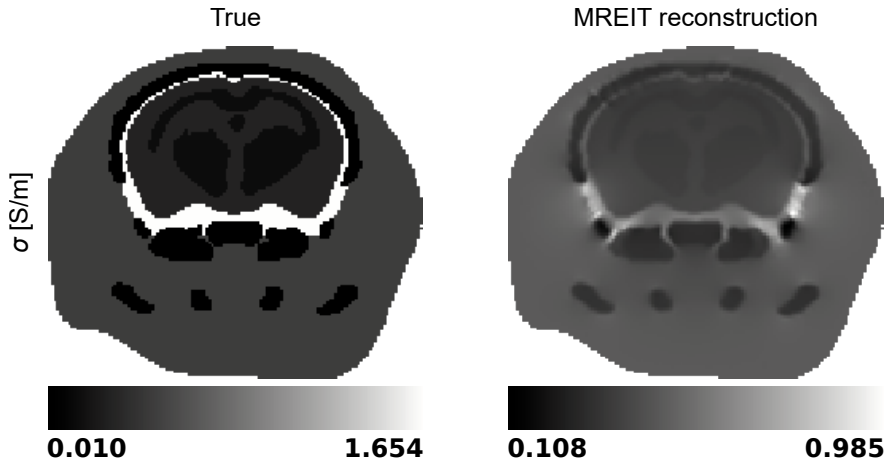

Figure 18 – Electric conductivity reconstruction in a representative slice of the mouse head model using the harmonic B_z algorithm.

MREIT, respectively, was presented. The numerical experiments were conducted with no added noise to mimic ideal conditions. This framework first allowed investigating the feasibility of such protocol, based on the magnitude of the brain's response across the MRE and MREIT mimicking simulations, and the impact of the Lorentz body forces on the mechanical characterization of the brain tissue.

When MRE and tACS are conducted simultaneously, which might be of interest according to [**14**], Lorentz force densities are generated according to Eq. 85, as shown in Fig. 14. The latter constitute motion sources and are usually not accounted for in the treatment of standard MRE data where the measured displacements are generated on the surface of the imaged domain. The motion maps presented in Fig. 15 show that typical

displacement fields induced by conventional mechanical actuators dominate those induced internally through Lorentz forces by more than three orders of magnitude. Consequently, the non-linear inversion using both displacement data types (Dirichlet and Dirichlet + Lorentz forces) led to accurate reconstructions for both storage and loss moduli, as shown in Fig. 16.a and 16.b. These results suggest that combined MRE and tACS experiments might be a realistic avenue to investigate the mechanical response of the brain to transcranial electric stimulation. However, the displacement fields induced by the tACS Lorentz force densities only are likely to not be measurable within tACS safety limits using current MR systems and sequences, which suggests that Lorentz force-based MRE would be difficult to achieve. From a reconstruction standpoint, the body force-free formulation of NLI could not lead to correct shear modulus distributions using the Lorentz force induced displacements, as exemplified in the representative slice shown in Fig. 16.c. This limit to characterization, even in regions distant from the electric current pathway where Lorentz forces are generated, suggests that points in the brain domain all belong to the "near-field", where shear and compression waves are coupled to a single entity [**160**].

The harmonic B_z algorithm has been consistently used in MREIT experiments and has demonstrated a good ability to differentiate structures of different impedances in the presence of data with high signal-to-noise ratio. This conclusion is confirmed in Figs. 17 and 18 where the noise-free magnetic flux densities allowed recovering distributions of the electric conductivity consistent with the material structure. Nevertheless, the presented reconstructions also show that the property maps are qualitative, which has also been observed in other published works [**234, 163**]. The aforementioned small amplitude of Lorentz force densities suggests that modeling body forces in the inverse problem of MRE through electrical conductivity imaging would not be a prerequisite in this situation. Consequently, combined MREIT, tACS, and MRE may be seen as a multi-physics approach where identification methods provide complementary characterizations rather than inter-dependent variables. The potential of electrical conductivity as a biomarker of pathological tissues has been investigated [**235, 236, 237, 238, 239**], but thus far, MREIT has not reached the potential of MRE as a

diagnostic imaging technique and is more approached as a tool allowing studying the brain's function and response to electric stimulation through modeling. Simulations of the electric field induced in different species during electrical stimulation has demonstrated a scale effect where field amplitudes were two orders of magnitude greater in the mouse brain than in the human's [**175**]. This also suggests that the proposed pipeline might be applicable to humans with no need to model body force distributions in the elastography reconstruction, so long as the safety limits for electric current application are fulfilled, thus producing Lorentz body forces of sufficiently low amplitude.

Few MRE and MREIT experiments have been conducted with 11-T MRI systems and published works have reported size and high-magnetic field related experimental challenges [**240, 241**]. Although the combined tACS, MRE, and MREIT approach would likely be impractical at 11 T, this high field was selected in our simulations to generate Lorentz force densities of plausible high amplitudes. Utilization of MRI systems with lower fields would result in weaker Lorentz forces, provided equivalent electric stimulation settings, which strengthens the assumption that MRE and tACS might be performed simultaneously. In the absence of MRE-specific motion encoding gradients (MEG), the phase of the MR signal during an MREIT acquisition is dominated by the electric current induced phase accumulation in the spin population, and the contribution of Lorentz force induced motion due to the MREIT current was assumed negligible. On the other hand, the tACS currents were also assumed to have a negligible effect on the MRE acquisition as many MRE sequences involve bipolar scans where the displacement field is sampled twice with opposite MEG polarities, thus canceling out persistent electric current related phase artifacts [**242**]. Finally, the eddy currents resulting from the oscillation of the conductive brain tissue in a magnetic field are second order effects and were not considered in this work.

In practice, MRE and electric stimulation may be performed during the same imaging session, either simultaneously (MRE + tACS) or successively (MRE + MREIT), without requiring to modify the experimental setup as the acoustic vibrations in MRE are usually transmitted using a bite-bar transducer placed in front of the mouse [**65, 243**], and electric

currents would be administered through scalp electrodes. An experimental challenge in combined MRE and tACS experiments at high magnetic fields would be to ensure the stability of the setup during acquisitions. The design of adjustable head holders with soft electrode pads would certainly be necessary.

This study contains several simplifications and limitations which can be discussed and put in perspective. First, five main anatomical domains were incorporated in the model to keep the simulation reasonably convenient to manipulate. Although a more detailed representation of structural constituents would better approximate real tissues and further challenge the reconstruction aspects, the proposed model was sufficiently detailed to address the questions specific to this study. Then, electrodes were modeled as simple disks on the surface of the mouse head to which a normal current density was applied. Whereas this setting does not physically model a metal electrode in contact with skin tissues, it does approximate the MREIT experimental condition where recessed electrodes are used in order to avoid radio-frequency shielding issues related to metal objects placed nearby the imaged field of view. Finally, the same actuation frequency for both the tACS current and the extrinsic MRE actuation was used. Experimentally, this would be similar to a mono-frequency actuation with a full-waveform encoding scheme where the frequency of the MEG is specifically chosen to match that of actuation, leading to the acquisition of both Lorentz force and external actuator induced displacements at 900 Hz. If the mechanical actuator and the tACS system were operating at different frequencies, each motion contribution could be investigated separately by selecting the MEG frequency accordingly. Experimentally, and as discussed above, Lorentz force displacements would likely be too weak to be detectable.

4.5. Conclusion

Numerical simulations of magnetic resonance elastography and magnetic resonance electrical impedance tomography in the context of MR-assisted transcranial electric stimulation of the mouse brain were presented. Simulation results suggest that simultaneous tACS and MRE would be experimentally viable (at magnetic field strengths lower than 11 T due to

space limits in the MR system). The added MREIT session would allow characterizing the tACS current flow patterns and help optimize the stimulation protocol. The benefits of multi-physics (and multi-modality) imaging approaches have been addressed previously in the context of breast cancer, where MRE, electrical impedance tomography, microwave-imaging, and near-infrared spectroscopy were seen as complementary to each other within a global diagnostic and computational framework [**244**]. The unification of electric stimulation along with the monitoring of mechanical and electrical brain responses may provide greater neuronal activity mapping and brain function characterization possibilities together than in isolation.

Chapitre 5

Imaging the subcellular viscoelastic properties of mouse oocytes

Ce chapitre repose sur l'article intitulé "Imaging the subcellular viscoelastic properties of mouse oocytes" publié en 2023 dans le journal *Proceedings of the National Academy of Sciences* par Guillaume Flé, Elijah Van Houten, Gaudeline Rémillard-Labrosse, Greg Fitz-Harris et Guy Cloutier.

Avant propos

La difficulté à générer et mesurer des ondes de cisaillement à des fréquences supérieures au kilohertz a longtemps contribué à définir l'élastographie harmonique comme une méthode d'imagerie macroscopique et basse fréquence. Les travaux de Grasland-Mongrain *et al.* en 2018 ont démontré la possibilité d'aborder l'élastographie à des fréquences supérieures à 10 kHz et à l'échelle microscopique de cellules individuelles grâce à la microélastographie optique (MEO) [**2**]. Les micro-déformations locales et harmoniques imposées à la cellule sont imagées par microscopie optique en champ clair combinée à une caméra ultra-rapide puis quantifiées par corrélation d'images sous forme de déplacements locaux. Les cartes tomographiques de déplacements obtenues constituent ainsi des jeux de données similaires à ceux produits en élastographie par résonance magnétique ou ultrasonore (EUS) et peuvent être en principe traités par le biais de méthodes de reconstruction spécifiques à ces modalités

d'imagerie. Une méthode d'inversion par corrélation de bruit principalement employée en EUS a ainsi permis de reconstruire des cartes de rigidité d'ovocytes de souris. La caractérisation mécanique de ces cellules reproductives suscite un intérêt croissant en sciences de la reproduction dans la mesure où leurs propriétés viscoélastiques évoluent au cours de leur maturation. Une compréhension approfondie de cette maturation d'un point de vue biomécanique pourrait ainsi contribuer à une meilleure sélection des ovocytes et embryons à traiter au cours de procédures de fécondation *in vitro*. De récents développement ont toutefois démontré qu'une caractérisation viscoélastique, par opposition à purement élastique, est nécessaire dans cette optique [**245**]. Cette observation a motivé les travaux décrits dans ce chapitre où la méthode d'inversion non-linéaire par sous zones (NLI), issue de l'ERM, est appliquée à de nouvelles images de déplacements dans des ovocytes de souris. L'approche NLI a démontré une excellente robustesse dans la littérature scientifique à travers de nombreuses applications à l'imagerie *in vivo* du cerveau humain et repose sur une description de viscoélasticité hétérogène dans un volume isotrope. Ce dernier aspect complexifie l'analyse des données de MEO tomographiques et actuellement disponibles dans une seule coupe positionnée au centre de la cellule. L'article rapporté dans ce chapitre décrit donc l'utilisation de la méthode NLI, présentée et employée au cours des chapitres précédents dans le cadre de l'ERM, et appliquée ici à des images de microélastographie optique.

Contribution des auteurs

Guillaume Flé : proposition du projet, acquisition des données expérimentales, analyse des données (estimation des déplacements et reconstructions), conception des simulations numériques, rédaction et révision de l'article.

Elijah Van Houten : mise à disposition et formation à l'utilisation de l'algorithme NLI, aide aux aspects relatifs à la résolution du problème inverse, révision de l'article.

Gaudeline Rémillard-Labrosse : formation à la collection et manipulation d'ovocytes.

Greg FitzHarris : mise à disposition du matériel expérimental, révision de l'article.

Guy Cloutier : direction générale, financement et révision de l'article.

Résumé

Les propriétés biomécaniques cellulaires ont récemment été examinées en vue d'identifier une alternative aux évaluations morphologiques pour la sélection des ovocytes en sciences de la reproduction. Toutefois, la reconstruction d'images de paramètres viscoélastiques distribués spatialement reste un défi majeur dans ces matériaux, malgré les enjeux liés à la caractérisation de la viscoélasticité cellulaire. Dans cette étude, une approche permettant la cartographie de la viscoélasticité à l'échelle sous-cellulaire est proposée et appliquée à des ovocytes de souris vivants. La stratégie repose sur les principes de la micro-élastographie optique pour le volet d'imagerie, combinée avec la technique d'inversion non linéaire par sous-zones pour la reconstruction du module de cisaillement complexe. La nature tridimensionnelle des équations de viscoélasticité a été prise en compte en appliquant au champ d'ondes mesuré un modèle de mouvement mécanique 3D basé sur la géométrie de l'ovocyte. Cinq domaines - le nucléolus, le noyau, le cytoplasme, l'espace périvitellin et la zone pellucide - ont pu être visuellement différenciés dans les cartes de modules de stockage et de perte des ovocytes, et des différences statistiquement significatives ont été observées entre la plupart de ces domaines dans chacune des reconstructions. La méthode proposée ici présente un excellent potentiel lié au suivi biomécanique de la santé des ovocytes et de leurs transformations complexes au cours du cycle de vie. La généralisation de cette méthode à des cellules de forme arbitraire à l'aide d'un équipement de microscopie conventionnel est également envisageable.

Mots clés : Viscoélasticité d'ovocytes, Micro-élastographie, Ondes élastiques, Reconstruction d'image, Biomécanique cellulaire

Abstract

In recent years, cellular biomechanical properties have been investigated as an alternative to morphological assessments for oocyte selection in reproductive science. Despite the high relevance of cell viscoelasticity characterization, the reconstruction of spatially distributed

viscoelastic parameter images in such materials remains a major challenge. Here, a framework for mapping viscoelasticity at the subcellular scale is proposed and applied to live mouse oocytes. The strategy relies on the principles of optical microelastography for imaging in combination with the overlapping subzone nonlinear inversion technique for complex-valued shear modulus reconstruction. The three-dimensional nature of the viscoelasticity equations was accommodated by applying an oocyte geometry-based 3D mechanical motion model to the measured wave field. Five domains - nucleolus, nucleus, cytoplasm, perivitelline space, and zona pellucida - could be visually differentiated in both oocyte storage and loss modulus maps, and statistically significant differences were observed between most of these domains in either property reconstruction. The method proposed herein presents excellent potential for biomechanical-based monitoring of oocyte health and complex transformations across lifespan. It also shows appreciable latitude for generalisation to cells of arbitrary shape using conventional microscopy equipment.
Key words: Oocyte viscoelasticity, Microelastography, Elastic waves, Image reconstruction, Cellular biomechanics

Significance statement

In reproductive science, viable and nonviable oocytes may be distinguished by the characterization of their concomitant elastic and viscous properties. However, the bulk characterization and high levels of cell deformation required with standard techniques hinder the nondestructive identification of cell structures and their contribution to developmental success. Using ultrafast microelastography and an optimization-based reconstruction technique, maps of oocyte viscoelasticity were produced noninvasively. The continuum model allowed for a complete viscoelastic description of the medium, free of rheological assumptions and restrictive approximations on the measured data. This robust approach may ultimately be of use to help establish viscoelasticity-based guidelines for egg selection in medically assisted reproduction procedures.

5.1. Introduction

Stiffness and viscosity changes in biological tissues have long been associated with various biomechanisms and diseases at the macroscales [**150, 246, 13**] and microscales [**247, 248, 249, 245, 250, 251, 252**]. In recent years, substantial efforts have been deployed in the field of reproductive science to identify efficient mechanical biomarkers of oocytes' and embryo's developmental potential [**245, 21, 253, 254**]. Notably, Yanez *et al.* [**245**] used a bulk assessment technique to demonstrate that a viscoelastic mechanical characterization differentiated viable versus nonviable embryos and predicted blastocyst formation within hours of fertilization, which visual examination of the zygotes failed to achieve. A multi-parameter viscoelastic characterization, as opposed to purely elastic, was found necessary to achieve this differentiation and was observed to provide a greater discriminating power than the individual elastic properties on their own. Mechanical changes in oocytes were also measured during maturation and correlated with embryo's development. In particular, the zona pellucida (ZP) was found to soften during maturation and stiffen after fertilization, which is likely to influence the oocyte's permeability to sperm [**245, 255, 256, 257**]. Cortex-tension-driven spindle migration and positioning during the asymmetric division of oocyte meiosis [**258, 259**] is another example supporting the relevance of oocyte stiffness monitoring, as overly soft oocytes were observed to correlate with chromosome misalignment, which is predictive of aneuploidy [**260, 261**]. Viscosity, notably more difficult to characterize than simple elastic stiffness, has mostly been assessed in the cytoplasm. Main findings underline: changes in cytoplasm viscosity from aqueous to viscous during maturation (concomitant with ZP softening) [**262**]; the viscosity dependence of oocyte spherical shape restoration after intracytoplasmic sperm injection (ICSI); and a hindered development in oocytes with increased cytoplasmic viscosity [**263**]. Overall, both stiffness and viscosity demonstrate potential as quantifiable measures of oocyte quality. The establishment of a correlation between cell biomechanics and cellular health raises the need for adapted mechanical characterization tools [**253**].

Current oocyte stiffness micromeasurement technologies essentially capitalize on the deformability of a material under tightly controlled external loads. In micropipette aspiration [**245**], compression [**264**], and indentation [**257, 265, 266, 267, 268**] techniques, a pipette is brought in contact with the oocyte and the induced geometrical deformation is analyzed and fitted to a rheological model. The levels of stress applied to the oocyte are often high and the sensitivity to mechanical contrast is limited due to the global stiffness assessment approach (notable exception: [**264**]). Similar indentation versus deformation principles apply to atomic force microscopy (AFM) [**269, 270**], which uses lower deformation rates and allows assessing cell surface boundaries with submicron resolutions [**271**]. Overall, both technologies often require cell dissection to isolate regions of interest [**258, 269**] and involve slow experimental procedures, potentially hindering the detection of faster biomechanical processes. To our knowledge, oocyte viscosity has only been measured globally through pipette indentation [**245**] or invasively in the vicinity of cytoplasmic endogenous vesicles using optical tweezers [**272**] and through the analysis of the size and persistence of an injection funnel after ICSI [**263**], wherein larger and more persistent funnels are indicative of greater cytoplasmic viscosity. Approaches to probe the biomechanics of different cell types, including particle tracking microrheology, cell indentation (local or global), optical trap, and bead-based techniques, have been reviewed and compared in Ref. [**20**]. In these examples, estimated elastic and viscous parameters showed a wide disparity (100 to 1000-fold variations, respectively) due to the different experimental procedures involved. Alternatively, microfluidic-based [**273, 274, 275, 276**] and optical [**277, 278, 2**] techniques have been introduced. Notably, optical microelastography (OME) relies on the analysis of induced high-frequency elastic wave patterns using standard bright-field microscopy imaging and a high-speed camera [**2**]. However, the pure shear wave assumption invoked in previous work is strongly challenged in the context of tiny confined cellular domains, which invalidates the conversion of wave parameters (wavelength λ or speed c) into a material mechanical property (shear stiffness μ_s) through the elastic relationship $\mu_s = \rho c^2$, where ρ is the material's density [**279**]. Additionally, the reconstruction of wave parameters through time-reversal-based

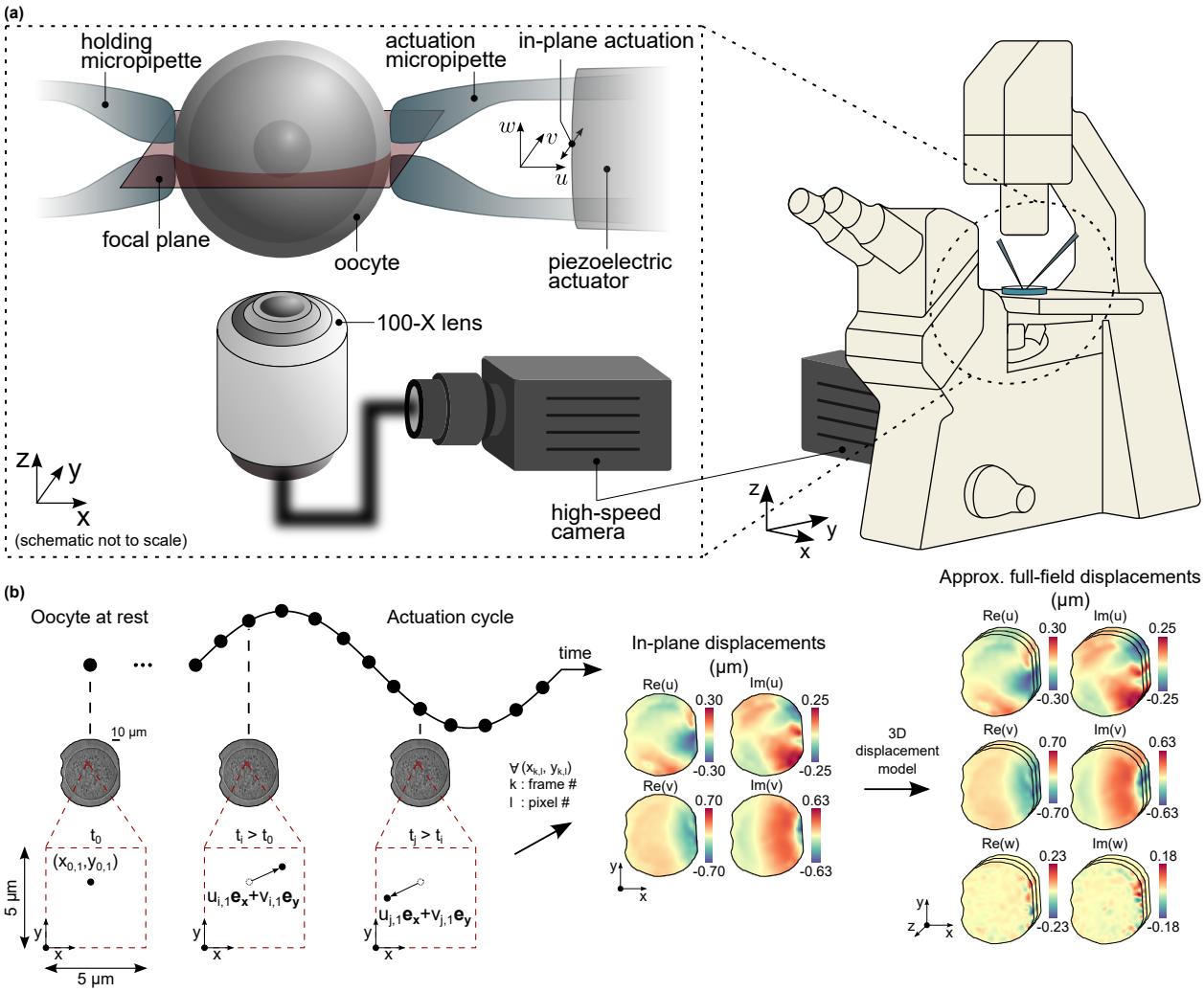

Figure 19 – Optical microelastography in mouse oocytes. a. Experimental setup. The selected oocyte is held by two micropipettes, the left side is immobile and the right side is connected to a piezoelectric crystal and pulses in the xOy plane. The focal plane is set at the center of the oocyte. A high-speed camera captures images of the oocyte being pulsed by the actuation micropipette. **b.** Images acquired with the camera at a 200 kHz frame rate during harmonic actuation are processed with an optical-flow method to estimate in-plane displacements (u and v). A full-field displacement data set (u, v, and w) is approximated using a 3D oocyte geometry-based model. The procedure is described in the Methods section.

techniques is also challenged in highly attenuating cellular media where the time symmetry of the undamped wave propagation equation is no longer fulfilled.

Here, we detail a robust strategy to image the viscoelastic properties of oocytes, noninvasively and at a subcellular level, through the reconstruction of the fully distributed storage and loss moduli. The method is applied to live mouse oocytes and numerical simulations, and is based on OME and the overlapping subzone nonlinear inversion (NLI) technique,

an optimization scheme for mechanical parameter identification. The generalized mechanical model involved allows for a heterogeneous viscoelastic description of the material, as opposed to wave characterization, and circumvents shear wave and rheology-based assumptions while eliminating the noise-enhancing operations performed in standard direct inversion techniques. To our knowledge, multiparametric viscoelasticity mapping at the subcellular scale has not been reported previously and represents a significant advance in microelastography. Fig. 19.a shows the OME experimental setup. On the platform of an inverted

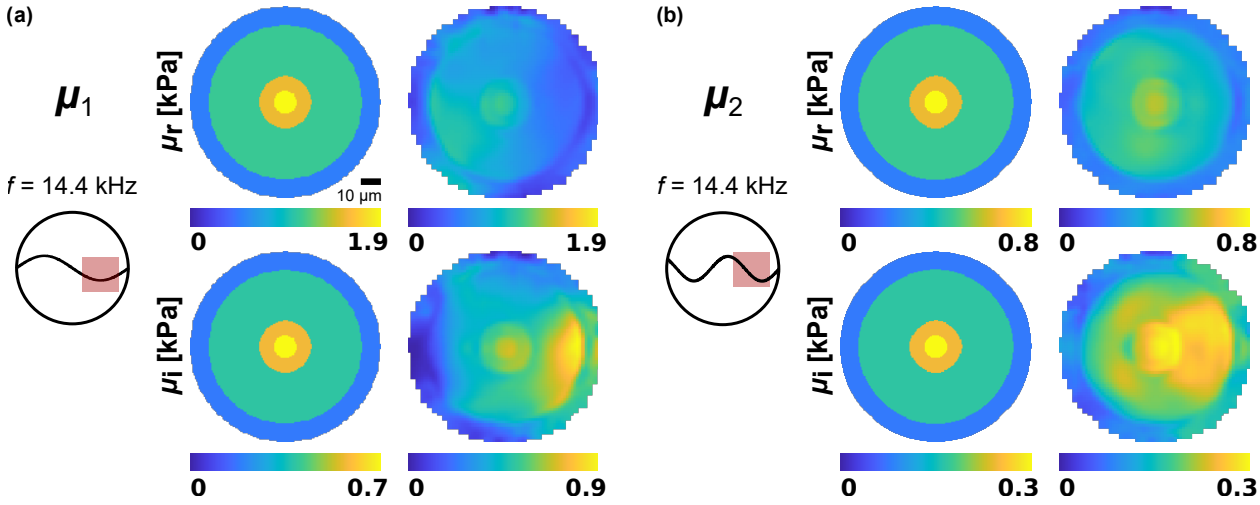

Figure 20 – Viscoelasticity reconstructions performed on simulated displacement data. Panels **a** and **b** represent the two experiment-based shear modulus distributions used in simulations, $\mu_1 = 2.5 \times \mu_{\text{exp}}$ and $\mu_2 = \mu_{\text{exp}}$, where μ_{exp} refers to the average distribution observed in experiments (see the Methods section for details). The individual domains in μ_{exp} were set to $\mu_{\text{exp,nucleolus}} = 768 + i268$ Pa, $\mu_{\text{exp,nucleus}} = 615 + i217$ Pa, $\mu_{\text{exp,cytoplam}} = 444 + i147$ Pa, and $\mu_{\text{exp,zp}} = 202 + i68$ Pa. For each simulation, the wavelength and isotropic 30-µm subzone are indicated in the first column of both panels by the sine curve in the spherical oocyte domain and the red square, respectively. For each panel, the second and third columns represent, respectively, the true and reconstructed distributions using the approximated full-field displacements.

microscope mounted with a 100× lens, the oocyte was lightly contracted by two retention micropipettes connected to micromanipulators for positioning. The pipette on the left-hand side resembled a standard ICSI "holding pipette" and was used to immobilize the oocyte, while the right-hand side was laterally pulsed by a piezo-electric crystal providing a 14.4-kHz harmonic in-plane actuation. The pulsing pipette induced mechanical elastic waves visualized as local structural deformations traveling across the cell. The deformations were captured

in the focal plane, set to cut through the center of the oocyte, by a high-speed camera and converted into local in-plane displacement values quantifying the deviations of the pulsed geometry from the shape of the oocyte at rest. Then, a full-field displacement data set, *i.e.*, three motion components (u, v, and w) in three contiguous planes, was approximated from the measured in-plane data using a 3D oocyte geometry-based displacement model. The model relied on the symmetrical nature of germinal vesicle-stage (GV) oocytes, the near-incompressibility property of biological tissues, and the in-plane actuation in the imaged slice. Fig. 19.b shows a schematic view of the harmonic actuation displacement estimation. See the Methods section for more details. Displacement data were then processed with the finite element-based overlapping subzone nonlinear inversion technique [**116, 233**]. Here, oocytes were modelled as a heterogeneous, viscoelastic, nearly incompressible, isotropic material. The optimization-based inversion procedure and the boundary value problem relating the material's mechanical parameters to the measured displacement field are detailed in the Methods section. Advantages of NLI over other reconstruction techniques are discussed and illustrated in the *Supplementary Note 1* and *Fig. 23*.

5.2. Results

The preprocessing step for full-field displacement approximation and the inversion procedure were first applied to synthetic data. This numerical study allowed to test the overall pipeline, and analyze the performance of the iterative inversion with the experiment-based actuation frequency $f = 14.4$ kHz, and with mechanical property distributions of relative magnitudes. Two scaled distributions were used, $\mu_1 = 2.5 \times \mu_{\text{exp}}$ and $\mu_2 = \mu_{\text{exp}}$, where μ_{exp} refers to the mechanical properties observed in experiments (see the Methods section for details). Fig. 20 shows storage (μ_r) and loss (μ_i) modulus reconstructions performed on displacements provided by a finite element simulation of an oocyte domain made of four concentric spherical structures (nucleolus, nucleus, cytoplasm, and ZP). As in experiments, in-plane motion data were processed with the 3D displacement model.

The 30-μm zone size used in NLI and the wavelength of the elastic field are illustrated in the first column of both Figs. 20.a and 20.b. The second columns indicate the true mechanical properties used in the simulations, and the third columns show reconstructions using simulation-based approximated full-field displacements. The basis for full-field displacement approximation is presented in the *Supplementary Note 2* and *Fig. 24*. Computational steps are detailed in the Methods section.

Then, 21 freshly collected live oocytes underwent the microelastography pipeline. Fig. 21.a shows anatomical and segmentation images of a representative oocyte. On the 21 oocyte data sets treated, all storage modulus and 13 loss modulus identifications converged to stable distributions ($\mu_{r,fc}$ and $\mu_{i,fc}$, respectively, where *fc* stands for fully converged), and 8 loss modulus reconstructions continued to progress toward lower values ($\mu_{i,pc}$ where *pc* stands for partially converged). Fig. 21.b, 21.c, and 21.d show the average values in main oocyte regions (nucleolus, nucleus, cytoplasm, perivitelline space (PS), and ZP) for each convergence profile (fully and partially converged). Fig. 21.e and 21.f show anatomical and segmentation images of two representative oocytes along with complex-valued shear modulus reconstructions where full- and partial-convergence were observed, respectively. *Supplementary Note 3* and *Fig. 25* presents the convergence profiles of these reconstructions.

Table 5 – Statistical differences between paired regions

***p*-values**	Cyto.-Nucleo.	Cyto.-Nucl.	Cyto.-PS	Cyto.-ZP	Nucleo.-Nucl.	Nucleo.-PS	Nucleo.-ZP	Nucl.-PS	Nucl.-ZP	PS-ZP
$\mu_{r,fc}$	$<$ 0.001	$<$ 0.001	$<$ 0.001	$<$ 0.001	$>$ 0.005	$<$ 0.001	$<$ 0.001	$<$ 0.001	$<$ 0.001	$>$ 0.005
$\mu_{i,fc}$	$<$ 0.005	$>$ 0.005	$<$ 0.001	$<$ 0.001	$>$ 0.005	$<$ 0.001	$<$ 0.001	$<$ 0.001	$<$ 0.001	$>$ 0.005
$\mu_{i,pc}$	$<$ 0.005	$>$ 0.005	$<$ 0.005	$<$ 0.005	$>$ 0.005	$<$ 0.001	$<$ 0.001	$<$ 0.001	$<$ 0.001	$>$ 0.005

Cyto.: cytoplasm, Nucleo.: nucleolus, Nucl.: nucleus, PS: perivitelline space, ZP: zona pellucida

Table 5 reports *p*-values obtained using a Wilcoxon rank sum test to quantify the statistical difference between each region for the fully and partially converged reconstructions.

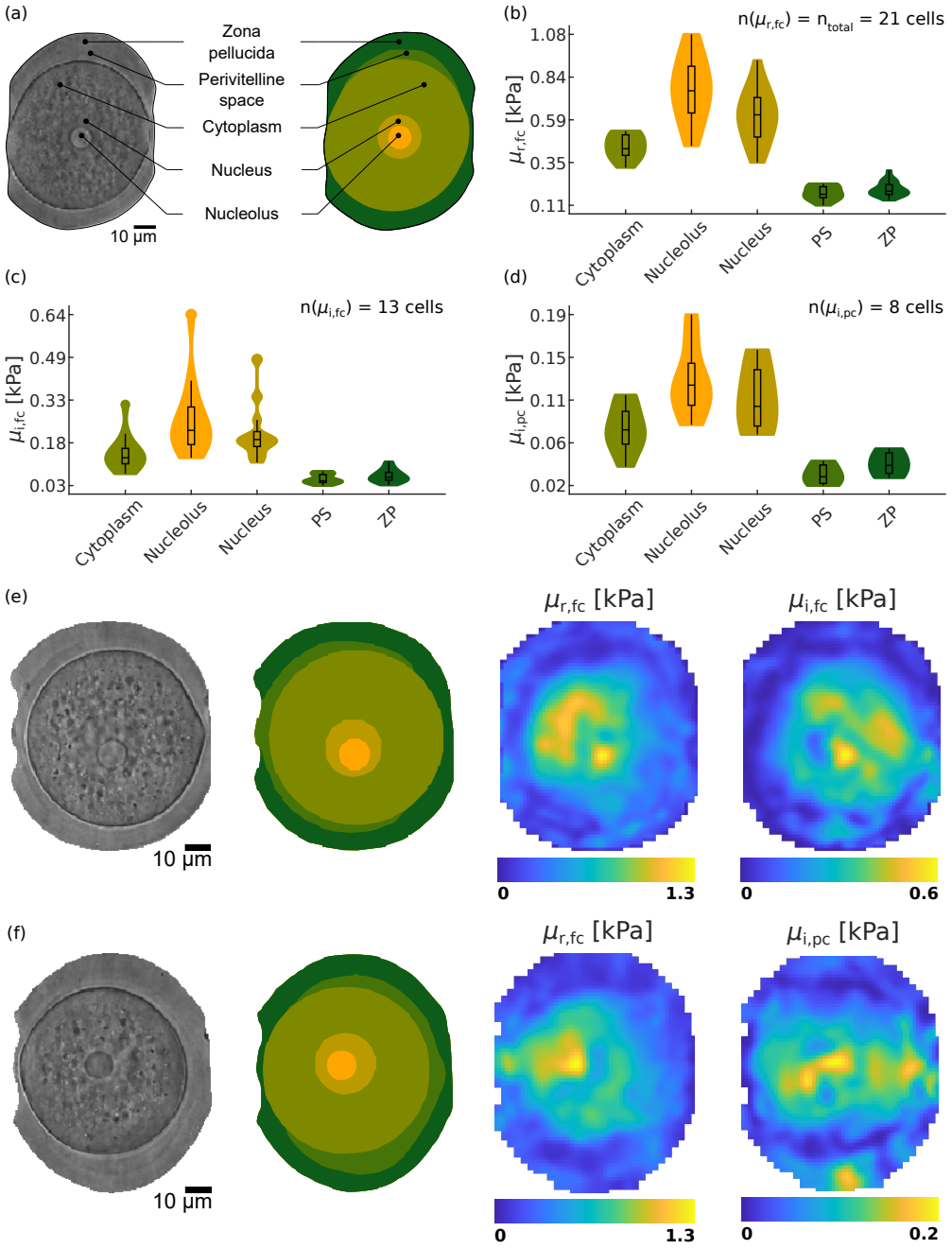

Figure 21 – Storage and loss modulus reconstructions in 21 mouse oocytes. a. Anatomical image of a representative mouse oocyte and corresponding segmented regions. **b.** Average values of storage modulus reconstructions performed on 21 oocytes. All reconstructions converged to stable distributions ($\mu_{r,fc}$). **c.** Average values of fully converged loss modulus reconstructions (13 out of 21) in the five segmented regions ($\mu_{r,fc}$). **d.** Average values of partially converged loss modulus reconstructions (8 out of 21) in the five segmented regions ($\mu_{r,pc}$). **e.** Representative oocyte for which both the storage and loss modulus reconstructions were complete. Images show the oocyte and corresponding segmented regions, and the storage and loss modulus reconstructions ($\mu_{r,fc}$ and $\mu_{i,fc}$, respectively). **f.** Representative oocyte for which the storage modulus reconstruction was complete, and the loss modulus reconstruction was partial. Images show the oocyte and corresponding segmented regions, and the storage and loss modulus reconstructions ($\mu_{r,fc}$ and $\mu_{i,pc}$, respectively).

A Bonferroni correction was applied to a significance base level $\alpha_0 = 0.05$ to account for the ten reported comparisons. The corrected significance level was $\alpha_{corr.} = 0.05/10 = 0.005$. Significant differences with p-values < 0.005 were found between most regions for both moduli.

The variability of the OME and NLI combination was assessed using images acquired though 15 repeated measurement cycles on the same oocyte. Fig. 22 shows reconstructed storage (μ_r) and loss (μ_i) moduli, along with shear stiffness (μ_s) and damping ratio (ξ). The shear stiffness, defined by $\mu_s = 2\frac{|\mu_r+i\mu_i|^2}{\mu_r+|\mu_r+i\mu_i|}$, was computed to allow comparing the presented results with our previous work, which relied on a correlation-based reconstruction technique (passive elastography) [**2**]. A side-by-side examination of previous and actual results is shown in the *Supplementary Fig. 23*. The damping ratio presented in Fig. 22, defined by $\xi = \frac{\mu_i}{2\mu_r}$, provides information about the relative elastic and viscous contributions of the tissue, where higher values indicate an attenuating fluid-like behaviour and lower values indicate an elastic solid-like behaviour. The first column shows reconstructed properties from a single measurement, the second column presents distributed values of coregistered property images averaged over the 15 measurements, and the third column depicts corresponding standard deviations expressed in percentage of the pixel-by-pixel property averaged values.

5.3. Discussion

A robust method for the viscoelastic characterization of oocytes was presented and applied to freshly collected mouse oocytes. The recovered images presented an unmatched cell structure differentiation based on their distributed viscoelastic properties. Full-field displacement data were approximated through a three-dimensional displacement model, and the storage and loss moduli were reconstructed using a nonlinear inversion algorithm based on reconstruction error minimization. Although the storage modulus, or attenuation-free shear stiffness, is mostly considered in elastography, the viscosity-related behaviour of biotissues has also proven to carry important information, notably on oocytes and embryos potential

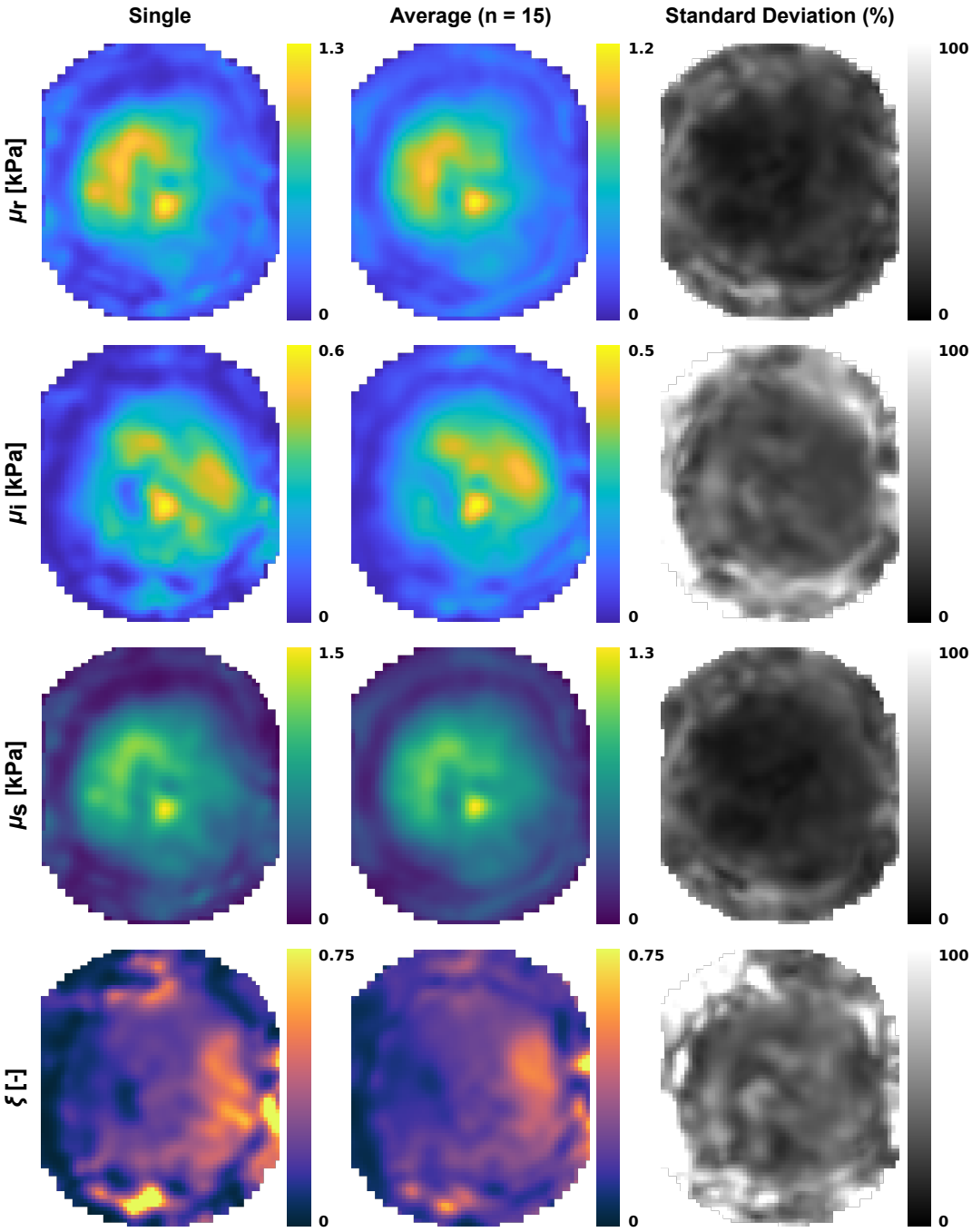

Figure 22 – Viscoelasticity reconstructions in 15 repeated measurements on the same oocyte. Four properties are represented: storage modulus μ_r, loss modulus μ_i, shear stiffness $\mu_s = 2\frac{|\mu_r+i\mu_i|^2}{\mu_r+|\mu_r+i\mu_i|}$, and damping ratio $\xi = \frac{\mu_i}{2\mu_r}$. The shear stiffness was computed to allow comparing the presented results with previous work [**2**]. A side-by-side examination of previous and actual results is shown in the *Supplementary Fig. 23*. The damping ratio is a measure of the relative elastic and viscous contributions of the tissue where higher values indicate an attenuating fluid-like behaviour and lower values indicate a rather elastic solid-like behaviour. The first column shows reconstructions performed from a single acquisition cycle. The second column shows distributed values of coregistered reconstructed properties averaged across 15 measurements. The third column shows corresponding pixel-by-pixel standard deviations expressed as a percentage of the mean values.

in *in vitro* fertilization [**245**], liver tumour types [**280**], and sex-related differences in brain cortical regions [**118**].

Kort and Behr [**253**] recently reviewed and highlighted the needs for better embryo and oocyte selection methods in *in vitro* fertilization procedures. Specifically, biomechanical properties were estimated critical for the function of these cells. As such, the subcellular viscoelasticity imaging technique presented herein demonstrates relevant criteria and may be used to address cell selection in embryology workflows. Moreover, the following attributes constitute significant advances in the field of microelastography. First, no restrictive assumption on the nature of the elastic field is needed, such as the pure-shear approximation, owing to the boundary value problem involved ((94)), which allows characterizing the material's biomechanics rather than wave properties (speed c or wavelength λ). This is a significant advantage in micron scale confined cellular domains where the presence of bulk shear waves is not guaranteed thus challenging the conventional elastic relationship $\mu_s = \rho c^2$, as suggested in Ref. [**279**]. Then, the difficult preselection of a rheological model is circumvented by the generalized viscoelasticity equilibrium ((94)). Finally, the iterative error minimization approach does not operate on the measured data directly, which ensures a higher tolerance to noise relative to direct inversion techniques, and avoids the arbitrary preselection of a motion component owing to the three-dimensional description of the material.

In simulations, the modeled shear modulus distributions were based on the mechanical contrasts recovered from experiments conducted at the same actuation frequency of 14.4 kHz. Fig. 20.a represents the worst case scenario where the zone size is smaller than half of the long wavelength induced in the simulated oocyte domain. Individual regions could still be distinguished but the reconstruction converged to scaled distributions, which is a typical effect in the presence of long wavelengths [**281, 282**]. In Fig. 20.b, the recovered distributions were closer to the true distributions as the modeled shear modulus values had a lower magnitude and consequently resulted in a wave field with a shorter wavelength. This illustrates that shorter wavelengths relative to the subzone size contribute to more accurate reconstructions. Finally, reconstructions accurate to numerical precision could be achieved

in simulations using true instead of approximated full-field displacement data, as shown in the *Supplementary Note 4* and *Fig. 26*.

In Figs. 21 and 22, an additional structure in the oocyte, the nucleolus, could be identified in comparison with our previous work [**2**]. From Fig. 21 and Table 5, most of the paired oocyte regions showed significant differences in both properties with p-values lower than 0.005, even in the case of partially converged reconstructions.

In an average sense, no significant property difference was found between the nucleus on one hand and the nucleolus and cytoplasm on the other hand across all cells, as shown in Table 5. This may be due to the small thickness of the nucleus, which is encompassed between the nucleolus and the cytoplasm. However, a local property contrast in μ_r and μ_i maps was observed in sufficiently thick portions of the nucleus, as seen in Figs. 21.e, 21.f, and 22. Similarly, the ZP remains a difficult structure to characterize due to its thinness. In most cases, it is bound by the fluid PS and the external medium (excluded from the geometry), which could alter the displacement estimation and consequently the reconstruction in this region. In both Figs. 21 and 22, the circular fluid PS could be differentiated in recovered images but the identified property values are considered inaccurate as a viscoelastic model was used in a fluid region. This part of the domain was maintained in the treated geometry in the interest of illustrating the capability of the proposed method to discriminate structural details in live cells.

During the fast imaging process, oocytes receive external vibrations for ≈ 0.75 ms per acquisition cycle, corresponding to a little more than 11.25 ms for the 15 repeated acquisition sessions on the same cell. The multiple measurements allowed by this short time scale increase the reliability of reconstructions through coregistration and pixel-by-pixel averaging. In Fig. 22, the recovered properties, μ_r, μ_i, μ_s, and ξ, were obtained from measurements on the representative oocyte shown in Fig. 21.e. The averaged reconstructions presented in Fig. 22 show distributions similar to the single measurement case and feature a unique visual contrast where the five oocyte structures can be finely identified in μ_r, μ_i, and μ_s maps. These reconstructions provide superior regional details relative to the damping-free

shear stiffness reported in our previous work [**2**], as shown by the side-by-side comparison presented in the *Supplementary Fig. 23*. Higher variability levels are observed in standard deviation maps of μ_i and ξ reconstructions on edges near the immobilizing pipette where wave illumination is low. Finally, piezo-driven ICSI procedures have been reported to be safe for oocytes, and improve survival and fertilization rates in comparison to conventional ICSI [**283, 284, 285**]. These particular characteristics demonstrate that the submicron piezo-induced vibrations do not damage the oocyte, even when used to break the plasma membrane. In optical microelastography, the pulsing pipette is non-invasive as it simply laterally sweeps along the surface of the ZP over about 1 µm without breaking it or even touching the plasma membrane, which suggests that optical microelastography should be safe.

5.4. Limitations and Future Work

In this work, the measured wave fields have a wavelength on the order of the oocyte diameter. As shown by simulations, this long wavelength condition challenges absolute mechanical property recovery and likely leads to scaled reconstructions. Although oocyte structures could be differentiated in both simulations and experiments, an absolute property recovery is desirable in view of clinical application. Generating elastic fields of shorter wavelengths requires to increase the actuation frequency. To date, displacement fields suitable for microelastography have been observed at frequencies up to 20 kHz in tissue mimicking phantoms [**279**]. Further analysis of the frequency content of the displacement data obtained in oocytes specifically, and future work involving mechanical actuators adapted to higher frequency delivery, will help address the usable frequency range in oocyte microelastography.

Oocytes were modeled as heterogeneous, viscoelastic, nearly incompressible, and isotropic biomaterials. Although this characterization reduces model-data mismatch errors related to previous purely elastic and locally homogeneous descriptions [**2**], additional violation of the current assumptions would contribute to other model-to-data mismatches and result in reconstruction inaccuracies. For instance, oocytes are made of structures with inherent

directionality, such as microtubules and microfilaments, and contain porous complexes, notably in the ZP [**286, 287**]. This suggests that anisotropy and poro-elasticity imaging are worth consideration. The effects of a viscoelastic isotropic characterization on a viscoelastic anisotropic or poro-elastic isotropic tissue have been evidenced using magnetic resonance elastography [**138, 288, 289**]. Guidelines on the suitability of these material models, established in other tissues [**290, 291, 292, 293, 294**] and at different harmonic actuation regimes [**289, 282**], will certainly help improve oocyte characterization in future works. The near-incompressible description of oocytes may also be revisited by using a compressible material model [**295**], and a true full-field displacement data set. However, the high water content in cells suggest a low level of bulk modulus-based cellular structure differentiability and an actual incompressible rather than compressible behaviour is expected, as described in [**231**]. Ultimately, extension of the single-plane imaging sequence to multi-plane and incorporation of 3D motion tracking throughout the acquired slices [**296**] would further improve the accuracy of the property maps reported in Figs. 21 and 22. It would also eliminate the need for geometry-based displacement modeling and central positioning of the focal plane, and thus contribute to broad application of the proposed method to cells of arbitrary shapes. For instance, the geometry assumptions made in this work no longer hold with metaphase-II stage oocytes and early fertilized embryo, which are clinically more useful than GV-stage oocytes. The acquisition of full-field displacement data would be necessary in this case to validate the overall procedure and avoid potential hurdles to clinical application. Future acquisition of a piezo-driven lens position controller should allow addressing multi-plane imaging with adjustable phase offsets by exploiting the harmonic actuation regime.

Work is under way to incorporate a pixel-wise displacement estimation in the pipeline, as opposed to the current region-based method, which will help provide more accurate motion estimates in thin or confined areas such as the nucleus or the zona pellucida, and consequently improve the reconstruction sensitivity in these regions [**297**]. Property maps may also be enhanced in future works by enabling total variation minimization or soft prior regularization [**119**]. Finally, incorporation of the presented microelastography procedure into

embryology workflows [**21**] would help address the detectability limit of subtle cell defects through the processing of larger sample sizes, oocytes at different stages of development, and early fertilized embryos.

5.5. Conclusions

Viscoelasticity images of live mouse oocytes were produced noninvasively through the recovery of storage and loss modulus distributions. These previously unseen reconstructions demonstrated unique structural detail levels at a subcellular scale. Based on Yanez *et al.* [**245**], there are fair reasons to suspect that oocyte and embryo quality might be reflected in these measurements in a way that might allow predictive selection as an alternative to morphological examination or expensive and invasive preimplantation genetic screenings.

5.6. Methods

5.6.1. Oocyte Imaging

The procedure reported here was conducted in accordance with guidelines of the Institutional Animal Care Committee of the University of Montreal Hospital Research Center and the study conformed with guidelines of the Canadian Council on Animal Care and the Guide for the Care and Use of Laboratory Animals. Oocyte growth was stimulated by injecting 5 IU of pregnant mare serum gonadotropin (PMSG) to the mouse between 44 and 48 h before collecting oocytes. Ovaries were then extracted and placed in 1 to 2 ml of M2 medium supplemented with 200 nM of 3-isobutyl-1-methyl-xanthine (IBMX), and GV-stage oocytes were recovered by puncturing follicles with a 27-gauge needle. Granulosa cells were removed by successive pipetting and washings in M2+IBMX droplets. Oocytes were then transferred to another M2+IBMX droplet in a dedicated petri dish, itself placed on the platform of an inverted microscope (Leica DM IL LED with 100× lens). Microelastography measurements were made from a total of 21 oocytes and each oocyte was manipulated using glass micropipettes. The pipette on the left-hand side (ICSI holding pipette) was held fixed while

that on the right-hand side was mounted on a piezo-electric pulsing unit (PMM-150FU, Prime Tech Ltd., Tsuchiura, Japan) used for harmonic motion generation in the oocyte. While operating, the pulsing pipette was oscillating laterally in the focal plane of the lens set at the center of the oocyte. The coupling of the piezo-driven ICSI equipment with the micro-pipette allowed a pulsation between $\approx$ 14 kHz and 16 kHz. A 14.4-kHz actuation provided an efficient motion transmission to the oocytes in this specific configuration. Images of the oocyte during the dynamic procedure were acquired at a 200 kHz frame rate with an isotropic pixel resolution of 0.5 µm using a high-speed camera (Photron, FastCam SA-Z, San Diego, USA) for subsequent estimation of local small tissue displacements in the cell (19.b).

5.6.2. In-Plane Displacement Estimation

Time harmonic displacements were estimated by applying the Lagrangian Speckle Model Estimator (LSME) algorithm to the image stack of the oocyte under actuation. LSME is based on a Lucas-Kanade optical flow variation where image correlation between two or more frames is performed [**298**]. Here, all displacements were calculated with respect to a reference frame of the oocyte at rest, imaged prior to actuation, to mimic motion encoding in MR elastography and ensure compatibility of the motion data format with the NLI procedure. The choice of LSME's intrinsic parameters (size of interrogating windows and overlapping percentage) was determined by testing different parameter sets on simulated optical images of the oocyte being deformed in time by a harmonic actuation of 14.4 kHz (see the Simulation paragraph below).

5.6.3. 3D-Oocyte Displacement Model

Estimated in-plane displacements were processed by a 3D-oocyte displacement model to approximate a full-field displacement data set (u, v, and w). First, the out-of-plane component w_1 in the measured slice, indicated by the subscript "1", was negated owing to the following assumption and experimental settings:

1) oocytes were assumed spherical, which is in line with common descriptions of GV-stage oocytes [**264**];

2) the focal plane of the lens was set to cut through the center of the oocyte, along the symmetry plane of the assumed spherical geometry [**160**]; and

3) the pulsing micropipette used to generate motion in the oocyte oscillated along an axis parallel to the focal plane, permitting Dirichlet boundary condition (BC) $w_{1,BC} = 0$ on the boundary of this symmetry plane.

The combination of these three assumptions leads to the hypothesis that $w_1 = 0$. Second, two artificial slices labelled "2" and "3" were derived from BCs and spherical geometry properties as follows. The out-of-plane components w_2 and w_3 in the extra two slices were estimated by assuming an incompressible medium, which is a common characteristic of biological tissues [**231**]. Mathematically, local incompressibility was enforced by:

$$\nabla \cdot \mathbf{u} = \frac{\partial u}{\partial x} + \frac{\partial v}{\partial y} + \frac{\partial w}{\partial z} = 0, \tag{88}$$

$$\Leftrightarrow w_{i+1} = -\left(\frac{\partial u}{\partial x} + \frac{\partial v}{\partial y}\right)\delta z + w_i, \tag{89}$$

where δz is the prescribed interslice distance of 1.25 μm. The selection of δz and its impact on the reconstruction are described in the *Supplementary Note 5* and illustrated in the *Supplementary Figs. 27* and *28*. First-order derivatives were approximated using third-order 2D-polynomial projection in 7×7 pixel^2 kernels. Finally, the local symmetry properties of $\left.\frac{\partial u}{\partial z}\right|_1$ and $\left.\frac{\partial v}{\partial z}\right|_1$ in the focal plane (slice 1) were invoked to approximate in-plane displacements in immediate neighbor slices 2 and 3 (*i.e.*, u_2, v_2, u_3, and v_3):

$$\left.\frac{\partial u}{\partial z}\right|_1 = \left.\frac{\partial v}{\partial z}\right|_1 = 0, \tag{90}$$

$$\left.\frac{\partial u}{\partial z}\right|_2 \approx \left.\frac{\partial v}{\partial z}\right|_2 \approx \left.\frac{\partial u}{\partial z}\right|_3 \approx \left.\frac{\partial v}{\partial z}\right|_3 \approx 0, \tag{91}$$

which led to:

$$u_1 \approx u_2 \approx u_3, \tag{92}$$

$$v_1 \approx v_2 \approx v_3. \tag{93}$$

5.6.4. Simulations

Synthetic 3D displacements were generated in a finite element model of a mouse oocyte assuming a viscoelastic, heterogeneous, nearly incompressible, and isotropic solid as described by (94). Simulations were programmed in Comsol Multiphysics using the Matlab interface (Comsol 5.5 and LiveLink for Matlab (Comsol Inc. Stockholm, Sweden); Matlab R2019b, The Mathworks, Massachusetts, USA). The oocyte model consisted of a four-domain geometry made of four concentric spheres representing the nucleolus, the nucleus, the cytoplasm, and the zona pellucida (ZP), as shown in Fig. 19.a. The nucleolus had a radius $r_{nucleo} = 5.6$ µm, the nucleus $r_{nucleus} = 12.3$ µm , the cytoplasm $r_{cyto} = 36.7$ µm, and the surrounding sphere binding the ZP $r_{zp} = 45.4$ µm (corresponding to a ZP with thickness of 8.6 µm). Dimensions were extracted from anatomical images of oocytes. Dirichlet boundary conditions were defined on the ZP in circular cross-sections of radii $r_{pip} = 18.0$ µm at opposite locations along the x axis to represent the fixed and pulsing pipettes, as shown in Fig. 19.a. Displacements oscillating along the y axis with an amplitude of 1 µm were prescribed to the pulsed boundary whereas the held area was maintained fixed (0 µm displacements along each axis). BCs were left unconstrained on the remaining surface of the ZP. Two relative experiment-based shear modulus distributions, μ_1 and μ_2, were considered in the simulations since experimental reconstructions were likely scaled because of the induced long wavelength. The property distribution μ_1 was set by multiplying the shear modulus recovered from experiments, μ_{exp}, by a scaling factor of 2.5 to reproduce the long wavelength condition observed at 14.4 kHz. The second shear modulus distribution μ_2 was set to $\mu_2 = \mu_{\text{exp}}$. The μ_{exp} distribution was defined by the average values obtained in each of the segmented regions shown in Fig. 21: $\mu_{\text{exp,nucleolus}} = 768 + i268$ Pa, $\mu_{\text{exp,nucleus}} = 615 + i217$ Pa,

$\mu_{\text{exp,cytoplam}} = 444 + i147$ Pa, and $\mu_{\text{exp,zp}} = 202 + i68$ Pa. Density ρ and bulk modulus K were held constant through all simulations at $\rho = 1000$ kg.m^{-3} and $K = 2.2 \times 10^9$ Pa.

Once computed, the finite element displacement fields were interpolated on an isotropic grid at the same resolution as the experimental images (0.5 μm). For reconstructions based on true full-field displacement data, the three motion components in a set of contiguous slices were extracted. To mimic the experimental measurements and the full-field approximation procedure, in-plane displacements only were extracted from the central slice of the 3D oocyte model. The complex-valued displacement data were then converted to time displacements by generating a suitable power spectral density and applying the inverse Fast Fourier transform using Matlab. The resulting time-domain displacements underwent the preprocessing procedure used for experimental data.

Then, optical images were simulated to select adequate parameters for motion tracking (LSME). First, a texture image was generated through a random distribution of gray-scale points convoluted with a $5 \times 5 \times 5$ pixel^3 kernel in a volume surrounding the imaged slice (xOy plane) in the oocyte model. Dynamic deformation images were generated for each time step by forcing each point of the texture image to move a distance given by the computed displacements u_c, v_c, and w_c in the simulation (μ_1 distribution). Finally, LSME was applied to the simulated optical images using successive sets of interrogation window sizes and overlaps. An isotropic size of 10×10 pixel^2 with 90 % overlap was found to produce reliable displacement maps and was used in the present work.

5.6.5. Inverse Problem

Originally developed for MR-based viscoelastic property identification, NLI is an optimization-based reconstruction method formulated on the minimization of the mismatch between measured displacements and displacements predicted by a heterogeneous finite-element mechanical model [**116, 233**]. The computational cost of the NLI property update for the complete region of interest is mitigated by decomposing the domain into overlapping subdomains, termed *subzones*. Subzones are randomly distributed across the domain,

processed in parallel, and eventually recombined to form a global property image. Here, oocytes were modelled as a heterogeneous, viscoelastic, nearly incompressible, and isotropic material. The corresponding boundary value problem relating the material's mechanical parameters to the measured displacement field is given by:

$$\begin{cases} \nabla \cdot (\mu \nabla \mathbf{u}) + \nabla (\mu \nabla \cdot \mathbf{u} - p) = -\rho \omega^2 \mathbf{u} & \text{in } \Omega, \\ Ktr(\boldsymbol{\varepsilon}) = -p & \text{in } \Omega, \\ \mathbf{u} = \mathbf{u}_0 & \text{on } \Gamma_u, \\ \mathbf{n} \cdot \boldsymbol{\sigma}_E = \mathbf{f}_0 & \text{on } \Gamma_\sigma, \end{cases} \tag{94}$$

where Ω is the oocyte domain, $\mathbf{u}$ is the displacement vector (m) containing three components (u, v, and w) along the three axes of the Cartesian coordinate system (x, y, and z, respectively), μ is the complex-valued shear modulus (Pa), p is the pressure field (Pa), ρ is the mass density (kg.m^{-3}), ω is the actuation angular frequency (rad.s^{-1}), K is the bulk modulus (Pa), tr is the trace operator, $\boldsymbol{\varepsilon}$ is the strain tensor, $\mathbf{u}_0$ is the displacement vector on the domain's boundary Γ_u, $\boldsymbol{\sigma}_E$ is the stress tensor, $\mathbf{n}$ is the unit vector normal to the surface boundary Γ_σ, and $\mathbf{f}_0$ is the traction force vector. In NLI, boundary conditions are extracted from the measured displacements so only Γ_u is defined. Parameters ρ and K were assumed known and constant throughout, and the properties of interest were the real and imaginary parts of the complex shear modulus $\mu \equiv \mu_r + \mu_i$, termed storage ($\mu_r \equiv G'$) and loss ($\mu_i \equiv G''$) moduli, respectively. The calculation of the solution to the inverse problem is then formulated as the minimization of the following objective function:

$$\Phi = \frac{1}{2} (\mathbf{u}_c(\boldsymbol{\theta}) - \mathbf{u}_m)^H (\mathbf{u}_c(\boldsymbol{\theta}) - \mathbf{u}_m), \tag{95}$$

where $\mathbf{u}_c$ is the displacement field computed through (94) using finite-elements, $\mathbf{u}_m$ is the measured displacement field, $\boldsymbol{\theta}$ is the vector containing the inferred mechanical properties, and H refers to the complex-conjugate transpose. The property distribution $\boldsymbol{\theta}$ that minimizes the objective function Φ is then considered the most likely approximation of the true distribution. The solution to (94) was computed on a 27-node hexahedral finite-element

mesh using quadratic shape functions. Displacement and property meshes had the same resolution as the displacement data. Subzones had an isotropic size of 30 μm^3 with a 20% overlap in all reconstructions. The selection of the subzone size for the nonlinear inversion is described in the *Supplementary Note 5* and illustrated in the *Supplementary Figs. 27* and *28*. The high resolution of optical images (0.5 μm, isotropic) allowed down-sampling of the displacement data by a factor of 2.5, permitting relatively large zone sizes while maintaining a reasonable runtime per iteration. The conjugate gradient (CG) method was used to solve the inverse problem. A maximum of 1000 global iterations was allowed in experiments and in the first simulation (μ_1 distribution), and CG involved 1 CG iteration per zone from global iterations 1 to 10, 3 CG iterations from global iterations 11 to 300, and 6 CG iterations from global iterations 301 to 1000. In the second simulation (μ_2 distribution), 500 global iterations were allowed, and CG involved 1 CG iteration per zone from global iterations 1 to 10, 3 CG iterations from global iterations 11 to 200, and 3 CG iterations from global iterations 201 to 500. Gaussian smoothing with a filter width of 1.2 μm was used to stabilize the reconstruction procedure, as in standard MR elastography-based NLI reconstructions. As in a vast majority of elastography protocols, a homogeneous density of 1000 $kg.m^{-3}$ was assumed and the bulk modulus was set to an homogeneous value $K = 2.2 \times 10^9$ Pa reflecting tissue incompressibility and low spatial variations, as described in [**231**]. Average reconstruction maps in Fig. 22 were obtained by co-registering anatomical images of the same oocyte at rest for each of the 15 acquisition cycles using an affine geometry transformation (translation, rotation, scale, and shear).

Discussion et Conclusion

6.7. Résumé

Les travaux présentés dans ce document explorent l'imagerie biomédicale d'élastographie à l'échelle macro et microscopique et étudient une possibilité de combinaison avec d'autres protocoles d'imagerie et de stimulation électrique. Les caractéristiques de l'élastographie harmonique communes aux méthodes d'élastographie par résonance magnétique et de micro-élastographie optique sont notamment mises à contribution dans le but de poursuivre le développement de cette dernière technologie, récemment mise au point au laboratoire.

Le premier projet aborde la problématique de la génération d'ondes élastiques dans le cadre d'une expérience conjointe d'élastographie par résonance magnétique et de stimulation électrique. Les observations expérimentales démontrent que les forces volumiques de Lorentz induites dans des fantômes conducteurs d'agar, exposés au champ magnétique de l'appareil d'IRM et soumis à une stimulation électrique, produisent des champs de déplacements mesurables par ERM et permettent la reconstruction de cartes de rigidité grâce à l'algorithme LFE. Ce dernier, notamment employé en ERM clinique, évalue la longueur d'onde locale du champ ondulatoire mesuré et garantit l'émission d'images paramétriques en quelques secondes à partir d'une formulation exempte de source de mouvement. Les cartes de rigidité ainsi produites affichent des contrastes mécaniques globaux cohérents avec les caractéristiques des fantômes fabriqués mais présentent toutefois des distributions factices localement hétérogènes dues aux réflexions des ondes élastiques sur les parois du porte-fantôme. Aucun impact significatif dû à la présence de forces volumiques de Lorentz dans le champ de mesure n'a été observé malgré l'inadéquation entre le modèle mécanique et les données expérimentales.

L'intensité du courant électrique délivré et l'amplitude des déplacements mesurés excluent à l'heure actuelle le recours à la force de Lorentz comme source locale d'onde élastique *in vivo* pour des raisons de sécurité liées à l'utilisation de courants élevés. Ces expériences suggèrent ainsi que les champs de déplacements générés au moyen de faibles courants délivrés par des dispositifs (pré-)cliniques de stimulation électrique seraient difficilement détectables et auraient peu d'influence sur les ondes mécaniques générées par un activateur externe dans le cadre d'expériences d'ERM et de stimulation électrique réalisées conjointement dans une même région d'intérêt. Cet aspect est discuté dans le paragraphe suivant.

Le deuxième projet évalue la faisabilité d'un protocole préliminaire de combinaison d'ERM et de stimulation électrique transcrânienne non-invasive à travers des simulations numériques dans un modèle 3D de cerveau de souris. Un volet de simulation de tomographie d'impédance électrique par IRM est également proposé étant donné l'importance de la modélisation des courants induits par stimulation électrique en neurostimulation et neuroimagerie. Dans un premier temps, l'impact des forces volumiques de Lorentz sur la reconstruction de cartes de viscoélasticité est étudié à l'aide de la méthode d'inversion nonlinéaire par sous-zones. Cette dernière identifie la distribution de paramètres viscoélastiques la plus probable grâce à un modèle mécanique discrétisé en éléments finis dans la région d'intérêt et une méthode d'optimisation numérique. Les déplacements simulés dans trois situations distinctes sont analysés. Tout d'abord, une sollicitation externe "standard" d'ERM est modélisée, *i.e.* sans force volumique, où le champ de déplacements est prescrit à partir de conditions limites de type Dirichlet. Cette situation mène à une reconstruction précise du module de cisaillement complexe, notamment permise par l'adéquation entre le modèle mécanique constituant du problème inverse et les déplacements simulés. Ensuite, la réalisation simultanée d'expériences d'ERM et de stimulation électrique, représentée par la simulation de déplacements induits par activation externe superposés aux déplacements induits par force volumique de Lorentz, démontre que ces derniers sont dominés de trois ordres de grandeur par la composante due à la sollicitation externe ($\sim 10\,\mathrm{nm}$ vs $\sim 10\,\mu\mathrm{m}$). Pour cette raison, la composante résultant de forces volumiques de Lorentz serait, en toute hypothèse, couverte par le bruit de

mesure dans le cadre d'une acquisition expérimentale. L'écart entre ces deux composantes permet une reconstruction précise de cartes de viscoélasticité dans la mesure où les forces volumiques constituent une contribution négligeable à l'équation du mouvement à l'équilibre. Enfin, ces simulations sont complétées par la reconstruction du module de cisaillement complexe à partir du champ ondulatoire généré par force volumique de Lorentz uniquement. Cette situation, bien que peu plausible expérimentalement, aboutit à des reconstructions empruntes d'erreurs importantes dues à l'absence de terme de source dans le modèle mécanique utilisé. Ces résultats numériques abondent dans le sens de l'hypothèse formulée à l'issue du premier projet et indiquent qu'une procédure conjointe d'ERM et de stimulation électrique non-invasive pourrait être envisagée expérimentalement dans une même région d'intérêt, sans nécessité de modifier la formulation du problème inverse par sous-zones. Une telle approche pourrait présenter un intérêt dans le cadre de la caractérisation de la réponse biomécanique du cerveau à une stimulation électrique. Dans un second temps, l'imagerie de la conductivité électrique du cerveau, utile à la modélisation des courants induits, est abordée par la simulation de la densité de flux magnétique induite au cours d'une acquisition par IRM de tomographie d'impédance électrique (TIE). Bien que la méthode de reconstruction utilisée, l'algorithme B_z harmonique, soit peu adaptée aux mesures bruitées et rencontre des difficultés dans les régions de faible conductivité, l'incorporation de ce volet d'imagerie à un protocole d'ERM et de stimulation électrique pourrait bénéficier à la neuroimagerie en apportant une quantification supplémentaire reposant sur la corrélation entre les zones stimulées électriquement et leur réponse mécanique. De plus, les séquences d'impulsion d'IRM utilisées en TIE sont, comme l'ERM, à contraste de phase et présentent des similarités d'intérêt dans une optique de développement d'un protocole d'élastographie et de TIE par IRM. Finalement, une approche d'optimisation par sous-zone pourrait également être envisagée pour la reconstruction de cartes de conductivité électrique.

Le dernier projet est consacré à la micro-élastographie optique (MEO) d'ovocytes de souris et s'appuie sur la méthode d'inversion par sous-zones employée précédemment pour la

reconstruction de cartes de viscoélasticité. Contrairement à la résonance magnétique, la microscopie optique en champ clair est une méthode d'imagerie intrinsèquement tomographique si bien que la déformation dynamique de la cellule au cours d'une expérience d'élastographie ne peut être imagée que dans le plan focal de l'objectif. Cette caractéristique restreint donc l'estimation des déplacements locaux au plan focal et complexifie l'acquisition de jeux de données complets, *i.e.*, dans des coupes successives séparées de distances finement contrôlées. La résolution du problème inverse par la méthode des sous-zones, formulée à partir d'une description tridimensionnelle du milieu imagé, requiert des champs de déplacements de dimension correspondante et nécessite ainsi une étape de traitement des champs tomographiques mesurés par microscopie optique dans le but d'approximer une représentation 3D d'onde élastique, compatible avec l'algorithme de reconstruction. La propriété de symétrie sphérique des ovocytes au stade de vésicule germinale ainsi qu'une contrainte sur leur compressibilité sont utilisées dans cette optique, sous réserve d'activation mécanique dans le plan focal fixé au centre de la cellule. Bien que sujette aux erreurs d'approximation 2D $\rightarrow$ 3D, cette approche permet la reconstruction inédite de cartes de viscoélasticité d'ovocytes de souris, les modules de stockage et de perte, dans lesquelles cinq domaines ont pu être identifiés : le nucleolus, le noyau, le cytoplasme, l'espace périvitellin et la zone pellucide. En l'état, une augmentation de la fréquence d'activation constituerait une première amélioration raisonnablement réalisable de la méthode de MEO dans le but de réduire la longueur d'onde du champ ondulatoire mesuré, en comparaison aux $\sim$ 15 kHz utilisés dans ces travaux. Cette modification permettrait une identification plus quantitative des paramètres reconstruits. Bien qu'aucune observation d'ondes élastiques autres que compressives n'ait été exposée dans la littérature scientifique pour des fréquences d'oscillation supérieures à 20 kHz, le contenu fréquentiel des champs de déplacements temporels estimés ici indiquent que des ondes acoustiques vraisemblablement adéquates à l'élastographie seraient accessibles dans la gamme ultrasonique basse fréquence. Finalement, la poursuite du développement de la micro-élastographie optique pourrait permettre d'établir la viscoélasticité d'ovocytes et

d'embryons comme bio-marqueurs de leur potentiel de développement dans le cadre de procédures de fécondation *in vitro*.

6.8. Vue d'ensemble et perspectives

Les trois projets développés dans ce document s'articulent autour de trois axes centraux de l'élastographie : l'activation à travers la stimulation mécanique par force volumique de Lorentz, la reconstruction et l'adéquation données-modèle mécanique à travers le traitement via l'algorithme NLI de déplacements induits par force de Lorentz, et l'imagerie tomographique de la propagation tridimensionnelle d'ondes mécaniques à travers la microélastographie optique. Bien que les applications envisagées suivent des trajectoires d'apparences distinctes, elles sont toutes soumises aux mêmes limitations et difficultés inhérentes à l'élastographie, traitées et discutées dans ce document à travers la résonance magnétique et la microscopie optique.

6.8.1. Fréquence d'activation et amortissement viscoélastique

La gamme des fréquences d'oscillations utilisables en élastographie harmonique demeure une estimation vivante dans la mesure où elle évolue avec la sophistication des méthodes d'acquisition et de traitement d'images. Des régimes de l'ordre du kilohertz sont aujourd'hui accessibles et utilisés en élastographie par résonance magnétique [**14**], ultrasonore [**299, 300**] et par cohérence optique [**301**]. En outre, la microélastographie optique en champ clair a récemment permis d'imager la propagation d'ondes élastiques émises à des fréquences d'activation supérieures à 15 kHz [**2, 302**]. L'augmentation de la fréquence d'activation entraîne la question légitime de l'atténuation par le milieu de propagation. Au delà de l'atténuation géométrique, la composante visqueuse des solides viscoélastiques contribue à l'absorption de l'énergie mécanique véhiculée par les ondes élastiques et augmente généralement avec la fréquence. Cette propriété naturelle des solides mous est inhérente à l'élastographie et non-spécifique à la modalité d'imagerie utilisée. Elle permet notamment de mettre en avant

quatre paramètres importants : la taille de l'objet, sa rigidité dynamique, son ratio d'amortissement et la fréquence d'activation. La fréquence d'activation et la rigidité dynamique (ratio d'amortissement) déterminent la longueur d'onde des oscillations (et leur atténuation), tandis que la longueur d'onde des oscillations relativement à la taille de l'objet (ou fenêtre de traitement) détermine la sensibilité de la reconstruction à des distributions relatives ou absolues des propriétés. À moins d'un intérêt pour une fréquence particulière, les fréquences d'activation les plus élevées exploitables sont généralement utilisées. L'intérêt que présente la dépendance fréquentielle de la réponse mécanique des tissus biologiques et les potentiels biomarqueurs qu'elle pourrait constituer justifient la recherche d'alternatives élargissant la gamme de fréquences utilisables en élastographie.

Runge *et al.* ont abordé le problème d'augmentation de l'atténuation avec la fréquence d'activation par le développement du "gravitational transducer" [**142**]. Ce transducteur est constitué d'une masse fixée à un axe de rotation et repose sur la force centripète pour produire des vibrations d'amplitudes croissantes avec la fréquence d'oscillation de la masse autour de son axe. Cette méthode consiste à compenser l'atténuation subie par l'onde mécanique par des niveaux d'activation plus élevés en surface. L'activation par force de Lorentz présentée dans ce document a été envisagée comme une alternative et vise à réduire la distance que l'onde a à parcourir entre les zones d'émission et d'intérêt par la génération de sources locales d'ondes mécaniques. Cette application semble hors d'atteinte à l'heure actuelle pour des raisons de sécurité liées à l'intensité des courants utilisés, malgré les plus hauts champs magnétiques et amplitudes de gradients d'encodage de mouvement disponibles avec les dispositifs pré-cliniques. Ces derniers oscillent dans l'ensemble entre 200 $mT.m^{-1}$ et 500 $mT.m^{-1}$ et permettent des acquisitions *in vivo* sensibles à des déplacements de l'ordre du micromètre, plusieurs ordres de grandeur supérieurs à l'amplitude simulée des champs de déplacements induits par force de Lorentz dans des conditions de stimulation électrique sûres du cerveau de souris. Cette approche pourrait toutefois être envisagée en microélastographie optique où les amplitudes de déplacement mesurées sont en partie inférieures au micromètre. L'activation pourrait être conçue dans l'environnement immédiat de la cellule de façon à éviter le contact

électrique tout en assurant la transmission mécanique des ondes produites. De multiples activations dans l'espace pourraient également être conçues dans le but de compenser des niveaux d'amortissement, en toute hypothèse, élevés. La microélastographie optique permettrait également de mettre en évidence le comportement fréquentiel de la réponse mécanique de bio-tissus à des régimes d'activation inexplorés et par conséquent d'en évaluer les niveaux d'atténuation. Ahmed *et al.* ont récemment estimé les composantes élastiques et visqueuses du cytoplasme d'ovocytes de souris de 1 Hz à $\approx 10^4$ Hz [**272**]. Leurs observations montrent un comportement relatif élastique-visqueux non-monotone en fonction de la fréquence si bien que la contribution visqueuse, bien qu'importante, ne domine pas systématiquement la contribution élastique aux fréquences élevées. Cette particularité justifie l'exploration de régimes d'oscillations à des fréquences supérieures aux ≈ 15 kHz utilisés en microélastographie optique, notamment vers la gamme inférieure du domaine ultrasonore.

La prise en compte de l'amortissement par le milieu de propagation entraine également la question de la reconstruction de la viscoélasticité. Le chapitre 1 décrit les méthodes principales de reconstruction utilisées en ERM, moins contraignante que la MEO du point de vue de la dimension volumique ou tomographique des données mesurées. En MEO, des données 2D seulement sont actuellement accessibles et influencent le choix de la technique reconstruction à utiliser. Les travaux de microélastographie présentés dans ce document poursuivent l'étude de Grasland-Mongrain *et al.* où des cartes de rigidité ont été reconstruites à partir d'une approche 2D de corrélations spatiotemporelles [**2**]. Bien que cette méthode et la LFE reposent sur des mécanismes différents, elles impliquent des caractéristiques et hypothèses comparables :

— le nombre d'onde local des ondes imagées est estimé pour chaque pixel,

— le milieu de propagation de ces ondes est purement élastique (et non viscoélastique),

— une seule composante du mouvement est nécessaire (parmi les deux composantes planaires estimées),

— les ondes élastiques mesurées sont supposées être de cisaillement,

— la rigidité dynamique est approximée à partir des cartes de longueurs d'ondes (supposées de cisaillement),

— les conditions aux frontières ne sont pas prises en compte,

— l'équation du mouvement considérée est de type Helmholtz.

L'objectif de caractérisation viscoélastique d'ovocytes de souris, sans recourir aux hypothèses formulées ci-dessus, a conduit au choix de l'algorithme NLI plutôt qu'à celui de l'inversion directe LFE : le modèle mécanique est viscoélastique, la description générale de l'équation du mouvement (Navier) et la résolution du problème direct prennent en compte les effets de bord et ne requièrent pas que le champ ondulatoire soit de cisaillement. Ce dernier aspect était essentiel dans la mesure où cette hypothèse est invalide au régime harmonique imposé à la cellule, en comparaison à sa taille et à sa rigidité dynamique. Le choix de NLI, malgré les contraintes liées à la formulation 3D du modèle, était alors plus indiqué que les approches 2D LFE et élastographie passive dans le cadre de nos travaux.

6.8.2. Vers l'élastographie des petites échelles

L'augmentation des fréquences d'activation accessibles en élastographie bénéficie au problème d'identification de structures fines par la reconstruction de contrastes mécaniques absolus plutôt que relatifs. Bien que cette caractéristique vaille à toute échelle d'application, elle représente un atout significatif pour l'imagerie de tissus microscopiques. Plus important que la fréquence, la résolution de l'image traitée détermine la résolution des cartes paramétriques reconstruites, définie comme la plus petite taille de contraste mécanique identifiable, par conséquent souvent supérieure à celle d'un pixel de l'image. À ce titre, les méthodes optiques bénéficient d'un avantage vis-à-vis de la résonance magnétique et de l'ultrasonographie. La microscopie en champ clair permet notamment de capturer des images à des résolutions sous-micrométriques avec une cadence d'acquisition suffisamment élevée pour respecter le critère de Nyquist à des fréquences d'activation élevées (>10 kHz). L'envergure des possibilités et applications permises par ces avantages reste toutefois à déterminer. Jusqu'à présent, les cellules caractérisées ont été relativement grandes ($\approx$ 100 µm de diamètre)

si bien que les structures internes présentant un contraste optique pouvaient être identifiées dans les images brutes puis dans les reconstructions, grâce à des distributions de viscoélasticité relatives dues aux grandes longueurs d'ondes émises. Les études conduites actuellement au laboratoire sur la mécanobiologie de macrophages, d'une longueur caractéristique d'environs 20 µm, permettront d'évaluer l'impact d'une réduction d'échelle d'un facteur ≈ 5 sur la procédure d'élastographie aux mêmes résolutions spatiales et temporelles. Par ailleurs, les limites de résolution de la microscopie optique en champ clair liées à la diffraction de la lumière devront être prises en compte dans des cellules de tailles supérieures à quelques micromètres mais constituées de nanostructures. Les méthodes de super-résolution optique permettent d'augmenter la netteté des images mais présentent des temps d'acquisition élevés, aujourd'hui incompatibles avec la méthode actuelle de microélastographie. En ERM, la résolution typique d'une image est de l'ordre du millimètre pour les systèmes 3 T tandis que les déplacements encodés dans la phase du signal sont de l'ordre de la dizaine de micromètres. Cette spécificité confère à l'ERM la qualité de super-résolution du point de vue de sa sensibilité au mouvement, à distinguer de la super-résolution optique sensible aux objets en deçà de la limite de diffraction. La diminution de la taille des pixels en IRM est notamment gouvernée par l'intensité des gradients d'encodage utilisés. Le paramétrage de ces gradients est également limitée ; ici par la stimulation des nerfs périphériques sensibles aux courants induits par la variation temporelle des champs magnétiques. Finalement, l'ERM présente l'avantage significatif d'être sensible au mouvement le long de trois axes choisis par l'utilisateur dans des coupes et volumes également ajustables. Cet aspect permet de traiter le problème inverse de viscoélasticité dans son entièreté par la mesure de champs de déplacements 3D dans un volume/plusieurs coupes. La microscopie optique est moins versatile dans ce domaine et permet, dans la majorité des dispositifs expérimentaux, la mesure de champs de déplacements 2D dans une seule coupe. L'absence de contrôle quantitatif sur l'élévation du plan focal, grâce à un positionnement motorisé par exemple, explique notre approche d'approximation de données 3D par un jeu de données tomographiques acquises dans un

seul plan. À cette difficulté s'ajoute celle de la profondeur de champ inhérente à chaque objectif de microscope. Celle-ci détermine l'épaisseur du plan focal à travers laquelle les objets observés sont nets. Dans le cas où des coupes successives pourraient théoriquement être imagées dans de grandes cellules (*e.g.* ovocytes), moyennant un dispositif adapté, l'acquisition de plusieurs plans focaux adjacents dans des cellules minces demeurerait plus complexe.

L'élastographie macroscopique est majoritairement décrite dans un régime de petites déformations autorisant une relation linéaire entre la contrainte appliquée au tissu et sa réponse (déformation et taux de déformation). La grande sensibilité de l'ERM aux petits déplacements, d'amplitude souvent inférieure d'un facteur ≈ 100 à la taille d'un pixel, garantit la validité de cette approximation d'élastographie linéaire où les propriétés mécaniques reconstruites sont indépendantes de l'amplitude des déformations locales. En revanche, la microélastographie optique en champ clair présente la particularité de quantifier les déplacements à partir d'images optiques déjà résolues spatialement. Bien que les techniques d'estimation de mouvement soient sensibles à des amplitudes de déplacements inférieures à la taille du pixel, celles-ci demeurent influencées par le ratio entre déformation et résolution spatiale. Cette caractéristique impose la recherche d'un compromis entre l'amplitude des déplacements, l'amortissement viscoélastique par le milieu et la fragilité du tissu. La microélastographie non-linéaire pourrait alors être envisagée dans la limite des grandes déformations applicables aux cellules. Des niveaux élevés de déformation ont déjà été présentés dans la littérature en particulier à travers des méthodes d'aspiration par micro-pipettes où d'importantes déformations locales, dans le canal d'aspiration de la pipette, sont imposées pour évaluer la rigidité globale de la cellule à partir de modèles rhéologiques. Ces dispositifs et autres techniques de micro-rhéologie globale ont été employées pour la caractérisation de nombreux types de cellules [**20**] mais ont une spécificité spatiale limitée voire inexistante et sont insensibles, d'un point de vue mécanique, aux contributions des structures internes à la fonction cellulaire. La microélastographie optique est une solution à cette limite et ouvre la voie à l'imagerie résolue des propriétés mécaniques de micro-structures, jusqu'alors inaccessible aux échelles spatiales et temporelles de l'ordre du micromètre et de la milliseconde, respectivement.

6.9. Conclusion

En conclusion, les travaux présentés ici constituent un incrément dans le domaine de l'élastographie harmonique à travers l'exploration d'applications multi-disciplinaires. Les résultats et limites discutés dans le cadre de chaque projet soutiennent, à leur échelle, une approche cohésive de l'imagerie des propriétés physiques des tissus biologiques.

Bibliographie

[1] Martins JR, Ning A. 4. In : Unconstrained gradient-based optimization. Cambridge University Press ; 2021. p. 77-151.

[2] Grasland-Mongrain P, Zorgani A, Nakagawa S, Bernard S, Paim LG, Fitzharris G, et al. Ultrafast imaging of cell elasticity with optical microelastography. Proceedings Of The National Academy Of Sciences. 2018 ;115(5) :861-6.

[3] Yamakoshi Y, Sato J, Sato T. Ultrasonic imaging of internal vibration of soft tissue under forced vibration. Ieee Transactions On Ultrasonics, Ferroelectrics, And Frequency Control. 1990 ;37(2) :45-53.

[4] Bercoff J, Tanter M, Fink M. Supersonic shear imaging : A new technique for soft tissue elasticity mapping. Ieee Transactions On Ultrasonics, Ferroelectrics, And Frequency Control. 2004 ;51(4) :396-409.

[5] Barr RG, Nakashima K, Amy D, Cosgrove D, Farrokh A, Schafer F, et al. Wfumb guidelines and recommendations for clinical use of ultrasound elastography : Part 2 : Breast. Ultrasound In Medicine And Biology. 2015 ;41(5) :1148-60.

[6] Yin M, Talwalkar JA, Glaser KJ, Manduca A, Grimm RC, Rossman PJ, et al. Assessment of hepatic fibrosis with magnetic resonance elastography. Clinical Gastroenterology And Hepatology. 2007 ;5(10) :1207-13.

[7] Hiscox LV, Johnson CL, McGarry MDJ, Perrins M, Littlejohn A, van Beek EJR, et al. High-resolution magnetic resonance elastography reveals differences in subcortical gray matter viscoelasticity between young and healthy older adults. Neurobiology Of Aging. 2018 ;65 :158-67.

[8] Elgeti T, Knebel F, Hättasch R, Hamm B, Braun J, Sack I. Shear-wave amplitudes measured with cardiac mr elastography for diagnosis of diastolic dysfunction. Radiology. 2014 ;271(3) :681-7.

[9] Zhu J, Miao Y, Qi L, Qu Y, He Y, Yang Q, et al. Longitudinal shear wave imaging for elasticity mapping using optical coherence elastography. Applied Physics Letters. 2017 ;110(20) :201101.

[10] Zhu J, Yu J, Qu Y, He Y, Li Y, Yang Q, et al. Coaxial excitation longitudinal shear wave measurement for quantitative elasticity assessment using phase-resolved optical coherence elastography. Optics Letters. 2018 ;43(10) :2388-91.

[11] Ambrozinski L, Song SZ, Yoon SJ, Pelivanov I, Li D, Gao L, et al. Acoustic micro-tapping for non-contact 4d imaging of tissue elasticity. Scientific Reports. 2016 ;6.

[12] Song S, Le NM, Huang Z, Shen T, Wang RK. Quantitative shear-wave optical coherence elastography with a programmable phased array ultrasound as the wave source. Optics Letters. 2015 ;40(21) :5007-10.

[13] Li H, Flé G, Bhatt M, Qu Z, Ghazavi S, Yazdani L, et al. Viscoelasticity imaging of biological tissues and single cells using shear wave propagation. Frontiers In Physics. 2021 ;9 :66-103.

[14] Patz S, Fovargue D, Schregel K, Nazari N, Palotai M, Barbone PE, et al. Imaging localized neuronal activity at fast time scales through biomechanics. Science Advances. 2019 ;5(4).

[15] Grasland-Mongrain P, Souchon R, Cartellier F, Zorgani A, Chapelon JY, Lafon C, et al. Imaging of shear waves induced by lorentz force in soft tissues. Physical Review Letters. 2014 ;113(3) :038101 1-5.

[16] Grasland-Mongrain P, Lu Y, Lesage F, Catheline S, Cloutier G. Generation of shear waves by laser in soft media in the ablative and thermoelastic regimes. Applied Physics Letters. 2016 ;109(22) :1-5.

[17] Basford AT, Basford JR, Kugel J, Ehman RL. Lorentz-force-induced motion in conductive media. Magnetic Resonance Imaging. 2005 ;23(5) :647-51.

[18] van Helvert S, Storm C, Friedl P. Mechanoreciprocity in cell migration. Nature Cell Biology. 2018 ;20(1) :8-20.

[19] Ladoux B, Mège RM. Mechanobiology of collective cell behaviours. Nature Reviews Molecular Cell Biology. 2017 ;18(12) :743-57.

[20] Wu PH, Aroush DRB, Asnacios A, Chen WC, Dokukin ME, Doss BL, et al. A comparison of methods to assess cell mechanical properties. Nature Methods. 2018 ;15(7) :491-8.

[21] Yanez LZ, Camarillo DB. Microfluidic analysis of oocyte and embryo biomechanical properties to improve outcomes in assisted reproductive technologies. Molecular Human Reproduction. 2017 ;23(4) :235-47.

[22] Ophir J, Cespedes I, Ponnekanti H, Yazdi Y, Li X. Elastography : A quantitative method for imaging the elasticicty of biological tissues. Ultrasonic Imaging. 1991 ;13(2) :111-34.

[23] D'Hooge J, Heimdal A, Jamal F, Kukulski T, Bijnens B, Rademakers F, et al. Regional strain and strain rate measurements by cardiac ultrasound : Principles, implementation and limitations. European Journal Of Echocardiography. 2000 ;1(3) :154-70.

[24] Sayseng V, Grondin J, Salgaonkar VA, Grubb CS, Basij M, Mehrmohammadi M, et al. Catheter ablation lesion visualization with intracardiac strain imaging in canines and humans. Ieee Transactions On Ultrasonics Ferroelectrics And Frequency Control. 2020 ;67(9) :1800-10.

[25] Sayseng V, Grondin J, Konofagou EE. Optimization of transmit parameters in cardiac strain imaging with full and partial aperture coherent compounding. Ieee Transactions On Ultrasonics Ferroelectrics And Frequency Control. 2018 ;65(5) :684-96.

[26] Smiseth OA, Torp H, Opdahl A, Haugaa KH, Urheim S. Myocardial strain imaging : How useful is it in clinical decision making ? European Heart Journal. 2016 ;37(15) :1196-U110.

[27] Cardinal MHR, Durand M, Chartrand-Lefebvre C, Soulez G, Tremblay C, Cloutier G, et al. Associative prediction of carotid artery plaques based on ultrasound strain imaging and cardiovascular risk factors in people living with hiv and age-matched control subjects of the chacs cohort. Journal Of Acquired Immune Deficiency Syndromes. 2022 ;91(1) :91-100.

[28] Roy Cardinal MH, Durand M, Chartrand-Lefebvre C, Fortin C, Baril JG, Trottier B, et al. Increased carotid artery wall stiffness and plaque prevalence in hiv infected patients measured with ultrasound elastography. European Radiology. 2020 ;30(6) :3178-87.

[29] Naim C, Douziech M, Therasse E, Robillard P, Giroux MF, Arsenault F, et al. Vulnerable atherosclerotic carotid plaque evaluation by ultrasound, computed tomography angiography, and magnetic resonance imaging : An overview. Canadian Association Of Radiologists Journal. 2014 ;65(3) :275-86.

[30] Kennedy KM, Ford C, Kennedy BF, Bush MB, Sampson DD. Analysis of mechanical contrast in optical coherence elastography. Journal Of Biomedical Optics. 2013 ;18(12) :121508.

[31] Kennedy BF, McLaughlin RA, Kennedy KM, Chin L, Curatolo A, Tien A, et al. Optical coherence micro-elastography : Mechanical-contrast imaging of tissue microstructure. Biomedical Optics Express. 2014 ;5(7) :2113-24.

[32] Rogowska J, Patel NA, Fujimoto JG, Brezinski ME. Optical coherence tomographic elastography technique for measuring deformation and strain of atherosclerotic tissues. Heart. 2004 ;90(5) :556-62.

[33] Chan RC, Chau AH, Karl WC, Nadkarni S, Khalil AS, Iftimia N, et al. Oct-based arterial elastography : Robust estimation exploiting tissue biomechanics. Optics Express. 2004 ;12(19) :4558-72.

[34] Chenevert TL, Skovoroda AR, O'Donnell M, Emelianov SY. Elasticity reconstructive imaging by means of stimulated echo mri. Magnetic Resonance In Medicine. 1998 ;39(3) :482-90.

[35] Steele DD, Chenevert TL, Skovoroda AR, Emelianov SY. Three-dimensional static displacement, stimulated echo nmr elasticity imaging. Physics In Medicine And Biology. 2000 ;45(6) :1633-48.

[36] Bishop J, Samani A, Sciarretta J, Plewes DB. Two-dimensional mr elastrography with linear inversion reconstruction : Methodology and noise analysis. Physics In Medicine And Biology. 2000 ;45(8) :2081-91.

[37] Plewes DB, Bishop J, Samani A, Sciarretta J. Visualization and quantification of breast cancer biomechanical properties with magnetic resonance elastography. Physics In Medicine And Biology. 2000 ;45(6) :1591-610.

[38] Krouskop T A. A pulsed doppler ultrasonic system for making noninvasive measurements of the mechanical properties of soft tissue. J Rehab Res and Dev. 1987 ;24(2) :1-8.

[39] Lerner RM, Huang SR, Parker KJ. "Sonoelasticity" images derived from ultrasound signals in mechanically vibrated tissues. Ultrasound in Medicine and Biology. 1990 ;16(3) :231-9.

[40] Parker KJ, Huang SR, Musulin RA, Lerner RM. Tissue response to mechanical vibrations for "sonoelasticity imaging". Ultrasound in Medicine and Biology. 1990 ;16(3) :241-6.

[41] Muthupillai R, Lomas DJ, Rossman PJ, Greenleaf JF, Manduca A, Ehman RL. Magnetic resonance elastography by direct visualization of propagating acoustic strain waves. Science. 1995 ;269(5232) :1854-7.

[42] Wu T, Felmlee JP, Greenleaf JF, Riederer SJ, Ehman RL. Mr imaging of shear waves generated by focused ultrasound. Magnetic Resonance In Medicine. 2000 ;43(1) :111-5.

[43] Souchon R, Salomir R, Beuf O, Milot L, Grenier D, Lyonnet D, et al. Transient mr elastography (t-mre) using ultrasound radiation force : Theory, safety, and initial experiments in vitro. Magnetic Resonance In Medicine. 2008 ;60(4) :871-81.

[44] Hofstetter LW, Odeen H, Bolster BD, Christensen DA, Payne A, Parker DL. Magnetic resonance shear wave elastography using transient acoustic radiation force excitations and sinusoidal displacement encoding. Physics In Medicine And Biology. 2021 ;66(5).

[45] Jacques SL, Kirkpatrick SJ. Acoustically modulated speckle imaging of biological tissues. Optics Letters. 1998 ;23(11) :879-81.

[46] Schmitt JM. Oct elastography : Imaging microscopic deformation and strain of tissue. Optics Express. 1998 ;3(6) :199-211.

[47] Wang S, Larin KV. Noncontact depth-resolved micro-scale corneal elastography. In : Conference On Optical Elastography And Tissue Biomechanics Ii. vol. 9327 of Proceedings of SPIE. SPIE ; 2015. p. 138-44.

[48] De Stefano VS, Ford MR, Seven I, Dupps WJ. Depth-dependent corneal biomechanical properties in normal and keratoconic subjects by optical coherence elastography. Translational Vision Science And Technology. 2020 ;9(7).

[49] Zvietcovich F, Nair A, Singh M, Aglyamov SR, Twa MD, Larin KV. Dynamic optical coherence elastography of the anterior eye : Understanding the biomechanics of the limbus. Investigative Ophthalmology And Visual Science. 2020 ;61(13).

[50] Lan GP, Gu BY, Larin KV, Twa MD. Clinical corneal optical coherence elastography measurement precision : Effect of heartbeat and respiration. Translational Vision Science And Technology. 2020 ;9(5).

[51] Jin Z, Chen SS, Dai YY, Bao CH, Ye SL, Zhou YH, et al. In vivo noninvasive measurement of spatially resolved corneal elasticity in human eyes using lamb wave optical coherence elastography. Journal Of Biophotonics. 2020 ;13(8).

[52] Zvietcovich F, Pongchalee P, Meemon P, Rolland JP, Parker KJ. Reverberant 3d optical coherence elastography maps the elasticity of individual corneal layers. Nature Communications. 2019 ;10.

[53] Wijesinghe P, Johansen NJ, Curatolo A, Sampson DD, Ganss R, Kennedy BF. Ultrahigh-resolution optical coherence elastography images cellular-scale stiffness of mouse aorta. Biophysical Journal. 2017 ;113(11) :2540-51.

[54] Qu YQ, Ma T, He YM, Yu MY, Zhu J, Miao YS, et al. Miniature probe for mapping mechanical properties of vascular lesions using acoustic radiation force optical coherence elastography. Scientific Reports. 2017 ;7.

[55] Zvietcovich F, Ge GR, Mestre H, Giannetto M, Nedergaard M, Rolland JP, et al. Longitudinal shear waves for elastic characterization of tissues in optical coherence elastography. Biomedical Optics Express. 2019 ;10(7) :3699-718.

[56] Nahas A, Tanter M, Nguyen TM, Chassot JM, Fink M, Boccara AC. From supersonic shear wave imaging to full-field optical coherence shear wave elastography. Journal Of Biomedical Optics. 2013 ;18(12).

[57] Gao GD, Yang SH, Xing D. Viscoelasticity imaging of biological tissues with phase-resolved photoacoustic measurement. Optics Letters. 2011 ;36(17) :3341-3.

[58] Wadamori N. Non-restrained measurement of young's modulus for soft tissue using a photoacoustic technique. Applied Physics Letters. 2014 ;105(10) :103707.

[59] Wang Q, Shi Y, Yang F, Yang S. Quantitative photoacoustic elasticity and viscosity imaging for cirrhosis detection. Applied Physics Letters. 2018 ;112(21) :211902.

[60] Hai P, Zhou Y, Liang J, Li C, Wang LV. Photoacoustic tomography of vascular compliance in humans. Journal Of Biomedical Optics. 2015 ;20(12) :126008.

[61] Sinkus R, Tanter M, Xydeas T, Catheline S, Bercoff J, Fink M. Viscoelastic shear properties of in vivo breast lesions measured by mr elastography. Magnetic Resonance Imaging. 2005 ;23(2) :159-65.

[62] Klatt D, Johnson CL, Magin RL. Simultaneous, multidirectional acquisition of displacement fields in magnetic resonance elastography of the in vivo human brain. Journal Of Magnetic Resonance Imaging. 2015 ;42(2) :297-304.

[63] Green MA, Bilston LE, Sinkus R. In vivo brain viscoelastic properties measured by magnetic resonance elastography. Nmr In Biomedicine. 2008 ;21(7) :755-64.

[64] Zhang J, Green MA, Sinkus R, Bilston LE. Viscoelastic properties of human cerebellum using magnetic resonance elastography. Journal Of Biomechanics. 2011 ;44(10) :1909-13.

[65] Clayton EH, Garbow JR, Bayly PV. Frequency-dependent viscoelastic parameters of mouse brain tissue estimated by mr elastography. Physics In Medicine And Biology. 2011 ;56(8) :2391-406.

[66] Garteiser P, Sahebjavaher RS, Ter Beek LC, Salcudean S, Vilgrain V, Van Beers BE, et al. Rapid acquisition of multifrequency, multislice and multidirectional mr elastography data with a fractionally encoded gradient echo sequence. Nmr In Biomedicine. 2013 ;26(10) :1326-35.

[67] Herzka DA, Kotys MS, Sinkus R, Pettigrew RI, Gharib AM. Magnetic resonance elastography in the liver at 3 tesla using a second harmonic approach. Magnetic Resonance In Medicine. 2009 ;62(2) :284-91.

[68] Sinkus R, Tanter M, Catheline S, Lorenzen J, Kuhl C, Sondermann E, et al. Imaging anisotropic and viscous properties of breast tissue by magnetic resonance-elastography. Magnetic Resonance In Medicine. 2005 ;53(2) :372-87.

[69] Reiter R, Majumdar S, Kearney S, Kajdacsy-Balla A, Macias V, Crivellaro S, et al. Prostate cancer assessment using mr elastography of fresh prostatectomy specimens at 9.4 t. Magnetic Resonance In Medicine. 2020 ;84(1) :396-404.

[70] Fovargue D, Kozerke S, Sinkus R, Nordsletten D. Robust mr elastography stiffness quantification using a localized divergence free finite element reconstruction. Medical Image Analysis. 2018 ;44 :126-42.

[71] Oliphant TE, Manduca A, Ehman RL, Greenleaf JF. Complex-valued stiffness reconstruction for magnetic resonance elastography by algebraic inversion of the differential equation. Magnetic Resonance In Medicine. 2001 ;45(2) :299-310.

[72] Manduca A, Oliphant TE, Dresner MA, Mahowald JL, Kruse SA, Amromin E, et al. Magnetic resonance elastography : Non-invasive mapping of tissue elasticity. Medical Image Analysis. 2001 ;5(4) :237-54.

[73] Manduca A, Lake DS, Kruse SA, Ehman RL. Spatio-temporal directional filtering for improved inversion of mr elastography images. Medical Image Analysis. 2003 ;7(4) :465-73.

[74] Klatt D, Hamhaber U, Asbach P, Braun J, Sack I. Noninvasive assessment of the rheological behavior of human organs using multifrequency mr elastography : A study of brain and liver viscoelasticity. Physics In Medicine And Biology. 2007 ;52(24) :7281-94.

[75] Asbach P, Klatt D, Hamhaber U, Braun J, Somasundaram R, Hamm B, et al. Assessment of liver viscoelasticity using multifrequency mr elastography. Magnetic Resonance In Medicine. 2008 ;60(2) :373-9.

[76] Streitberger KJ, Sack I, Krefting D, Pfüller C, Braun J, Paul F, et al. Brain viscoelasticity alteration in chronic-progressive multiple sclerosis. Plos One. 2012 ;7(1) :e29888.

[77] Sack I, Rump J, Elgeti T, Samani A, Braun J. Mr elastography of the human heart : Noninvasive assessment of myocardial elasticity changes by shear wave amplitude variations. Magnetic Resonance In Medicine. 2009 ;61(3) :668-77.

[78] Wuerfel J, Paul F, Beierbach B, Hamhaber U, Klatt D, Papazoglou S, et al. Mr-elastography reveals degradation of tissue integrity in multiple sclerosis. Neuroimage. 2010 ;49(3) :2520-5.

[79] Sack I, Streitberger KJ, Krefting D, Paul F, Braun J. The influence of physiological aging and atrophy on brain viscoelastic properties in humans. Plos One. 2011 ;6(9) :e23451.

[80] Boulet T, Kelso ML, Othman SF. Microscopic magnetic resonance elastography of traumatic brain injury model. Journal Of Neuroscience Methods. 2011 ;201(2) :296-306.

[81] Hirsch S, Guo J, Reiter R, Papazoglou S, Kroencke T, Braun J, et al. Mr elastography of the liver and the spleen using a piezoelectric driver, single-shot wave-field acquisition, and multifrequency dual parameter reconstruction. Magnetic Resonance In Medicine. 2014 ;71(1) :267-77.

[82] Dittmann F, Hirsch S, Tzschätzsch H, Guo J, Braun J, Sack I. In vivo wideband multifrequency mr elastography of the human brain and liver. Magnetic Resonance In Medicine. 2016 ;76(4) :1116-26.

[83] Tzschätzsch H, Guo J, Dittmann F, Hirsch S, Barnhill E, Jöhrens K, et al. Tomoelastography by multifrequency wave number recovery from time-harmonic propagating shear waves. Medical Image Analysis. 2016 ;30 :1-10.

[84] Meyer T, Garcia SM, Tzschatzsch H, Herthum H, Shahryari M, Stencel L, et al. Comparison of inversion methods in mr elastography : An open-access pipeline for processing multifrequency shear-wave data and demonstration in a phantom, human kidneys, and brain. Magnetic Resonance In Medicine. 2022 ;88(4) :1840-50.

[85] Aldoj N, Biavati F, Dewey M, Hennemuth A, Asbach P, Sack I. Fully automated quantification of in vivo viscoelasticity of prostate zones using magnetic resonance elastography with dense u-net segmentation. Scientific Reports. 2022 ;12(1).

[86] Lilaj L, Herthum H, Meyer T, Shahryari M, Bertalan G, Caiazzo A, et al. Inversion-recovery mr elastography of the human brain for improved stiffness quantification near fluid-solid boundaries. Magnetic Resonance In Medicine. 2021 ;86(5) :2552-61.

[87] Bertalan G, Guo J, Tzschatzsch H, Klein C, Barnhill E, Sack I, et al. Fast tomoelastography of the mouse brain by multifrequency single-shot mr elastography. Magnetic Resonance In Medicine. 2019 ;81(4) :2676-87.

[88] Westin CF. A tensor framework for multidimensional signal processing [Thesis] ; 1994.

[89] Knutsson H, Westin C, Granlund G. Local multiscale frequency and bandwidth estimation. In : Proceedings Of 1st International Conference On Image Processing. vol. 1. IEEE Computer Society ; 1994. p. 36-40.

[90] Braun J, Buntkowsky G, Bernarding J, Tolxdorff T, Sack I. Simulation and analysis of magnetic resonance elastography wave images using coupled harmonic oscillators and gaussian local frequency estimation. Magnetic Resonance Imaging. 2001 ;19(5) :703-13.

[91] McGee KP, Lake D, Mariappan Y, Hubmayr RD, Manduca A, Ansell K, et al. Calculation of shear stiffness in noise dominated magnetic resonance elastography data based on principal frequency estimation. Physics In Medicine And Biology. 2011 ;56(14) :4291-309.

[92] Oliphant TE. Direct methods for dynamic elastography reconstruction : Optimal inversion of the interior helmholtz problem [Thesis] ; 2001.

[93] Mariappan YK, Glaser KJ, Hubmayr RD, Manduca A, Ehman RL, McGee KP. Mr elastography of human lung parenchyma : Technical development, theoretical modeling and in vivo validation. Journal Of Magnetic Resonance Imaging. 2011 ;33(6) :1351-61.

[94] Venkatesh SK, Yin M, Glockner JF, Takahashi N, Araoz PA, Talwalkar JA, et al. Mr elastography of liver tumors : Preliminary results. American Journal Of Roentgenology. 2008 ;190(6) :1534-40.

[95] Yin M, Kolipaka A, Woodrum DA, Glaser KJ, Romano AJ, Manduca A, et al. Hepatic and splenic stiffness augmentation assessed with mr elastography in an in vivo porcine portal hypertension model. Journal Of Magnetic Resonance Imaging. 2013 ;38(4) :809-15.

[96] Fattahi N, Arani A, Perry A, Meyer F, Manduca A, Glaser K, et al. Mr elastography demonstrates increased brain stiffness in normal pressure hydrocephalus. American Journal Of Neuroradiology. 2016 ;37(3) :462-7.

[97] Clayton EH, Genin GM, Bayly PV. Transmission, attenuation and reflection of shear waves in the human brain. Journal Of The Royal Society Interface. 2012 ;9(76) :2899-910.

[98] Kolipaka A. 7. In : Constantinides C, editor. Cardiac magnetic resonance elastography. Cham : Springer International Publishing ; 2018. p. 237-59.

[99] Yin Z, Magin RL, Klatt D. Simultaneous mr elastography and diffusion acquisitions : Diffusion-mre (dmre). Magnetic Resonance In Medicine. 2014 ;71(5) :1682-8.

[100] Barnhill E, Davies PJ, Ariyurek C, Fehlner A, Braun J, Sack I. Heterogeneous multifrequency direct inversion (hmdi) for magnetic resonance elastography with application to a clinical brain exam. Medical Image Analysis. 2018 ;46 :180-8.

[101] Sanchez CA, Drapaca CS, Sivaloganathan S, Vrscay ER. Elastography of biological tissue : Direct inversion methods that allow for local shear modulus variations. In : Campilho A, Kamel M, editors. Image Analysis And Recognition. Iciar 2010. vol. 6112. Springer, Berlin, Heidelberg ; 2010. p. 195-206.

[102] Honarvar M, Sahebjavaher R, Sinkus R, Rohling R, Salcudean SE. Curl-based finite element reconstruction of the shear modulus without assuming local homogeneity : Time harmonic case. Ieee Transactions On Medical Imaging. 2013 ;32(12) :2189-99.

[103] Honarvar M, Sahebjavaher RS, Salcudean SE, Rohling R. Sparsity regularization in dynamic elastography. Physics In Medicine And Biology. 2012 ;57(19) :5909-27.

[104] Honarvar M, Rohling R, Salcudean SE. A comparison of direct and iterative finite element inversion techniques in dynamic elastography. Physics In Medicine And Biology. 2016 ;61(8) :3026-48.

[105] Zienkiewicz OC, Taylor RL. 12. In : Incompressible materials, mixed methods and other procedures of solution. Butterworth-Heinemann ; 2000. p. 307-45.

[106] Catheline S, Souchon R, Rupin M, Brum J, Dinh AH, Chapelon JY. Tomography from diffuse waves : Passive shear wave imaging using low frame rate scanners. Applied Physics Letters. 2013 ;103(1).

[107] Fink M. Time reversal of ultrasonic fields. I. Basic principles. Ieee Transactions On Ultrasonics Ferroelectrics And Frequency Control. 1992 ;39(5) :555-66.

[108] Brum J, Benech N, Gallot T, Negreira C. Shear wave elastography based on noise correlation and time reversal. Frontiers In Physics. 2021 ;9 :617445.1-9.

[109] Gallot T, Catheline S, Roux P, Brum J, Benech N, Negreira C. Passive elastography : Shear-wave tomography from physiological-noise correlation in soft tissues. Ieee Transactions On Ultrasonics, Ferroelectrics, And Frequency Control. 2011 ;58(6) :1122-6.

[110] Brum J, Benech N, Negreira C, Catheline S, Gallot T, Ieee. Quantitative imaging using time reversal elastography : A feasibility study. In : Ieee International Ultrasonics Symposium (Ius). IEEE International Ultrasonics Symposium ; 2011. p. 1160-2.

[111] Zorgani A, Souchon R, Dinh AH, Chapelon JY, Ménager JM, Lounis S, et al. Brain palpation from physiological vibrations using mri. Proceedings Of The National Academy Of Sciences. 2015 ;112(42) :12917-21.

[112] Kallel F, Bertrand M. Tissue elasticity reconstruction using linear perturbation method. Ieee Transactions On Medical Imaging. 1996 ;15(3) :299-313.

[113] Oberai AA, Gokhale NH, Feijóo GR. Solution of inverse problems in elasticity imaging using the adjoint method. Inverse Problems. 2003 ;19(2) :297-313.

[114] Samani A, Bishop J, Plewes DB. A constrained modulus reconstruction technique for breast cancer assessment. Ieee Transactions On Medical Imaging. 2001 ;20(9) :877-85.

[115] Van Houten EEW, Miga MI, Weaver JB, Kennedy FE, Paulsen KD. Three-dimensional subzone-based reconstruction algorithm for mr elastography. Magnetic Resonance In Medicine. 2001 ;45(5) :827-37.

[116] Van Houten EEW, Paulsen KD, Miga MI, Kennedy FE, Weaver JB. An overlapping subzone technique for mr-based elastic property reconstruction. Magnetic Resonance In Medicine. 1999 ;42(4) :779-86.

[117] McGarry MDJ. Rayleigh damped magnetic resonance elastography [Thesis] ; 2008.

[118] Hiscox LV, McGarry MDJ, Schwarb H, Van Houten EEW, Pohlig RT, Roberts N, et al. Standard-space atlas of the viscoelastic properties of the human brain. Human Brain Mapping. 2020 ;41(18) :5282-300.

[119] McGarry M, Johnson CL, Sutton BP, Van Houten EEW, Georgiadis JG, Weaver JB, et al. Including spatial information in nonlinear inversion mr elastography using soft prior regularization. Ieee Transactions On Medical Imaging. 2013 ;32(10) :1901-9.

[120] Golnabi A, Meaney P, Geimer S, Paulsen K. Comparison of no-prior and soft-prior regularization in biomedical microwave imaging. Journal Of Medical Physics. 2011 ;36(3) :159-70.

[121] Golnabi AH, Meaney PM, Paulsen KD. Tomographic microwave imaging with incorporated prior spatial information. Ieee Transactions On Microwave Theory And Techniques. 2013 ;61(5) :2129-36.

[122] Tan L, McGarry MDJ, Van Houten EEW, Ji M, Solamen L, Weaver JB, et al. Gradient-based optimization for poroelastic and viscoelastic mr elastography. Ieee Transactions On Medical Imaging. 2017 ;36(1) :236-50.

[123] Shewchuk JR. An introduction to the conjugate gradient method without the agonizing pain ; 1994.

[124] Nocedal J, Wright SJ. 5. In : Conjugate gradient methods. New York : NY : Springer New York ; 2006. p. 101-33.

[125] Goenezen S, Barbone P, Oberai AA. Solution of the nonlinear elasticity imaging inverse problem : The incompressible case. Computer Methods In Applied Mechanics And Engineering. 2011 ;200(13-16) :1406-20.

[126] Gokhale NH, Barbone PE, Oberai AA. Solution of the nonlinear elasticity imaging inverse problem : The compressible case. Inverse Problems. 2008 ;24(4).

[127] Liew HL, Pinsky PM. Recovery of shear modulus in elastography using an ajoint method with b-spline representation. Finite Elements In Analysis And Design. 2005 ;41(7-8) :778-99.

[128] Oberai AA, Gokhale NH, Doyley MM, Bamber JC. Evaluation of the adjoint equation based algorithm for elasticity imaging. Physics In Medicine And Biology. 2004 ;49(13) :2955-74.

[129] Friedrich-Rust M, Poynard T, Castera L. Critical comparison of elastography methods to assess chronic liver disease. Nature Reviews Gastroenterology And Hepatology. 2016 ;13(7) :402-11.

[130] Hiscox LV, Johnson CL, Barnhill E, McGarry MDJ, Huston J, Van Beek EJR, et al. Magnetic resonance elastography (mre) of the human brain : Technique, findings and clinical applications. Physics In Medicine And Biology. 2016 ;61(24) :R401-37.

[131] Mousavi SR, Rivaz H, Sadeghi-Naini A, Czarnota GJ, Samani A. Breast ultrasound elastography using full inversion-based elastic modulus reconstruction. Ieee Transactions On Computational Imaging. 2017 ;3(4) :774-82.

[132] Petitclerc L, Sebastiani G, Gilbert G, Cloutier G, Tang A. Liver fibrosis : Review of current imaging and mri quantification techniques. Journal Of Magnetic Resonance Imaging. 2017 ;45(5) :1276-95.

[133] Lifshitz EM, Kosevich AM, Pitaevskii LP. Elastic Waves. In : Elastic waves. Oxford : Butterworth-Heinemann ; 1986. p. 87-107.

[134] Kennedy BF, Kennedy KM, Sampson DD. A review of optical coherence elastography : Fundamentals, techniques and prospects. Ieee Journal On Selected Topics In Quantum Electronics. 2014 ;20(2) :272-88.

[135] Gennisson JL, Deffieux T, Fink M, Tanter M. Ultrasound elastography : Principles and techniques. Diagnostic And Interventional Imaging. 2013 ;94(5) :487-95.

[136] Manduca A, Muthupillai R, Rossman PJ, Greenleaf JF, Ehman RL. Local wavelength estimation for magnetic resonance elastography. In : Proceedings Of 3rd Ieee International Conference On Image Processing. vol. 3. IEEE ; 1996. p. 527-30.

[137] Venkatesh SK. Clinical applications of liver magnetic resonance elastography : Chronic liver disease. In : Venkatesh SK, Ehman RL, editors. Clinical applications of liver magnetic resonance elastography : Chronic liver disease. New York, NY : Springer New York ; 2014. p. 39-60.

[138] Anderson AT, Van Houten EEW, McGarry MDJ, Paulsen KD, Holtrop JL, Sutton BP, et al. Observation of direction-dependent mechanical properties in the human brain with multi-excitation mr elastography. Journal Of The Mechanical Behavior Of Biomedical Materials. 2016 ;59 :538-46.

[139] Kolipaka A, McGee KP, Araoz PA, Glaser KJ, Manduca A, Romano AJ, et al. Mr elastography as a method for the assessment of myocardial stiffness : Comparison with an established pressure–volume model in a left ventricular model of the heart. Magnetic Resonance In Medicine. 2009 ;62(1) :135-40.

[140] Johnson CL, Holtrop JL, McGarry MDJ, Weaver JB, Paulsen KD, Georgiadis JG, et al. 3d multislab, multishot acquisition for fast, whole-brain mr elastography with high signal-to-noise efficiency. Magnetic Resonance In Medicine. 2014 ;71(2) :477-85.

[141] Guo J, Hirsch S, Fehlner A, Papazoglou S, Scheel M, Braun J, et al. Towards an elastographic atlas of brain anatomy. Plos One. 2013 ;8(8) :e71807.

[142] Runge JH, Hoelzl SH, Sudakova J, Dokumaci AS, Nelissen JL, Guenthner C, et al. A novel magnetic resonance elastography transducer concept based on a rotational eccentric mass : Preliminary experiences with the gravitational transducer. Physics In Medicine And Biology. 2019 ;64(4) :045007.

[143] Weaver JB, Pattison AJ, McGarry MD, Perreard IM, Swienckowski JG, Eskey CJ, et al. Brain mechanical property measurement using mre with intrinsic activation. Physics In Medicine And Biology. 2012 ;57(22) :7275-87.

[144] Hirsch S, Klatt D, Freimann F, Scheel M, Braun J, Sack I. In vivo measurement of volumetric strain in the human brain induced by arterial pulsation and harmonic waves. Magnetic Resonance In Medicine. 2013 ;70(3) :671-83.

[145] Solamen LM, McGarry MDJ, Fried J, Weaver JB, Lollis SS, Paulsen KD. Poroelastic mechanical properties of the brain tissue of normal pressure hydrocephalus patients during lumbar drain treatment using intrinsic actuation mr elastography. Academic Radiology. 2021 ;28(4) :457-66.

[146] Grasland-Mongrain P, Miller-Jolicoeur E, Tang A, Catheline S, Cloutier G. Contactless remote induction of shear waves in soft tissues using a transcranial magnetic stimulation device. Physics In Medicine And Biology. 2016 ;61(6) :2582-93.

[147] Sun Z, Giammarinaro B, Birer A, Liu G, Catheline S. Shear wave generation by remotely stimulating aluminum patches with a transient magnetic field and its preliminary application in elastography. Ieee Transactions On Biomedical Engineering. 2020 :1.

[148] Griffiths DJ. Introduction to electrodynamics. 4th ed. Cambridge : Cambridge University Press ; 2017.

[149] Venkatesh SK, Yin M, Ehman RL. Magnetic resonance elastography of liver : Technique, analysis, and clinical applications. Journal Of Magnetic Resonance Imaging. 2013 ;37(3) :544-55.

[150] Hirsch S, Braun J, Sack I. Magnetic resonance elastography : Physical background and medical applications. John Wiley and Sons ; 2017.

[151] Royer D, Dieulesaint E. Elastic waves in solids i : Free and guided propagation. Springer Science and Business Media ; 1999.

[152] Doyley MM, Perreard I, Patterson AJ, Weaver JB, Paulsen KM. The performance of steady-state harmonic magnetic resonance elastography when applied to viscoelastic materials. Medical Physics. 2010 ;37(8) :3970-9.

[153] McIlvain G, Ganji E, Cooper C, Killian ML, Ogunnaike BA, Johnson CL. Reliable preparation of agarose phantoms for use in quantitative magnetic resonance elastography. Journal Of The Mechanical Behavior Of Biomedical Materials. 2019 ;97 :65-73.

[154] Garcia D. Robust smoothing of gridded data in one and higher dimensions with missing values. Computational Statistics And Data Analysis. 2010 ;54(4) :1167-78.

[155] Garcia D. A fast all-in-one method for automated post-processing of piv data. Experiments In Fluids. 2011 ;50(5) :1247-59.

[156] Herráez MA, Burton DR, Lalor MJ, Gdeisat MA. Fast two-dimensional phase-unwrapping algorithm based on sorting by reliability following a noncontinuous path. Applied Optics. 2002 ;41(35) :7437-44.

[157] Ghiglia DC, Romero LA. Robust two-dimensional weighted and unweighted phase unwrapping that uses fast transforms and iterative methods. Journal Of The Optical Society Of America A. 1994 ;11(1) :107-17.

[158] Firman. 2d weighted phase unwrapping. MATLAB Central File Exchange. 2016.

[159] Frohlich F. Noninvasive Brain Stimulation. In : Frohlich F, editor. Chapter 15 - noninvasive brain stimulation. San Diego : Academic Press ; 2016. p. 197-210.

[160] Aki K, Richards PG. Elastic waves from a point dislocation source. In : Elastic waves from a point dislocation source. University Science Books ; 2002. p. 63-117.

[161] Chatelin S, Charpentier I, Corbin N, Meylheuc L, Vappou J. An automatic differentiation-based gradient method for inversion of the shear wave equation in magnetic resonance elastography : Specific application in fibrous soft tissues. Physics In Medicine And Biology. 2016 ;61(13) :5000-19.

[162] Testu J, McGarry MDJ, Dittmann F, Weaver JB, Paulsen KD, Sack I, et al. Viscoelastic power law parameters of in vivo human brain estimated by mr elastography. Journal Of The Mechanical Behavior Of Biomedical Materials. 2017 ;74 :333-41.

[163] Seo JK, Woo EJ. Magnetic resonance electrical impedance tomography (mreit). Siam Review. 2011 ;53(1) :40-68.

[164] Sajib SZK, Lee MB, Kim HJ, Woo EJ, Kwon OI. Extracellular total electrolyte concentration imaging for electrical brain stimulation (ebs). Scientific Reports. 2018 ;8(1) :290.

[165] Bland NS, Sale MV. Current challenges : The ups and downs of tacs. Experimental Brain Research. 2019 ;237(12) :3071-88.

[166] Bächinger M, Zerbi V, Moisa M, Polania R, Liu Q, Mantini D, et al. Concurrent tacs-fmri reveals causal influence of power synchronized neural activity on resting state fmri connectivity. The Journal Of Neuroscience. 2017 ;37(18) :4766.

[167] Millward JM, Guo J, Berndt D, Braun J, Sack I, Infante-Duarte C. Tissue structure and inflammatory processes shape viscoelastic properties of the mouse brain. Nmr In Biomedicine. 2015 ;28(7) :831-9.

[168] Lee S, Lee C, Park J, Im CH. Individually customized transcranial temporal interference stimulation for focused modulation of deep brain structures : A simulation study with different head models. Scientific Reports. 2020 ;10(1) :11730 1-11.

[169] Sajib SZK, Katoch N, Kim HJ, Kwon OI, Woo EJ. Software toolbox for low-frequency conductivity and current density imaging using mri. Ieee Transactions On Biomedical Engineering. 2017 ;64(11) :2505-14.

[170] Oh SH, Lee BI, Woo EJ, Lee SY, Cho MH, Kwon O, et al. Conductivity and current density image reconstruction using harmonic b-z algorithm in magnetic resonance electrical impedance tomography. Physics In Medicine And Biology. 2003 ;48(19) :3101-16.

[171] Seo JK, Jeon K, Lee CO, Woo EJ. Non-iterative harmonic b-z algorithm in mreit. Inverse Problems. 2011 ;27(8).

[172] Seo JK, Woo EJ. Magnetic Resonance Electrical Impedance Tomography. In : Magnetic resonance electrical impedance tomography. John Wiley and Sons ; 2013. p. 295-334.

[173] Seo JK, Woo EJ, Katscher U, Wang Y. Electro-magnetic tissue properties mri. vol. Volume 1 of Modelling and simulation in medical imaging. IMPERIAL COLLEGE PRESS ; 2013.

[174] Kim HJ, Jeong WC, Sajib SZK, Kim MO, Kwon OI, Woo EJ, et al. Simultaneous imaging of dual-frequency electrical conductivity using a combination of mreit and mrept. Magnetic Resonance In Medicine. 2014 ;71(1) :200-8.

[175] Alekseichuk I, Mantell K, Shirinpour S, Opitz A. Comparative modeling of transcranial magnetic and electric stimulation in mouse, monkey, and human. Neuroimage. 2019 ;194 :136-48.

[176] Silvanto J, Cowey A, Lavie N, Walsh V. Striate cortex (v1) activity gates awareness of motion. Nature Neuroscience. 2005 ;8(2) :143-4.

[177] Plewnia C, Reimold M, Najib A, Brehm B, Reischl G, Plontke SK, et al. Dose-dependent attenuation of auditory phantom perception (tinnitus) by pet-guided repetitive transcranial magnetic stimulation. Human Brain Mapping. 2007 ;28(3) :238-46.

[178] Muellbacher W, Ziemann U, Wissel J, Dang N, Kofler M, Facchini S, et al. Early consolidation in human primary motor cortex. Nature. 2002 ;415(6872) :640-4.

[179] Polania R, Nitsche MA, Ruff CC. Studying and modifying brain function with non-invasive brain stimulation. Nature Neuroscience. 2018 ;21(2) :174-87.

[180] Reis J, Schambra HM, Cohen LG, Buch ER, Fritsch B, Zarahn E, et al. Noninvasive cortical stimulation enhances motor skill acquisition over multiple days through an effect on consolidation. Proceedings Of The National Academy Of Sciences Of The United States Of America. 2009 ;106(5) :1590-5.

[181] Bolognini N, Rossetti A, Maravita A, Miniussi C. Seeing touch in the somatosensory cortex : Atms study of the visual perception of touch. Human Brain Mapping. 2011 ;32(12) :2104-14.

[182] Tarapore PE, Findlay AM, Honma SM, Mizuiri D, Houde JF, Berger MS, et al. Language mapping with navigated repetitive tms : Proof of technique and validation. Neuroimage. 2013 ;82 :260-72.

[183] Holland R, Leff AP, Josephs O, Galea JM, Desikan M, Price CJ, et al. Speech facilitation by left inferior frontal cortex stimulation. Current Biology. 2011 ;21(16) :1403-7.

[184] Sparing R, Thimm M, Hesse MD, Kuest J, Karbe H, Fink GR. Bidirectional alterations of interhemispheric parietal balance by non-invasive cortical stimulation. Brain. 2009 ;132 :3011-20.

[185] Ashbridge E, Walsh V, Cowey A. Temporal aspects of visual search studied by transcranial magnetic stimulation. Neuropsychologia. 1997 ;35(8) :1121-31.

[186] Oliveri M, Turriziani P, Carlesimo GA, Koch G, Tomaiuolo F, Panella M, et al. Parieto-frontal interactions in visual-object and visual-spatial working memory : Evidence from transcranial magnetic stimulation. Cerebral Cortex. 2001 ;11(7) :606-18.

[187] Wang JX, Rogers LM, Gross EZ, Ryals AJ, Dokucu ME, Brandstatt KL, et al. Targeted enhancement of cortical-hippocampal brain networks and associative memory. Science. 2014 ;345(6200) :1054-7.

[188] Kadosh RC, Soskic S, Iuculano T, Kanai R, Walsh V. Modulating neuronal activity produces specific and long-lasting changes in numerical competence. Current Biology. 2010 ;20(22) :2016-20.

[189] Santarnecchi E, Polizzotto NR, Godone M, Giovannelli F, Feurra M, Matzen L, et al. Frequency-dependent enhancement of fluid intelligence induced by transcranial oscillatory potentials. Current Biology. 2013 ;23(15) :1449-53.

[190] Philiastides MG, Auksztulewicz R, Heekeren HR, Blankenburg F. Causal role of dorsolateral prefrontal cortex in human perceptual decision making. Current Biology. 2011 ;21(11) :980-3.

[191] Beharelle AR, Polania R, Hare TA, Ruff CC. Transcranial stimulation over frontopolar cortex elucidates the choice attributes and neural mechanisms used to resolve exploration-exploitation trade-offs. Journal Of Neuroscience. 2015 ;35(43) :14544-56.

[192] Marechal MA, Cohn A, Ugazio G, Ruff CC. Increasing honesty in humans with noninvasive brain stimulation. Proceedings Of The National Academy Of Sciences Of The United States Of America. 2017 ;114(17) :4360-4.

[193] Strang S, Gross J, Schuhmann T, Riedl A, Weber B, Sack AT. Be nice if you have to - the neurobiological roots of strategic fairness. Social Cognitive And Affective Neuroscience. 2015 ;10(6) :790-6.

[194] Ruff CC, Ugazio G, Fehr E. Changing social norm compliance with noninvasive brain stimulation. Science. 2013 ;342(6157) :482-4.

[195] Knoch D, Pascual-Leone A, Meyer K, Treyer V, Fehr E. Diminishing reciprocal fairness by disrupting the right prefrontal cortex. Science. 2006 ;314(5800) :829-32.

[196] Buss SS, Fried PJ, Pascual-Leone A. Therapeutic noninvasive brain stimulation in alzheimer's disease and related dementias. Current Opinion in Neurology. 2019 ;32(2) :292-304.

[197] Gonsalvez I, Baror R, Fried P, Santarnecchi E, Pascual-Leone A. Therapeutic noninvasive brain stimulation in alzheimer's disease. Current Alzheimer Research. 2017 ;14(4) :362-76.

[198] Menardi A, Rossi S, Koch G, Hampel H, Vergallo A, Nitsche MA, et al. Toward noninvasive brain stimulation 2.0 in alzheimer's disease. Ageing Research Reviews. 2022 ;75.

[199] Brechet L, Yu WT, Biagi MC, Ruffini G, Gagnon M, Manor B, et al. Patient-tailored, home-based non-invasive brain stimulation for memory deficits in dementia due to alzheimer's disease. Frontiers in Neurology. 2021 ;12.

[200] Hsu WY, Ku YX, Zanto TP, Gazzaley A. Effects of noninvasive brain stimulation on cognitive function in healthy aging and alzheimer's disease : A systematic review and meta-analysis. Neurobiology of Aging. 2015 ;36(8) :2348-59.

[201] Madrid J, Benninger DH. Non-invasive brain stimulation for parkinson's disease : Clinical evidence, latest concepts and future goals : A systematic review. Journal of Neuroscience Methods. 2021 ;347.

[202] Rektorova I, Anderkova L. Noninvasive brain stimulation and implications for nonmotor symptoms in parkinson's disease. Nonmotor Parkinson's : the Hidden Face - Management and the Hidden Face of Related Disorders. 2017 ;134 :1091-110.

[203] Zheng HB, Liu B, Shen J, Xie F, Ji QM, Zhu XY. Non-invasive brain stimulation for treating psychiatric symptoms in parkinson's disease : A systematic review and meta-analysis. Journal of Clinical Neuroscience. 2022 ;106 :83-90.

[204] Ni R, Yuan Y, Yang L, Meng QJ, Zhu Y, Zhong YY, et al. Novel non-invasive transcranial electrical stimulation for parkinson's disease. Frontiers in Aging Neuroscience. 2022 ;14.

[205] Cosentino G, Todisco M, Blandini F. In : Quartarone A, Ghilardi MF, Boller F, editors. Chapter 12 - noninvasive neuromodulation in parkinson's disease : Neuroplasticity implication and therapeutic perspectives. vol. 184. Elsevier ; 2022. p. 185-98.

[206] Datta A, Bansal V, Diaz J, Patel J, Reato D, Bikson M. Gyri-precise head model of transcranial direct current stimulation : Improved spatial focality using a ring electrode versus conventional rectangular pad. Brain Stimulation. 2009 ;2(4) :201-7.

[207] Grossman N, Bono D, Dedic N, Kodandaramaiah SB, Rudenko A, Suk HJ, et al. Noninvasive deep brain stimulation via temporally interfering electric fields. Cell. 2017 ;169(6) :1029-41.e16.

[208] di Biase L, Falato E, Di Lazzaro V. Transcranial focused ultrasound (tfus) and transcranial unfocused ultrasound (tus) neuromodulation : From theoretical principles to stimulation practices. Frontiers In Neurology. 2019 ;10.

[209] Sajib SZK, Sadleir R. Magnetic Resonance Electrical Impedance Tomography. In : Sadleir R, Minhas AS, editors. Magnetic resonance electrical impedance tomography. Cham : Springer International Publishing ; 2022. p. 157-83.

[210] Eroglu HH, Puonti O, Goksu C, Gregersen F, Siebner HR, Hanson LG, et al. On the reconstruction of magnetic resonance current density images of the human brain : Pitfalls and perspectives. Neuroimage. 2021 ;243.

[211] Goksu C, Hanson LG, Siebner HR, Ehses P, Scheffler K, Thielscher A. Human in-vivo brain magnetic resonance current density imaging (mrcdi). Neuroimage. 2018 ;171 :26-39.

[212] Goksu C, Scheffler K, Ehses P, Hanson LG, Thielscher A. Sensitivity analysis of magnetic field measurements for magnetic resonance electrical impedance tomography (mreit). Magnetic Resonance In Medicine. 2018 ;79(2) :748-60.

[213] Forouhandehpour R, Bernier M, Gilbert G, Butler R, Whittingstall K, Van Houten E. Cerebral stiffness changes during visual stimulation : Differential physiological mechanisms characterized by opposing mechanical effects. Neuroimage : Reports. 2021 ;1(2) :100014.

[214] Delgorio PL, Hiscox LV, Daugherty AM, Sanjana F, McIlvain G, Pohlig RT, et al. Structure-function dissociations of human hippocampal subfield stiffness and memory performance. Journal Of Neuroscience. 2022 ;42(4) :7957-68.

[215] Daugherty AM, Schwarb HD, McGarry MDJ, Johnson CL, Cohen NJ. Magnetic resonance elastography of human hippocampal subfields : Ca3-dentate gyrus viscoelasticity predicts relational memory accuracy. Journal Of Cognitive Neuroscience. 2020 ;32(9) :1704-13.

[216] Hiscox LV, Johnson CL, McGarry MDJ, Schwarb H, van Beek EJR, Roberts N, et al. Hippocampal viscoelasticity and episodic memory performance in healthy older adults examined with magnetic resonance elastography. Brain Imaging And Behavior. 2020 ;14(1) :175-85.

[217] Schwarb H, Johnson CL, Daugherty AM, Hillman CH, Kramer AF, Cohen NJ, et al. Aerobic fitness, hippocampal viscoelasticity, and relational memory performance. Neuroimage. 2017 ;153 :179-88.

[218] McIlvain G, Tracy JB, Chaze CA, Petersen DA, Villermaux GM, Wright HG, et al. Brain stiffness relates to dynamic balance reactions in children with cerebral palsy. Journal Of Child Neurology. 2020 ;35(7) :463-71.

[219] Dogdas B, Stout D, Chatziioannou AF, Leahy RM. Digimouse : A 3d whole body mouse atlas from ct and cryosection data. Physics In Medicine And Biology. 2007 ;52(3) :577-87.

[220] Chan E, Kovacevic N, Ho SKY, Henkelman RM, Henderson JT. Development of a high resolution three-dimensional surgical atlas of the murine head for strains 129s1/svimj and c57bi/6j using magnetic resonance imaging and micro-computed tomography. Neuroscience. 2007 ;144(2) :604-15.

[221] Hikishima K, Komaki Y, Seki F, Ohnishi Y, Okano HJ, Okano H. In vivo microscopic voxel-based morphometry with a brain template to characterize strain-specific structures in the mouse brain. Scientific Reports. 2017 ;7.

[222] Yushkevich PA, Piven J, Hazlett HC, Smith RG, Ho S, Gee JC, et al. User-guided 3d active contour segmentation of anatomical structures : Significantly improved efficiency and reliability. Neuroimage. 2006 ;31(3) :1116-28.

[223] Yazdanian H, Saturnino GB, Thielscher A, Knudsen K. Fast evaluation of the biot-savart integral using fft for electrical conductivity imaging. Journal Of Computational Physics. 2020 ;411.

[224] Suk Hoon O, Byung Il L, Eung Je W, Soo Yeol L, Min Hyoung C, Ohin K, et al. Conductivity and current density image reconstruction using harmonic bz algorithm in magnetic resonance electrical impedance tomography. Physics In Medicine And Biology. 2003 ;48(19) :3101.

[225] Scott GC, Joy MLG, Armstrong RL, Henkelman RM. Measurement of nonuniform current-density by magnetic-resonance. Ieee Transactions On Medical Imaging. 1991 ;10(3) :362-74.

[226] Hain EG, Klein C, Munder T, Braun J, Riek K, Mueller S, et al. Dopaminergic neurodegeneration in the mouse is associated with decrease of viscoelasticity of substantia nigra tissue. Plos One. 2016 ;11(8).

[227] Gabriel S, Lau RW, Gabriel C. The dielectric properties of biological tissues .2. Measurements in the frequency range 10 hz to 20 ghz. Physics In Medicine And Biology. 1996 ;41(11) :2251-69.

[228] Hirsch S, Braun J, Sack I. In : Motion encoding and mre sequences. Wiley online books ; 2017. p. 41-59.

[229] Fang Q, Boas DA, Ieee. Tetrahedral mesh generation from volumetric binary and gray-scale images. 2009 Ieee International Symposium On Biomedical Imaging : From Nano To Macro, Vols 1 And 2. 2009 :1142-5.

[230] Tran AP, Yan S, Fang Q. Improving model-based functional near-infrared spectroscopy analysis using mesh-based anatomical and light-transport models. Neurophotonics. 2020 ;7(1) :015008-8.

[231] Sarvazyan AP, Rudenko OV, Swanson SD, Fowlkes JB, Emelianov SY. Shear wave elasticity imaging : A new ultrasonic technology of medical diagnostics. Ultrasound In Medicine And Biology. 1998 ;24(9) :1419-35.

[232] Klein C, Hain EG, Braun J, Riek K, Mueller S, Steiner B, et al. Enhanced adult neurogenesis increases brain stiffness : In vivo magnetic resonance elastography in a mouse model of dopamine depletion. Plos One. 2014 ;9(3).

[233] McGarry MDJ, Van Houten EEW, Johnson CL, Georgiadis JG, Sutton BP, Weaver JB, et al. Multiresolution mr elastography using nonlinear inversion. Medical Physics. 2012 ;39(10) :6388-96.

[234] Meng ZJ, Sajib SZK, Chauhan M, Sadleir RJ, Kim HJ, Kwon OI, et al. Numerical simulations of mreit conductivity imaging for brain tumor detection. Computational And Mathematical Methods In Medicine. 2013 ;2013.

[235] Surowiec AJ, Stuchly SS, Barr JR, Swarup A. Dielectric-properties of breast-carcinoma and the surrounding tissues. Ieee Transactions on Biomedical Engineering. 1988 ;35(4) :257-63.

[236] Jossinet J. Variability of impedivity in normal and pathological breast tissue. Medical and Biological Engineering and Computing. 1996 ;34(5) :346-50.

[237] Jossinet J. The impedivity of freshly excised human breast tissue. Physiological Measurement. 1998 ;19(1) :61-75.

[238] Haemmerich D, Staelin ST, Tsai JZ, Tungjitkusolmun S, Mahvi DM, Webster JG. In vivo electrical conductivity of hepatic tumours. Physiological Measurement. 2003 ;24(2) :251-60.

[239] Zou Y, Guo Z. A review of electrical impedance techniques for breast cancer detection. Medical Engineering and Physics. 2003 ;25(2) :79-90.

[240] Othman SF, Xu HH, Royston TJ, Magin RL. Microscopic magnetic resonance elastography (mu mre). Magnetic Resonance In Medicine. 2005 ;54(3) :605-15.

[241] Sadleir R, Grant S, Zhang SU, Oh SH, Lee BI, Woo EJ. High field mreit : Setup and tissue phantom imaging at 11 t. Physiological Measurement. 2006 ;27(5) :S261-70.

[242] Flé G, Gilbert G, Grasland-Mongrain P, Cloutier G. Lorentz force induced shear waves for magnetic resonance elastography applications. Scientific Reports. 2021 ;11(1) :12785.

[243] Riek K, Millward JM, Hamann I, Mueller S, Pfueller CF, Paul F, et al. Magnetic resonance elastography reveals altered brain viscoelasticity in experimental autoimmune encephalomyelitis. Neuroimage-Clinical. 2012 ;1(1) :81-90.

[244] Poplack S, Wells W, Paulsen K. Four Alternative Breast Imaging Modalities. In : Paulsen KD, Meaney PM, Gilman LC, editors. Four alternative breast imaging modalities. Boston, MA : Springer US ; 2005. p. 1-24.

[245] Yanez LZ, Han J, Behr BB, Pera RAR, Camarillo DB. Human oocyte developmental potential is predicted by mechanical properties within hours after fertilization. Nature Communications. 2016 ;7(1) :10809.1-12.

[246] Nenadic IZ, Urban MW, Greenleaf JF, Gennisson JL, Bernal M, Tanter M. In : Section viii clinical elastography applications. John Wiley and Sons ; 2019. p. 471-566.

[247] Charras GT, Mitchison TJ, Mahadevan L. Animal cell hydraulics. Journal Of Cell Science. 2009 ;122(18) :3233-41.

[248] Cross SE, Jin YS, Rao J, Gimzewski JK. Nanomechanical analysis of cells from cancer patients. Nature Nanotechnology. 2007 ;2(12) :780-3.

[249] Bufi N, Saitakis M, Dogniaux S, Buschinger O, Bohineust A, Richert A, et al. Human primary immune cells exhibit distinct mechanical properties that are modified by inflammation. Biophysical Journal. 2015 ;108(9) :2181-90.

[250] Andolfi L, Bourkoula E, Migliorini E, Palma A, Pucer A, Skrap M, et al. Investigation of adhesion and mechanical properties of human glioma cells by single cell force spectroscopy and atomic force microscopy. Plos One. 2014 ;9(11) :e112582.1-9.

[251] Lekka M. Discrimination between normal and cancerous cells using afm. Bionanoscience. 2016 ;6(1) :65-80.

[252] Rosendahl P, Plak K, Jacobi A, Kraeter M, Toepfner N, Otto O, et al. Real-time fluorescence and deformability cytometry. Nature Methods. 2018 ;15(5) :355-8.

[253] Kort J, Behr B. Biomechanics and developmental potential of oocytes and embryos. Fertility And Sterility. 2017 ;108(5) :738-41.

[254] Guck J, Chilvers Edwin R. Mechanics meets medicine. Science Translational Medicine. 2013 ;5(212) :212fs41.1-3.

[255] Papi M, Brunelli R, Sylla L, Parasassi T, Monaci M, Maulucci G, et al. Mechanical properties of zona pellucida hardening. European Biophysics Journal. 2010 ;39(6) :987-92.

[256] Murayama Y, Mizuno J, Kamakura H, Fueta Y, Nakamura H, Akaishi K, et al. Mouse zona pellucida dynamically changes its elasticity during oocyte maturation, fertilization and early embryo development. Human Cell. 2006 ;19(4) :119-25.

[257] Murayama Y, Yoshida M, Mizuno J, Nakamura H, Inoue S, Watanabe Y, et al. Elasticity measurement of zona pellucida using a micro tactile sensor to evaluate embryo quality. Journal Of Mammalian Ova Research. 2008 ;25(1) :8-16.

[258] Chaigne A, Campillo C, Gov NS, Voituriez R, Azoury J, Umaña-Diaz C, et al. A soft cortex is essential for asymmetric spindle positioning in mouse oocytes. Nature Cell Biology. 2013 ;15(8) :958-66.

[259] Chaigne A, Campillo C, Gov NS, Voituriez R, Sykes C, Verlhac MH, et al. A narrow window of cortical tension guides asymmetric spindle positioning in the mouse oocyte. Nature Communications. 2015 ;6(1) :6027.1-10.

[260] Bennabi I, Crozet F, Nikalayevich E, Chaigne A, Letort G, Manil-Ségalen M, et al. Artificially decreasing cortical tension generates aneuploidy in mouse oocytes. Nature Communications. 2020 ;11(1) :1649.1-14.

[261] Mihajlovic AI, Haverfield J, FitzHarris G. Distinct classes of lagging chromosome underpin age-related oocyte aneuploidy in mouse. Developmental Cell. 2021 ;56(16) :2273-83.

[262] Krause I, Pohler U, Grosse S, Shebl O, Petek E, Chandra A, et al. Characterization of the injection funnel during intracytoplasmic sperm injection reflects cytoplasmic maturity of the oocyte. Fertility And Sterility. 2016 ;106(5) :1101-6.

[263] Ebner T, Moser M, Sommergruber M, Puchner M, Wiesinger R, Tews G. Developmental competence of oocytes showing increased cytoplasmic viscosity. Human Reproduction. 2003 ;18(6) :1294-8.

[264] Shen T, Benet E, Sridhar SL, Abadie J, Piat E, Vernerey FJ. Separating the contributions of zona pellucida and cytoplasm in the viscoelastic response of human oocytes. Acta Biomaterialia. 2019 ;85 :253-62.

[265] Murayama Y, Constantinou CE, Omata S. Micro-mechanical sensing platform for the characterization of the elastic properties of the ovum via uniaxial measurement. Journal Of Biomechanics. 2004 ;37(1) :67-72.

[266] Murayama Y, Omata S. Fabrication of micro tactile sensor for the measurement of micro-scale local elasticity. Sensors And Actuators A : Physical. 2004 ;109(3) :202-7.

[267] Liu X, Shi J, Zong Z, Wan KT, Sun Y. Elastic and viscoelastic characterization of mouse oocytes using micropipette indentation. Annals Of Biomedical Engineering. 2012 ;40(10) :2122-30.

[268] Yu S, Wan KT, Roberts KP, Bischof JC, Nelson BJ. Mechanical property characterization of mouse zona pellucida. Ieee Transactions On Nanobioscience. 2003 ;2(4) :279-86.

[269] Boccaccio A, Frassanito MC, Lamberti L, Brunelli R, Maulucci G, Monaci M, et al. Nanoscale characterization of the biomechanical hardening of bovine zona pellucida. Journal Of The Royal Society Interface. 2012 ;9(76) :2871-82.

[270] Andolfi L, Greco SLM, Tierno D, Chignola R, Martinelli M, Giolo E, et al. Planar afm macro-probes to study the biomechanical properties of large cells and 3d cell spheroids. Acta Biomaterialia. 2019 ;94 :505-13.

[271] Dufrene YF, Martínez-Martin D, Medalsy I, Alsteens D, Müller DJ. Multiparametric imaging of biological systems by force-distance curve–based afm. Nature Methods. 2013 ;10(9) :847-54.

[272] Ahmed WW, Fodor E, Almonacid M, Bussonnier M, Verlhac MH, Gov N, et al. Active mechanics reveal molecular-scale force kinetics in living oocytes. Biophysical Journal. 2018 ;114(7) :1667-79.

[273] Gossett DR, Tse HTK, Lee SA, Ying Y, Lindgren AG, Yang OO, et al. Hydrodynamic stretching of single cells for large population mechanical phenotyping. Proceedings Of The National Academy Of Sciences Of The United States Of America. 2012 ;109(20) :7630-5.

[274] Byun S, Son S, Amodei D, Cermak N, Shaw J, Kang JH, et al. Characterizing deformability and surface friction of cancer cells. Proceedings Of The National Academy Of Sciences Of The United States Of America. 2013 ;110(19) :7580-5.

[275] Lange JR, Steinwachs J, Kolb T, Lautscham LA, Harder I, Whyte G, et al. Microconstriction arrays for high-throughput quantitative measurements of cell mechanical properties. Biophysical Journal. 2015 ;109(3) :26-34.

[276] Mietke A, Otto O, Girardo S, Rosendahl P, Taubenberger A, Golfier S, et al. Extracting cell stiffness from real-time deformability cytometry : Theory and experiment. Biophysical Journal. 2015 ;109(10) :2023-36.

[277] Scarcelli G, Polacheck WJ, Nia HT, Patel K, Grodzinsky AJ, Kamm RD, et al. Noncontact three-dimensional mapping of intracellular hydromechanical properties by brillouin microscopy. Nature Methods. 2015 ;12(12) :1132-4.

[278] Elsayad K, Werner S, Gallemi M, Kong JX, Guajardo ERS, Zhang LJ, et al. Mapping the subcellular mechanical properties of live cells in tissues with fluorescence emission-brillouin imaging. Science Signaling. 2016 ;9(435).

[279] Laloy-Borgna G, Zorgani A, Catheline S. Micro-elastography : Toward ultrasonic shear waves in soft solids. Applied Physics Letters. 2021 ;118(11) :113701.1-6.

[280] Garteiser P, Doblas S, Daire JL, Wagner M, Leitao H, Vilgrain V, et al. Mr elastography of liver tumours : Value of viscoelastic properties for tumour characterisation. European Radiology. 2012 ;22(10) :2169-77.

[281] Gordon-Wylie SW, Solamen LM, McGarry MDJ, Zeng W, VanHouten E, Gilbert G, et al. Mr elastography at 1 hz of gelatin phantoms using 3d or 4d acquisition. Journal Of Magnetic Resonance. 2018 ;296 :112-20.

[282] McGarry M, Van Houten E, Solamen L, Gordon-Wylie S, Weaver J, Paulsen K. Uniqueness of poroelastic and viscoelastic nonlinear inversion mr elastography at low frequencies. Physics In Medicine And Biology. 2019 ;64(7) :075006.

[283] Fujii Y, Endo Y, Mitsuhata S, Hayashi M, Motoyama H. Evaluation of the effect of piezo-intracytoplasmic sperm injection on the laboratory, clinical, and neonatal outcomes. Reproductive Medicine And Biology. 2020 ;19(2) :198-205.

[284] Furuhashi K, Saeki Y, Enatsu N, Iwasaki T, Ito K, Mizusawa Y, et al. Piezo-assisted icsi improves fertilization and blastocyst development rates compared with conventional icsi in women aged more than 35 years. Reproductive Medicine And Biology. 2019 ;18(4) :357-61.

[285] Hiraoka K, Kitamura S, Kuwayama M. Piezo-icsi using ultra-thin needle dramatically improves oocyte survival and fertilization without detrimental effect on embryo development and implantation ability as compared with conventional-icsi. Fertility And Sterility. 2014 ;102(3) :e32.

[286] Grover AR, Fegley B, Duncan TV, Duncan FE. In : Skinner MK, editor. The oocyte. Oxford : Academic Press ; 2018. p. 21-8.

[287] Stracuzzi A, Dittmann J, Bol M, Ehret AE. Visco- and poroelastic contributions of the zona pellucida to the mechanical response of oocytes. Biomechanics And Modeling In Mechanobiology. 2021 ;20(2) :751-65.

[288] McGarry M, Van Houten E, Guertler C, Okamoto R, Smith D, Sowinski D, et al. A heterogenous, time harmonic, nearly incompressible transverse isotropic finite element brain simulation platform for mr elastography. Physics In Medicine And Biology. 2021 ;66(5) :055029.1-19.

[289] McGarry MDJ, Johnson CL, Sutton BP, Georgiadis JG, Van Houten EEW, Pattison AJ, et al. Suitability of poroelastic and viscoelastic mechanical models for high and low frequency mr elastography. Medical Physics. 2015 ;42(2) :947-57.

[290] Babaei B, Fovargue D, Lloyd RA, Miller R, Jugé L, Kaplan M, et al. Magnetic resonance elastography reconstruction for anisotropic tissues. Medical Image Analysis. 2021 ;74 :102212.

[291] McGarry M, Van Houten E, Sowinski D, Jyoti D, Smith DR, Caban-Rivera DA, et al. Mapping heterogenous anisotropic tissue mechanical properties with transverse isotropic nonlinear inversion mr elastography. Medical Image Analysis. 2022 ;78 :102432.1-10.

[292] Jyoti D, McGarry M, Van Houten E, Sowinski D, Bayly PV, Johnson CL, et al. Quantifying stability of parameter estimates for in vivo nearly incompressible transversely-isotropic brain mr elastography. Biomedical Physics And Engineering Express. 2022 ;8(3).

[293] Smith DR, Caban-Rivera DA, McGarry MDJ, Williams LT, McIlvain G, Okamoto RJ, et al. Anisotropic mechanical properties in the healthy human brain estimated with multi-excitation transversely isotropic mr elastography. Brain Multiphysics. 2022 ;3 :100051.

[294] Jyoti D, McGarry M, Caban-Rivera DA, Van Houten E, Johnson CL, Paulsen K. Transversely-isotropic brain in vivo mr elastography with anisotropic damping. Journal Of The Mechanical Behavior Of Biomedical Materials. 2023 ;141 :105744.

[295] Van Houten EEW, Doyley MM, Kennedy FE, Paulsen KD, Weaver JB. A three-parameter mechanical property reconstruction method for mr-based elastic property imaging. Ieee Transactions On Medical Imaging. 2005 ;24(2) :311-24.

[296] Alessandrini M, Heyde B, Queirós S, Cygan S, Zontak M, Somphone O, et al. Detailed evaluation of five 3d speckle tracking algorithms using synthetic echocardiographic recordings. Ieee Transactions On Medical Imaging. 2016 ;35(8) :1915-26.

[297] Li H, Poree J, Chayer B, Roy-Cardinal MH, Cloutier G. Parameterized strain estimation for vascular ultrasound elastography with sparse representation. Ieee Transactions On Medical Imaging. 2020 ;39(12) :3788-800.

[298] Poree J, Garcia D, Chayer B, Ohayon J, Cloutier G. Noninvasive vascular elastography with plane strain incompressibility assumption using ultrafast coherent compound plane wave imaging. Ieee Transactions On Medical Imaging. 2015 ;34(12) :2618-31.

[299] Weng CC, Chen PY, Chou D, Shih CC, Huang CC. High frequency ultrasound elastography for estimating the viscoelastic properties of the cornea using lamb wave model. IEEE Transactions on Biomedical Engineering. 2021 ;68(9) :2637-44.

[300] Schmitt C, Hadj Henni A, Cloutier G. Ultrasound dynamic micro-elastography applied to the viscoelastic characterization of soft tissues and arterial walls. Ultrasound in Medicine and Biology. 2010 ;36(9) :1492-503.

[301] Feng X, Li GY, Ramier A, Eltony AM, Yun SH. In vivo stiffness measurement of epidermis, dermis, and hypodermis using broadband rayleigh-wave optical coherence elastography. Acta Biomaterialia. 2022 ;146 :295-305.

[302] Flé G, Van Houten E, Rémillard-Labrosse G, FitzHarris G, Cloutier G. Imaging the subcellular viscoelastic properties of mouse oocytes. Proceedings of the National Academy of Sciences. 2023 ;120(21) :e2213836120.

[303] Kraack JP. Biophysics : Ultrarapid microquakes. Research Highlights, Nature Physics. 2018 ;14(3) :206-6.

[304] Brum J, Catheline S, Benech N, Negreira C. Quantitative shear elasticity imaging from a complex elastic wavefield in soft solids with application to passive elastography. Ieee Transactions On Ultrasonics, Ferroelectrics, And Frequency Control. 2015 ;62(4) :673-85.

[305] Perriñez PR, Kennedy FE, Houten EEWV, Weaver JB, Paulsen KD. Modeling of soft poroelastic tissue in time-harmonic mr elastography. Ieee Transactions On Biomedical Engineering. 2009 ;56(3) :598-608.

[306] Bhatt M, Moussu MAC, Chayer B, Destrempes F, Gesnik M, Allard L, et al. Reconstruction of viscosity maps in ultrasound shear wave elastography. Ieee Transactions On Ultrasonics, Ferroelectrics, And Frequency Control. 2019 ;66(6) :1065-78.

[307] Bernard S, Kazemirad S, Cloutier G. A frequency-shift method to measure shear-wave attenuation in soft tissues. Ieee Transactions On Ultrasonics, Ferroelectrics, And Frequency Control. 2017 ;64(3) :514-24.

[308] Zorgani A, Ghafour TA, Lescanne M, Catheline S, Bel-Brunon A. Optical elastography : Tracking surface waves with digital image correlation. Physics In Medicine And Biology. 2019 ;64(5) :055007.1-9.

[309] Anderson AT, Johnson CL, McGarry M, Paulsen KD, Sutton BP, Van Houten EE, et al. Inversion parameters based on convergence and error metrics for nonlinear inversion mr elastography. In : Proc. Intl. Soc. Mag. Reson. Med. vol. 25 ; 2017. p. 1139.

[310] Solamen LM, McGarry MD, Tan L, Weaver JB, Paulsen KD. Phantom evaluations of nonlinear inversion mr elastography. Physics In Medicine And Biology. 2018 ;63(14) :145021.1-14.

[311] Sarvazyan AP, Skovoroda AR, Emelianov SY, Fowlkes JB, Pipe JG, Adler RS, et al. Chapter 23. In : Biophysical bases of elasticity imaging. Springer ; 1995. p. 223-40.

[312] Chatelin S, Oudry J, Perichon N, Sandrin L, Allemann P, Soler L, et al. In vivo liver tissue mechanical properties by transient elastography : Comparison with dynamic mechanical analysis. Biorheology. 2011 ;48(2) :75-88.

[313] Klatt D, Friedrich C, Korth Y, Vogt R, Braun J, Sack I. Viscoelastic properties of liver measured by oscillatory rheometry and multifrequency magnetic resonance elastography. Biorheology. 2010 ;47(2) :133-41.

[314] Lin H, Shen Y, Chen X, Zhu Y, Zheng Y, Zhang X, et al. Viscoelastic properties of normal rat liver measured by ultrasound elastography : Comparison with oscillatory rheometry. Biorheology. 2016 ;53(5-6) :193-207.

[315] Shahmirzadi D, Bruck HA, Hsieh AH. Measurement of mechanical properties of soft tissues in vitro under controlled tissue hydration. Experimental Mechanics. 2012 ;53(3) :405-14.

[316] Vappou J, Breton E, Choquet P, Goetz C, Willinger R, Constantinesco A. Magnetic resonance elastography compared with rotational rheometry for in vitro brain tissue viscoelasticity measurement. Magnetic Resonance Materials In Physics, Biology And Medicine. 2007 ;20(5) :273-8.

[317] Skovoroda AR, Emelianov SY, Lubinski MA, Sarvazyan AP, Donnell MO. Theoretical analysis and verification of ultrasound displacement and strain imaging. Ieee Transactions On Ultrasonics, Ferroelectrics, And Frequency Control. 1994 ;41(3) :302-13.

[318] Biot MA. Theory of propagation of elastic waves in a fluid-saturated porous solid. I. Low-frequency range. The Journal Of The Acoustical Society Of America. 1956 ;28(2) :168-78.

[319] Biot MA. Theory of propagation of elastic waves in a fluid-saturated porous solid. Ii. Higher frequency range. The Journal Of The Acoustical Society Of America. 1956 ;28(2) :179-91.

[320] Cheng Alexander HD, Badmus T, Beskos Dimitri E. Integral equation for dynamic poroelasticity in frequency domain with bem solution. Journal Of Engineering Mechanics. 1991 ;117(5) :1136-57.

[321] Hirsch S, Braun J, Sack I. Magnetic resonance elastography - physical background and medical applications. Wiley-VCH ; 2017.

[322] Romano A, Scheel M, Hirsch S, Braun J, Sack I. In vivo waveguide elastography of white matter tracts in the human brain. Magnetic Resonance In Medicine. 2012 ;68(5) :1410-22.

[323] Meyers MA, Chawla KK. Mechanical behavior of materials. vol. 2nd ed. New York : The Cambridge University Press ; 2008.

[324] Rus G, Faris IH, Torres J, Callejas A, Melchor J. Why are viscosity and nonlinearity bound to make an impact in clinical elastographic diagnosis ? Sensors. 2020 ;20(8) :2379.

[325] Schiessel H, Metzler R, Blumen A, Nonnenmacher TF. Generalized viscoelastic models : Their fractional equations with solutions. Journal Of Physics A : Mathematical And General. 1995 ;28(23) :6567.

[326] Greenwood MS, Bamberger JA. Measurement of viscosity and shear wave velocity of a liquid or slurry for on-line process control. Ultrasonics. 2002 ;39(9) :623-30.

[327] Kelly P. Solid mechanics part i : An introduction to solid mechanics. Solid mechanics lecture notes ; 2013.

[328] Serra-Aguila A, Puigoriol-Forcada JM, Reyes G, Menacho J. Viscoelastic models revisited : Characteristics and interconversion formulas for generalized kelvin–voigt and maxwell models. Acta Mechanica Sinica. 2019 ;35(6) :1191-209.

[329] Parker KJ, Doyley MM, Rubens DJ. Imaging the elastic properties of tissue : The 20 year perspective. Physics In Medicine And Biology. 2012 ;57(16) :5359-60.

[330] Barnes HA, Hutton JF, Walters K. An introduction to rheology. vol. 3. Elsevier ; 1989.

[331] Li S, Zhao G, Chen H. The relationship between steady shear viscosity and complex viscosity. Journal Of Dispersion Science And Technology. 2005 ;26(4) :415-9.

[332] Ophir J, Alam SK, Garra B, Kallel F, Konofagou E, Krouskop T, et al. Elastography : Ultrasonic estimation and imaging of the elastic properties of tissues. Proceedings Of The Institution Of Mechanical Engineers, Part H : Journal Of Engineering In Medicine. 1999 ;213(3) :203-33.

[333] Cheeke JDN. Fundamentals and applications of ultrasonic waves. CRC press ; 2017.

[334] Lerner RM, Parker KJ, Holen J, Gramiak R, Waag RC. Sono-elasticity : Medical elasticity images derived from ultrasound signals in mechanically vibrated targets. In : Sono-elasticity : Medical elasticity images derived from ultrasound signals in mechanically vibrated targets. Springer ; 1988. p. 317-27.

[335] Fatemi M, Greenleaf JF. Ultrasound-stimulated vibro-acoustic spectrography. Science. 1998 ;280(5360) :82-5.

[336] Kazemirad S, Bernard S, Hybois S, Tang A, Cloutier G. Ultrasound shear wave viscoelastography : Model-independent quantification of the complex shear modulus. Ieee Transactions On Ultrasonics, Ferroelectrics, And Frequency Control. 2016 ;63(9) :1399-408.

[337] McAleavey SA, Menon M, Orszulak J. Shear-modulus estimation by application of spatially-modulated impulsive acoustic radiation force. Ultrasonic Imaging. 2007 ;29(2) :87-104.

[338] Sandrin L, Catheline S, Tanter M, Hennequin X, Fink M. Time-resolved pulsed elastography with ultrafast ultrasonic imaging. Ultrasonic Imaging. 1999 ;21(4) :259-72.

[339] Tang A, Cloutier G, Szeverenyi NM, Sirlin CB. Ultrasound elastography and mr elastography for assessing liver fibrosis : Part 1, principles and techniques. American Journal Of Roentgenology. 2015 ;205(1) :22-32.

[340] Tang A, Cloutier G, Szeverenyi NM, Sirlin CB. Ultrasound elastography and mr elastography for assessing liver fibrosis : Part 2, diagnostic performance, confounders, and future directions. American Journal Of Roentgenology. 2015 ;205(1) :33-40.

[341] Arena U, Vizzutti F, Corti G, Ambu S, Stasi C, Bresci S, et al. Acute viral hepatitis increases liver stiffness values measured by transient elastography. Hepatology. 2007 ;47(2) :380-4.

[342] Castéra L, Vergniol J, Foucher J, Le Bail B, Chanteloup E, Haaser M, et al. Prospective comparison of transient elastography, fibrotest, apri, and liver biopsy for the assessment of fibrosis in chronic hepatitis c. Gastroenterology. 2005 ;128(2) :343-50.

[343] Nightingale K. Acoustic radiation force impulse (arfi) imaging : A review. Current Medical Imaging. 2011 ;7(4) :328-39.

[344] Cassinotto C, Boursier J, de Lédinghen V, Lebigot J, Lapuyade B, Cales P, et al. Liver stiffness in nonalcoholic fatty liver disease : A comparison of supersonic shear imaging, fibroscan, and arfi with liver biopsy. Hepatology. 2016 ;63(6) :1817-27.

[345] Lee MS, Bae JM, Joo SK, Woo H, Lee DH, Jung YJ, et al. Prospective comparison among transient elastography, supersonic shear imaging, and arfi imaging for predicting fibrosis in nonalcoholic fatty liver disease. Plos One. 2017 ;12(11) :e0188321.

[346] Amador C, Urban MW, Chen S, Greenleaf JF. Loss tangent and complex modulus estimated by acoustic radiation force creep and shear wave dispersion. Physics In Medicine And Biology. 2012 ;57(5) :1263-82.

[347] Rouze NC, Palmeri ML, Nightingale KR. An analytic, fourier domain description of shear wave propagation in a viscoelastic medium using asymmetric gaussian sources. The Journal Of The Acoustical Society Of America. 2015 ;138(2) :1012-22.

[348] Chen S, Sanchez W, Callstrom MR, Gorman B, Lewis JT, Sanderson SO, et al. Assessment of liver viscoelasticity by using shear waves induced by ultrasound radiation force. Radiology. 2013 ;266(3) :964-70.

[349] Orescanin M, Wang Y, Insana MF. 3-d fdtd simulation of shear waves for evaluation of complex modulus imaging. Ieee Transactions On Ultrasonics, Ferroelectrics, And Frequency Control. 2011 ;58(2) :389-98.

[350] Bernard S, Cloutier G. Forward and inverse viscoelastic wave scattering by irregular inclusions for shear wave elastography. The Journal Of The Acoustical Society Of America. 2017 ;142(4) :2346-64.

[351] Montagnon E, Hadj-Henni A, Schmitt C, Cloutier G. Rheological assessment of a polymeric spherical structure using a three-dimensional shear wave scattering model in dynamic spectroscopy elastography. Ieee Transactions On Ultrasonics, Ferroelectrics, And Frequency Control. 2014 ;61(2) :277-87.

[352] Ouared A, Kazemirad S, Montagnon E, Cloutier G. Ultrasound viscoelasticity assessment using an adaptive torsional shear wave propagation method. Medical Physics. 2016 ;43(4) :1603-14.

[353] Henni AH, Schmitt C, Trop I, Cloutier G. Shear wave induced resonance elastography of spherical masses with polarized torsional waves. Applied Physics Letters. 2012 ;100(13) :133702.

[354] Nenadic IZ, Urban MW, Heng Z, Sanchez W, Morgan PE, Greenleaf JF, et al. Application of attenuation measuring ultrasound shearwave elastography in 8 post-transplant liver patients. In : Ieee International Ultrasonics Symposium ; 2014. p. 987-90.

[355] Engel AJ, Bashford GR. A new method for shear wave speed estimation in shear wave elastography. Ieee Transactions On Ultrasonics, Ferroelectrics, And Frequency Control. 2015 ;62(12) :2106-14.

[356] Rouze NC, Deng Y, Trutna CA, Palmeri ML, Nightingale KR. Characterization of viscoelastic materials using group shear wave speeds. Ieee Transactions On Ultrasonics, Ferroelectrics, And Frequency Control. 2018 ;65(5) :780-94.

[357] Deffieux T, Montaldo G, Tanter M, Fink M. Shear wave spectroscopy for in vivo quantification of human soft tissues visco-elasticity. Ieee Transactions On Medical Imaging. 2009 ;28(3) :313-22.

[358] Ambrozinski L, Packo P, Pieczonka L, Stepinski T, Uhl T, Staszewski WJ. Identification of material properties – efficient modelling approach based on guided wave propagation and spatial multiple signal classification. Structural Control And Health Monitoring. 2015 ;22(7) :969-83.

[359] Alleyne D, Cawley P. A two-dimensional fourier transform method for the measurement of propagating multimode signals. The Journal Of The Acoustical Society Of America. 1991 ;89(3) :1159-68.

[360] Brum J, Bernal M, Gennisson JL, Tanter M. In vivo evaluation of the elastic anisotropy of the human achilles tendon using shear wave dispersion analysis. Physics In Medicine And Biology. 2014 ;59(3) :505-23.

[361] Chatelin S, Gennisson JL, Bernal M, Tanter M, Pernot M. Modelling the impulse diffraction field of shear waves in transverse isotropic viscoelastic medium. Physics In Medicine And Biology. 2015 ;60(9) :3639-54.

[362] Rouze NC, Wang MH, Palmeri ML, Nightingale KR. Finite element modeling of impulsive excitation and shear wave propagation in an incompressible, transversely isotropic medium. Journal Of Biomechanics. 2013 ;46(16) :2761-8.

[363] Dines KA, Kak AC. Ultrasonic attenuation tomography of soft tissues. Ultrasonic Imaging. 1979 ;1(1) :16-33.

[364] Fink M, Hottier F, Cardoso JF. Ultrasonic signal processing for in vivo attenuation measurement : Short time fourier analysis. Ultrasonic Imaging. 1983 ;5(2) :117-35.

[365] Quan Y, Harris JM. Seismic attenuation tomography using the frequency shift method. Geophysics. 1997 ;62(3) :895-905.

[366] Barr RG. Elastography in clinical practice. Radiologic Clinic. 2014 ;52(6) :1145-62.

[367] Sigrist RMS, Liau J, Kaffas AE, Chammas MC, Willmann JK. Ultrasound elastography : Review of techniques and clinical applications. Theranostics. 2017 ;7(5) :1303-29.

[368] Zaleska-Dorobisz U, Kaczorowski K, Pawluś A, Puchalska A, Inglot M. Ultrasound elastography–review of techniques and its clinical applications. Adv Clin Exp Med. 2014 ;23(4) :645–655.

[369] El-Serag HB. Hepatocellular carcinoma and hepatitis c in the united states. Hepatology. 2002 ;36(5B) :s74-83.

[370] Kose S, Ersan G, Tatar B, Adar P, Erturk Sengel B. Evaluation of percutaneous liver biopsy complications in patients with chronic viral hepatitis. The Eurasian Journal Of Medicine. 2015 ;47(3) :161-4.

[371] Bamber J, Cosgrove D, Dietrich C, Fromageau J, Bojunga J, Calliada F, et al. Efsumb guidelines and recommendations on the clinical use of ultrasound elastography. Part 1 : Basic principles and technology. Ultraschall In Der Medizin - European Journal Of Ultrasound. 2013 ;34(02) :169-84.

[372] Ferraioli G, Tinelli C, Zicchetti M, Poma G, Gregorio MD, Filice C. Reproducibility of real-time shear wave elastography in the evaluation of liver elasticity. European Journal Of Radiology. 2012 ;81(11) :3102-6.

[373] Ferraioli G. Point shear wave elastography method for assessing liver stiffness. World Journal Of Gastroenterology. 2014 ;20(16).

[374] Ganne-Carrié N, Ziol M, de Ledinghen V, Douvin C, Marcellin P, Castera L, et al. Accuracy of liver stiffness measurement for the diagnosis of cirrhosis in patients with chronic liver diseases. Hepatology. 2006 ;44(6) :1511-7.

[375] Nahon P, Kettaneh A, Tengher-Barna I, Ziol M, de Lédinghen V, Douvin C, et al. Assessment of liver fibrosis using transient elastography in patients with alcoholic liver disease. Journal Of Hepatology. 2008 ;49(6) :1062-8.

[376] Millonig G, Friedrich S, Adolf S, Fonouni H, Golriz M, Mehrabi A, et al. Liver stiffness is directly influenced by central venous pressure. Journal Of Hepatology. 2010 ;52(2) :206-10.

[377] Millonig G, Reimann FM, Friedrich S, Fonouni H, Mehrabi A, Büchler MW, et al. Extrahepatic cholestasis increases liver stiffness (fibroscan) irrespective of fibrosis. Hepatology. 2008 ;48(5) :1718-23.

[378] Friedrich-Rust M, Nierhoff J, Lupsor M, Sporea I, Fierbinteanu-Braticevici C, Strobel D, et al. Performance of acoustic radiation force impulse imaging for the staging of liver fibrosis : A pooled meta-analysis. Journal Of Viral Hepatitis. 2012 ;19(2) :e212-9.

[379] Takahashi H, Ono N, Eguchi Y, Eguchi T, Kitajima Y, Kawaguchi Y, et al. Evaluation of acoustic radiation force impulse elastography for fibrosis staging of chronic liver disease : A pilot study. Liver International. 2010 ;30(4) :538-45.

[380] Carey E, Carey WD. Noninvasive tests for liver disease, fibrosis, and cirrhosis : Is liver biopsy obsolete ? Cleveland Clinic Journal Of Medicine. 2010 ;77(8) :519-27.

[381] Ferraioli G, Tinelli C, Dal Bello B, Zicchetti M, Filice G, Filice C. Accuracy of real-time shear wave elastography for assessing liver fibrosis in chronic hepatitis c : A pilot study. Hepatology. 2012 ;56(6) :2125-33.

[382] Sugimoto K, Moriyasu F, Oshiro H, Takeuchi H, Yoshimasu Y, Kasai Y, et al. Clinical utilization of shear wave dispersion imaging in diffuse liver disease. Ultrasonography. 2020 ;39(1) :3-10.

[383] Athanasiou A, Tardivon A, Tanter M, Sigal-Zafrani B, Bercoff J, Deffieux T, et al. Breast lesions : Quantitative elastography with supersonic shear imaging—preliminary results. Radiology. 2010 ;256(1) :297-303.

[384] Krouskop TA, Wheeler TM, Kallel F, Garra BS, Hall T. Elastic moduli of breast and prostate tissues under compression. Ultrasonic Imaging. 1998 ;20(4) :260-74.

[385] Kolb TM, Lichy J, Newhouse JH. Comparison of the performance of screening mammography, physical examination, and breast us and evaluation of factors that influence them : An analysis of 27,825 patient evaluations. Radiology. 2002 ;225(1) :165-75.

[386] Berg WA, Cosgrove DO, Doré CJ, Schäfer FKW, Svensson WE, Hooley RJ, et al. Shear-wave elastography improves the specificity of breast us : The be1 multinational study of 939 masses. Radiology. 2012 ;262(2) :435-49.

[387] Evans A, Whelehan P, Thomson K, McLean D, Brauer K, Purdie C, et al. Quantitative shear wave ultrasound elastography : Initial experience in solid breast masses. Breast Cancer Research. 2010 ;12(6) :R104.

[388] Xue Y, Yao S, Li X, Zhang H. Benign and malignant breast lesions identification through the values derived from shear wave elastography : Evidence for the meta-analysis. Oncotarget. 2017 ;8(51) :89173.

[389] Lee SH, Chang JM, Kim WH, Bae MS, Seo M, Koo HR, et al. Added value of shear-wave elastography for evaluation of breast masses detected with screening us imaging. Radiology. 2014 ;273(1) :61-9.

[390] Lee SH, Chung J, Choi HY, Choi SH, Ryu EB, Ko KH, et al. Evaluation of screening us–detected breast masses by combined use of elastography and color doppler us with b-mode us in women with dense breasts : A multicenter prospective study. Radiology. 2017 ;285(2) :660-9.

[391] Kumar V, Denis M, Gregory A, Bayat M, Mehrmohammadi M, Fazzio R, et al. Viscoelastic parameters as discriminators of breast masses : Initial human study results. Plos One. 2018 ;13(10) :e0205717.

[392] Evans A, Armstrong S, Whelehan P, Thomson K, Rauchhaus P, Purdie C, et al. Can shear-wave elastography predict response to neoadjuvant chemotherapy in women with invasive breast cancer ? British Journal Of Cancer. 2013 ;109(11) :2798-802.

[393] Jing H, Cheng W, Li ZY, Ying L, Wang QC, Wu T, et al. Early evaluation of relative changes in tumor stiffness by shear wave elastography predicts the response to neoadjuvant chemotherapy in patients with breast cancer. Journal Of Ultrasound In Medicine. 2016 ;35(8) :1619-27.

[394] Woo S, Suh CH, Kim SY, Cho JY, Kim SH. Shear-wave elastography for detection of prostate cancer : A systematic review and diagnostic meta-analysis. American Journal Of Roentgenology. 2017 ;209(4) :806-14.

[395] Zhao CK, Xu HX. Ultrasound elastography of the thyroid : Principles and current status. Ultrasonography. 2019 ;38(2) :106-24.

[396] Aubry S, Nueffer JP, Tanter M, Becce F, Vidal C, Michel F. Viscoelasticity in achilles tendonopathy : Quantitative assessment by using real-time shear-wave elastography. Radiology. 2015 ;274(3) :821-9.

[397] Miyamoto N, Hirata K, Kanehisa H, Yoshitake Y. Validity of measurement of shear modulus by ultrasound shear wave elastography in human pennate muscle. Plos One. 2015 ;10(4) :e0124311.

[398] Castéra L, Bernard PH, Le Bail B, Foucher J, Trimoulet P, Merrouche W, et al. Transient elastography and biomarkers for liver fibrosis assessment and follow-up of inactive hepatitis b carriers. Alimentary Pharmacology And Therapeutics. 2011 ;33(4) :455-65.

[399] Gerber L, Kasper D, Fitting D, Knop V, Vermehren A, Sprinzl K, et al. Assessment of liver fibrosis with 2-d shear wave elastography in comparison to transient elastography and acoustic radiation force impulse imaging in patients with chronic liver disease. Ultrasound In Medicine And Biology. 2015 ;41(9) :2350-9.

[400] Barry CT, Mills B, Hah Z, Mooney RA, Ryan CK, Rubens DJ, et al. Shear wave dispersion measures liver steatosis. Ultrasound In Medicine And Biology. 2012 ;38(2) :175-82.

[401] Ferraioli G, Parekh P, Levitov AB, Filice C. Shear wave elastography for evaluation of liver fibrosis. Journal Of Ultrasound In Medicine. 2014 ;33(2) :197-203.

[402] Dietrich CF, Bamber J, Berzigotti A, Bota S, Cantisani V, Castera L, et al. Efsumb guidelines and recommendations on the clinical use of liver ultrasound elastography, update 2017 (long version). Ultraschall In Der Medizin - European Journal Of Ultrasound. 2017 ;38(4) :e16-47.

[403] Boursier J, Isselin G, Fouchard-Hubert I, Oberti F, Dib N, Lebigot J, et al. Acoustic radiation force impulse : A new ultrasonographic technology for the widespread noninvasive diagnosis of liver fibrosis. European Journal Of Gastroenterology And Hepatology. 2010 ;22(9) :1074-84.

[404] Ormachea J, Parker KJ. Comprehensive viscoelastic characterization of tissues and the inter-relationship of shear wave (group and phase) velocity, attenuation and dispersion. Ultrasound In Medicine And Biology. 2020 ;46(12) :3448-59.

[405] Hudson JM, Milot L, Parry C, Williams R, Burns PN. Inter- and intra-operator reliability and repeatability of shear wave elastography in the liver : A study in healthy volunteers. Ultrasound In Medicine And Biology. 2013 ;39(6) :950-5.

[406] Sugimoto K, Moriyasu F, Oshiro H, Takeuchi H, Yoshimasu Y, Kasai Y, et al. Viscoelasticity measurement in rat livers using shear-wave us elastography. Ultrasound In Medicine And Biology. 2018 ;44(9) :2018-24.

[407] Ormachea J, Parker KJ, Barr RG. An initial study of complete 2d shear wave dispersion images using a reverberant shear wave field. Physics In Medicine And Biology. 2019 ;64(14) :145009.

[408] Goddi A, Bonardi M, Alessi S. Breast elastography : A literature review. Journal Of Ultrasound. 2012 ;15(3) :192-8.

[409] Barr RG, Zhang Z. Shear-wave elastography of the breast : Value of a quality measure and comparison with strain elastography. Radiology. 2015 ;275(1) :45-53.

[410] Athanasiou A, Latorre-Ossa H, Criton A, Tardivon A, Gennisson JL, Tanter M. Feasibility of imaging and treatment monitoring of breast lesions with three-dimensional shear wave elastography. Ultraschall In Der Medizin - European Journal Of Ultrasound. 2015 ;38 :51-9.

[411] Crombé A, Hurtevent-Labrot G, Asad-Syed M, Palussière J, MacGrogan G, Kind M, et al. Shear-wave elastography quantitative assessment of the male breast : Added value to distinguish benign and malignant palpable masses. The British Journal Of Radiology. 2018 ;91(1082) :20170676.

[412] Gu J, Du L, Bai M, Chen H, Jia X, Zhao J, et al. Preliminary study on the diagnostic value of acoustic radiation force impulse technology for differentiating between benign and malignant thyroid nodules. Journal Of Ultrasound In Medicine. 2012 ;31(5) :763-71.

[413] Zhan J, Jin JM, Diao XH, Chen Y. Acoustic radiation force impulse imaging (arfi) for differentiation of benign and malignant thyroid nodules–a meta-analysis. European Journal Of Radiology. 2015 ;84(11) :2181-6.

[414] Veyrieres JB, Albarel F, Lombard JV, Berbis J, Sebag F, Oliver C, et al. A threshold value in shear wave elastography to rule out malignant thyroid nodules : A reality ? European Journal Of Radiology. 2012 ;81(12) :3965-72.

[415] Cantisani V, Lodise P, Grazhdani H, Mancuso E, Maggini E, Di Rocco G, et al. Ultrasound elastography in the evaluation of thyroid pathology. Current status. European Journal Of Radiology. 2014 ;83(3) :420-8.

[416] Magri F, Chytiris S, Capelli V, Alessi S, Nalon E, Rotondi M, et al. Shear wave elastography in the diagnosis of thyroid nodules : Feasibility in the case of coexistent chronic autoimmune hashimoto's thyroiditis. Clinical Endocrinology. 2012 ;76(1) :137-41.

[417] Dong FJ, Li M, Jiao Y, Xu JF, Xiong Y, Zhang L, et al. Acoustic radiation force impulse imaging for detecting thyroid nodules : A systematic review and pooled meta-analysis. Medical Ultrasonography. 2015 ;17(2) :192-9.

[418] Slapa RZ, Piwowonski A, Jakubowski WS, Bierca J, Szopinski KT, Slowinska-Srzednicka J, et al. Shear wave elastography may add a new dimension to ultrasound evaluation of thyroid nodules : Case series with comparative evaluation. Journal Of Thyroid Research. 2012 ;2012 :657147.

[419] Bhatia KSS, Cho CCM, Tong CSL, Yuen EHY, Ahuja AT. Shear wave elasticity imaging of cervical lymph nodes. Ultrasound In Medicine And Biology. 2012 ;38(2) :195-201.

[420] Sebag F, Vaillant-Lombard J, Berbis J, Griset V, Henry JF, Petit P, et al. Shear wave elastography : A new ultrasound imaging mode for the differential diagnosis of benign and malignant thyroid nodules. The Journal Of Clinical Endocrinology And Metabolism. 2010 ;95(12) :5281-8.

[421] Szczepanek-Parulska E, Woliński K, Stangierski A, Gurgul E, Biczysko M, Majewski P, et al. Comparison of diagnostic value of conventional ultrasonography and shear wave elastography in the prediction of thyroid lesions malignancy. Plos One. 2013 ;8(11) :e81532.

[422] Hu L, He NA, Xie L, Ye X, Liu X, Pei C, et al. Evaluation of the perinodular stiffness potentially predicts the malignancy of thyroid nodules. Journal Of Ultrasound In Medicine. 2020 ;39(11) :2183-93.

[423] You J, Chen J, Xiang F, Song Y, Khamis S, Lu C, et al. The value of quantitative shear wave elastography in differentiating the cervical lymph nodes in patients with thyroid nodules. Journal Of Medical Ultrasonics. 2018 ;45(2) :251-9.

[424] Samir AE, Dhyani M, Anvari A, Prescott J, Halpern EF, Faquin WC, et al. Shear-wave elastography for the preoperative risk stratification of follicular-patterned lesions of the thyroid : Diagnostic accuracy and optimal measurement plane. Radiology. 2015 ;277(2) :565-73.

[425] Wang M, Byram B, Palmeri M, Rouze N, Nightingale K. Imaging transverse isotropic properties of muscle by monitoring acoustic radiation force induced shear waves using a 2-d matrix ultrasound array. Ieee Transactions On Medical Imaging. 2013 ;32(9) :1671-84.

[426] Gennisson JL, Deffieux T, Macé E, Montaldo G, Fink M, Tanter M. Viscoelastic and anisotropic mechanical properties of in vivo muscle tissue assessed by supersonic shear imaging. Ultrasound In Medicine And Biology. 2010 ;36(5) :789-801.

[427] Eby SF, Cloud BA, Brandenburg JE, Giambini H, Song P, Chen S, et al. Shear wave elastography of passive skeletal muscle stiffness : Influences of sex and age throughout adulthood. Clinical Biomechanics. 2015 ;30(1) :22-7.

[428] Koo TK, Guo JY, Cohen JH, Parker KJ. Quantifying the passive stretching response of human tibialis anterior muscle using shear wave elastography. Clinical Biomechanics. 2014 ;29(1) :33-9.

[429] Cortes DH, Suydam SM, Silbernagel KG, Buchanan TS, Elliott DM. Continuous shear wave elastography : A new method to measure viscoelastic properties of tendons in vivo. Ultrasound In Medicine And Biology. 2015 ;41(6) :1518-29.

[430] Aubry S, Risson JR, Kastler A, Barbier-Brion B, Siliman G, Runge M, et al. Biomechanical properties of the calcaneal tendon in vivo assessed by transient shear wave elastography. Skeletal Radiology. 2013 ;42(8) :1143-50.

[431] Chen XM, Cui LG, He P, Shen WW, Qian YJ, Wang JR. Shear wave elastographic characterization of normal and torn achilles tendons : A pilot study. Journal Of Ultrasound In Medicine. 2013 ;32(3) :449-55.

[432] Bhatt M, Montagnon E, Destrempes F, Chayer B, Kazemirad S, Cloutier G. Acoustic radiation force induced resonance elastography of coagulating blood : Theoretical viscoelasticity modeling and ex-vivo experimentation. Physics In Medicine And Biology. 2018 ;63(6) :065018.

[433] Mfoumou E, Tripette J, Blostein M, Cloutier G. Time-dependent hardening of blood clots quantitatively measured in vivo with shear-wave ultrasound imaging in a rabbit model of venous thrombosis. Thrombosis Research. 2014 ;133(2) :265-71.

[434] Mercado-Shekhar KP, Kleven RT, Aponte Rivera H, Lewis R, Karani KB, Vos HJ, et al. Effect of clot stiffness on recombinant tissue plasminogen activator lytic susceptibility in vitro. Ultrasound In Medicine And Biology. 2018 ;44(12) :2710-27.

[435] Zheng X, Ji P, Mao H, Hu J. A comparison of virtual touch tissue quantification and digital rectal examination for discrimination between prostate cancer and benign prostatic hyperplasia. Radiology And Oncology. 2012 ;46(1) :69-74.

[436] Ahmad S, Cao R, Varghese T, Bidaut L, Nabi G. Transrectal quantitative shear wave elastography in the detection and characterisation of prostate cancer. Surgical Endoscopy. 2013 ;27(9) :3280-7.

[437] Rouvière O, Melodelima C, Hoang Dinh A, Bratan F, Pagnoux G, Sanzalone T, et al. Stiffness of benign and malignant prostate tissue measured by shear-wave elastography : A preliminary study. European Radiology. 2017 ;27(5) :1858-66.

[438] Boehm K, Salomon G, Beyer B, Schiffmann J, Simonis K, Graefen M, et al. Shear wave elastography for localization of prostate cancer lesions and assessment of elasticity thresholds : Implications for targeted biopsies and active surveillance protocols. The Journal Of Urology. 2015 ;193(3) :794-800.

[439] Woo S, Kim SY, Lee MS, Cho JY, Kim SH. Shear wave elastography assessment in the prostate : An intraobserver reproducibility study. Clinical Imaging. 2015 ;39(3) :484-7.

[440] Barr RG, Memo R, Schaub CR. Shear wave ultrasound elastography of the prostate : Initial results. Ultrasound Quarterly. 2012 ;28(1) :13-20.

[441] Correas JM, Tissier AM, Khairoune A, Vassiliu V, Méjean A, Hélénon O, et al. Prostate cancer : Diagnostic performance of real-time shear-wave elastography. Radiology. 2015 ;275(1) :280-9.

[442] Kolipaka A, McGee KP, Manduca A, Anavekar N, Ehman RL, Araoz PA. In vivo assessment of mr elastography-derived effective end-diastolic myocardial stiffness under different loading conditions. Journal Of Magnetic Resonance Imaging. 2011 ;33(5) :1224-8.

[443] Low G, Owen NE, Joubert I, Patterson AJ, Graves MJ, Glaser KJ, et al. Reliability of magnetic resonance elastography using multislice two-dimensional spin-echo echo-planar imaging (se-epi) and three-dimensional inversion reconstruction for assessing renal stiffness. Journal Of Magnetic Resonance Imaging. 2015 ;42(3) :844-50.

[444] Numano T, Mizuhara K, Hata J, Washio T, Homma K. A simple method for mr elastography : A gradient-echo type multi-echo sequence. Magnetic Resonance Imaging. 2015 ;33(1) :31-7.

[445] Perrinez PR, Kennedy FE, Van Houten EEW, Weaver JB, Paulsen KD. Magnetic resonance poroelastography : An algorithm for estimating the mechanical properties of fluid-saturated soft tissues. Ieee Transactions On Medical Imaging. 2010 ;29(3) :746-55.

[446] Asbach P, Klatt D, Schlosser B, Biermer M, Muche M, Rieger A, et al. Viscoelasticity-based staging of hepatic fibrosis with multifrequency mr elastography. Radiology. 2010 ;257(1) :80-6.

[447] Murphy MC, Huston J, Jack CR, Glaser KJ, Manduca A, Felmlee JP, et al. Decreased brain stiffness in alzheimer's disease determined by magnetic resonance elastography. Journal Of Magnetic Resonance Imaging. 2011 ;34(3) :494-8.

[448] Braun J, Guo J, Lützkendorf R, Stadler J, Papazoglou S, Hirsch S, et al. High-resolution mechanical imaging of the human brain by three-dimensional multifrequency magnetic resonance elastography at 7t. Neuroimage. 2014 ;90 :308-14.

[449] Riek K, Klatt D, Nuzha H, Mueller S, Neumann U, Sack I, et al. Wide-range dynamic magnetic resonance elastography. Journal Of Biomechanics. 2011 ;44(7) :1380-6.

[450] Rump J, Klatt D, Braun J, Warmuth C, Sack I. Fractional encoding of harmonic motions in mr elastography. Magnetic Resonance In Medicine. 2007 ;57(2) :388-95.

[451] Sahebjavaher RS, Frew S, Bylinskii A, ter Beek L, Garteiser P, Honarvar M, et al. Prostate mr elastography with transperineal electromagnetic actuation and a fast fractionally encoded steady-state gradient echo sequence. Nmr In Biomedicine. 2014 ;27(7) :784-94.

[452] Strasser J, Haindl MT, Stollberger R, Fazekas F, Ropele S. Magnetic resonance elastography of the human brain using a multiphase dense acquisition. Magnetic Resonance In Medicine. 2019 ;81(6) :3578-87.

[453] Doyley MM, Van Houten EE, Weaver JB, Poplack S, Duncan L, Kennedy F, et al. Shear modulus estimation using parallelized partial volumetric reconstruction. Ieee Transactions On Medical Imaging. 2004 ;23(11) :1404-16.

[454] Yin Z, Kearney SP, Magin RL, Klatt D. Concurrent 3d acquisition of diffusion tensor imaging and magnetic resonance elastography displacement data (dti-mre) : Theory and in vivo application. Magnetic Resonance In Medicine. 2017 ;77(1) :273-84.

[455] Papazoglou S, Hirsch S, Braun J, Sack I. Multifrequency inversion in magnetic resonance elastography. Physics In Medicine And Biology. 2012 ;57(8) :2329-46.

[456] Streitberger KJ, Diederichs G, Guo J, Fehlner A, Hamm B, Braun J, et al. In vivo multifrequency magnetic resonance elastography of the human intervertebral disk. Magnetic Resonance In Medicine. 2015 ;74(5) :1380-7.

[457] Streitberger KJ, Reiss-Zimmermann M, Freimann FB, Bayerl S, Guo J, Arlt F, et al. High-resolution mechanical imaging of glioblastoma by multifrequency magnetic resonance elastography. Plos One. 2014 ;9(10) :e110588.

[458] Neumann W, Schad LR, Zöllner FG. A novel 3d-printed mechanical actuator using centrifugal force for magnetic resonance elastography. In : 2017 39th Annual International Conference Of The Ieee Engineering In Medicine And Biology Society (Embc) ; 2017. p. 3541-4.

[459] Numano T, Kawabata Y, Mizuhara K, Washio T. Magnetic resonance elastography using an air ball-actuator. Magnetic Resonance Imaging. 2013 ;31(6) :939-46.

[460] Guenthner C, Kozerke S. Encoding and readout strategies in magnetic resonance elastography. Nmr In Biomedicine. 2018 ;31(10) :1-29.

[461] Hahn EL. Detection of sea-water motion by nuclear precession. Journal Of Geophysical Research. 1960 ;65(2) :776-7.

[462] Moran PR. A flow velocity zeugmatographic interlace for nmr imaging in humans. Magnetic Resonance Imaging. 1982 ;1(4) :197-203.

[463] Haacke EM, Brown RW, Thompson MR, Venkatesan R. Magnetic resonance imaging : Physical principles and sequence design. John Wiley and Sons ; 2014.

[464] Hahn EL. Free nuclear induction. Physics Today. 1953 ;6(11) :4-9.

[465] Muthupillai R, Rossman PJ, Lomas DJ, Greenleaf JF, Riederer SJ, Ehman RL. Magnetic resonance imaging of transverse acoustic strain waves. Magnetic Resonance In Medicine. 1996 ;36(2) :266-74.

[466] Okamoto RJ, Clayton EH, Bayly PV. Viscoelastic properties of soft gels : Comparison of magnetic resonance elastography and dynamic shear testing in the shear wave regime. Physics In Medicine And Biology. 2011 ;56(19) :6379-400.

[467] Sinkus R, Daire JL, Van Beers BE, Vilgrain V. Elasticity reconstruction : Beyond the assumption of local homogeneity. Comptes Rendus - Mecanique. 2010 ;338(7-8) :474-9.

[468] Sack I, McGowan CK, Samani A, Luginbuhl C, Oakden W, Plewes DB. Observation of nonlinear shear wave propagation using magnetic resonance elastography. Magnetic Resonance In Medicine. 2004 ;52(4) :842-50.

[469] Latta P, Gruwel MLH, Debergue P, Matwiy B, Sboto-Frankenstein UN, Tomanek B. Convertible pneumatic actuator for magnetic resonance elastography of the brain. Magnetic Resonance Imaging. 2011 ;29(1) :147-52.

[470] Solanas PS, Tse K, Koon V, Ratiney H, Millioz F, Caussy C, et al. Harmonic wideband simultaneous dual-frequency mr elastography. Nmr In Biomedicine. 2020 :e4442.

[471] Elgeti T, Steffen IG, Knebel F, Hättasch R, Hamm B, Braun J, et al. Time-resolved analysis of left ventricular shear wave amplitudes in cardiac elastography for the diagnosis of diastolic dysfunction. Investigative Radiology. 2016 ;51(1) :1-6.

[472] Elgeti T, Tzschätzsch H, Hirsch S, Krefting D, Klatt D, Niendorf T, et al. Vibration-synchronized magnetic resonance imaging for the detection of myocardial elasticity changes. Magnetic Resonance In Medicine. 2012 ;67(4) :919-24.

[473] Rump J, Warmuth C, Braun J, Sack I. Phase preparation in steady-state free precession mr elastography. Magnetic Resonance Imaging. 2008 ;26(2) :228-35.

[474] Bieri O, Maderwald S, Ladd ME, Scheffler K. Balanced alternating steady-state elastography. Magnetic Resonance In Medicine. 2006 ;55(2) :233-41.

[475] Doyley MM. Model-based elastography : A survey of approaches to the inverse elasticity problem. Physics In Medicine And Biology. 2012 ;57(3) :R35.

[476] Klatt D, Asbach P, Rump J, Papazoglou S, Somasundaram R, Modrow J, et al. In vivo determination of hepatic stiffness using steady-state free precession magnetic resonance elastography. Investigative Radiology. 2006 ;41(12) :841-8.

[477] Manduca A, Oliphant TE, Dresner MA, Lake DS, Greenleaf JF, Ehman RL. Comparative evaluation of inversion algorithms for magnetic resonance elastography. In : Proceedings Ieee International Symposium On Biomedical Imaging ; 2002. p. 997-1000.

[478] Babuska I, Suri M. Locking effects in the finite element approximation of elasticity problems. Numerische Mathematik. 1992 ;62(1) :439-63.

[479] Park E, Maniatty AM. Shear modulus reconstruction in dynamic elastography : Time harmonic case. Physics In Medicine And Biology. 2006 ;51(15) :3697-721.

[480] Eskandari H, Salcudean SE, Rohling R, Bell I. Real-time solution of the finite element inverse problem of viscoelasticity. Inverse Problems. 2011 ;27(8) :085002.

[481] Guo Z, You S, Wan X, Bićanić N. A fem-based direct method for material reconstruction inverse problem in soft tissue elastography. Computers And Structures. 2010 ;88(23-24) :1459-68.

[482] Hansen PC. Getting to Business : Discretizations of Linear Inverse Problems. In : Getting to business : Discretizations of linear inverse problems. Society for Industrial and Applied Mathematics ; 2010. p. 23-51.

[483] Zhang Y, Hall LO, Goldgof DB, Sarkar S. A constrained genetic approach for computing material property of elastic objects. Ieee Transactions On Evolutionary Computation. 2006 ;10(3) :341-57.

[484] McGarry MDJ, Van Houten EEW, Perrinez PR, Pattison AJ, Weaver JB, Paulsen KD. An octahedral shear strain-based measure of snr for 3d mr elastography. Physics In Medicine And Biology. 2011 ;56(13) :N153-64.

[485] Van Houten EEW, Viviers DvR, McGarry MDJ, Perriñez PR, Perreard II, Weaver JB, et al. Subzone based magnetic resonance elastography using a rayleigh damped material model. Medical Physics. 2011 ;38(4) :1993-2004.

[486] Van Houten EEW, Weaver JB, Miga MI, Kennedy FE, Paulsen KD. Elasticity reconstruction from experimental mr displacement data : Initial experience with an overlapping subzone finite element inversion process. Medical Physics. 2000 ;27(1) :101-7.

[487] Singh S, Venkatesh SK, Loomba R, Wang Z, Sirlin C, Chen J, et al. Magnetic resonance elastography for staging liver fibrosis in non-alcoholic fatty liver disease : A diagnostic accuracy systematic review and individual participant data pooled analysis. European Radiology. 2016 ;26(5) :1431-40.

[488] Singh S, Venkatesh SK, Wang Z, Miller FH, Motosugi U, Low RN, et al. Diagnostic performance of magnetic resonance elastography in staging liver fibrosis : A systematic review and meta-analysis of individual participant data. Clinical Gastroenterology And Hepatology. 2015 ;13(3) :440-51.e6.

[489] Huwart L, Peeters F, Sinkus R, Annet L, Salameh N, ter Beek LC, et al. Liver fibrosis : Non-invasive assessment with mr elastography. Nmr In Biomedicine. 2006 ;19(2) :173-9.

[490] Huwart L, Sempoux C, Salameh N, Jamart J, Annet L, Sinkus R, et al. Liver fibrosis : Non-invasive assessment with mr elastography versus aspartate aminotransferase–to-platelet ratio index. Radiology. 2007 ;245(2) :458-66.

[491] Salameh N, Larrat B, Abarca-Quinones J, Pallu S, Dorvillius M, Leclercq I, et al. Early detection of steatohepatitis in fatty rat liver by using mr elastography. Radiology. 2009 ;253(1) :90-7.

[492] Ronot M, Lambert SA, Wagner M, Garteiser P, Doblas S, Albuquerque M, et al. Viscoelastic parameters for quantifying liver fibrosis : Three-dimensional multifrequency mr elastography study on thin liver rat slices. Plos One. 2014 ;9(4) :e94679.

[493] Hiscox LV, Schwarb H, McGarry MDJ, Johnson CL. Aging brain mechanics : Progress and promise of magnetic resonance elastography. Neuroimage. 2021 ;232 :117889.

[494] Schregel K, Nazari N, Nowicki MO, Palotai M, Lawler SE, Sinkus R, et al. Characterization of glioblastoma in an orthotopic mouse model with magnetic resonance elastography. Nmr In Biomedicine. 2018 ;31(10) :e3840.

[495] Fehlner A, Behrens JR, Streitberger KJ, Papazoglou S, Braun J, Bellmann-Strobl J, et al. Higher-resolution mr elastography reveals early mechanical signatures of neuroinflammation in patients with clinically isolated syndrome. Journal Of Magnetic Resonance Imaging. 2016 ;44(1) :51-8.

[496] Schwarb H, Johnson CL, McGarry MDJ, Cohen NJ. Medial temporal lobe viscoelasticity and relational memory performance. Neuroimage. 2016 ;132 :534-41.

[497] Sandroff BM, Johnson CL, Motl RW. Exercise training effects on memory and hippocampal viscoelasticity in multiple sclerosis : A novel application of magnetic resonance elastography. Neuroradiology. 2017 ;59(1) :61-7.

[498] Johnson CL, Schwarb H, Horecka KM, McGarry MDJ, Hillman CH, Kramer AF, et al. Double dissociation of structure-function relationships in memory and fluid intelligence observed with magnetic resonance elastography. Neuroimage. 2018 ;171 :99-106.

[499] Schwarb H, Johnson CL, Dulas MR, McGarry MDJ, Holtrop JL, Watson PD, et al. Structural and functional mri evidence for distinct medial temporal and prefrontal roles in context-dependent relational memory. Journal Of Cognitive Neuroscience. 2019 ;31(12) :1857-72.

[500] Sinkus R, Lorenzen J, Schrader D, Lorenzen M, Dargatz M, Holz D. High-resolution tensor mr elastography for breast tumour detection. Physics In Medicine And Biology. 2000 ;45(6) :1649-64.

[501] Qin EC, Sinkus R, Geng G, Cheng S, Green M, Rae CD, et al. Combining mr elastography and diffusion tensor imaging for the assessment of anisotropic mechanical properties : A phantom study. Journal Of Magnetic Resonance Imaging. 2013 ;37(1) :217-26.

[502] Schmidt JL, Tweten DJ, Badachhape AA, Reiter AJ, Okamoto RJ, Garbow JR, et al. Measurement of anisotropic mechanical properties in porcine brain white matter ex vivo using magnetic resonance elastography. Journal Of The Mechanical Behavior Of Biomedical Materials. 2018 ;79 :30-7.

[503] Lilaj L, Fischer T, Guo J, Braun J, Sack I, Hirsch S. Separation of fluid and solid shear wave fields and quantification of coupling density by magnetic resonance poroelastography. Magnetic Resonance In Medicine. 2021 ;85(3) :1655-68.

[504] Majeed W, Kalra P, Kolipaka A. Simultaneous multislice rapid magnetic resonance elastography of the liver. Nmr In Biomedicine. 2020 ;33(4) :1-15.

[505] Kennedy BF, Wijesinghe P, Sampson DD. The emergence of optical elastography in biomedicine. Nature Photonics. 2017 ;11(4) :215-21.

[506] Ingber DE. Mechanobiology and diseases of mechanotransduction. Annals Of Medicine. 2003 ;35(8) :564-77.

[507] Di Carlo D. A mechanical biomarker of cell state in medicine. Journal Of Laboratory Automation. 2012 ;17(1) :32-42.

[508] Yang VXD, Munce N, Pekar J, Gordon ML, Lo S, Marcon NE, et al. Micromachined array tip for multifocus fiber-based optical coherence tomography. Optics Letters. 2004 ;29(1754-1756).

[509] Wang S, Singh M, Tran TT, Leach J, Aglyamov SR, Larina IV, et al. Biomechanical assessment of myocardial infarction using optical coherence elastography. Biomedical Optics Express. 2018 ;9(2) :728-42.

[510] Qu Y, Ma T, He Y, Zhu J, Dai C, Yu M, et al. Acoustic radiation force optical coherence elastography of corneal tissue. Ieee Journal Of Selected Topics In Quantum Electronics. 2016 ;22(3) :288-94.

[511] Crecea V, Oldenburg AL, Liang X, Ralston TS, Boppart SA. Magnetomotive nanoparticle transducers for optical rheology of viscoelastic materials. Optics Express. 2009 ;17(25) :23114-22.

[512] Li C, Huang Z, Wang RK. Elastic properties of soft tissue-mimicking phantoms assessed by combined use of laser ultrasonics and low coherence interferometry. Optics Express. 2011 ;19(11) :10153-63.

[513] Razani M, Mariampillai A, Sun C, Luk TWH, Yang VXD, Kolios MC. Feasibility of optical coherence elastography measurements of shear wave propagation in homogeneous tissue equivalent phantoms. Biomedical Optics Express. 2012 ;3(5) :972-80.

[514] Wang RK, Ma Z, Kirkpatrick SJ. Tissue doppler optical coherence elastography for real time strain rate and strain mapping of soft tissue. Applied Physics Letters. 2006 ;89(14) :144103.

[515] Zhu J, Qi L, Miao Y, Ma T, Dai C, Qu Y, et al. 3d mapping of elastic modulus using shear wave optical micro-elastography. Scientific Reports. 2016 ;6(1) :1-9.

[516] Nahas A, Bauer M, Roux S, Boccara AC. 3d static elastography at the micrometer scale using full field oct. Biomedical Optics Express. 2013 ;4(10) :2138-49.

[517] Nguyen TM, Song S, Arnal B, Huang Z, O'Donnell M, Wang RK. Visualizing ultrasonically induced shear wave propagation using phase-sensitive optical coherence tomography for dynamic elastography. Optics Letters. 2014 ;39(4) :838-41.

[518] Zhu J, Qu Y, Ma T, Li R, Du Y, Huang S, et al. Imaging and characterizing shear wave and shear modulus under orthogonal acoustic radiation force excitation using oct doppler variance method. Optics Letters. 2015 ;40(9) :2099-102.

[519] Nguyen TM, Arnal B, Song S, Huang Z, Wang RK, O'Donnell M. Shear wave elastography using amplitude-modulated acoustic radiation force and phase-sensitive optical coherence tomography. Journal Of Biomedical Optics. 2015 ;20(1) :016001.

[520] Wang S, Larin KV. Shear wave imaging optical coherence tomography (swi-oct) for ocular tissue biomechanics. Optics Letters. 2014 ;39(1) :41-4.

[521] Pitre J J J, Kirby MA, Li DS, Shen TT, Wang RK, O'Donnell M, et al. Nearly-incompressible transverse isotropy (niti) of cornea elasticity : Model and experiments with acoustic micro-tapping oce. Scientific Reports. 2020 ;10(1) :12983.

[522] Pelivanov I, Gao L, Pitre J, Kirby MA, Song S, Li D, et al. Does group velocity always reflect elastic modulus in shear wave elastography. Journal Of Biomedical Optics. 2019 ;24(7) :076003.

[523] Kirby MA, Pelivanov I, Song S, Ambrozinski L, Yoon SJ, Gao L, et al. Optical coherence elastography in ophthalmology. Journal Of Biomedical Optics. 2017 ;22(12) :1-28.

[524] Ambrozinski L, Pelivanov I, Song S, Yoon SJ, Li D, Gao L, et al. Air-coupled acoustic radiation force for non-contact generation of broadband mechanical waves in soft media. Applied Physics Letters. 2016 ;109(4) :043701.

[525] Alonso-Caneiro D, Karnowski K, Kaluzny BJ, Kowalczyk A, Wojtkowski M. Assessment of corneal dynamics with high-speed swept source optical coherence tomography combined with an air puff system. Optics Express. 2011 ;19(15) :14188-99.

[526] Wang S, Li J, Manapuram RK, Menodiado FM, Ingram DR, Twa MD, et al. Noncontact measurement of elasticity for the detection of soft-tissue tumors using phase-sensitive optical coherence tomography combined with a focused air-puff system. Optics Letters. 2012 ;37(24) :5184-6.

[527] Wang LV, Hu S. Photoacoustic tomography : In vivo imaging from organelles to organs. Science. 2012 ;335(6075) :1458-62.

[528] Liu Y, Yuan Z. Multi-spectral photoacoustic elasticity tomography. Biomedical Optics Express. 2016 ;7(9) :3323-34.

[529] Upputuri PK, Pramanik M. Recent advances toward preclinical and clinical translation of photoacoustic tomography : A review. Journal Of Biomedical Optics. 2017 ;22(4) :41006.

[530] Singh MS, Jiang H. Elastic property attributes to photoacoustic signals : An experimental phantom study. Optics Letters. 2014 ;39(13) :3970-3.

[531] Singh MS, Jiang H. Ultrasound (us) transducer of higher operating frequency detects photoacoustic (pa) signals due to the contrast in elastic property. Aip Advances. 2016 ;6(2) :025210.

[532] Zhao Y, Yang S, Chen C, Xing D. Simultaneous optical absorption and viscoelasticity imaging based on photoacoustic lock-in measurement. Optics Letters. 2014 ;39(9) :2565-8.

[533] Drakonaki EE, Allen GM, Wilson DJ. Ultrasound elastography for musculoskeletal applications. The British Journal Of Radiology. 2012 ;85(1019) :1435-45.

[534] Arnal B, Pernot M, Tanter M. Monitoring of thermal ablation therapy based on shear modulus changes : Shear wave thermometry and shear wave lesion imaging. In : 2010 Ieee International Ultrasonics Symposium ; 2010. p. 1522-5.

[535] Castera L, Denis J, Babany G, Roudot-Thoraval F. Evolving practices of non-invasive markers of liver fibrosis in patients with chronic hepatitis c in france : Time for new guidelines ? Journal Of Hepatology. 2007 ;46(3) :528-9.

[536] Deffieux T, Gennisson JL, Bousquet L, Corouge M, Cosconea S, Amroun D, et al. Investigating liver stiffness and viscosity for fibrosis, steatosis and activity staging using shear wave elastography. Journal Of Hepatology. 2015 ;62(2) :317-24.

[537] Golatta M, Schweitzer-Martin M, Harcos A, Schott S, Gomez C, Stieber A, et al. Evaluation of virtual touch tissue imaging quantification, a new shear wave velocity imaging method, for breast lesion assessment by ultrasound. Biomed Research International. 2014 ;2014 :960262.

[538] Palmeri ML, Wang MH, Rouze NC, Abdelmalek MF, Guy CD, Moser B, et al. Noninvasive evaluation of hepatic fibrosis using acoustic radiation force-based shear stiffness in patients with nonalcoholic fatty liver disease. Journal Of Hepatology. 2011 ;55(3) :666-72.

[539] Song P, Macdonald MC, Behler RH, Lanning JD, Wang MH, Urban MW, et al. Shear wave elastography on the ge logiq e9 with comb-push ultrasound shear elastography (cuse) and time aligned sequential tracking (tast). In : 2014 Ieee International Ultrasonics Symposium ; 2014. p. 1101-4.

[540] Tanter M, Fink M. Ultrafast imaging in biomedical ultrasound. Ieee Transactions On Ultrasonics, Ferroelectrics, And Frequency Control. 2014 ;61(1) :102-19.

[541] Zhou J, Zhan W, Chang C, Zhang J, Yang Z, Dong Y, et al. Role of acoustic shear wave velocity measurement in characterization of breast lesions. Journal Of Ultrasound In Medicine. 2013 ;32(2) :285-94.

[542] Aristizabal S, Amador Carrascal C, Nenadic IZ, Greenleaf JF, Urban MW. Application of acoustoelasticity to evaluate nonlinear modulus in ex vivo kidneys. Ieee Transactions On Ultrasonics, Ferroelectrics, And Frequency Control. 2018 ;65(2) :188-200.

[543] Caenen A, Pernot M, Peirlinck M, Mertens L, Swillens A, Segers P. An in silico framework to analyze the anisotropic shear wave mechanics in cardiac shear wave elastography. Physics In Medicine And Biology. 2018 ;63(7) :075005.

[544] Chen YL, Gao Y, Chang C, Wang F, Zeng W, Chen JJ. Ultrasound shear wave elastography of breast lesions : Correlation of anisotropy with clinical and histopathological findings. Cancer Imaging. 2018 ;18(1) :1-11.

[545] Gennisson J, Aristizabal S. Nonlinear shear elasticity. In : Nonlinear shear elasticity. John Wiley and Sons ; 2018. p. 451-69.

[546] Islam MT, Chaudhry A, Unnikrishnan G, Reddy JN, Righetti R. An analytical model of tumors with higher permeability than surrounding tissues for ultrasound elastography imaging. Journal Of Engineering And Science In Medical Diagnostics And Therapy. 2018 ;1(3) :031006.

[547] Islam MT, Reddy JN, Righetti R. An analytical poroelastic model of a nonhomogeneous medium under creep compression for ultrasound poroelastography applications—part i. Journal Of Biomechanical Engineering. 2019 ;141(6) :060902.

[548] Mariani A, Kwiecinski W, Pernot M, Balvay D, Tanter M, Clement O, et al. Real time shear waves elastography monitoring of thermal ablation : In vivo evaluation in pig livers. Journal Of Surgical Research. 2014 ;188(1) :37-43.

[549] Sapin-de Brosses E, Gennisson JL, Pernot M, Fink M, Tanter M. Temperature dependence of the shear modulus of soft tissues assessed by ultrasound. Physics In Medicine And Biology. 2010 ;55(6) :1701-18.

[550] Bohte AE, Nelissen JL, Runge JH, Holub O, Lambert SA, de Graaf L, et al. Breast magnetic resonance elastography : A review of clinical work and future perspectives. Nmr In Biomedicine. 2018 ;31(10) :e3932.

[551] Davids M, Guérin B, vom Endt A, Schad LR, Wald LL. Prediction of peripheral nerve stimulation thresholds of mri gradient coils using coupled electromagnetic and neurodynamic simulations. Magnetic Resonance In Medicine. 2019 ;81(1) :686-701.

[552] Yuan L, Glaser KJ, Rouviere O, Gorny KR, Chen S, Manduca A, et al. Preliminary assessment of one-dimensional mr elastography for use in monitoring focused ultrasound therapy. Physics In Medicine And Biology. 2007 ;52(19) :5909-19.

[553] Chen J, Woodrum DA, Glaser KJ, Murphy MC, Gorny K, Ehman R. Assessment of in vivo laser ablation using mr elastography with an inertial driver. Magnetic Resonance In Medicine. 2014 ;72(1) :59-67.

[554] Corbin N, Vappou J, Breton E, Boehler Q, Barbé L, Renaud P, et al. Interventional mr elastography for mri-guided percutaneous procedures. Magnetic Resonance In Medicine. 2016 ;75(3) :1110-8.

[555] Wu T, Felmlee JP, Greenleaf JF, Riederer SJ, Ehman RL. Assessment of thermal tissue ablation with mr elastography. Magnetic Resonance In Medicine. 2001 ;45(1) :80-7.

[556] Guenthner C, Sethi S, Troelstra M, van Gorkum RJH, Gastl M, Sinkus R, et al. Unipolar mr elastography : Theory, numerical analysis and implementation. Nmr In Biomedicine. 2020 ;33(1) :e4138.

[557] Girardo S, Träber N, Wagner K, Cojoc G, Herold C, Goswami R, et al. Standardized microgel beads as elastic cell mechanical probes. Journal Of Materials Chemistry B. 2018 ;6(39) :6245-61.

[558] Guck J. Some thoughts on the future of cell mechanics. Biophysical Reviews. 2019 ;11(5) :667-70.

[559] Hao Y, Cheng S, Tanaka Y, Hosokawa Y, Yalikun Y, Li M. Mechanical properties of single cells : Measurement methods and applications. Biotechnology Advances. 2020 ;45 :107648.

[560] Fu J, Pierron F, Ruiz PD. Elastic stiffness characterization using three-dimensional full-field deformation obtained with optical coherence tomography and digital volume correlation. Journal Of Biomedical Optics. 2013 ;18(12) :121512.

[561] Curatolo A, Villiger M, Lorenser D, Wijesinghe P, Fritz A, Kennedy BF, et al. Ultrahigh-resolution optical coherence elastography. Optics Letters. 2016 ;41(1) :21-4.

[562] Leroux CE, Palmier J, Boccara AC, Cappello G, Monnier S. Elastography of multicellular aggregates submitted to osmo-mechanical stress. New Journal Of Physics. 2015 ;17(7) :073035.

[563] Pokharel D, Wijesinghe P, Oenarto V, Lu JF, Sampson DD, Kennedy BF, et al. Deciphering cell-to-cell communication in acquisition of cancer traits : Extracellular membrane vesicles are regulators of tissue biomechanics. Journal Of Integrative Biology. 2016 ;20(8) :462-9.

[564] Graff KF. Wave motion in elastic solids. Courier Corporation ; 2012.

Chapitre A

Informations supplémentaires pour l'article "Imaging the subcellular viscoelastic properties of mouse oocytes"

A.1. Note 1 : Advantages of NLI over other reconstruction techniques

In the first description of optical microelastography [**2, 303**], the "passive elastography" scheme was employed to recover shear stiffness distributions μ_s using a single motion component along with a purely elastic mechanical model (no damping) assuming local homogeneity, as detailed elsewhere [**304, 109, 108**]. However, biological tissues are known to be better described as heterogeneous viscoelastic or poroelastic materials [**305**]. Passive elastography relies on an undamped formulation of the Helmholtz wave equation, where the symmetry with respect to time is invoked to evaluate the time-reversed wave field from spatiotemporal correlations of the measured displacements across the image. The diameters of resulting focal spots relate to the approximate wavelengths λ of the elastic field according to the Rayleigh criterion. Although elegant and time efficient, this time-reversal approach is no longer valid in viscoelastic, *i.e.*, damped materials, where the material-driven attenuation of mechanical oscillations breaks the time reciprocity. Additionally, the elastic approximation

$\mu_s = \rho\,(\lambda f)^2$, where f is the actuation frequency and ρ is the material's density, requires the measured elastic field be shear waves. This shear wave assumption is significantly challenged in micron and submicron scale confined cellular domains which restricts the reconstruction to wave parameters (λ or speed c), instead of material biomechanical properties, as suggested in [**279**]. Finally, guidelines for the preselection of the motion component to use in the inversion procedure are rarely discussed.

The direct inversion of the algebraic wave equation has attracted a wide interest for the evaluation of the complex-valued viscoelastic shear modulus despite the required evaluation of second- to third-order displacement derivatives [**13, 61**]. Other schemes relating measurements of wave propagation velocity and attenuation on one hand to the complex shear modulus on the other hand have also been investigated [**306, 89, 307**]. Although reasonably simple to implement and computationally affordable, these techniques operate directly on the measured displacement field, rendering the reconstruction process prone to high sensitivity to noise. Moreover, restrictive assumptions on the wave front geometry (plane, cylindrical, spherical), wave type (pure shear versus general elastic), and tissue nature, such as local homogeneity, weaken the interpretability of final mechanical parameter estimates. The inherent heterogeneity of biological tissues and the proven pathology-driven structural changes highlight the importance of a heterogeneous mechanical parameter support [**13**]. To date, contributions to the field of optical microelastography have focused on wave tracking [**308**] and high frequency elastic wave behaviour in gel phantoms [**279**], but no work has been reported on alternative characterization procedures to image the viscoelasticity in live cells.

Here, the overlapping subzone NLI approach [**116**] was used to recover complex-valued shear modulus distributions. Among the many options available in the literature, this choice was motivated by three criteria. First, heterogeneous property descriptions are supported as opposed to most direct strategies where property gradients are neglected to stabilize local inversions [**65, 71, 136, 89, 61**]. Second, the low compressibility found in most biological tissues [**231**] is handled by the introduction of both an additional equation and a pressure term as in [**122**]. This approach is distinguished from the more common isolation of the elastic

field's compression component through extensive spatial filtering or formal extraction of the shear component, at the cost of high-order differentiation of the noisy displacement data. Finally, complex elastic fields of relatively large wavelengths (on the order of the domain scale), similarly to that generated under the available actuation frequency in optical microelastography, cannot be associated to simple shear waves and have been shown to depend on mechanical properties and domain geometry, thus requiring explicit integration of boundary condition information in the reconstruction process [**279**]. In NLI, the generalized boundary value problem does not assume the presence of bulk shear waves. Numerical simulations of the boundary value problem are computed iteratively using successive sets of material property updates until the simulated displacements match the measured displacements in a least-squared sense. Boundary conditions are thus supplied to the forward finite element algorithm under the form of displacement values extracted from the actual measured data. Fig. 23 shows microelastography reconstructions from previous (using the same data set as [**2**]) and presented works. The attenuation-free shear stiffness map from previous work has been converted back to speed values, *i.e.*, $c = \sqrt{\mu_s/\rho}$, due to the violation of the shear wave assumption [**279**]. For comparison, the transparency map in previous work has been removed and anatomical and property images are displayed side-by-side instead of superimposed. The shear stiffness computed with NLI is defined by $\mu_s = 2\frac{|\mu_r+i\mu_i|^2}{\mu_r+|\mu_r+i\mu_i|}$, where μ_r and μ_i are the reconstructed storage and loss moduli, respectively. The presented microelastography pipeline results in more detailed property maps where individual regions (nucleolus, nucleus, cytoplasm, perivitelline space, and zona pellucida) are clearly outlined and distinguishable.

A.2. Note 2 : Full-field displacement approximation

The rationale for full-field displacement data approximation from in-plane measurements is described in this section. GV-stage oocytes have been commonly described as symmetrical cells. This characteristic, combined with an in-plane actuation at the central symmetry level of the oocyte, allows to infer the motion component variations in the vicinity of this central slice. A 3D oocyte displacement model was built to demonstrate the assumptions underlying

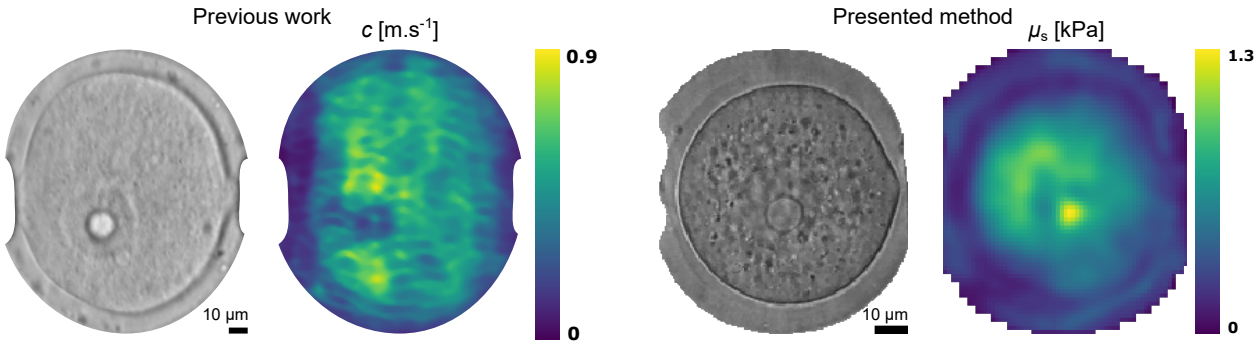

Figure 23 – Microelastography reconstructions from previous [2] and presented works. c is the speed of the elastic wave satisfying the wave propagation equation, and μ_s is the shear stiffness of the oocyte.

the approximation of full-field displacements. Fig 24 shows the variations of motion component amplitudes $|u|$, $|v|$, and $|w|$ averaged in (x,y) planes along the z axis in the upper half ($z = 0\,\mu$m to $z = 45\,\mu$m) of a simulated 3D oocyte domain. The slice located at $z = 0\,\mu$m is the plane of symmetry of the oocyte model and motion components u, v, and w are oriented along the x, y, and z axes, respectively.

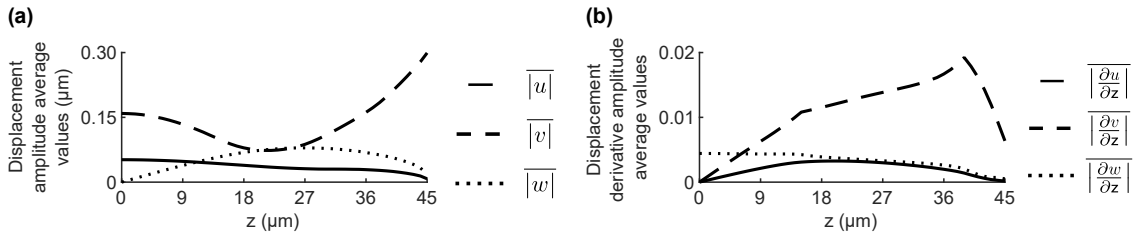

Figure 24 – Variations along the z axis of motion component amplitude average values.

In Fig. 24.a, components $\overline{|u|}$ and $\overline{|v|}$ are nonzero at every slice location along the z axis, whereas $\overline{|w|}$ is zero in the central plane and progressively increases. This indicates the following motion variations :

$$\begin{cases} w = 0 & \text{if } z = 0, \\ w \neq 0 & \text{if } z \neq 0, \\ u \neq 0 & \forall z, \\ v \neq 0 & \forall z. \end{cases} \tag{96}$$

In Fig. 24.b, $\overline{\left|\frac{\partial u}{\partial z}\right|}$ and $\overline{\left|\frac{\partial v}{\partial z}\right|}$ are zero or small in the central plane and its vicinity, respectively, and grow at increased distances from $z = 0$ µm. On the contrary, $\overline{\left|\frac{\partial w}{\partial z}\right|}$ is nonzero at $z = 0$ µm and progressively decreases. This indicates the following motion variations :

$$u_{z_0} \approx u_{z_0+\delta z}, \tag{97}$$

$$v_{z_0} \approx v_{z_0+\delta z}, \tag{98}$$

$$w_{z_0} \neq w_{z_0+\delta z}, \tag{99}$$

where $z_0 = 0$ µm. These observations support the effort for displacement recovery in the neighborhood of the measured central plane. In particular, the incompressibility of biological tissues [**231**] enables the approximation of the out-of-plane component w through $\nabla \cdot \mathbf{u} = 0$ (local incompressibility), which represents an alternative to the more common approach of invoking plane strain when tomographic data are measured.

A.3. Note 3 : Experiment-based full and partial convergence rates from two representative oocytes

Two typical convergence profiles were observed in the presented work and are shown in Fig. S3 through two representative oocytes. The storage modulus reconstructions performed on the 21 treated oocytes all converged to a stable distribution (μ_r curves for the representative oocytes 1 and 2 in Fig. S3). Out of the 21 corresponding loss modulus reconstructions, 13 converged to a stable distribution (plateau in the convergence profile of the representative oocyte 1 for μ_i) and 8 continued to progress towards lower values (slope in the convergence profile of the representative oocyte 2 for μ_i). In general, the loss modulus is responsible for subtle variations in the shape of the induced wave field and is more difficult to identify, especially when the wavelength is long, than the storage modulus, which is most responsible for this wavelength. This explains the overall higher sensitivity of the algorithm to storage than loss modulus contrasts.

The partial convergence observed here suggests that the algorithm has identified a relative distribution of loss modulus values and pursues the reconstruction by promoting property updates that lead to a global scaling with additional iterations. This is shown in Figs. 3.e and 3.f in the article, where the map of the partially converged loss modulus is consistent with its fully converged counterpart but shows lower magnitude values and spatial variations of lower definition.

This characteristics might be indicative of a natural biological variability where the elastic wave attenuating behavior of some oocytes might be slightly lower than in others, and which would translate into attenuation effects even harder to detect in the measured wave field. Although the oocytes in question would remain fully viscoelastic in terms of the elastic versus viscous contribution, slightly lower loss modulus values in this already low and narrow range (within a few hundreds of Pascals) might have hindered the generation of a quantitative property update.

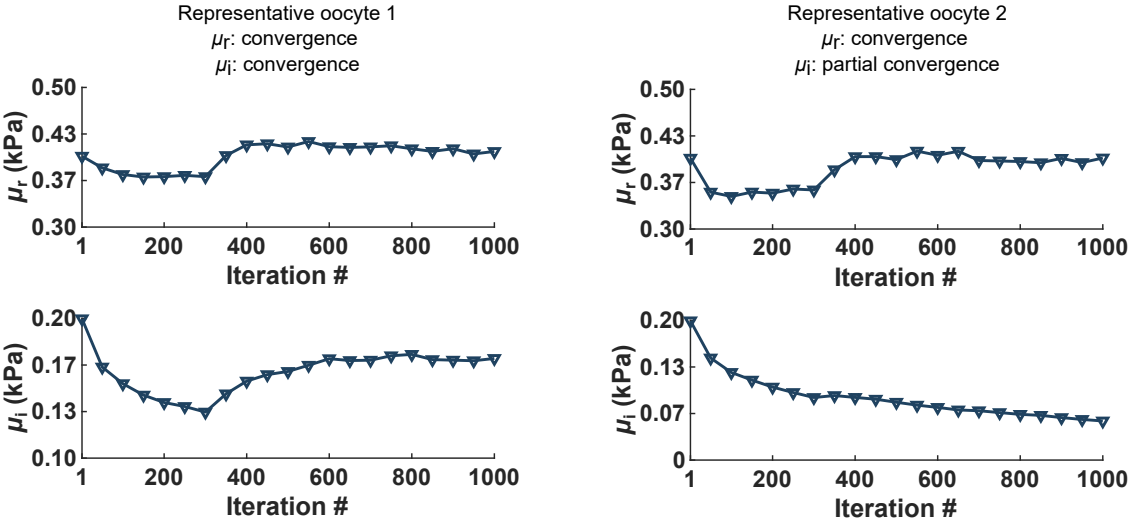

Figure 25 – Full and partial convergence rates from two representative oocytes.

A.4. Note 4 : Reconstructions from true full-field displacements

The proposed method introduces an important advance in the field of optical microelastography. However, future work involving metaphase-II stage oocytes and early fertilized

embryos in the context of *in vitro* fertilization will require the measurement of actual true volume data to leverage the full potential of the proposed pipeline, and extend its applicability to cells of arbitrary shapes. Fig. 26 shows maps of relative reconstruction errors when the true 14.4-kHz full-field displacements simulated in the oocyte model, with the shear modulus distributions μ_1 and μ_2 described in the article, are used for inversion. Storage modulus reconstructions with reasonable to numerical precision accuracy could be recovered from both μ_1 and μ_2 displacement data, the loss modulus reconstructed from μ_2 displacement data also presented a reasonable accuracy, and the loss modulus reconstructed from μ_1 displacement data showed the highest error levels, which was expected due to the long wavelength of the induced vibrations.

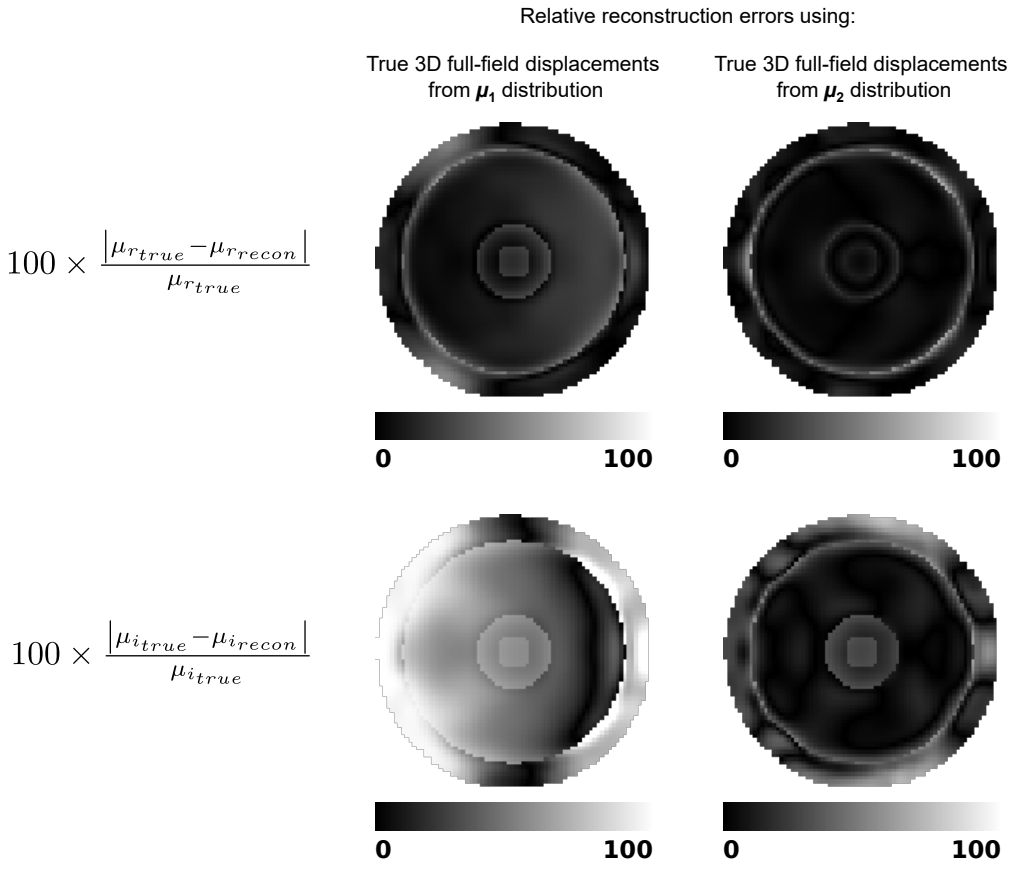

Figure 26 – Maps of the NLI reconstruction errors using simulated true 3D full-field displacements.

A.5. Note 5 : Selection of the zone size and interslice distance

The division of the total region of interest into a collection of subzones randomly distributed permits to handle the reconstruction and its computational cost, irrespective of the mechanical property's potential spatial variations, which cannot always be anticipated. Nevertheless, constraints are placed on the size of those subzones relatively to the wavelength of the measured wave field, which is governed by the mechanical properties of the scanned tissue and the actuation frequency. Once the subzone size is fixed, no constraint is placed on the storage and loss modulus relative spatial variations, *i.e.*, the algorithm identifies the property updates freely.

Previous works have demonstrated that the subzone size plays an important role in the reconstruction process and that mechanical contrasts in the imaged material could be recovered from the collected motion fields with subzone size to wavelength ratios of various extents [**309, 310, 281, 282**]. In particular, experimental conditions involving different wavelengths were investigated and allowed establishing guidelines to resolve property distributions in the material. However, these guidelines were established using true 3D-displacement data acquired with magnetic resonance elastography.

In our work, 2D displacements were estimated from optical microscopy images and expanded to an approximated 3D data set using an oocyte geometry-based 3D mechanical motion model. This step introduced an additional parameter to optimize (the interslice distance), which, together with the subzone size, were found to be competing reconstruction variables in the present situation where elastic fields of long wavelengths were induced. Consequently, guidelines adapted to our experimental conditions were proposed by studying these two parameters and their joint impact on the recovered property maps.

In practice, inversion configurations allowing stable reconstructions while minimizing the computational needs are preferred. A stability study was conducted in this respect to identify a suitable subzone size - interslice distance combination. Five interslice distances ranging from $\delta z_1 = 0.25$ µm to $\delta z_5 = 1.25$ µm were used to assess the impact of the local

approximation discretization, which remains valid in the vicinity of the central plane, along with three subzone isotropic sizes, $zs_1 = 20$ µm, $zs_2 = 30$ µm, and $zs_3 = 40$ µm. Zone sizes smaller than 20 µm would cover less than 25 % of the wavelength, which would further challenge the reconstruction, and sizes greater than 40 µm would be inconsistent with the advantages of the subzone decomposition.

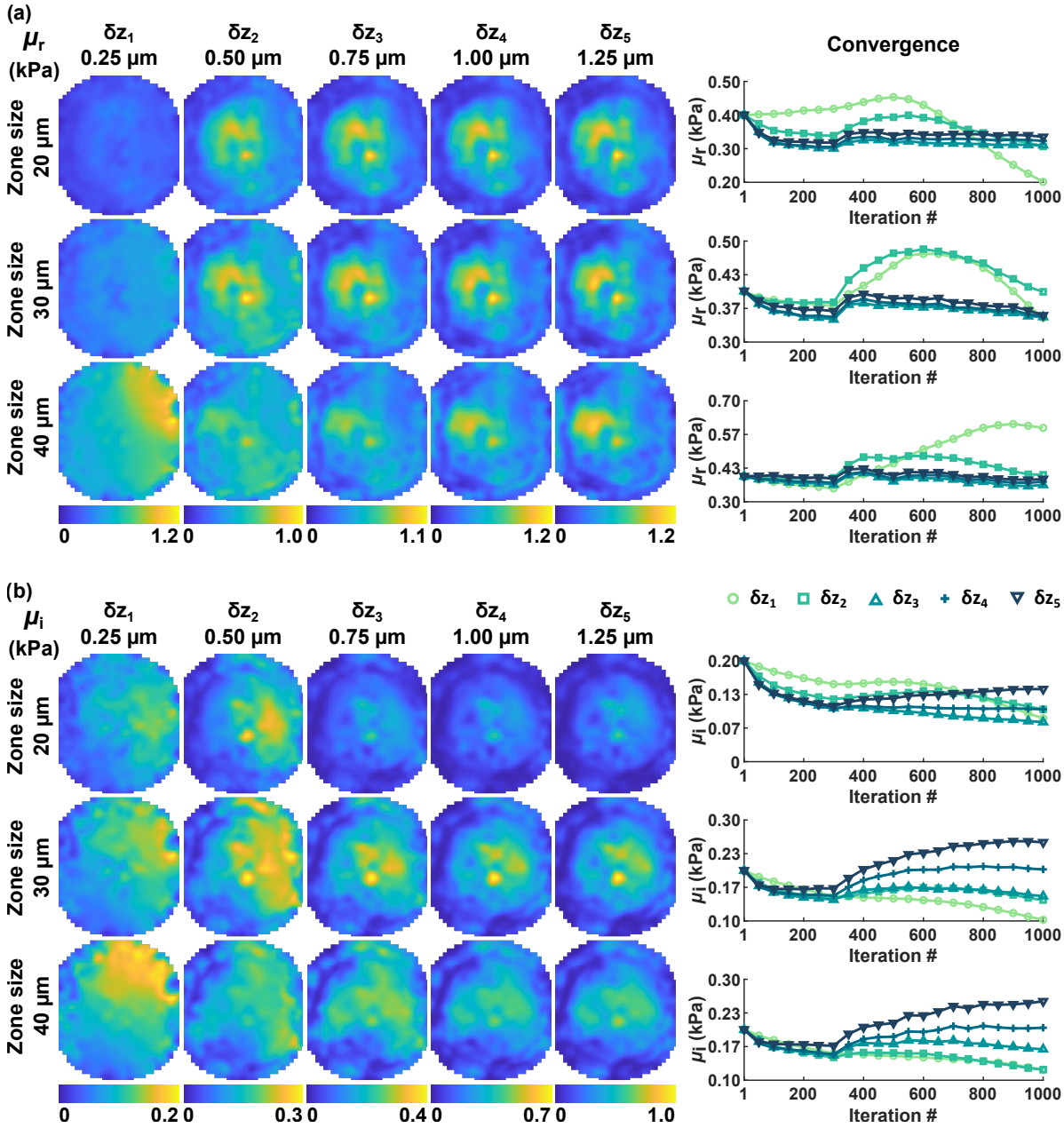

Figure 27 – Impact of the interslice distance δz and of the zone size zs on the recovered property images.

Fig. 27.a shows reconstructions of the storage modulus with the five interslice distances and three zone sizes. Fig. 27.b shows the corresponding reconstructions of the loss modulus. The property images indicate that the computation of the inverse problem performed better with a larger discretization of the local divergence-free approximation, as the smallest interslice distance ($\delta z_1 = 0.25$ µm) resulted in the poorest contrast quality between inner structures of the representative oocyte. The different scales observed in the estimated properties, alongside zone size variations, are consistent with reconstruction behaviours reported in low frequency and intrinsic MR elastography, where the low-frequency, long-wavelength condition precludes absolute property recovery [**282**]. The right panels of Fig. 27.a and 27.b display the convergence rates of the iterative reconstructions indicated by the average value of the property across the entire domain.

In this context of optical microelastography, the selection of the optimal interslice distance and zone size was addressed by evaluating the relative variations of the recovered properties with respect to each parameter using finite-difference derivatives, *i.e.*, $\overline{\left|\frac{\partial \theta}{\partial zs}\right|}/\sigma_\theta$ and $\overline{\left|\frac{\partial \theta}{\partial \delta z}\right|}/\sigma_\theta$, where θ represents the storage (μ_r) or loss (μ_i) modulus. Fig. 28 shows these relative variations for each combination of interslice distance and subzone size. The optimal

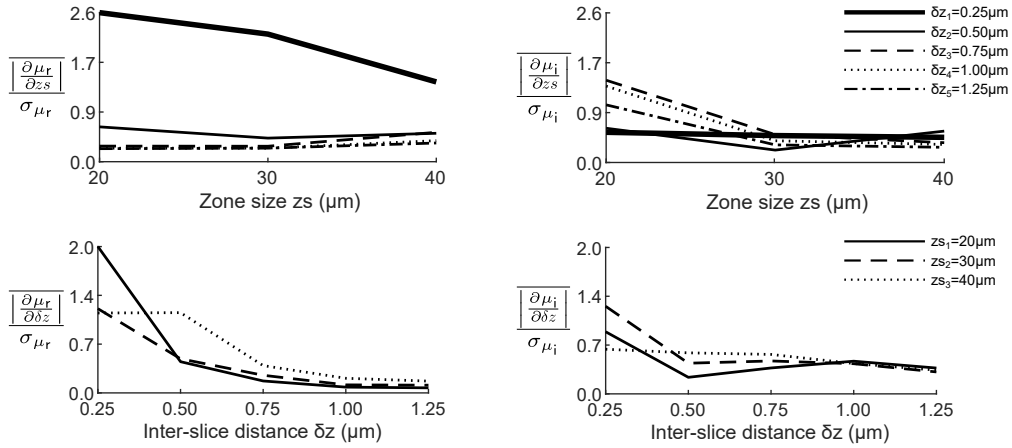

Figure 28 – Selection of the optimal interslice distance and zone size. The relative variations of the reconstructed properties are reported in percentage of the property's standard deviation calculated in each segment (nucleolus, nucleus, cytoplasm, perivitelline space, and zona pellucida) and averaged across all segments.

configuration was identified by the minimum values of $\overline{\left|\frac{\partial \theta}{\partial zs}\right|}/\sigma_\theta$ and $\overline{\left|\frac{\partial \theta}{\partial \delta z}\right|}/\sigma_\theta$ shared by μ_r and μ_i. Reconstructions involving δz_1 and δz_2 were discarded due to their poor convergence

rates, as indicated in Fig. 28. Amongst the remaining parameters, δz_3 to δz_5 and zs_1 to zs_3, a shared minimum was found for the ($\delta z_5 = 1.25$ µm, $zs_2 = 30$ µm) combination.

Chapitre B

Viscoelasticity imaging of biological tissues and single cells using shear wave propagation

Ce chapitre repose sur l'article intitulé "Viscoelasticity imaging of biological tissues and single cells using shear wave propagation" publié en 2021 dans le journal *Frontiers in Physics* par Hongliang Li*, Guillaume Flé*, Manish Bhatt, Zhen Qu, Sajad Ghazavi, Ladan Yazdani, Guillaume Bosio, Iman Rafati et Guy Cloutier.

Contribution des auteurs

Hongliang Li et Guillaume Flé partagent le rôle d'auteur principal de cet article, comme indiqué sur la version publiée, en raison de leurs contributions majeures et égales à la revue bibliographique ainsi qu'à la conception du document.

Hongliang Li* : supervision et structuration de la revue, rédaction de l'introduction et de la conclusion, contribution à la sous-section "Generation and detection of shear waves",

Guillaume Flé* : supervision et structuration de la revue, rédaction de la sous-section "General concepts in shear wave elastography" et de la section "Magnetic resonance elastography",

Manish Bhatt : rédaction des sous-sections "Optical cohérence elastography imaging" et "Photoacoustic elastography",

Zhen Qu : rédaction de la sous-section “Characterization of tissue viscoelasticity” et contribution à la sous-section “Generation and detection of shear waves”,

Sajad Ghazavi : rédaction de la sous-section “Cellular shear wave elastography”,

Ladan Yazdani : rédaction de la sous-section “Viscoelasticity reconstruction and applications in ultrasound”,

Guillaume Bosio : rédaction de la sous-section “Clinical applications of ultrasound shear wave elastography”,

Iman Rafati : contribution à la section “Ultrasound shear wave elastography”,

Guy Cloutier : réception de l’invitation à la rédaction de la revue, contribution à la supervision générale de tous les auteurs, révision du document pour approbation finale, édition et financement.

Résumé

Les changements de propriétés biomécaniques des tissus mous biologiques sont souvent associés à des dysfonctionnements physiologiques. La teneur en eau de ces tissus rend la viscoélasticité appropriée à la description de leur composante solide à l’aide de l’élasticité et de leur composante fluide à l’aide de la viscosité. L’élastographie par ondes de cisaillement, développée en vue d’applications cliniques d’imagerie non-invasive, présente des atouts d’intérêt pour la caractérisation de la viscoélasticité de divers tissus. Celle-ci repose sur la mesure et l’analyse des vitesses et de l’atténuation de ces ondes mécaniques à travers le suivi de leur propagation dans le milieu imagé. Cette revue de littérature expose les principes de la méthode d’élastographie par ondes de cisaillement permettant la caractérisation de la viscoélasticité de différents tissus, de l’organe entier à la cellule unique, et présente les modalités d’imagerie employées pour le suivi de la propagation des ondes de cisaillement : les ultrasons, la résonance magnétique, les approches optiques et photoacoustiques. Les méthodes de génération de ces ondes sont présentées, du transducteur macroscopique aux micro-pipettes vibrantes en passant par la pression de radiation acoustique et la force de Lorentz. Des

exemples d'application sont donnés et illustrent la mise en oeuvre de chaque approche de l'élastographie. Enfin, les limites actuelles et orientations futures sont discutées.
Mots clés : Viscoelasticité linéaire, élastographie, ondes de cisaillement, imagerie ultrasonore, imagerie par résonance magnétique, imagerie optique, tomographie de cohérence optique, imagerie photoacoustique

Abstract

Changes in biomechanical properties of biological soft tissues are often associated with physiological dysfunctions. Since biological soft tissues are hydrated, viscoelasticity is likely suitable to represent its solid-like behavior using elasticity and fluid-like behavior using viscosity. Shear wave elastography is a non-invasive imaging technology invented for clinical applications that has shown promise to characterize various tissue viscoelasticity. It is based on measuring and analyzing velocities and attenuations of propagated shear waves. In this review, principles and technical developments of shear wave elastography for viscoelasticity characterization from organ to cellular levels are presented, and different imaging modalities used to track shear wave propagation are described. At a macroscopic scale, techniques for inducing shear waves using an external mechanical vibration, an acoustic radiation pressure or a Lorentz force are reviewed along with imaging approaches proposed to track shear wave propagation, namely ultrasound, magnetic resonance, optical, and photoacoustic means. Then, approaches for theoretical modeling and tracking of shear waves are detailed. Following it, some examples of applications to characterize the viscoelasticity of various organs are given. At a microscopic scale, a novel cellular shear wave elastography method using an external vibration and optical microscopy is illustrated. Finally, current limitations and future directions in shear wave elastography are presented.
Mots clés: Linear Viscoelasticity, Elastography, Mechanical Shear Waves, Ultrasound Imaging, Magnetic Resonance Imaging, Optical Imaging, Optical Coherence Tomography, Photoacoustic Imaging

B.1. Introduction

Changes in mechanical properties of biological soft tissues are often associated with physiological dysfunctions. Viscoelasticity is an important mechanical biomarker to characterize structural changes and/or constituents of tissues. However, the assessment of elasticity through imaging has been more often exploited than viscosity, and an historical perspective of development has been to replace manual palpation by physicians and to answer an ultimate and natural question: "is the region hard or soft?" The elasticity, represented by the Young's modulus E, is able to characterize tissue deformation by using a linear relationship between stress σ and strain ϵ as $E = \sigma/\epsilon$. The rationale behind the elasticity assessment of biological soft tissues is that Young's moduli of different types of human tissues differ by a few orders of magnitude [**311**], and are affected by the presence of a pathology.

Since biological soft tissues are hydrated, they are not only represented by their solid-like behavior using elasticity, but also by their fluid-like behavior using viscosity. Viscosity represents the hysteretic effect between stress and strain applied on a tissue. It is becoming an important biomarker of pathological changes in biological tissues. Mechanical test is the most basic method to measure the viscosity of *ex vivo* soft tissues. To this end, a constant strain is applied to a test specimen. The stress relaxation with time is used to characterize the viscosity of the tissue. Another way of mechanical test is dynamic mechanical analysis. Periodic strain or stress is imposed on a specimen. The dynamic responses in terms of different incentive frequencies are associated with tissue viscoelasticity. Relevant works on mechanical testing of biological soft tissues can be found in [**312, 82, 313, 314, 315, 316**]. Alternatively, imaging-based approaches are becoming more popular for *in vivo* viscoelasticity assessment. These approaches exploit tissue deformations in acoustic, magnetic or optical fields to characterize viscoelasticity in a non-invasive manner. Soft tissues can maintain their function during the measurement avoiding destructive testing. Based on a clinical perspective, the *in situ* and localized assessment of tissue viscoelasticity through imaging had major impacts on diagnosis (*e.g.*, cancers, liver fibrosis, musculoskeletal disorders, cardiovascular

diseases, etc). Since biological tissues consist of cells, extracellular matrices, structural proteins, a recent field of development has been to study sub-cellular biomechanical properties associated with pathological processes through imaging. This finding encouraged researchers to impel bio-elasticity research further into a microscopic scale.

This review aims to provide a state-of-the-art summary of developments made in the field of shear wave elastography, which concerns elasticity and viscosity imaging through mechanical shear wave analysis. This technology requires a shear wave source, the tracking of shear wave propagation through imaging, and the processing of the shear wave propagation characteristics through physical models or image processing algorithms. Shear waves can be generated by external or internal vibrating sources. An external mechanical actuator in physical contact with an organ or cell is a common way to induce shear wave propagation from the surface to the core, whereas acoustic radiation or Lorentz forces can be used as internal *in situ* localized shear wave sources. The detection of the shear wave propagation is usually performed using ultrasound (US), magnetic resonance (MR), optical or photoacoustic imaging methods. Elasticity and viscosity can be obtained from estimations of shear storage and loss moduli, which require the determination of the shear wave velocity and attenuation into the interrogated medium. In the following sections, the generation and tracking of shear waves are described. Determining elasticity and viscosity maps through the solution of an inverse problem based on elastic wave propagation equations and underlying assumptions are also addressed throughout the text. Note that this review is not intended to detail artefacts and confounders of shear wave imaging because these are organ, tissue structure, and tissue pathology specific. Nevertheless, such information is presented briefly in some sections.

B.2. Biomechanical principles of shear wave elastography

B.2.1. General concepts in shear wave elastography

The major approach since the early steps of elastography imaging has been to approximate the tissue as isotropic and purely elastic. This situation has been widely described so the main constitutive relations essential to understand the shear wave elastography (SWE) technique are recalled here. The relationship between the applied stress and the strain response of the solicited tissue is given by Hooke's law:

$$\sigma_{ij}\left(\mathbf{r},t\right) = c_{ijkl}\left(\mathbf{r},t\right)\epsilon_{kl}\left(\mathbf{r},t\right), \tag{100}$$

where T and S are the stress and strain tensors, respectively, and c_{ijkl} contain the elastic parameters of interest. Under the assumption of small deformations, the strain tensor is given by:

$$\epsilon_{ij}\left(\mathbf{r},t\right) = \frac{1}{2}\left(\nabla\mathbf{u} + \left(\nabla\mathbf{u}\right)^{T}\right), \tag{101}$$

where $\mathbf{u}$ is the 3-dimensional motion field in unit of (m) induced by stressing the tissue. The time domain wave equation describing the propagation of the local displacements is obtained using Newton's second law:

$$\rho\frac{\partial^2\mathbf{u}\left(\mathbf{r},t\right)}{\partial t^2} = \nabla\cdot\sigma\left(\mathbf{r},t\right) + \mathbf{f}\left(\mathbf{r},t\right), \tag{102}$$

where ρ is the material's density in ($\mathrm{kg.m^{-3}}$) and $\mathbf{f}$ ($\mathrm{N.m^{-3}}$) is the source term. After Fourier transform into the frequency domain, equations (100), (101) and (102) are expressed as:

$$\tilde{\sigma}_{ij}\left(\mathbf{r},t\right) = c^{*}_{ijkl}\left(\mathbf{r},t\right)\tilde{\epsilon}_{kl}\left(\mathbf{r},t\right), \tag{103}$$

$$\tilde{\epsilon}_{ij}\left(\mathbf{r},t\right) = \frac{1}{2}\left(\nabla\tilde{\mathbf{u}} + \left(\nabla\tilde{\mathbf{u}}\right)^{T}\right), \tag{104}$$

$$\rho\frac{\partial^2\tilde{\mathbf{u}}\left(\mathbf{r},t\right)}{\partial t^2} = \nabla\cdot\tilde{\sigma}\left(\mathbf{r},t\right) + \tilde{\mathbf{f}}\left(\mathbf{r},t\right), \tag{105}$$

where $\omega = 2\pi f$, with f the frequency, and the tilde ($\sim$) and star ($*$) notations refer to complex numbers. Full development of Eq. (102) (available in Ref. [**151**]) leads to the governing equation of motion propagation in locally-homogeneous elastic solids known as the Navier's equation:

$$\rho \frac{\partial^2 \mathbf{u}\left(\mathbf{r},t\right)}{\partial t^2} = \mu \nabla^2 \mathbf{u} + \left(\lambda + \mu\right) \nabla \left(\nabla \cdot \mathbf{u}\right), \tag{106}$$

where μ is the shear modulus in (Pa) reflecting the amount of energy the tissue can store as elastic deformation, and λ is the first Lamé coefficient in (Pa) reflecting the tissue's compressibility. The Navier's equation does not rely on rheological models and conveys an approximation of the material's natural properties based on physical assumptions. The same development applied to Eq. (105) leads to:

$$-\rho\omega^2 \tilde{\mathbf{u}} = \mu^* \nabla^2 \tilde{\mathbf{u}} + \left(\lambda^* + \mu^*\right) \nabla \left(\nabla \cdot \tilde{\mathbf{u}}\right), \tag{107}$$

where $\mu^* = \mu_r + i\mu_i$ is the general notation of the complex shear modulus in the frequency domain Navier's equation, μ_r is the shear storage modulus that reflects the amount of mechanical energy stored as shear deformation in the solid, and μ_i is the shear loss modulus reflecting the amount of mechanical energy dissipated due to shear viscosity. Similarly, $\lambda^* = \lambda_r + i\lambda_i$ is the complex Lamé coefficient where λ_r and λ_i are the compression storage and loss moduli respectively reflecting the amount of energy stored and lost in the solid due to compression deformation and compressional viscosity. In purely elastic solids, the wave field does not dissipate and shows an instantaneous response to the load. In such cases, the loss moduli equal zero and $\mu^* = \mu_r = \mu$ and $\lambda^* = \lambda_r = \lambda$. The Young's modulus E, characterizing the solid's resistance to deformation under loading, and the Poisson's ratio ν characterizing the tissue's compressibility, are defined by:

$$E = \frac{\mu\left(3\lambda + 2\mu\right)}{\lambda + \mu}, \tag{108}$$

and

$$\nu = \frac{\lambda}{2\left(\lambda + \mu\right)}. \tag{109}$$

The motion field $\mathbf{u}$ propagates as compression and shear waves of which velocities v_c and v_s are, respectively, given by (see Ref. [**151**] for details):

$$v_c = \sqrt{\frac{(\lambda + 2\mu)}{\rho}}, \tag{110}$$

and

$$v_s = \sqrt{\frac{\mu}{\rho}}. \tag{111}$$

The large difference between the two velocities observed in biological tissues (typically v_c is around 1540 m.s^{-1} and v_s is found around 1 to 10 m.s^{-1}) suggests that λ is much greater than μ, thus allowing for the following approximation often used to report SWE measurements:

$$E \approx 3\mu. \tag{112}$$

This observation is directly linked to the tissue incompressibility assumption, which causes λ to approach infinity [**317**]. Additionally, λ was shown to vary slightly as opposed to μ, which spans a few orders of magnitude in biological tissues . Consequently, the shear modulus, or the Young's modulus, is the mechanical parameter considered in elastography reconstruction processes.

Another approach much less often used to reconstruct material mechanical properties in SWE is to model the solid as isotropic and viscoelastic instead of purely elastic. Here, the response of the loaded tissue shows a delay with respect to actuation and elastic waves attenuate due to energy dissipation in the solid, which is specific to viscous materials. Attenuation may be accounted for in the time-domain Navier's equation by introducing a damping term, and linking it to viscosity using rheological models such as the generalized Maxwell, standard linear solid, or Kelvin-Voigt, which are further discussed in the next section. Here, the stress-strain relationships used to derive wave equations from Newton's second law are presented for the three aforementioned models:

A different option to integrate viscoelastic properties into the description of the material is to formulate the problem in the frequency domain, provided a harmonic actuation. In this case, the complex shear modulus, as described in Eq. 107, has a non-zero imaginary

Model	Stress-strain relationship	
Kelvin-Voigt	$\sigma = c\epsilon + \eta\frac{\partial\epsilon}{\partial t}$	(113)
Maxwell	$\eta\frac{\partial\sigma}{\partial t} + E\sigma = E\eta\frac{\partial\epsilon}{\partial t}$	(114)
Standard linear solid	$(E_1 + E_2)\,\sigma + \eta\frac{\partial\epsilon}{\partial t} = E_1E_2\epsilon + E_1\eta\frac{\partial\epsilon}{\partial t}$	(115)

Table 6 – Stress-strain relationships for three common rheological models accounting for the viscoelastic behavior of soft tissues. Details about these models are reported in the next section. σ, ϵ, and η are the stress, strain, and viscosity tensors respectively, E, E_1, and E_2 are Young's moduli specific to the Maxwell and standard linear solid models.

part accounting for shear wave dissipation due to the material's shear viscosity. Relating μ_i values to actual viscosity values depends on rheological modeling, as discussed in the next section. For instance, in the case of a solid described by the Kelvin-Voigt model, the complex shear modulus is given by $\mu^*(\mathbf{r}) = \mu_r(\mathbf{r}) + i\mu_i(\mathbf{r}) = \mu_r(\mathbf{r}) + i\omega\eta(\mathbf{r})$ where $\eta(\mathbf{r})$ is the local shear viscosity.

For μ_r and μ_i estimation, the displacement field $\tilde{\mathbf{u}}$ may be used as the solution to the Navier's equation in direct or iterative inversion, or the shear wave velocity at frequency $\omega/2\pi$ may be measured. Here, the complex wave number is noted as $k = k_r + ik_i = \omega/\sqrt{\frac{\mu^*}{\rho}}$, in analogy with the complex shear modulus notation, and the dispersion relation is given by $k_r = \omega/v_p$, where v_p is the phase velocity of the shear wave at the frequency $\omega/2\pi$. Considering a plane wave decomposition of the wave field, the i$^{\text{th}}$ component has the form $U_j(r_j,t) = A\exp\left(-i\left(k_j^*,r_j\right) - \omega t\right) = A\exp\left((-i\left(k_{r,j},r_j\right) - \omega t) - k_{i,j},r_j\right)$. The imaginary number k_i is often noted α and is the shear wave attenuation coefficient (m^{-1}). Thus, a linear system of two equations may be raised and independent experimental evaluations of v_p and α from the displacement field allows assessing μ_r and μ_i. Also, the Young's modulus becomes complex-valued in viscoelastic models. However, most viscoelasticity reconstruction processes stick to the evaluation of μ_r and μ_i. Finally, it is to be noted that the equivalence between longitudinal and compression waves on one hand, and transverse and shear waves on the other hand, is true for plane waves only.

To date, isotropic elastic and viscoelastic characterization of soft matters have mostly been considered in shear wave elastography, owing to the availability of various inversion schemes. However, the anisotropic and poroelastic nature of certain biological tissues, such as the brain, has long been acknowledged. In poroelasticity, the medium is modeled as a porous solid matrix crossed by flowing fluid, and thus contains two separate phases, as opposed to more common models containing one phase. Consequently, the motion field measured in imaging protocols is not only due to the solid tissue deformation but also to the pressure gradient in fluid pores. Although poroelasticity was early studied using quasi-static deformations, implementation in shear wave elastography imaging remains in its infancy. Oscillatory deformations in poroelasticity have first been described by Biot [**318, 319**], and later by Cheng *et al.* [**320**]. Assuming a viscous fluid flow, fluid saturation in pores, and a compressible linearly elastic solid, poroelasticity equations of propagation are given by:

$$-\omega^2 \left(\rho - \beta\rho_f\right) \tilde{\mathbf{u}} = \nabla \cdot \left(\mu \nabla \tilde{\mathbf{u}}\right) + \nabla \left(\left(\lambda + \mu\right) \left(\nabla \cdot \tilde{\mathbf{u}}\right)\right) - \left(1 - \beta\right) \nabla p, \tag{116}$$

$$\frac{\omega^2 \rho_f \left(1 - \beta\right)}{\beta} \left(\nabla \cdot \tilde{\mathbf{u}}\right) + \nabla^2 p = 0, \tag{117}$$

$$\beta = \frac{\omega \phi_p^2 \rho_f \kappa}{i\phi_p^2 + \omega\kappa \left(\rho_a + \phi_p \rho_f\right)}, \tag{118}$$

where μ is the shear modulus, λ the first Lamé's parameter, $\tilde{\mathbf{u}}$ the complex time harmonic displacement field, β the effective stress coefficient (dimensionless), p the complex time harmonic pressure field, ω the actuation frequency, ρ the bulk density, ρ_f the pore fluid density, ϕ_p the material porosity, κ the hydraulic conductivity, and ρ_a the apparent mass density.

Finally, anisotropy has been considered for biomechanical modeling in the context of shear wave elastography. In such cases, the material's mechanical response (strain) is dependent on the direction in which it is solicited (stress). Full derivation of relevant mechanical parameters under different symmetry assumptions is beyond the scope of this review, and the interested reader is referred to the excellent pedagogical development in [**321**]. Briefly,

Hooke's law describes the relationship between applied stress and material strain:

$$\sigma_{ij} = \sum_{k,l=1}^{3} c_{ijkl}\epsilon_{kl}, \tag{119}$$

where σ and ϵ are the stress and strain tensors, respectively. In isotropic materials, the tensor c_{ijkl} is fully described by two parameters, E and ν. In anisotropic materials, more constants are needed to account for the direction dependance of c. The most used anisotropic model is transverse isotropy, which is particularly used to characterize fibrous tissues (*e.g.*, muscles). Transversely isotropic materials are organized in layers where in-plane mechanical properties are isotropic, and out-of-plane ones are anisotropic. In such cases, 5 parameters are necessary to describe c_{ijkl}. Two of them, μ_{13} and μ_{12}, characterize the shear motion in directions parallel and perpendicular to the fiber axis, respectively. The other three, E_1, E_2, and E_3 characterize the compression motion in directions parallel, perpendicular in-plane, and perpendicular out-of-plane to the fiber axis, respectively. Injection of Hooke's law into Newton's second equation allows to derive equations of shear wave propagation along directions of dependency the same way as to derive the Navier's equation of elasticity. Other anisotropic models exist, such as the orthotropic one which shows a lower level of symmetry (three perpendicular planes) than the transverse isotropy model. The orthotropic model has been used to develop waveguide elastography which describes the propagation of the different polarizations of shear waves along separate directions. The orthotropic tensor along with equations of polarized wave propagation are described in detail in [**322**].

B.2.2. Characterization of tissue viscoelasticity

Most soft bio-tissues contain more than 70-w% of water, thus they can be considered as fluid-like solids, which means these materials have characteristics of both solids and fluids [**311**]. Elasticity refers to the solid property that describes the ability of a material to return to its original shape after a stress is removed [**323**]. The fluid property is given by the viscosity (η) that describes the ability of a material to resist to its deformation due to a tensile stress or shear stress [**323**]. Three categories of properties are often used to characterize the

viscoelasticity of a soft material: its compressibility, which is usually measured by the bulk modulus (K) and the Poisson's ratio (ν); its tension, which mainly refers to the Young's modulus (E); and shear properties, described by the second Lamé coefficient (μ) and the complex shear modulus (μ^*).

The complex shear modulus is self-sufficient to describe the viscoelasticity of biological tissues. It defines the ratio of shear stress and shear strain of a material. In general, the storage modulus μ_r reflects the shear elastic property while the loss modulus μ_i reflects the viscous response of the material. Alternatively, rheological models were considered to relate experimental measurements to elastic and viscous properties of tissues. Mathematically, the Kelvin-Voigt and Maxwell models have been considered most frequently to describe viscoelastic tissues [**324, 325**], *i.e.*, quantifying the shear elasticity and viscosity. The two models are represented by a purely elastic spring connected to a purely viscous dashpot in parallel (Kelvin-Voigt) or in series (Maxwell), respectively. A material with only elasticity is called a purely elastic material (only a spring), while a material with only viscosity (only a dashpot) is called a Newtonian fluid [**326**]. A soft tissue or soft tissue-like material falls between these two extreme conditions and can be called as a viscoelastic material . Other material models are used less frequently, while most of them are constructed with different combinations of single/multiple spring(s) and dashpot(s) in more complicated arrangements, such as the Zener model, generalized Maxwell model, and generalized Kelvin-Voigt model [**327, 328**].

Note that in the field of SWE, the complex shear modulus μ^* may be sometimes confused with the storage modulus μ_r and the second Lamé coefficient μ (also known as the shear modulus). Although the storage modulus reflects the tissue's elasticity, they are not rigorously the same. For sake of clarity, in this review, the elasticity is denoted by μ, *i.e.*, the magnitude of the second Lamé coefficient. Therefore, for incompressible soft tissues (*i.e.*, for a Poisson's ratio close to 0.5) with a negligible viscous component, it can be assumed that such a tissue is a purely elastic material so that μ^* solely represents the real shear elasticity

and so $\mu^* = \mu_r = \mu$ [**329**]. Otherwise, the calculation of elasticity (as well as the viscosity) is rheological model dependent.

Mathematical relations between tissue excitation and response may be divided into two groups according to the temporal difference of the excitation: namely quasi-static measurements and dynamic measurements (also termed shear wave (SW) measurements). The quasi-static measurement methods mainly analyze the stress-strain behavior. On the other hand, SW measurement methods determine the complex shear modulus by tracing and analyzing a propagated SW in the specimen.

During the past years, studies in the field of SWE measurements have often targeted absolute values of elasticity $|\mu|$ and viscosity η. To do so, rheological models of the material are needed to derive those parameters. For instance, when the Kelvin-Voigt model or Maxwell model is considered, the complex shear modulus can be written as follows [**330, 331**]:

$$\mu_{KV} = |\mu| + i\omega\eta, \tag{120}$$

$$\mu_M = \frac{i\omega\eta\,|\mu|}{|\mu| + i\omega\eta}, \tag{121}$$

where μ_{KV} represents μ of the Kelvin-Voigt model, and μ_M is that for the Maxwell model, both satisfy the general form $\mu = \mu_r + i\mu_i$. In Eqs. 120 and 121, ω is the angular frequency of the SW. Alternatively, by solving the wave equation in Eq. 107, a general solution of μ_r and μ_i, without considering a rheological model, can be obtained, as in :

$$\mu_r = \rho\omega^2 v_s^2 \cdot \frac{\omega^2 - \alpha^2 v_s^2}{\left(\omega^2 + \alpha^2 v_s^2\right)^2}, \tag{122}$$

$$\mu_i = 2\rho\omega^2 v_s^2 \cdot \frac{\omega\alpha v_s}{\left(\omega^2 + \alpha^2 v_s^2\right)^2}. \tag{123}$$

Here, as synergized with Eq. 107, one can see that both $|\mu|$ and η are functions of v_s, α, and ω. Since v_s and α can be experimentally measured at certain ω, $|\mu|$ and η, in a specified rheological model, can be thereafter calculated.

In common practice, when the viscosity η is taken into account for tissue characterization, it can be determined either directly using both v_s and α with knowing the corresponding

ω, or alternatively by evaluating the dispersion of v_s with respect to ω without determining the value of α, *i.e.*, by knowing multiple pairs of v_s and ω [**327, 332**]. However, one should also notice that the viscoelastic property of biological tissues are rather complex, depend on the tissue type, and on the presence of a pathological condition, so that there is not simply a best, or a most appropriate material model for all tissues. Furthermore, pathological changes with time of a tissue could also lead to a major change of its viscoelastic property, thus a certain material model may no longer be suitable for the tissue when it becomes abnormal and progresses toward a more severe pathological state. Meanwhile, the derivation of elasticity $|\mu|$, and viscosity η, are rather different among different material models. That means, using different models with same measures (such as v_s and α) would lead to different results, and hence would be meaningless to clinical studies. Therefore, nowadays it is always suggested that no rheological model is assumed, and instead of that, directly access the shear storage μ_r and loss μ_i moduli would be not only more rigorous and appropriate, but also mathematically convenient to describe tissue viscoelastic properties.

B.3. Ultrasound shear wave elastography

B.3.1. Generation and Detection of Shear Waves

A shear wave, also called a transverse wave, is a moving mechanical wave that consists of particle oscillations occurring perpendicular to the direction of the energy transfer [**333**]. As introduced, SWs in ultrasound imaging can be generated either from an external vibration source (such as a mechanical vibrator/shaker) [**334, 3**], or internally by an acoustic radiation force (ARF) [**4, 335, 336, 337**], as illustrated in Fig. 29. The control of the SW amplitude and frequency of the ARF is considered in [**231**]. In terms of waveforms, the SW can also be generated as continuous waves [**335, 334, 3**] or impulse waves [**4, 336, 337**], as can be seen in the examples of Fig. 30. In ultrasound imaging, the probe fires longitudinal pressures and detects particle displacements along the axial direction, therefore only SWs that propagate along the lateral direction of the ultrasound beam, or SW components whose displacements occurred on the axial direction, can be detected.

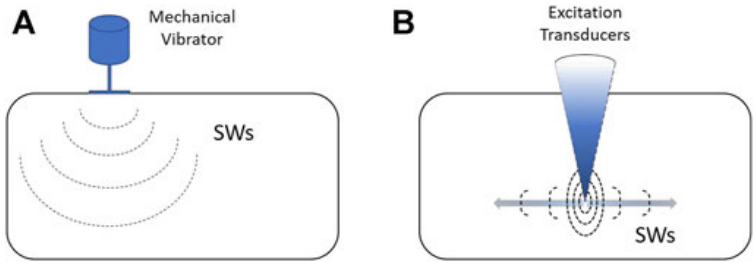

Figure 29 – Shear wave generation sources: **a.** an external vibration source, and **b.** an internal acoustic radiation force.

Many remarkable techniques were invented over the past 30 years based upon different combinations of external or internal SW sources, and continuous or impulse SWs. In 1988, Lerner *et al.* proposed a method to map the propagation of low frequency SWs with a Doppler ultrasound displacement detection technique to assess tissue stiffness [**334**]. Later in 1990, Yamakoshi *et al.* proposed a dynamic measurement method to determine the SW speed v_s using an external mechanical vibration source [**3**], as seen in Fig. 30(a). The parameter v_s was determined by analyzing the wavelength of a continuously propagated SW using the Doppler ultrasound technique. Catheline *et al.* developed in 1999 an impulse SW measurement technique. In this method, an ultrasonic probe was located on one side of the specimen to capture the propagation of the impulse SW generated by a mechanical vibrator located on the other side of the specimen. A plane wave ultrasound system was used, enabling a high frame rate in detection mode, then the parameter v_s was determined through the time-of-flight (TOF) technique applied on successive images. See below for more information on the TOF method. Since such a method used an impulse SW, it is also called transient SW imaging, or transient elastography (TE). Nowadays, the largely used clinical device Fibroscan [**338**] is based on TE. In 2004, a method using two external SW sources to generate continuous SWs toward each other with slightly different SW frequencies was proposed. Due to the frequency difference, interfered SW patterns termed as "crawling waves" moved with a much slower speed than the expected v_s. This allowed the observation of propagated crawling waves with a conventional low frame rate B-mode imaging system. Once the speed of the crawling wave was obtained, v_s could be derived.

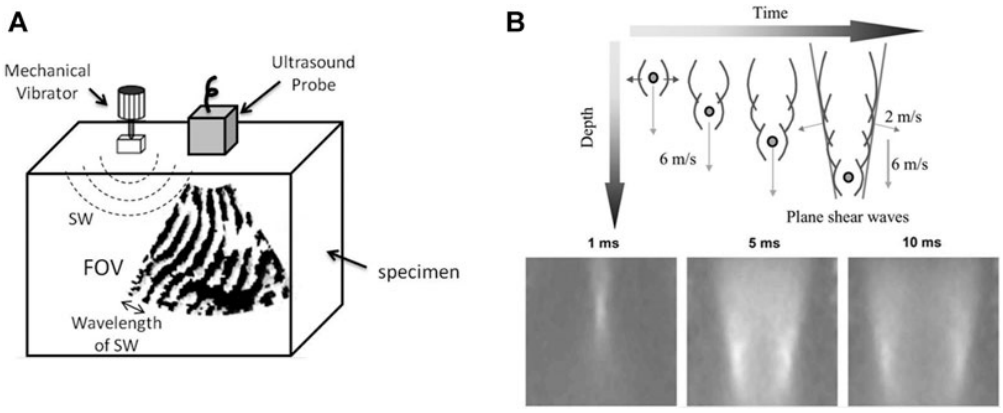

Figure 30 – Examples of the generation of **a.** continuous shear waves, adapted from [**3**] copyright 1990 IEEE, and **b.** impulse shear waves, reproduced with permission from [**4**] copyright 2004 IEEE.

In 1998, Sarvazyan *et al.* developed a SW measurement method, termed shear wave elasticity imaging (SWEI), relying on a SW generated remotely by an ARF of a focused ultrasound beam. In this method, a transient SW pulse was firstly produced at the focus of the ultrasound beam and propagated along sideways. Then, imaging transducers were used to trace the moving of SW fronts and viscoelastic parameters were derived thereafter. The same year, Fatemi and Greenleaf developed a method to produce an oscillatory ARF by mixing two ultrasound beams with different frequencies [**335**]. A short period of harmonic (continuous) or tone-burst SWs was generated and propagated along sideways, which made the SW narrow-band (while the SW generated by Sarvazyan's method was broadband) and then v_s could be determined by finding the phase difference of the SW at two apart locations. By repeating the measurement with continuous SWs at different frequencies, or retrieving different frequency components of a tone-burst SW, both μ_r and η could be derived. This method is termed as SW dispersion ultrasound vibrometry (SDUV). Later in 2004, based on the combination of Catheline's impulse SW method and the ARF technique, Bercoff *et al.* developed an advanced SW measurement method known as supersonic shear imaging (SSI) [**4**]. With this method, an ultra-high-speed scanner is used, then multiple ARF impulses are triggered consecutively and very quickly at different depths. Each impulse produces a SW point-like source then all these SWs interfere constructively and result in two SW planes propagating in opposite directions, as can be seen in Fig. 30.b. A two-dimensional v_s image

is obtained with this method. Moreover, since this technique is creating broadband SWs, tissue viscosity can also be estimated through the v_s dispersion method (using the same principle as SDUV). In 2012, Song *et al.* developed a SW method, which also used multiple lateral ARFs as in [**337**]; the method was termed as comb-push ultrasound shear elastography (CUSE). It firstly generates multiple ARF excitations at different spatial locations to produce multiple impulse SWs by using the push mode of the ultrasound probe, and then quickly switches to the scanning mode of the probe to detect the SW propagation. Therefore, v_s could be measured through the TOF technique by tracing the movement of the SW front from each SW source. The use of the comb-push excitation provided multiple SW sources in the specimen so that such method is effectively compensating for the worse signal-to-noise ratio (SNR) due to the SW attenuation at the location far away from a given SW source.

Knowing that $v_s = \lambda_s f_s$, one may like to measure v_s through the TOF technique, or instead to determine λ_s in the spatial domain. For most biological tissues, v_s travels at a few $m.s^{-1}$, which means it only takes a couple of ms for a SW to travel through the entire field of view (FOV) of a common ultrasound probe. Physically, a focused ultrasound system triggers transducer elements sequentially from one edge to another to complete a B-mode scan, as a result the frame rate is typically less than 100 $frames.s^{-1}$ in such a system, which is not fast enough to measure the TOF without a particular modification of the experimental setup. Therefore, measuring λ_s becomes the realistic option. In this scenario, the spatial resolution is determined and limited by λ_s. Although increasing f_s is reducing λ_s, and so is improved the resolution, one should also notice that a higher frequency would cause a quick attenuation of the SW propagation. Thus, empirically f_s is usually adjusted to a few hundreds of Hz, which leads the lateral resolution of elastography images to a sub-centimeter level with using standard focused ultrasound beamforming. On the other hand, a plane wave system can trigger all transducer elements of the probe at the same time to emit a plane compression wave, enabling it to have a very high frame rate in B-mode (up to 10,000 $frames.s^{-1}$) [**4**]. Thus, in this scenario, the TOF technique is applicable, and theoretically the distance that a SW travels within two consecutive frames could be as short

as a few-tenth of millimetres. Since the distance is comparable to the physical interval of two adjacent transducer elements in a common ultrasound array probe, the lateral spatial resolution of SWE with using a plane wave system is approximately the same as that of B-mode imaging. It is also worth noting that, when tissue boundaries/layers exist under the FOV, and a propagating SW passes through those interfaces, physical phenomena such as reflection, refraction, diffraction, and mode conversion could occur at the interfaces and cause artefacts. Although directional filters are usually applied to mitigate those effects, practically it is still difficult to remove all the unwanted waves. Therefore, the v_s measured within approximately one λ_s from the interfaces are usually considered unreliable, which to some extent would downgrade the spatial resolution at those areas.

B.3.2. Viscoelasticity reconstruction

As introduced earlier, ultrasound SWE contributed to the non-invasive assessment of mechanical properties of soft tissues [**135, 339, 340**]. One method largely used clinically is transient elastography (TE) [**341, 342**], which utilizes a dynamic compression generated by the vibration of the transducer on the skin to produce shear waves. No structural imaging is provided with this method to guide the measure. Moreover, in some patients with morbid obesity and ascites, the attenuation of shear waves travelling from the surface of the body to the organ of interest (typically the liver) may prevent reliable measurements. The acoustic radiation force impulse (ARFI) [**343**] and supersonic shear imaging (SSI) [**4, 344**] methods use a radiation pressure to locally induce shear waves within the organ of interest. TE, ARFI and SSI are assessing tissue elasticity (no viscosity) based on the measurement of the shear wave speed [**345**]. The Young's modulus is estimated and displayed as an image using $E = 3\,|\mu| = 3\rho v_s^2$. Alternatively, different approaches have been developed to retrieve and display the viscous component of a tissue [**346, 336, 347**]. Such approaches have not yet been validated on large clinical cohorts, nor implemented on clinical scanners. Details on technologies proposed to determine tissue viscoelasticity are given next.

Most studies utilized a rheological model, which has been introduced earlier, *e.g.*, the Kelvin-Voigt model, to find the viscosity after the reconstruction of elasticity [**348**]. The complex shear modulus μ^* was also estimated using different approaches, such as measuring the acoustic radiation force-induced creep [**346**], solving the Navier's wave equation numerically [**349**], inverting analytically the solution of the shear wave scattering from a mechanical inclusion [**350, 351**], and using a finite-element based method [**352**]. Note that a torsional SW source was used in the latter method, as originally proposed in [**353**].

Kazemirad *et al.* [**336**] developed a method for the quantitative measurement of viscoelastic parameters μ_r and μ_i at various frequencies, based on the assumption of a cylindrical shear wave front produced by a radiation pressure, allowing to avoid wave diffraction effects. Other studies have also used the same geometrical assumption for quantitative viscoelastic measurements [**354, 347**]. Notice that the cylindrical wave front assumption would not necessarily hold when considering inhomogeneous media, such as a tissue embedding a tumor. A recent method for estimating tissue viscosity without geometrical assumption on the wave front was proposed by Bhatt *et al.*, which utilized the shear wave velocity v_s and attenuation α computed by the frequency shift method [**307**]. Recently, Ormachea and Parker performed a study to characterize viscoelastic properties of oil-in-gel viscoelastic phantoms and *in vivo* human livers. They found that the shear wave dispersion and attenuation were linked together and related to the tissue viscosity. As reviewed above, the shear wave speed and attenuation are widely used for reconstructing viscoelastic properties. Experimental methods to obtain those shear wave properties are separately described below.

B.3.2.1. *Shear wave speed*

One of the widely used methods implemented on clinical scanners is the group velocity [**355, 356**] that assumes the tissue as elastic, homogeneous, isotropic, linear, and of infinite dimension with respect to the wavelength. The group velocity is estimated using time-of-flight based algorithms for particle displacement or particle velocity assessments in the time domain. TOF–based algorithms usually rely on cross-correlation (CC) and time-to-peak (TTP) methods [**355**]. Basically, the CC provides a moving average estimate of the

shear wave speed using all sample points, and performs multiple cross-correlations along the direction of the wave propagation, which may result in artefacts for periodic shear wave patterns, whereas TTP estimates the velocity based on the tracking of the movement of one point on the waveform [**355**]. Although group velocity estimation methods are considered robust [**356**], they are theoretically applicable to strictly elastic materials thus requiring resorting to other techniques for the evaluation of the viscous behavior.

The variation of the shear wave velocity with frequency refers to the wave dispersion occurring in a viscoelastic medium. Some methods have used this phenomenon to evaluate viscoelastic properties of tissues [**357**]. Measuring shear wave velocities at specific frequencies is known as phase velocity estimation. Beside the viscoelastic property of a tissue, its finite thickness can also affect the dispersion due to reflections during propagation, which may result in wave mode conversion [**358**]. The phase velocity and the group velocity are not equal in the presence of dispersion. It has been shown that the phase velocity has a lower value by a factor of 8-9% compared with the group velocity in soft tissues.

One technique to measure the phase velocity is the phase gradient approach, which estimates the velocity using the phase difference evaluated at different spatial locations for specific frequencies [**357**]. An alternative method to estimate the shear wave phase velocity is performed by two-dimensional Fourier transform (2D-F) analysis, which converts spatio-temporal data to a wave number in the frequency domain, and uses the peak magnitude distribution to estimate the phase velocity [**359**]. The dispersion either from the phase gradient or 2D-F can be fitted to rheological models to quantify viscoelastic parameters of the medium. The attenuating nature of a tissue is the cause of the dispersion of the phase velocity. The shear wave dispersion and attenuation can be estimated by the computation of a power law coefficient, with the assumption of a power law rheological model for the tissue.

Local phase velocity imaging (LPVI) is another method that can produce a phase velocity map. The LPVI requires applying bandpass filters to obtain the maximal frequency range for the phase velocity. Although this method demonstrates good reconstructions of 2D shear

wave phase velocity, results are sensitive to the frequency range selected, and they may change when using different transducers, focal configurations, and focal depths.

B.3.2.2. *Shear wave attenuation*

The dependency of the wave amplitude with distance is attributed to geometrical spreading of the wave energy and to viscoelastic attenuation. Wave diffraction by geometrical spreading can be reduced by using the method of Kazemirad *et al.* [**336**] that is considering cylindrical shear waves produced by a supersonic radiation pressure source. Other methods including this assumption were based on a 2-D Fourier transform and the computation of the spectral width to assess the frequency dependent attenuation [**347**]. A robust method assuming a cylindrical wavefront and no rheological model is the attenuation-measuring ultrasound shear wave elastography (AMUSE) algorithm. This method, however, does not provide any attenuation map since the computation requires all datasets within the selected region-of-interest. Since biological tissues such as the kidney, muscles, and tendons are anisotropic, and because the wave produced by a linear SW front may no longer be cylindrical in those media; then, above-mentioned algorithms may lead to inaccurate results [**360, 361, 357, 362**].

Frequency-shift methods used for compression and seismic wave analyses [**363, 364, 365**] inspired the field of shear wave elastography to assess tissue viscosity. Frequency-shift methods are not based on wave amplitude, so the dependency of these methods to geometrical wave spreading is released [**365**]. Bernard *et al.* developed such a frequency-shift method for shear wave attenuation by model-fitting of the amplitude spectrum [**307**]. This method made a few assumptions, which may not hold in all viscoelastic media such as fatty liver. A two-point frequency-shift method was later proposed by Kijanka and Urban to soften assumptions made by Bernard *et al.*. In their report, they considered a varying shape parameter of the gamma distribution used to fit the shear wave amplitude spectrum. This technique used only two spatial points instead of all points along the propagation path, as in [**307**], to estimate the attenuation coefficient. Using only two spatial points reduces the computation time but may affect robustness in cases of noisy shear wave displacement maps.

Viscosity maps based on the cylindrical wavefront assumption of Kazemirad *et al.* [**336**] or frequency-shift method of Bernard *et al.* [**307**] can be found in [**306**] .

B.3.3. Applications

A few examples of ultrasound shear wave viscoelasticity imaging applications are presented next. The reader may refer to recent review papers on this subject for other examples [**366, 367, 368**]. The focus below is on the liver and breast as those organs were largely investigated in clinical studies using SWE.

B.3.3.1. *Liver*

Liver fibrosis occurs when an abnormal large amount of liver tissue becomes scarred. It can lead to cirrhosis, its long-term sequel, and further evolve as hepatocellular carcinoma [**369**]. Liver fibrosis can be differentiated into 5 categories, from F0 for a normal liver to F4 for cirrhosis; these categories have been obtained by biopsy intervention, which is the gold standard for liver classification. However, liver biopsy is invasive, could lead to bleeding or worse outcomes, and even death [**370**], and because a small amount of tissues is taken, it is not always representative of the full liver due to sampling errors [**371, 366**]. Fibrosis is one pathology known to increase liver stiffness [**372, 373, 374, 375**] along with inflammation, oedema, congestion and extra hepatic cholestasis [**341, 376, 377**]. Shear wave elastography was mainly used to classify fibrosis based on liver elasticity using different cut-off values. This imaging method is accurate to assess liver fibrosis of stage 2 and higher [**372, 378, 379**], has a good repeatability, and may allow to diminish the number of biopsy [**380**]. Yet the impact of steatosis on liver stiffness is uncertain [**381**]. To overcome this, some teams proposed investigating viscous properties. If no clear consensus is reached yet, a few studies showed promising results based on shear wave dispersion and attenuation to assess steatosis stages or necroinflammation [**382**]. Shear wave elastography presents some limitations for liver imaging, such as difficult measurements in obese patients, and confounding impact of factors such as inflammation, which can increase liver stiffness or change the liver stiffness threshold for classification. In addition to fibrosis assessment and classification, SWE was also proven

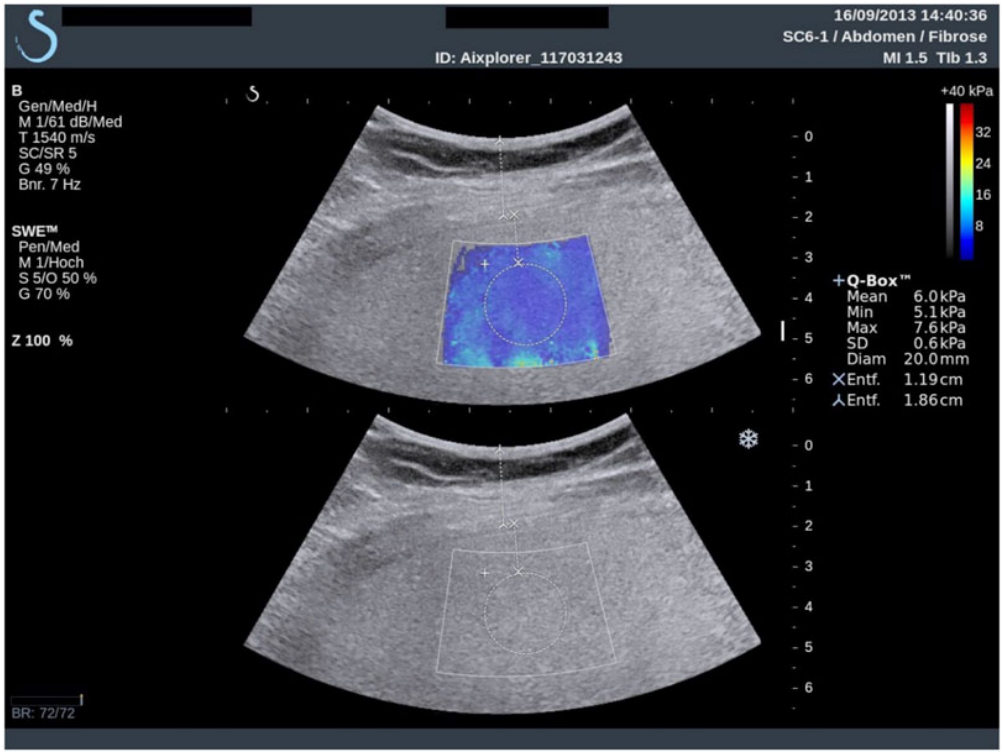

Figure 31 – Example superimposing the shear wave elastogram on the corresponding B-scan in a 34-y-old man with histologic F1 fibrosis. The dynamic range of Young's moduli was set between 0 kPa to 40 kPa during the clinical exam, which was sufficient to cover the range of values expected for the four stages of liver fibrosis. Reproduced with permission from . Copyright 2015, Elsevier.

useful to follow patients with chronic liver disease. An example of a liver SWE image is given in Fig. 31.

B.3.3.2. *Breast*

Shear wave elastography is used to help identify breast cancers, since it has been shown that malignant tissues appear stiffer than their healthy counterpart [**383, 384, 22**]. X-ray mammography, MR imaging and ultrasonography are used to detect tissue lesions or to classify suspicious masses into different categories, typically classification 0 for incomplete data to 6 for histologically proven malignancy. Nonetheless, excluding the expensive MR imaging method, these approaches have poor specificity and mammography often finds false negative results in dense breasts [**385**]. Category 4, which corresponds to suspicion for malignant tissues, has a degree of certainty varying from 2 to 95% to assess malignancy

proven by biopsy, and has a cancer detection rate of 10 to 30%. Shear wave elastography allowed improving breast lesion characterization [**386, 387, 388**], and reducing the number of unnecessary invasive biopsy due to the improvement in specificity [**386, 389, 390**]. Elasticity parameters such as the maximum or mean Young's modulus E within the lesion, and in surrounding tissues, are used to separate benign from malignant masses. Recent works investigated viscosity behavior using the shear viscosity [**391**], linear dispersion slope, and storage and loss moduli to differentiate malignant from benign tissues. Ultrasound data on the viscous behavior of breast lesions are scarce but may prove to be of clinical value in the future. Some studies investigated the use of SWE as a tool to monitor cancer treatment performance, with a decrease in malignant mass elasticity during treatment, or for early prediction of therapy successes [**392, 393**], with a better treatment response for softer tumors. Fig. 32 gives examples of Young's modulus elasticity maps of breast lesions.

B.3.3.3. *Other applications*

Although SWE has targeted mainly the liver and breast, other organs and techniques have been developed. Prostate cancers [**394**], thyroid cancer nodules [**395**], and blood clot characterization have been investigated, to name a few examples, with the Young's modulus as the descriptive mechanical parameter. If the assumption of an isotropic medium is generally accepted for most organs, it is not the case for muscles and tendons. Anisotropic and transversely isotropic models using shear waves have been recently investigated, some other teams explored viscoelastic properties using different probe orientations [**396, 397**]. A non-exhaustive list of SWE clinical applications can be found in Table 7.

B.4. Magnetic resonance elastography

Magnetic resonance elastography (MRE) is an emerging non-invasive imaging technology used for assessing the mechanical properties of soft tissues. Since its first description by Muthupillai *et al.* in 1995, MRE has been integrated into clinical routines for liver disease detection, and has shown great potential for other organs, notably the brain, of which only

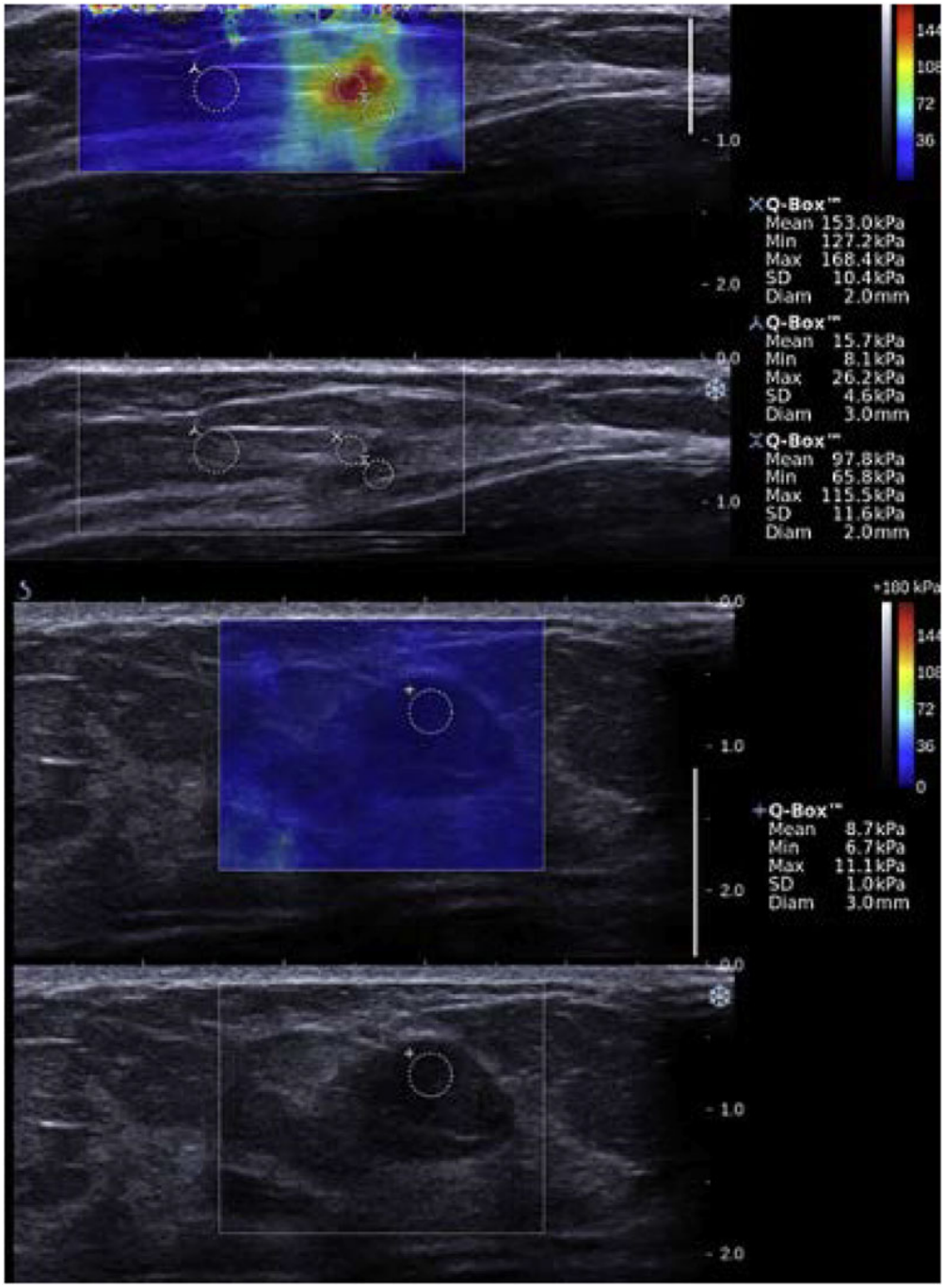

Figure 32 – Examples of shear wave elastography images of breast tissues. (Top two panels): A 50-year-old woman with an abnormality in her left breast on screening mammography is presented. Biopsy was made on the red region (high Young's modulus), and concluded that the lesion was an invasive carcinoma (pT1a, pN0). The first panel gives the SWE map superimposed on the B-mode image, whereas the bottom panel is the B-mode image. (Bottom two panels): A 48-year-old woman who presented with an abnormality in her left breast on screening ultrasound is presented. Biopsy was made on the suspicious region, and concluded that the lesion was a fibroadenoma (benign tumor). The blue color on the shear wave elastography image indicates a low Young's modulus. The third panel gives the SWE map superimposed on the B-mode image, whereas the bottom panel is the B-mode image. The range of Young's moduli on the colorbar is from 0 to 180 kPa. Reproduced with permission from [**5**]. Copyright 2015, Elsevier.

MRE can assess the *in vivo* viscoelastic components without surgical intervention. Principles of MRE investigation are similar to those of any SWE method (Fig. 33). A major feature of MRE resides in its ability to measure 3D displacement fields by simply changing the axes of encoding gradients, which is an advantage over other imaging devices operating elastography. The main drawback may be found in the longer scan times relative to ultrasound elastography for instance. MRE has a poor temporal resolution and relies on a stroboscopic-like recording arrangement to generate time resolved images, as opposed to ultrasound SWE where burst measurements are performed at a high acquisition rate. Typically, MRE data contain 4 to 8 images per harmonic actuation cycle. Spatially, MRE is sometimes referred to as a super resolution imaging modality as measured displacement amplitudes are much smaller than the image pixel size (tens of microns versus one to three millimetre). We review in this section the main three steps in MRE investigation, namely motion generation strategies, motion encoding techniques, and inversion methods. Finally, applications to the liver and brain are discussed. These organs were subjectively chosen as liver disease diagnosis is the only MRE protocol clinically established, and non-invasive *in vivo* brain mechanics assessment is not enabled by any elastography techniques other than MRE.

B.4.1. Generation of acoustic waves in MRE

In MRE, most applications involve the generation of time-harmonic wave fields using external surface actuators. These actuators must meet the requirements imposed by magnetic resonance safety rules, in other words they must be made of non-magnetic materials and be adaptable to fit into the experimental or clinical magnet bore of the scanner. Design of actuators has been shown to be application dependent; we review in this section the main techniques to induce motion in soft tissues in the context of MRE. Loudspeakers have been widely used to transmit motion to tissues and may be divided into pneumatic and rigid categories. In the pneumatic one, air pulses are transmitted from the loudspeaker's pulsing membrane to the investigated tissue by means of a wave guide

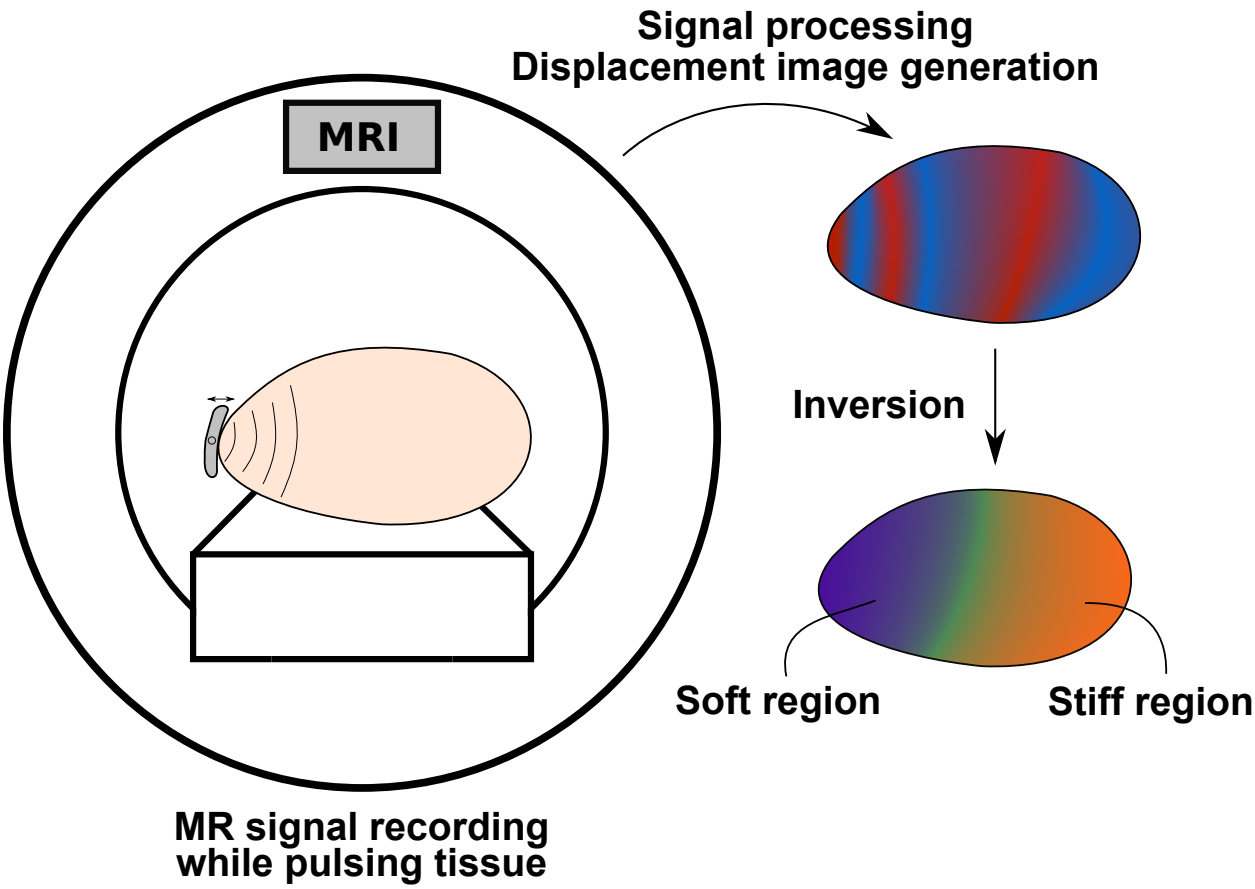

Figure 33 – Workflow in MRE investigation. Small time harmonic deformations are generated in the scanned tissue using an external actuator or natural body pulsation. These small deformations are recorded by the MR scanner using tailored acquisition sequences to produce time series propagation images. The complex MR signal is then processed to extract the motion field data, which is finally used as an entry to physical modeling allowing for calculation of mechanical parameters

(plastic tube). The tube is connected to an interface attached to the surface of the tissue. Plastic pads with a soft membrane and air cushions are the main examples of such interfaces. Main advantages are versatility allowing for applications to various organs [**96, 62, 139, 442, 443, 93, 444, 445, 95**], and the electricity-free transmission system (pneumatic) requiring no electrical current inside the magnetic resonance imaging (MRI) room. The main drawback may be the limitation to simple mono-frequency waveforms only. In the rigid category, loudspeakers transmit motion to tissues via a rigid rod attached to the membrane on one end, and to the patient on the other end. This configuration is also versatile [**75, 446, 140, 74, 289, 447, 77, 76**] and handles arbitrary waveforms but requires

the loudspeaker to be inside the MRI room. Lorentz-coil actuators have also been used to generate motion in various organs [**448, 66, 63, 449, 450, 451, 61, 64**], and rely on the coupling of the MRI magnetic field $\mathbf{B}_0$ with an electrical current injected into the coil. These actuators must be designed according to the targeted organ as they are placed relative to $\mathbf{B}_0$. Piezoelectric drivers allow to deliver arbitrary waveform pulses to tissues while avoiding the constraint of positioning relative to $\mathbf{B}_0$. Significant displacement fields could be obtained using this technique in various conditions (human abdomen [**81, 83**], human brain [**141, 452**], human breast [**453**], and mouse brain [**65, 454**]).

A major bottleneck in generating sufficiently high motion deflection in tissues is the decrease of the motion amplitude with increasing excitation frequencies. Using a wide range of mechanical excitation finds its application in the analysis of frequency dependent mechanical behavior of soft tissues [**75, 448, 65, 82, 455, 456, 457, 162**]. The more frequencies, the more valuable is the information. Centrifugal force based MRE drivers have been proposed to circumvent this limitation at high frequencies. The centrifugal force allows to maintain the displacement amplitude high regardless of the frequency [**458**]. The "air-ball" actuator and "gravitational actuator" are the first examples of the centrifugal force implementation. The air-ball actuator [**459**] consists in a ball circulating in a circular chamber under injection of compressed air. The revolution speed of the ball is imposed by the input air of which the pressure determines the actuator vibration frequency. The gravitational transducer is made of a mass attached to and rotating about an axis. The rotation speed is driven by the rotating axis connected to a motor [**142**]. All the aforementioned techniques consist in shaking the surface of the probed tissue, which implies that elastic waves propagate to the region of interest with sufficient amplitude. This can be an issue if the imaged domain is deep under the surface thus increasing the risk of high attenuation. Producing a wave field *in situ* may be an alternative way to ensure that a sufficient amount of displacement remains in the region of interest. In that regard, focused ultrasounds have been used to generate shear waves along with an MR scanner for motion detection [**42**]. This technique requires a heavy experimental setup compatible with the MR environment and has not been,

to date, more than a proof of concept. Instead of using external devices to produce motion at chosen locations, the concept of intrinsic actuation taking advantage of natural internal vibrations has gained interest. This method consists in encoding motion induced in organs by the natural pulsation of the heart and arteries, and presents the significant advantage of not requiring any additional equipment. Tailored MRE protocols must be adopted to adapt to the low frequency characteristics of natural pulsations (around 1 Hz). For now, intrinsic actuation has been used in brain studies [**144, 145, 143, 111**].

B.4.2. Acoustic wave detection

Whereas most magnetic resonance imaging protocols attempt to reduce or compensate for motion, MR elastography seeks to take advantage of small vibrations in the scanned tissue. Numerous MRE specific pulse sequences (chronologically sorted application of radiofrequency (RF)-pulses and magnetic gradients to generate and manipulate the MR signal) have been designed to acquire driven or natural motion in biological tissues, while maintaining reasonable scan times and image quality. We review, in this section, the main concepts of MR elastography pulse sequences allowing detecting acoustic wave propagation. More specific details and theory, along with fast acquisition strategies are available elsewhere [**460, 321**]. Motion encoding principles in MRI were first introduced by measuring sea-water velocity [**461**], and further applied in the context of angiography to measure blood flow [**462**]. The proof consisted in relying spin velocities to the phase shift spins experienced when space and time varying bipolar magnetic fields were applied. A similar concept, leading to MRE, was developed in which motion of spins around their position at rest is encoded in the phase of the complex MR signal using magnetic-field gradients, named motion encoding gradients (MEGs). The accumulated net phase of moving spins varies according to their trajectory while a time dependent MEG is applied. This net phase thus allows to track local motion of tissue eventually providing the displacement maps required for retrieving mechanical parameters. MRE sequences are generally based on existing MR encoding schemes outfitted with MEGs. Not only are their setting key to be compatible with the characteristics of the

induced motion but so are other inherent MR imaging parameters, leading to a broad variety of MRE sequences.

The timing of the chosen MR based-sequence imposes constraints regarding scan time, motion sensitivity, and image quality. The MR sequence design and underlying physics are beyond the scope of the present review, thus only the main concepts relevant to an overall understanding of MRE is briefly discussed. For in-depth details, see [**463, 321**]. When a tissue is placed in the strong static magnetic field $\mathbf{B}_0$ of an MR scanner, a net magnetization aligned with the magnetic field is produced from the contribution of each uncoupled individual nuclear spin (those of hydrogen nuclei in clinical scanners) [**463**]. The key concept in MR signal generation consists in tipping the net magnetization of the desired portion of the scanned tissue out of its resting state using some excitation radiofrequency pulses tuned at the Larmor frequency of the spins in the scanner [**464**]. Magnetization enters a precession motion about $\mathbf{B}_0$'s axis under the effect of this RF-pulse. Once excited, the magnetization is no longer aligned with $\mathbf{B}_0$ and tends to realign and reach its resting state back again. This process called relaxation occurs at a certain time rate dictated by the interactions between spins themselves and with their environment. The time constant T_1 characterizes the exponential regrowth of the magnetization parallel to $\mathbf{B}_0$ (longitudinal component of the magnetization) due to spin-lattice interactions. Time constants T_2 and T_2^* characterize the exponential decay of the transverse magnetization component (perpendicular to the longitudinal one) due to spin-spin interactions and magnetic field inhomogeneity (combined with the spin-spin interaction), respectively.

Timewise, $T_2^* < T_2 < T_1$ and decay rates are given by $R_2^* = 1/T_2^*$ and $R_2 = 1/T_2$, where $R_2^* > R_2$. The time evolution of the MR signal immediately following the RF-pulse excitation is named free induction decay (FID) and is governed by T_2^* effects. Receive coils are used to monitor relaxation by measuring the voltage induced by the precessing magnetization according to Faraday's law. Manipulation of the magnetization allows to generate MR signal peaks at adjustable delays after the application of the excitation RF-pulse, *i.e.* during the FID, or later when the signal appears to have vanished. MR sequences may be divided into

two main categories of mechanisms leading to different timing for data acquisition. Spin echo (SE) sequences employ a second RF-pulse called refocusing RF-pulse, occurring after the FID, and allowing for compensation of T_2^* effects (magnetic field inhomogeneity). Some of the MR signal can thus be recovered after the FID. In this case, the limiting time constant becomes $T_2 > T_2^*$. Passed the exponential decay due to T_2 effects, the MR signal can no longer be recovered. The peak of the recovered MR signal, the echo, occurs at the "echo time" T_E after the application of the RF-pulse excitation. Gradient recalled echo (GRE) sequences, however, typically operate within the FID (occurring immediately after the RF-pulse excitation) and do not allow for magnetic field inhomogeneity effects compensation. The operating window in such sequences is thus limited by the T_2^* weighted decay, and thus leads to much faster acquisition protocols. Magnetic field gradients are used, instead of a second RF-pulse, to manipulate the magnetization and generate a signal echo at T_E. As aforementioned, MRE sequences usually consist in incorporating motion encoding gradients into an MR based-sequence. This modification is consequently subjected to timing limits of the base-sequence. The short timing of gradient echo type sequences presents a narrower time slot for the MEGs to operate than that of spin echo type sequences. The impact of such inherent characteristics is discussed below.

The first descriptions of the motion encoding mechanism in MRE were reported in Refs. [**41, 465**]. As aforementioned, a spin moving in the presence of a magnetic-field gradient G experiences a phase shift ϕ:

$$\phi(\tau) = \gamma \int_0^\tau \mathbf{G}(t) \cdot \mathbf{r}(t)\, \mathrm{d}t, \tag{124}$$

where γ is the gyromagnetic ratio of the material ($\mathrm{rad.s^{-1}.T^{-1}}$) and $\mathbf{r}(t)$ is the time-dependent position vector of the spin. From this equation appears that the phase shift depends on both the spin trajectory $\mathbf{r}$ and the applied $\mathbf{G}$. Consequently, a given arbitrary spin motion results in different accumulated phases depending on the magnetic gradient waveform. Hence, the remaining definition of $\mathbf{G}$ sets the type of motion the encoding process is sensitive to. Since the inherent function of magnetic field gradients is to add a controlled space-dependency to the static and homogeneous magnetic field $\mathbf{B}_0$, even static spins experience a space dependent

phase accumulation while MEGs are switched on. In order to cancel this unwanted phase accumulation, **G** can be set to oscillate in time allowing the phase accumulated during the first half of the gradient oscillation period to be compensated during the second half. This technique is called zeroth moment nulling [**321**]. Non-oscillating MEGs are called unbalanced gradients and are thus rarely used in conventional MRE sequences. Additionally, the effect of constant velocity and constant acceleration background components in moving spins may also need to be cancelled. This can be achieved by applying first and second moment nulling, respectively [**321**]. Both consist in adjusting the MEGs oscillation profile so that the accumulated phase in Eq. 124 goes to zero for unwanted spin motion.

Many MRE applications have resorted to full wave encoding (MEGs tuned to the same frequency as that of the motion oscillation) with zeroth [**80, 65, 453, 466, 449, 467, 99**] and first moment nulling [**96, 62, 443, 447, 162**]. For all types of oscillating gradients, the area under the curve of MEGs over the operation time must equal zero for proper motion encoding. Early in MRE, several examples of motion encoding strategies were derived in the case of time-harmonic excitation, leading to time-harmonic spin trajectories and involving full-wave encoding [**465**]. Spin trajectories **r** can then be written as:

$$\mathbf{r}\left(t\right) = \mathbf{r}_0 + \xi_0 \cos\left(\mathbf{kr} - \omega t + \theta\right), \tag{125}$$

where $\mathbf{r}_0$ is the position vector of spins at rest, ξ_0 is the spins displacement amplitude, $\mathbf{k}$ the wave vector, $\mathbf{r}$ the position vector, ω the oscillation frequency, and θ some initial phase offset. Solving Eq. 124 using Eq. 125 and the MEG temporal profile allows to quantify the encoding efficiency, which is defined as the amount of phase shift in the signal per displacement unit. Encoding efficiency formulas for common MEG waveforms are available in Refs. [**460, 321**].

Full wave encoding scheme ensures a good motion sensitivity but compels the minimum achievable value of the echo time dependent on the driver actuation period. GRE sequence short timing due to T_2^* effects is well suited to high actuation frequencies (short time slot for MEGs to operate); however, it limits the applicable number of MEG cycles [**453, 466, 449, 468**]. The optimal setting resides at the trade-off between the SNR increase permitted

by short T_E and the higher motion sensitivity permitted by multiple MEG cycles. A similar conclusion can be drawn with regards to SE sequences, which present a more flexible timing enabled by their inherent longer echo and repetition times [**463**]. Multiple MEG cycles can thus be incorporated into the sequence while maintaining the echo intensity sufficiently high. SE sequences are often implemented with fast readout strategies, for instance echo planar imaging (EPI) necessitating only one or few combinations of excitation- and refocusing-RF pulses to generate a whole image, which allows to circumvent the use of many long repetition times (T_R) [**96, 62, 447, 162**].

So far, single actuation frequency cases have been presented. Full-wave encoding can also be used to extract a frequency of interest from a multi-frequency oscillating wave field by selecting proper MEG profile (frequency and number of cycles) [**74, 136, 468**]. This configuration presents little interest in cases where the actuation frequency is chosen by the user. The only way of performing multi-frequency acquisitions using full-wave encoding is to repeat the encoding for each frequency separately [**80, 448, 65, 469, 449, 457**], which has an impact on the acquisition time. However, multiple frequency components can be simultaneously encoded in a single acquisition using wide band MEGs, and manually selected using a temporal Fourier transform [**75, 446, 74, 77, 79, 470, 76, 78, 111**]. The main advantage of simultaneous multi-frequency encoding is the time saving making them more suited to *in vivo* studies compared with repeated single frequency acquisitions over a given frequency range. The main drawback is the overall lower motion amplitude at each frequency of the multi-frequency actuation compared with the repeated acquisition scheme, due to total energy deposition divided into the total number of frequencies.

The wideband property of MEGs has been further extended to fractional encoding where the frequency of the mechanical oscillation is smaller than that of MEGs, and the mechanical time period is larger or equal to the repetition time [**450**]. With shorter MEG time periods, scan duration can be reduced and higher SNR can be obtained by shortening the echo time accordingly [**66**]. A major advantage of this approach is found in measurement of low frequency induced motion, such as heart pulsation driven actuation (around 1 Hz), where

full-wave encoding would lead to impractical echo times [**281, 144, 145, 143**]. Despite the lower motion sensitivity in fractional encoding, this method has proven successful using fast acquisition protocols (spoiled GRE and GRE/SE equipped with EPI readout strategy) [**448, 8, 471, 66, 67, 144, 442, 93, 77, 451, 457**]. Besides multi-frequency acquisitions, reduced T_E and T_R permitted by fractional encoding have also been exploited in balanced steady state free precession MRE [**472, 450, 473**], despite the original development circumventing the use of MEGs [**474**]. Although high phase-to-noise ratios were reported, this sequence type presents significant timing constraints (actuation frequency linked to T_R), and non-linear phase accumulation between consecutive T_R leading to additional signal post-processing steps. It has consequently been used only sporadically [**66, 460, 321**].

B.4.3. Inverse problem in MRE

The previous section reviewed some acquisition approaches to measure motion induced in the tissue of interest. The last step in elastography consists in relying these displacements to mechanical parameters using physical models. This section addresses the most reported inversion schemes employed in MRE. More specific information about processing times and modelling details can be found in Ref. [**475, 476**]. A major strength of magnetic resonance is the capacity of encoding motion in the three directions of space, allowing for full 3D inversion of the Navier's equation. This strength comes at the cost of overall longer scan times for which alternatives have been discussed above. Despite the availability of fast 3D MRE sequences, all mechanical parameter reconstruction methods do not make use of complete displacement data sets and take advantage of physical assumptions allowing processing of reduced dimension displacement data. We propose to classify inversion schemes into two categories. The direct approach consists in formulating the inverse problem with the mechanical parameters as unknowns. The displacements data measured experimentally are inserted into the equations of elasticity, and quantities of interest are extracted through direct inversion. The iterative approach consists in iteratively solving the forward problem for displacements starting from an initial set of guessed mechanical parameters. These mechanical parameters

are iteratively updated to minimize the difference between experimental displacement data and computed displacement solution. The final solution is the set of mechanical parameters that makes that difference converge to a global minimum.

B.4.3.1. *Direct methods*

The first inversion method reported in the context of MRE, assuming isotropy, local homogeneity, no attenuation, and incompressibility, consisted in estimating the local wavelength of the measured wave field. This technique is termed LFE (local frequency estimation). Briefly, pairs of filters centred on spatial frequencies usually separated by one octave are applied to the wave field. The ratio of displacements filtered by each filter of one pair equals the local wavelength [**89**]. To ensure that local spatial frequency is included in the bandwidth of the filter pair, the process is repeated over a certain range of frequencies. From the evaluated wavelength (inverse of spatial frequency), the magnitude of the shear modulus $|\mu|$ is retrieved using $|\mu| = \rho v_s^2 = \rho\,(\lambda_s f)^2$, where λ_s is the local wavelength and f is the temporal actuation frequency. We recall here that ρ is the tissue's mass density, v_s the shear wave speed, and that such assessment assumes a purely elastic tissue (no viscosity). The original publication describing LFE [**136**] employed log-normal quadrature filters but other functions have been studied [**90, 91**]. This method has been widely used in all types of study [**96, 93, 444, 95, 99**], as it is fast and only requires a single component of the displacement field. LFE has also proven a certain robustness against noise as it does not directly compute spatial derivative of the image, thus circumventing noise enhancement. To date, LFE is the only reconstruction method used and marketed for routine clinical practice. Although the LFE in itself provides no insight into the viscous behavior of the investigated tissue, this method has been combined with an attenuation model to estimate both μ_r and μ_i, thus avoiding calculation of 2nd or 3rd order derivatives. Phase gradient methods allow for simple estimation of the wave number k, similarly to LFE, which is used to quantify elasticity only. They have been sporadically used given their insensitivity to wave attenuation and their dependency on planar waves.

Early in MRE were also reported direct methods assuming viscoelastic materials, as described in section B.2.1, and using the strong formulation of the Helmholtz equation [**65, 466**]. The underlying assumptions of isotropy, local homogeneity, and incompressibility are used to neglect the stiffness gradient across the tissue, and to decouple motion components in the equation system. From there, a single motion component can be used to retrieve the complex-valued shear modulus μ^*. Planar assumption allows to consider the 2D, instead of 3D, curvature of the wave field, which further decreases the required amount of data to solve the inverse problem. This method has also been widely used [**75, 80, 74, 73, 77, 79, 76, 78**] given its relative simplicity and low computational cost but strongly depends on data filtering and evaluation of second derivatives [**477**]. Using this scheme, stiffness reconstruction was shown to be altered by the neglected first Lamé parameter (Eq. 107) [**68**]. Applying the Helmholtz decomposition to the wave field allows to separate divergence-free (shear) from irrotational (compressional) components. Taking the curl of the Helmholtz equation increases the differentiation order but physically isolates the shear component of interest. This approach has become prominent when the Helmholtz equation is employed to retrieve storage and loss moduli [**65, 66, 63, 67, 62, 69, 68, 454, 64**]. To improve resolution and stabilize the direct inversion of the mono-frequency Helmholtz equation, a multi-frequency approach named MDEV (multi-frequency dual elasto visco inversion) was introduced [**455**]. A multi-frequency wave field is built upon data sets of individual different frequencies, ignoring the dispersion of mechanical parameters with respect to frequency, reducing the risk of nodes due to standing waves and stabilizing the equation system by adding equations with the same unknown. Various studies have resorted to inversion schemes based on this method [**82, 81, 83**]. As an alternative to the 2nd order derivative assessment required by MDEV, a phase-gradient based method termed k-MDEV was proposed. It consists in evaluating the complex wave number k^* of a plane wave (see section B.2.1), which can then be related to both phase velocity for elastic modulus estimation and attenuation for viscous behavior quantification [**83**].

A finite-element (FE) based inversion method was recently proposed, also assuming local homogeneity, for storage and loss moduli assessment. It takes advantage of the weak form of the equations of motion to reduce the differentiation order, and exploits divergence-free test functions to lower the impact of the compression field [**70**]. So far, most of the discussed approaches have in common the assumption of local homogeneity, neglecting the gradient of mechanical parameters across the tissue, and incompressibility, invoked to neglect terms involving the divergence of displacements (unless the curl operator is applied). The local homogeneity assumption was shown to alter the reconstructed mechanical parameters in regions where the latter are not constant [**467**], that is in most clinical cases and notably tumorous tissues. Direct methods, still employing the strong form of the Navier's equation and neglecting the divergence of the wave field, were proposed to consider heterogeneity using single [**101**] and multifrequency (HMDI – heterogeneous multifrequency direct inversion) [**100**] approaches. To address the compression aspect in nearly incompressible materials, which was shown to lead to artefacts and inaccuracies [**478, 479**] when disregarded [**479**] or processed using displacement formulation only [**480, 481**], direct FE formulations of the inverse problem have been proposed using curl-based [**102**] and mixed displacement-pressure [**104, 102, 479**] schemes.

B.4.3.2. *Iterative methods*

Overall, iterative methods make less restrictive assumptions on tissue mechanical properties than direct ones relying on the algebraic strong formulation of the elasticity equations, and have been reported to solve for more unknowns than FE-based direct methods by adjusting the number of parameters to update in the minimization process. From a computational standpoint, solving forward problems, that is, mapping data information (*i.e.*, displacement field) from source information (*i.e.*, elasticity distribution) is a smoothing process. On the contrary, inverse problem consisting in mapping source information (*i.e.*, elasticity distribution) from data information (*i.e.*, displacement field) is a noise-enhancing process [**482**]. Consequently, iterative approaches tend to be more robust against noise than direct ones. Following FE discretization approaches, iterative schemes have been developed [**112, 114, 483**].

Near incompressibility is often assumed and requires to modify the formulation of elasticity equations in order to solve for pressure in addition to displacements (aforementioned mixed "pressure-displacement" formulation), and material heterogeneity is mostly considered [**104, 113**]. In MRE, the subzone technique has gained significant interest amongst iterative processes [**116**]. It consists in dividing the imaged domain into overlapping subdomains, termed subzones, and solving iteratively the forward problem for displacements in each subdomain parallelly [**453**]. Once the solution in each subzone has been computed, subzones are randomly redistributed over the domain and the iterative solution calculation is performed again. Retrieved mechanical parameter distributions, corresponding to each subzone distribution, are finally averaged to form the final solution. This reconstruction method has been applied to phantoms, brain [**233, 162**] and breast [**484, 485**] data, and has proven its capacity to reconstruct multiple variables at various actuation frequencies using elastic and viscoelastic physical models (compressible elastic [**295**], compressible viscoelastic [**486**], and nearly incompressible viscoelastic [**281, 289, 233, 484, 305, 122, 162, 295**]). Additionally, poroelastic models have been introduced for accurate consideration of the biphasic nature of entangled solid-liquid structures in biological tissues [**289, 282, 305, 445, 145, 122**]).

B.4.4. Applications

B.4.4.1. *Liver*

MRE can be applied to virtually any organ provided sufficient displacement data quality and suitable inversion scheme. We mainly restrict our discussion to liver applications due to the clinical availability of the technique, and to brain of which *in vivo* mechanical properties have yet only been non-invasively accessible using this elastography method. MRE in clinics has so far been restricted to liver scanning for fibrosis, and diagnosis of chronic liver diseases using purely elastic models, *i.e.*, assessing the shear modulus only and ignoring the tissue's viscous behavior. Under these assumptions, meta-analyses over the past few years on liver MRE have highlighted the high performance of the method in distinguishing liver fibrosis stages in non-alcoholic fatty liver disease, and cirrhosis considering the stiffness increase

under this condition [**487, 488**]. Viscoelastic parameters in human liver diseases have also been early investigated using multi-frequency MRE to assess the frequency dispersion of storage and loss moduli in healthy and fibrotic patients [**446**]. Results showed an increase in both μ_r and μ_i in fibrotic with respect to healthy livers. Evaluation of the elastic modulus and viscosity using a standard linear solid model in healthy and fibrotic human livers led to a similar conclusion, where both elasticity and viscosity increased in pathological liver tissues [**75**]. This trend was also reported in [**489**], and in a study on the performance of MRE in the detection of fibrotic livers [**490**]. Overall, stiffness only or both stiffness and viscosity increases have been observed against the fibrotic stage. Interestingly, a case of liver steatosis in rats where only viscosity varied while stiffness remained unchanged has been reported in [**491**]. Despite these findings, the storage modulus was found to correlate better with stages of liver fibrosis than viscosity [**492**]. Additionally, measurement of wave damping for viscosity characterisation is influenced by reflections off boundaries and renders its measurement troublesome. To date, stiffness variations for estimation of liver fibrosis severity has been mostly investigated.

B.4.4.2. *Brain*

MRE has also been proven successful and robust in the brain. Its high water content and the observed shear wave attenuation in MRE acquisitions suggest that restriction to purely elastic models may lack of accuracy. The healthy brain's viscoelastic behavior has been highlighted by evaluating the dispersion of reconstructed mechanical parameters at varying frequencies in humans [**82**] and rats [**65**]. Both storage and loss moduli tended to increase with frequency. Additionally, cerebral viscoelasticity was shown to follow a frequency power law, where all reconstructed parameters varied independently [**162**]. These reconstructions suggested that the falx cerebri's viscous behavior is singular in comparison with other brain regions. Along similar lines in healthy brain characterization, viscoelasticity changes due to physiological ageing have been considered [**7, 77, 79**]. From these studies appear that the brain softens but sees its relative viscous-to-elastic behavior unchanged over time. Such investigations along with MRE of neurological diseases have underlined the high potential of

this technique in detecting neurodegenerative pathologies [**493**]. Non-invasive differentiation of natural structures of the brain based on their mechanical response to stimulus imparts MRE a significant advantage. For instance, the cerebellum has been shown to be softer and tends to be less viscous than the cerebrum [**64**].

High resolution mapping of stiffness and dispersion effects have suggested that cortical white matter is stiffer and more viscous than grey matter [**448**]. MRE has also been used to quantify the viscoelastic changes of altered brains. Notably, Alzheimer's disease was shown to reduce the brain's stiffness (elasticity only) [**447**]. Glioblastoma has been shown to take lower stiffness and viscosity values using multi-frequency MRE in humans [**457**], and mono-frequency MRE in a rat model [**494**]. A similar softening trend was observed in multiple sclerosis [**495, 76, 78**], where viscoelasticity was assessed using a global parameter. On the other hand, normal pressure hydrocephalus appears to trigger the opposite effect [**96, 145**]. Recent research on brain viscoelasticity has opened new avenues in the understanding of connexions between cerebral functions and tissue mechanical behavior. For instance, joint investigation of hippocampus viscoelasticity (shear stiffness and damping ratio), and relational memory has allowed to correlate hippocampal viscoelastic variations to performance in completion of spatial reconstruction tasks [**496**]. Viscoelasticity was characterised using an adjusted damping ratio that indicates the dominant tissue behavior between elasticity and viscosity. Results showed that better relational memory performance correlated with a rather elastic mechanical behavior of the hippocampus. This constituted the first observation of the kind.

The same principle was applied to assess the correlation between cardiovascular health through aerobic fitness exercises, relational memory performance through spatial reconstruction tasks, and hippocampal viscoelasticity using MRE. The study showed that better memory performance was associated with higher values of the adjusted damping ratio, which was itself associated with better aerobic fitness performance [**217**]. Light fitness exercise has also been shown to have a potential impact on hippocampal viscoelasticity and associated cerebral functions in multi-sclerosis patients [**497**]. These investigations laid the first stone

for the characterisation of relationships between physical and cerebral functional behaviors, and brain viscoelasticity [**216, 498, 218, 499**].

B.4.4.3. *Brain anisotropy and poroelasticity*

Finally, most advanced improvements in viscoelasticity characterisation embed tissue anisotropy, which is particularly relevant in the brain given its fibrous structure. As a deviation from brain applications: the first use of anisotropy in MRE was proposed for breast tumor detection through the evaluation of an assumed symmetrical stiffness tensor [**500**]. Results suggested that carcinoma have an anisotropic structure revealing a preferred orientation, certainly due to vascularisation, and suggesting transverse isotropy. Breast cancer was then also characterized assuming a transversely isotropic model leading to a 5-parameter reconstruction [**68**]. Again, results showed a preferred orientation in the tumor structure. Transversely isotropic mechanical property recovery was experimentally validated in fibrous tissues using MRE and diffusion tensor imaging (DTI) [**501**]. *In vivo* brain anisotropic stiffness assessment in humans assuming separately orthotropy and transverse isotropy suggested that white matter exhibits a transverse isotropy structure [**322**]. Shear wave speed analysis was performed from prior knowledge of fiber orientation using DTI. Two shear wave modes were then observed, a faster longitudinal mode relatively to a slower transverse mode. The transverse anisotropy of white matter was later nuanced in favor of a mild only anisotropy in a study on *ex vivo* porcine brain, where a purely transverse shear wave mode was generated and used to estimate three isotropic parameters in the absence of longitudinal modes [**502**]. Human brain anisotropy was also highlighted using variations in reconstructed stiffness distribution depending on actuation direction. This constitutes a direct measurement of the anisotropy impact in isotropic models. Such observation was quantified using a finite element formulation of a heterogeneous, nearly incompressible, and transverse isotropic model providing benchmark displacement fields for inversion testing.

In addition to the significant research effort in evaluating and understanding cerebral viscoelasticity, the high water content of the brain has motivated to consider it poroelastic, *i.e.*, made of two, solid and liquid, entangled phases. The impact of poroelasticity versus

viscoelasticity on reconstruction has been shown to be relevant at low frequencies (a few Hertz) using the forward problem formulation in the harmonic regime, and the aforementioned subzone iterative scheme [**289**]. At higher frequencies, viscoelasticity seems to remain a more suitable model than poroelasticity. Overall, poroelasticity and low frequency intrinsic actuation thus constitute an interesting and original package in MRE investigation. This setup circumventing resorting to pulsing equipment has been used in a few studies, and holds promise for more accurate detection of brain pathologies [**145, 143**]. Another approach to highlight brain poroelasticity was to solve for both shear and bulk moduli using the algebraic inversion technique, which resulted in a bulk modulus much lower than expected, confirming the poroelastic nature of the brain (compressible solid matrix and incompressible fluid channels) [**144**]. More recently was proposed an improvement in MR poroelastography acquisition processes allowing to separate solid and fluid contributions to the shear motion field using an inversion recovery sequence adapted to MRE, along with a tailored MR signal modeling [**503**].

To conclude, Fig. 34 illustrates typical wave maps and elastograms from MRE acquisitions in the liver, breast, heart, and brain. Table 8 presents an overview of main components constituting MRE investigations, from motion generation techniques to inversion categories described in previous paragraphs.

B.5. Optical shear wave elastography

Elastography based on ultrasonography or MRI has found popular clinical applications facilitated by the implementation of those imaging technologies on clinical systems. These tools can provide images over centimeter to whole-body depth ranges. However, many applications require sub-millimeter spatial resolution images, which can only be made possible using optical means. For example, on the cellular scale, the measurement of mechanical properties requires higher resolutions to focus on the understanding of how cells respond to

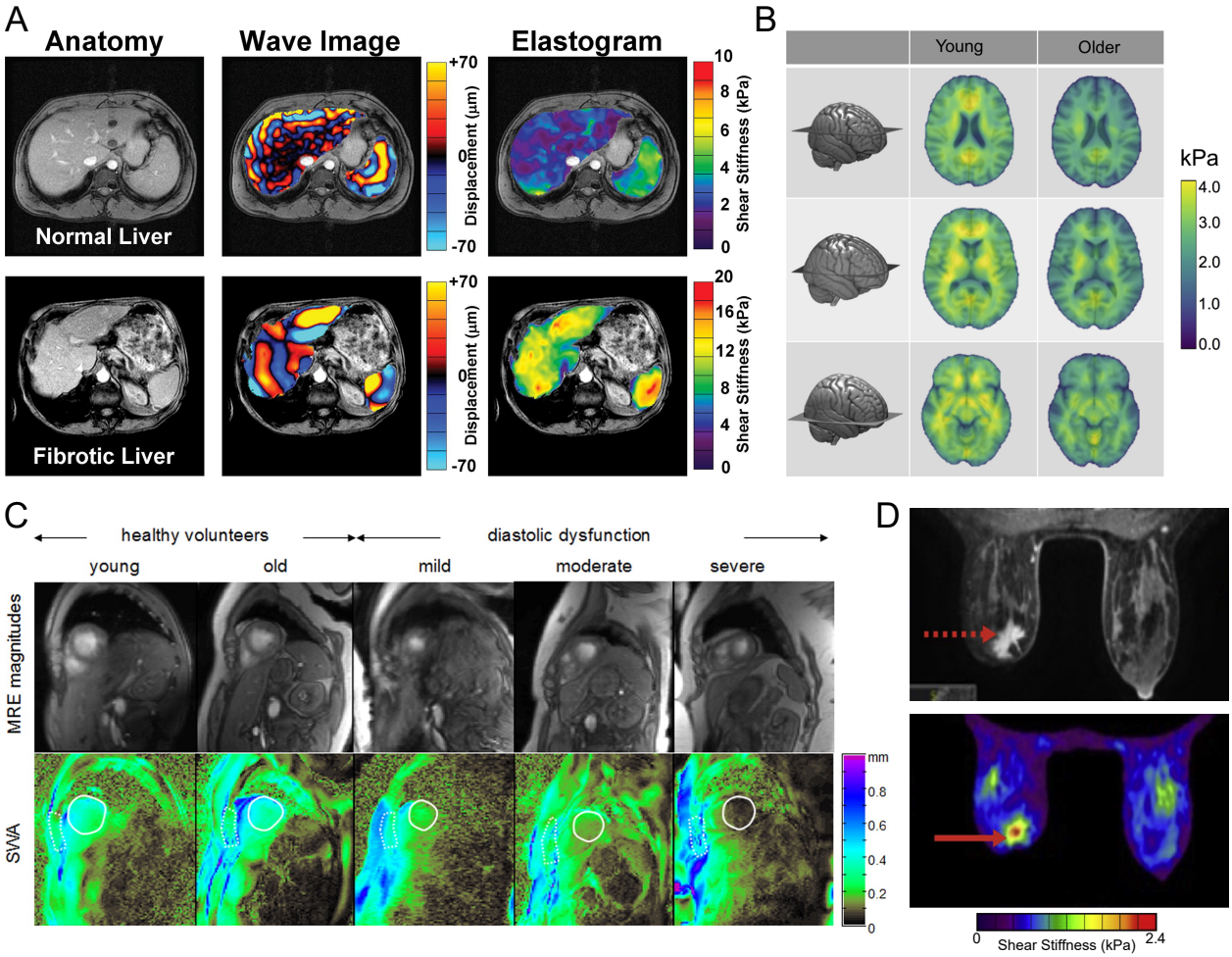

Figure 34 – a. MRE of the liver. Anatomic images, displacement and shear stiffness maps of healthy and stage 4 fibrotic livers. Reproduced with permission from [**6**]. Copyright 2007 AGA Institute. **b.** MRE of the brain. Mean shear stiffness of the cerebrum in young and older adults. Reproduced with permission from [**7**]. Copyright 2018, Elsevier. **c.** MRE of the heart. Shear wave amplitude maps of a healthy heart versus hearts with diastolic dysfunction. Reproduced with permission from [**8**]. Copyright 2014 RSNA. **d.** MRE of the breast. Anatomic image and shear stiffness map of a biopsy-proven invasive ductal carcinoma. Reproduced with permission from . Copyright 2020 Elsevier.

physical forces. Thus, the use of optical elastography provides an opportunity for microscale imaging and for numerous applications in fundamental research [**505**].

Within the last two decades, developments in this new area of imaging led to multiple scientific advancements at the interface between optics and mechanics, which included biomedical applications in ophthalmology, oncology, and cell mechanics. The following subsections discuss recent developments in cellular and optical elastography, and their applications across biomedical and life sciences.

B.5.1. Cellular shear wave elastography

Tissue elasticity at a microscopic scale is determined by the cell and the extracellular matrix elasticity. Main components of a cell are the membrane, cytoplasm, and cytoskeleton. The latter structure contributes to the cell mechanical stability and characteristics, and to its morphology. An imbalance in the mechanical homeostasis and defect in the cellular mechanotransduction can contribute to various human diseases. Therefore, cellular viscoelasticity can be viewed as a biomarker for determining the cellular state [**506**]. Determining mechanical properties of a cell during different stages of the disease progression could help to develop novel treatments by considering the role of mechanical factors into genetic and drug therapies [**507**]. As recently reviewed, there are several techniques for measuring cell mechanical properties, most of them requiring a mechanical stress (*e.g.*, micropipette aspiration and atomic force microscopy). However, in this review, the focus is on rheological properties assessed using a mechanical stress based on acoustical shear wave propagation.

Grasland-Mongrain *et al.* [**2**] developed a novel method called optical microelastography, also labeled as "cell quake elastography". This technique uses a high frequency shear wave excitation and an optical microscope to assess cell elasticity. High frequency shear waves inside the cell are produced by a vibrating micropipette at a wavelength comparable to the cell's size. The wave propagation is captured optically by a high frame rate camera coupled to the microscope. The sampling rate of the camera is selected to avoid shear wave frequency aliasing with sufficient samples per wavelength to allow efficient speckle tracking. The spatial resolution of captured images should also be sufficient to track the shear wave speed from displacement maps (knowing the time elapsed between images). The proof-of-concept in [**2**] was made by using an ultrasound speckle tracking method adapted to optical images for obtaining displacement maps [**298**]. A passive elastography algorithm was used as a reconstruction method to obtain shear modulus images [**109**]. The passive elastography method was inspired by the seismology field [**111**], so the name "cell quake elastography" for this method. The main advantage of this technology compared with other cell elasticity

methods is the time resolution of a few microseconds to produce elasticity maps with a good spatial resolution, which may allow studying dynamic cellular processes.

First experiments were performed on mouse oocytes, making a shear wave inside the cell using a 15 kHz vibrating micropipette, and capturing optical images of the travelling wave at a 200,000 acquisition frame rate [**2**]. The sensitivity and spatial resolution of the technique allowed to distinguish the shear modulus of different regions/zones of a cell (Fig. 35). The technique was recently applied on mouse macrophage-like RAW 264.7 cell clusters, Abelson leukemia virus-transformed cell line derived from mice, using a 18 kHz stimulation and a 100,000 frames per second image capturing rate. Shear wave displacement maps at 10 microsecond intervals are given in Fig.36. Future developments should aim at assessing the viscous component of single cells, likely using finite-elements modeling (FEM) reconstruction methods.

B.5.2. Optical coherence elastography imaging

Optical coherence elastography (OCE) is a technique that can non-invasively assess tissue mechanical properties by measuring the localized deformation, strain or shear wave propagation properties inside a sample. In OCE, a stimulation technique is utilized to load the tissue and its response is recorded with an OCT-based detection method. The high resolution structural images of OCE (1 - 10 μm *in vivo*) provides it an advantage over the ultrasound or MRI modality [**508**], that stretches its potential for micron and sub-micron imaging of elastic properties of biological tissues. Micro-structures of biological tissues can be quantified based on optical scattering properties of the tissue under investigation. OCE holds great potential for diagnosis of many clinical conditions and pathologies, particularly for detection and monitoring of cancers, cardiovascular diseases [**509**], and eye diseases [**510**].

While optical contrast signals are detected based on differences in two or multiple optical scattering events, the mechanical contrast requires only one scattering event to obtain an OCT signal. Thus, structural inclusions that cannot be detected by OCT can be revealed by OCE if a mechanical contrast exists for the inclusion. The first few studies in OCE

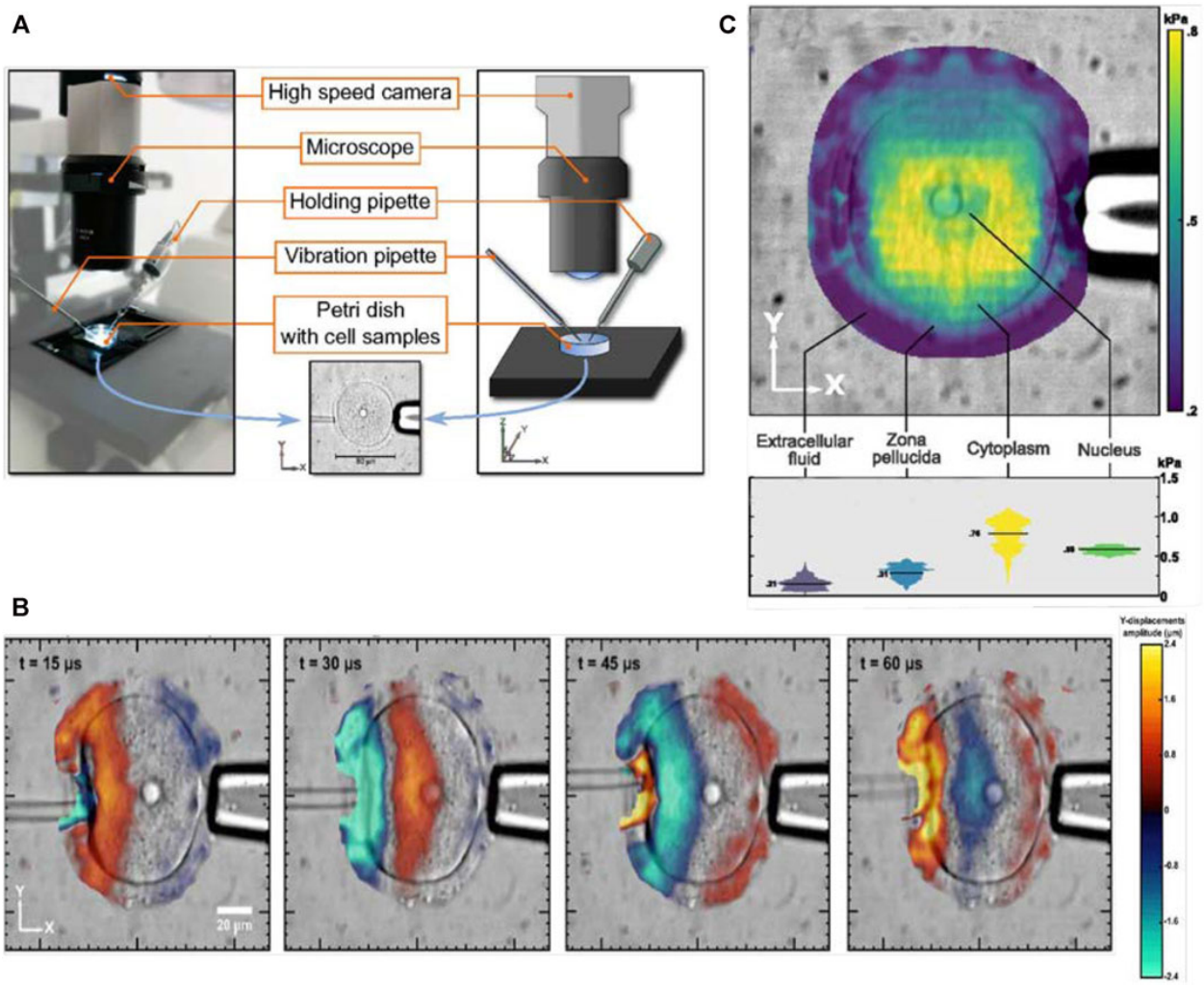

Figure 35 – **a.** Experimental set up for optical microelastography, **b.** Intracellular displacement map through time, **c.** elasticity map of the cell into the zona pellucida, cytoplasm, and nucleus. Adapted with permission from [**2**]. Copyright 2018, National Academy of Sciences.

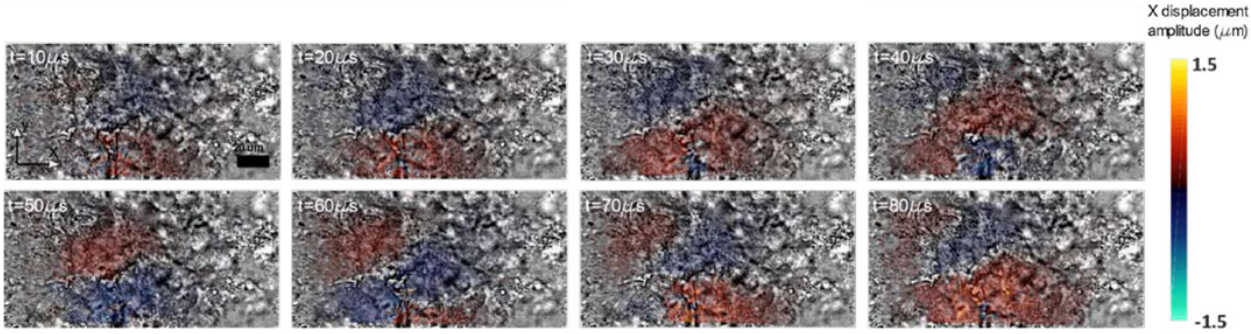

Figure 36 – Displacements of the shear wave propagation within adhesive cell clusters of macrophages RAW 264.7

development focused on static mechanical contact loading (*i.e.*, no shear wave involved) [**32**]. Later, the emergence of phase resolved OCT, which is detecting the interferometric phase information from complex OCT signals, enabled the assessment of tissue deformation with a high accuracy for tissue elasticity reconstruction [**511, 512, 513, 514**]. A shear wave stimulus was involved in studies of Crecea *et al.* [**511**] and Razani *et al.* [**513**].

The latest developments include OCE resolution to improve over the range from several microns to hundreds of microns. The lowest range of OCE spatial resolution is similar to the cell quake elastography imaging method described earlier. In comparison, the spatial resolution of ultrasound or MRI elasticity imaging methods remain at a macroscopic level with a typical resolution of hundreds of micrometers to several millimeters, respectively [**448**]. OCE is a great alternative to traditional elastography methods in terms of spatial resolution, acquisition speed, sub-nanometer mechanical displacement sensitivity, but at the cost of a lower penetration depth into the probed tissue than ultrasound or MRI. Additionally, shear wave OCE as a 3D imaging modality may enable its clinical applications in many areas, such as ophthalmology and cardiology using intravascular devices [**12, 515**]. Shear wave based OCE has shown potential for measuring local elasticity changes of mouse brains [**516, 55**]. Details on these methods are given next.

B.5.2.1. *Systems and methods*

An OCE system has two main components: a loading system that can deform the biological tissue, and an OCT imaging system for detection. Shear wave methods in OCE are relatively in the very early stages of development. Shear waves-based OCE utilizes an excitation from a noncontact air-puff or air-coupled ultrasonic probe [**517, 518**], or piezo-transducers (PZT). In addition, an OCT mechanism is then employed to detect the displacement field of generated shear waves. By monitoring the shear wave propagation in the sample, elasticity, shear wave speed, or the shear modulus can be quantified. Shear wave visualization was performed in tissue mimicking phantoms with phase sensitive optical coherence elastography [**519**]. Razani *et al.* [**513**] were one of the first to measure the shear wave speed and its associated properties with OCT phase maps. They utilized an external acoustic radiation

force mechanism for excitation and a swept-source OCT system to acquire phase images. The central wavelength of the laser was 1310 nm and the bandwidth was ≈110 nm. The system could register a lateral resolution of 13 μmin gelatin mixed with titanium dioxide phantoms. Images could be acquired at a depth of 3 mm. Song *et al.* used a piezoelectric point loading to generate shear waves within samples. More recently, Zhu *et al.* [**10**] developed a PZT-based system to induce longitudinal shear waves and they visualized the signals using OCT for the quantified mapping of shear moduli. A brief detail of their technique is presented next.

The OCE system included an OCT imaging unit and a PZT excitation unit, as shown in Fig. 37.a. Elastic waves were induced by a ring PZT actuator driven by a PZT amplifier. The vibrating mechanism of the PZT system could excite three types of waves in the sample under investigation: (a) Rayleigh waves, (b) compressional waves travelling from the top surface to the deep region, and (c) transverse and longitudinal shear waves travelling through the interior of the sample, as shown in the Fig. 37.b. Rayleigh waves propagate at the surface of the sample. Compressional waves propagate parallel to the oscillation direction of the vibrator. Transverse shear waves propagate perpendicular to the displacement direction. Additionally, in the near field of the planar vibration source, which contained multiple sub-sources, a longitudinal shear wave much slower than the compressional wave also propagate along the displacement direction. This longitudinal shear wave is present due to the sum contributions of diffracted transverse shear waves [**10**]. These longitudinal shear waves could be visualized with the attached OCT imaging unit. The OCT system was based on a swept source at a central wavelength of 1310 nm, and a wavelength tuning range of 141 nm. Axial and lateral resolutions of the employed OCT unit were 7.6 μm and 17.7 μm, respectively. The PZT unit utilized for excitation was driven by a function generator producing a sine wave cycle with a frequency of 1 kHz. The displacement observed in the near field was close to 10 μm.

As introduced above, noncontact shear wave imaging optical coherence tomography (SWI-OCT) system has been developed using a focused air-puff device for localized tissue

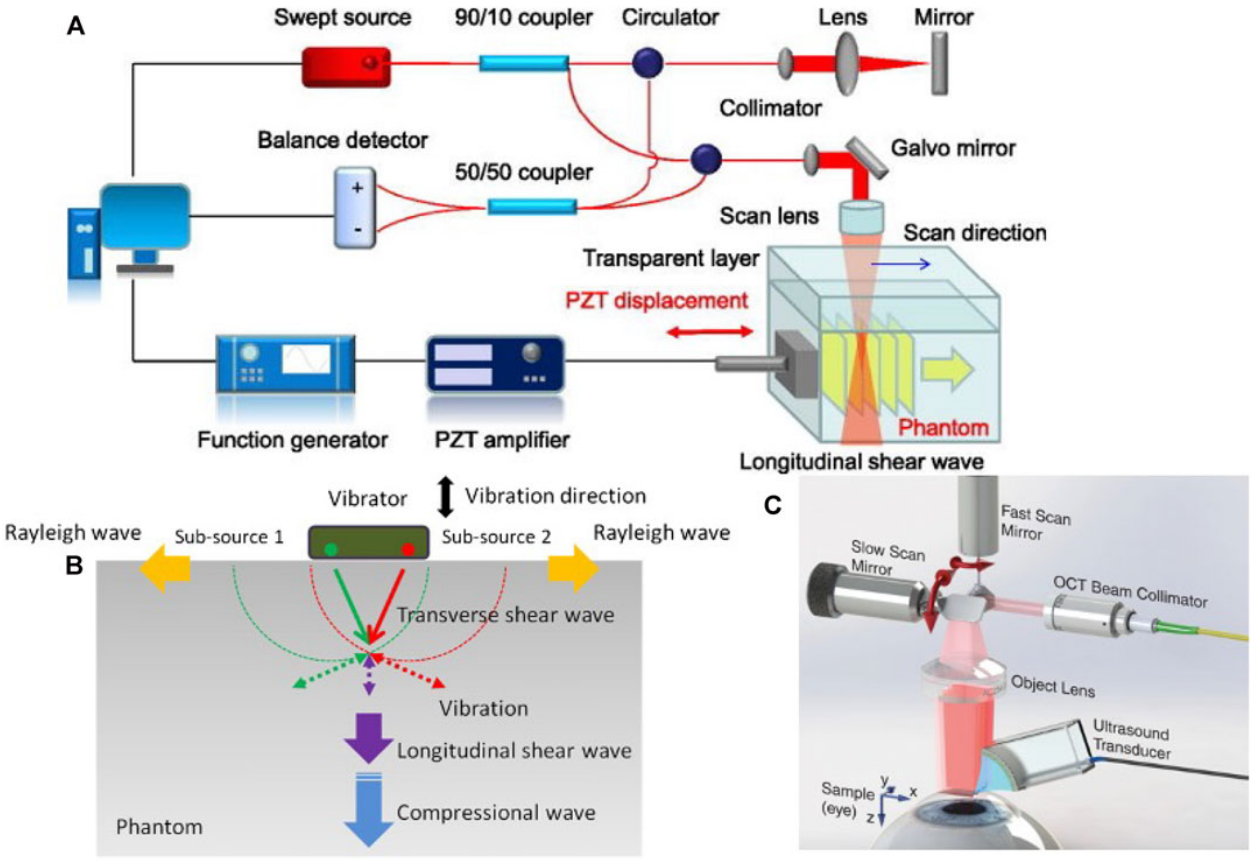

Figure 37 – a. Schematic of the OCE system. The system employs a swept source OCT unit and a PZT excitation unit. The PZT unit induces displacements within the sample, and the OCT unit detects the signals and visualizes the longitudinal shear wave propagation. Reproduced with permission from [**9**]. Copyright 2017, AIP Publishing. **b.** A representation of waves generated by the PZT unit: transverse shear waves, longitudinal shear waves, compressional waves, and Rayleigh waves. Reproduced with permission from [**10**]. Copyright 2017, AIP Publishing. **c.** Schematic of the acoustic micro-tapping phase sensitive OCT imaging system developed by Ambrozinski *et al.* Reproduced with permission from [**11**]. Copyright 2016, Nature Research

deformation [**520**]. The noncontact mechanical excitation in a sample could be performed with a PZT transducer that was specially designed to launch an US beam through air that was focused onto the air-medium interface. The reflection of the beam at this interface could produce significant acoustic radiation force toward the sample medium. This induced a transient displacement at the surface, including shear waves. The large difference in acoustic impedances of air and soft tissues could increase the efficiency of the acoustic energy conversion even to the extent of one hundred percent. Ambrozinski *et al.* developed a non-invasive

system that needed transient displacements to be only about one μm, and the acoustic pressure only a few kPa, which was within safety limits for clinical applications. This acoustic micro-tapping method had enabled 4D imaging of tissue stiffness by employing a focused air-coupled US to induce mechanical deformations at the boundary of a tissue. A schematic representation of their system is shown in Fig. 37.c. In here, the cornea surface was aligned at the transducer focus and the US radiation push was sent through with a repetition period of 3 ms. The driving signal was having a bandwidth range of 0.95 MHz to 1.05 MHz. The measured pressure amplitude at the transducer focus was about 7 kPa.

Wang *et al.* performed a quantitative biomechanical characterization of cardiac muscles and corneas using a noncontact SWI-OCT system. Shear waves had a frequency range of 0-2.5 kHz. This method employed a multi-wave imaging technique, where shear wave measurements in the tissue enabled mapping of the mechanical contrast in elastograms, and the OCT unit enabled improving the imaging resolution from a millimeter scale to a micron scale. The system was capable of simultaneously providing structural images with depth wise maps of the tissue stiffness. Recently, a confocal air-coupled US probe could also be co-focused with a phase-sensitive OCT system to generate elastic waves up to a 4 kHz frequency for quantitative elastography. These noncontact excitation methods have found wide applications in ophthalmology and dermatology [**521, 522, 523**].

Spatial resolution in dynamic shear wave based OCE is governed by temporal and spatial characteristics of mechanical waves rather than optical waves. Hence, the mechanical resolution in dynamic OCE is different from the usual optical resolution of OCT systems. Spatial resolution ideally should match the spatial resolution of the detection system, however, propagating mechanical waves undergo mode conversions at tissue interfaces causing artefacts in the elasticity image. The geometry of the tissue interface and its elasticity contrast can produce complex propagating fields near the tissue boundary affecting both the spatial resolution and contrast of the final reconstructed image.

Recent dynamic OCE systems provided elasticity information from local group velocity measurements, however, the complex geometry of bounded tissues like the cornea may not

reflect a simple relationship between group velocity and elasticity [**522**]. Dynamic OCE has been successfully utilized in elasticity mapping of the cornea using noncontact excitation methods based on air-puffs and acoustic micro tapping [**11, 524, 525, 520, 526**]. Inversion of moduli from experimental data, especially in the case of bounded and anisotropic tissues such as cornea, is a challenging and complicated process in dynamic elastography. Recently, a nearly-incompressible transverse isotropic (NITI) model addressed this challenge and characterized corneal biomechanics while accounting for corneal microstructure and anisotropy and presented a more accurate model for cornea shear moduli computation. Viscosity assessment in shear wave OCE is in its early phase of development. Proposed methods used shear wave frequency dispersion, storage and loss moduli using a rheological model, and the elastic wave attenuation.

A trade-off in OCE is its reduced depth of field while evolving for higher resolution measurements due to the requirement of higher numerical aperture for such systems. On the other hand, the ability to measure and record depth scans with a single spectral acquisition can be used as an advantageous feature to enable phase-sensitive displacement measurements. Of course, the tissue penetration attained with OCE, although sufficient for numerous applications, is not comparable to ultrasound or MRI elastography methods. Song *et al.* implemented a beam-steering US as a wave source for shear wave optical coherence elastography of retinal and choroidal tissues within a porcine eyes ball *ex vivo*. Shear wave propagation imaged on a porcine retina by their system is shown in Fig. 38 [**12**].

B.5.3. Photoacoustic elastography

Photoacoustic elastography (PAE) research is rapidly growing due to its potential and promising features of clinical interest [**527**]. PAE can exhibit a mechanical contrast in biological tissues while also providing high spatial resolution images and an excellent penetration depth compared to commercially available optical imaging modalities. It has the promise to provide great scalability, ranging from cellular levels to entire body with multiple resolution levels. Recent studies have demonstrated recovery of mechanical properties of biological

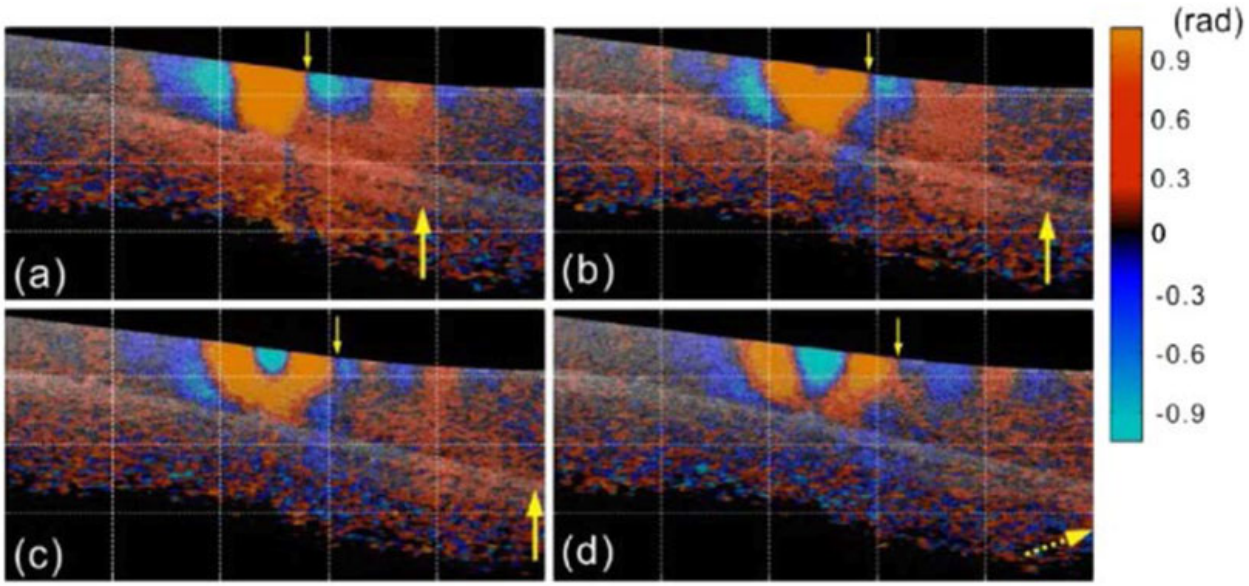

Figure 38 – Images of shear wave propagation in a porcine retina generated with a single acoustic radiation force ultrasound push. The images are taken snapshots at **(a)** 0.2, **(b)** 0.25, **(c)** 0.3, and **(d)** 0.35 ms after the push. Lateral scale: 0.5 mm.div^{-1}; axial (depth) scale: 0.25 mm.div^{-1}. Reproduced with permission from [**12**]. Copyright 2015, OSA Publishing.

tissues using PAE [**57, 528, 58, 529**]. Several studies demonstrated computation of elastic properties of soft tissues [**528, 530, 531, 530, 59, 532**]. Nevertheless, clinical translation of PAE is still far way for research studies to accomplish, the development of the PAE technology has shown the potential to be used in life threatening diseases, such as breast and prostate cancers, and brain tumors. Photoacoustic elastography can be used for mapping elastic properties of diseased tissues with highly vascularized structures, such as carcinoma and glioblastoma. Most PAE studies have focused on qualitative imaging and quantitative PAE is still a challenge. Moreover, PAE using propagating shear waves still need to be clearly addressed. A recent study by Wang *et al.* did develop a PA viscoelasticity technique for quantitative imaging of liver cirrhosis based on a PA shear wave model [**59**]. This viscoelasticity imaging model was inspired by the acoustic radiation force impulse (ARFI) technique (see Section B.3). In this model, a laser beam was focused into a tissue that resulted in the tissue thermal expansion and a PA pressure field was generated. The pressure field induced a localized ultrasound impulse similar to ARFI, and subsequently a tissue displacement field

could be observed. The study assumed that these forward propagating PA waves could be modeled using shear wave equations.

As a summary of methods addressed in this review, Table 9 compares photoacoustic elastography with other elastography modalities in term of performance.

B.6. Challenges and perspectives

B.6.1. Ultrasoud shear wave elastography

Many notable ultrasound elastography methods have been translated into clinical applications, and adopted by clinicians for diagnosis of several organs, as introduced in Section B.3.3. A limitation lies in the depth of SW penetration due to attenuation, especially for the diagnosis of liver fibrosis and steatosis, which could result in unsuccessful measurements with large patients or patients with ascites [**329**]. Note that SW attenuation is a concern for any shear wave elastography method. Consequently, measurements on superficial regions showed a higher success rate, such as the diagnosis of breast lesions and tumors. Another limitation lies in the assumption often used in shear wave elastography, notably considering the tissue as isotropic and homogeneous. Certain tissues such as muscles or tendons do not respect the isotropy hypothesis and are rather considered as anisotropic or transverse isotropic media. To address this problem, teams have developed stiffness tensors for assessing shear wave propagation and for evaluating mechanical properties in several directions, even in three dimensions. Bones, brains, or lungs are parts of the body that can be considered porous and for which the assumption of homogeneity is limited. Poroelasticity based on the estimation of the temporal response of tissues to compression is a technique derived from strain elastography. Although a little off topic because it does not rely on shear wave propagation, its development in the characterization of tumors is promising. Other applications, such as the characterization of muscles, Achilles tendons, the cardiovascular system, and lymph nodes [**360, 533**], have shown good results that allowed reflecting the difference between normal and abnormal tissues.

At present, the measurement of the tissue's elasticity has dominated the field, and technologies, such as the transient elastography, SSI, ARFI, and comb push ARFs are available on clinical scanners [**534, 360, 535, 342, 536, 537, 538, 539, 540, 541**]. In fact, most manufacturers have today a shear wave elastography package for clinical use, and the spatial resolution of those elastography systems are as good as ultrasound B-mode imaging. However for measurements on more complex tissues, such as anisotropic, layered, or near close to interface results should be taken with caution. The characterization of human tissue viscoelasticity without using a rheological model, and studies on viscosity, anisotropy, porosity, and nonlinearity, are important topics in development [**542, 306, 543, 544, 545, 546, 547, 324**]. While those innovations have not yet received clinical approval, further validation with robustness and reproducibility results should allow manufacturers to consider these biomarkers. New applications of SW ultrasound elastography are also in developments. Studies pointed out that the measurement of the elastic property could be used to monitor thermal ablation [**534, 548, 549**].

B.6.2. Magnetic resonance shear wave elastography

Magnetic resonance elastography has been proven successful and robust in a broad range of applications, from clinical diagnosis of liver diseases [**149**] to brain and breast [**550**] pathologies. However, generalization of MRE in clinics is impacted by the scan time required for the acquisition of complete data sets necessary for accurate reconstruction. Clinical sequences currently acquire one component of the motion field at one frequency, and rely on a 1D direct inversion assuming isotropy, incompressibility, local homogeneity, and pure elasticity. This package is fast and guaranties results. Mechanical solicitation of the tissue under multi-frequency loads may be a first step into the characterization of tissue viscoelastic responses by providing valuable information on the frequency dependent biomechanics in pathological cases [**457**]. Motion encoding may also reach a limit at high frequencies in the case of oscillating gradients due to peripheral nerve stimulation [**551**]. The actuation regime also determines the physics to consider for inferring mechanical parameters from

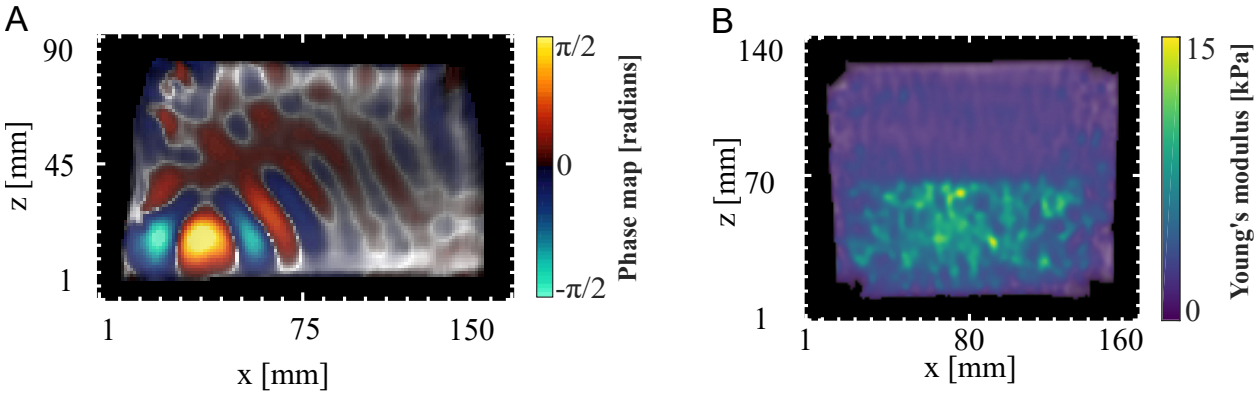

Figure 39 – Preliminary results of Lorentz force MRE in gel phantoms. **a.** Phase map resulting from Lorentz force induced displacements. **b.** Young's modulus map of a heterogeneous phantom reconstructed from the Lorentz force induced motion.

experimental datasets [**289**]. An elegant avenue circumventing the use of external actuators is intrinsic actuation from low frequency heart beats along with poroelastic modeling of the tissue [**145**]. Along the same lines, natural vibrations in the brain have been exploited using the novel passive elastography technique based on time reversal concepts to quantify the vibration wavelengths, assumed to be related to brain stiffness [**111**]. A potential solution to shear wave attenuation in soft viscoelastic tissues may be to place motion sources closer to the region of interest. This may be achieved using ultrasound transducers generating an acoustic radiation force impulse (ARFI) along with MRE acquisition [**43, 42**]. Alternatively, a promising approach that may prove feasible with clinical MRI scanner is Lorentz force elastography for *in situ* actuation at different frequencies [**16**]. An elasticity reconstruction obtained using a Lorentz force and a clinical MRI scanner is displayed in Fig. 39, in the case of a gel phantom.

On a similar note, localized motion generation using ARFI has been employed with MRE to measure elasticity changes during high intensity focused ultrasound ablations in *ex vivo* porcine muscle samples. Such monitoring requires sufficient displacement amplitude [**552**]. Assessment of stiffness changes due to ablation or percutaneous procedures has been performed both during [**553, 554**], and separately before and after ablation [**555**], all cases reporting a stiffness increase after the intervention.

On the acquisition side, significant efforts have been put into MR sequence developments to reduce scan time while preserving 3D motion encoding and signal amplitude. Although equipping an MR sequence with bipolar magnetic field gradients prevails, recent implementations took advantage of MR sequence inherent gradients to encode motion, thus keeping the timing shorter than conventional use of MEG [**556**]. As in any MRI scan, artefacts may occur due to patient motion. Sequence dependent artefacts include and are not restricted to signal loss in GRE sequences due to irregular geometries, and associated magnetic field inhomogeneity and distortion in echo-planar sequences. Specific to MRE, phase wrapping occurs when motion cannot be encoded in the $[-\pi\pi]$ range leading to phase jumps within this range. Three solutions appear and consist in either decreasing the gradient sensitivity, decreasing the motion generator strength, or using a phase unwrapping algorithm. Whilst a weakness of MRE may be viewed as a lack of universal protocol applicable to any organ, its strength resides in the capacity of providing usable data in multiple cases owing to various hardware and MR sequences, and in the availability of physical models to process produced experimental data for stiffness estimation. This technology is still mainly used in the context of clinical research, and additional validations might be required for robust viscosity, porosity, and anisotropy assessments.

B.6.3. Optical shear wave elastography

B.6.3.1. *Cellular shear wave elastography*

Although the optical microelastography technique has an unprecedented temporal resolution with the capability of producing elasticity images, its spatial resolution is not as good as other rheology methods, such as atomic force microscopy. The spatial resolution of this technique is currently limited to approximately 10 μm, but it could be improved to resolutions close to optical microscopy ($\approx$ 1 μm) by utilizing a higher stimulus frequency and by improvements in the reconstruction process. This technique is currently limited to elasticity measurements but viscosity might become available through FEM modeling, or by considering shear wave attenuation [**336**].

More improvements need to be done beyond solving limitations mentioned above. The mechanical behavior of the cell should be further investigated in a range of frequencies. One remaining difficulty is the absence of good standard rheology method to validate the microelastography technique at frequencies in the kHz range. This makes it difficult to compare results from different techniques on a similar cell type. Other reasons for the lack of concordance of results, obtained with different cell elasticity technologies, were recently addressed [**20**] and apply to the reported microelastography method. Recent developments might allow using mechanically stable micro-beads to compare different cell elasticity methods [**557**], which may reduce variability when performing such comparisons at different (non-overlapping) frequencies.

Also, to make these techniques more applicable and practical for biologists, and to promote using cell mechanics as a biomarker, improvements are required for the technique to be automatic, high throughput while being robust, accurate, and sensitive with high time and space resolutions. This might be done by coupling the optical microelastography technique with other methods, such as microfluidics with a high throughput [**558, 559**].

B.6.3.2. *Optical coherence elastography*

Higher resolution OCE may face computational challenges due to the fact that the speckle decorrelation length scales with the speckle size [**560**]. This would reduce the maximum displacement that can be measured between frames. Many studies have made progress to further demonstrate substantial improvements in resolution [**561, 562**]. High resolution OCE systems can be used to assess mechanical properties of cells and a few preliminary studies have showed this potential [**562, 563**]. These are relatively new developments and the hope remains that OCE would be able to characterize cell aggregates, with penetration depth going up to several hundred microns, whilst maintaining a sub-cellular scale resolution.

There has been several studies on elastogram image reconstruction in OCE by inverse problem approaches. Sridhar *et al.* used an inverse problem approach to understand how stromal tissues affect the broad spectrum of the viscoelastic response, by minimizing the mean squared error between computed and measured displacements. Different methods to

constrain the optimization algorithm has been summarized by Le Floc'h *et al.*, in the context of ultrasound strain elastography. Basic principles are also applicable to OCE. However, one challenge that often prevails in these scenarios is the optimization of the regularization parameter for efficient reconstruction, especially in the context of *in vivo* experiments.

Another area of interest representing some challenges is the quantitative assessment of tissue viscoelastic properties with OCE. This research is still in its early years acknowledging the fact that the viscosity is not accounted for in the simple approach [**564**], but hopefully with the development of new models, OCE would be able to convert elastic wave speed and attenuation into quantitative values for clinical diagnosis based on tissue viscoelasticity.

Despite several advancements, very few studies have been done in the area of validation of performance. This would require phantoms that are developed for optics rather than mechanics. Rigorous assessment of sensitivity and specificity for diagnostic applications would be required for translating the method to the clinics.

B.6.3.3. *Photoacoustic elastography*

Photoacoustic elastography imaging is relatively a new development and it still needs to overcome many challenges. The PA signal contrast detected by ultrasound transducers is low due to lower variation in the tissue elasticity distribution in comparison to the optical absorption coefficient. This can potentially be overcome by additionally employing an ultrasound modulation of the laser pulse to provide external mechanical simulation of the tissue. In addition, elasticity can also be estimated from the resonance frequency of the tissue material observed in the measurement of PA signal strength against the operating frequency of the external (ultrasound) mechanical stimulation. Another challenge is the development of quantitative PAE imaging systems, as the first few studies in the field reported only qualitative assessment of elastic properties. However, Hai *et al.* were the first to develop a quantitative PAE system. It would also be interesting to detect the contrast in the PA signal due to elastic property variation separately from that of other parameters (including the optical absorption coefficient). Grasland-Mongrain *et al.* generated shear waves in soft tissues in ablative and thermoelastic regimes with a 532 nm Nd:YAG laser [**16**]. However, it

remained a challenge to keep the laser beam energy within safety limits for use in biomedical applications. This can potentially be overcome by use of other types of laser or by emission of the high energy laser beam onto a protective absorbing layer, such as a black sheet, that can cover the tissue externally. In conclusion, PAE is still in the beginning phase of its development compared to ultrasound, MRI or OCT elastography, and there definitely remains scope for many promising improvements to increase its potential for various imaging applications.

Table 7 – An overview of main applications and viscoelastic properties in ultrasound SWE.

	Generation of SW			Viscoelastic parameters						
	Mechanical pushes	Focused acoustic beams		Young's modulus	Viscosity	Shear modulus	Shear wave speed		Shear wave dispersion	Shear wave attenuation	Rheological model
	TE	ARFI	SSI				Group velocity	Phase velocity			
Liver	[339, 398, 399, 366, 375, 376, 400, 401, 401, 402, 380, 378, 377, 341, 374]	[399, 366, 403, 401, 339, 401, 402, 378, 379]	[399, 404, 405, 406, 339, 401, 402, 407, 382, 372]	[375, 376, 403, 405, 401, 401, 402, 380, 377, 372, 341, 398]	[382]		[404, 401, 401, 402, 379]	[404, 366, 400, 406, 407, 382]	[404, 400, 406, 407, 382]	[404]	[404, 406, 407, 382]
Breast	[22]	[408, 391, 409]	[407, 409, 388, 410, 387, 392, 383, 386, 389, 390, 393, 411, 409]	[407, 22, 408, 409, 388, 410, 387, 392, 383, 386, 389, 390, 393, 411]	[391]	[391]	[22, 408, 388, 383, 386, 409, 409, 412, 395, 413, 414]	[407, 391]	[407]		[407] (power law) [391]
Thyroid		[415, 412, 395, 416, 413, 417]	[395, 418, 419, 420, 421, 422, 423, 414, 424]	[415, 416, 417, 418, 419, 420, 421, 422, 414, 424]		[423]	[412, 395, 413, 414]				
Muscle		[425]	[426, 397, 427, 428]			[426, 397, 427, 428]	[426, 397, 427, 428]	[425, 426]			[426]
Tendon	[429]		[430, 431, 396]	[430, 431]			[430]	[429]			[429]
Blood clot		[432]	[433, 434]	[433, 434]	[432]	[432]	[433, 434]	[432]			[432]
Prostate		[435]	[436, 437, 438, 439, 440, 441]	[436, 437, 439, 440, 441]		[438]	[435, 436, 437, 438, 439, 440, 441]				

Table 8 – An overview of main applications and technical developments in MRE.

	Sequence type		Moment nulling		Encoding		Actuation				Inversion	
	SE	GRE	0^{th}	1^{st}	Fractional/ multi-frequency	Full wave	Loud-speaker	Electro-magnetic	Piezo-electric	Intrinsic	Direct	Iterative
Brain	[96, 447, 74, 80, 65, 76, 77, 79, 78, 448, 457, 62, 162, 82, 144, 289, 138, 140, 141]	[111, 289, 145, 143, 97]	[74, 80, 65, 76, 111, 77, 79, 78, 162, 82, 289, 145, 143]	[96, 447, 448, 457, 62, 82, 144, 138, 140, 97, 141]	[74, 76, 111, 77, 79, 78, 448, 457, 82, 144, 289, 141]	[96, 447, 80, 65, 62, 162, 289, 138, 140, 97]	[96, 447, 74, 76, 77, 79, 78, 62, 144, 289, 138, 140, 97]	[448]	[80, 65, 457, 162, 82, 141]	[111, 144, 145, 143]	[96, 447, 74, 80, 65, 76, 111, 77, 79, 78, 448, 457, 62, 82, 144, 97, 141]	[162, 289, 145, 143, 138, 140]
Muscle		[444]	[444]			[444]	[444]				[444]	
Liver	[446, 75, 82, 66, 95, 83]	[449, 66, 504]	[449, 446, 75, 82, 66]	[82, 95, 504, 83]	[446, 75, 82, 66, 504, 83]	[449, 95]	[446, 75, 95, 504]	[449, 66]	[82, 83]		[449, 446, 75, 82, 66, 95, 504, 83]	
Prostate	[69]	[451]	[451]	[69]	[451]	[69]		[451]	[69]		[69, 451]	
Kidney	[443]			[443]		[443]	[443]				[443]	
Heart		[77, 8, 471, 442]	[77, 8, 471]	[442]	[77, 8, 471, 442]		[77, 8, 471, 442]				[77, 442]	
Breast	[61]	[453]	[453]			[453]		[61]	[453]		[61]	[453]
Spleen	[81, 83]			[81, 83]	[81, 83]				[81, 83]		[81, 83]	
Phantom	[99, 445]	[41]	[99]	[41]		[41, 99]	[445]	[41]	[99]		[41, 99]	[445]

Table 9 – Overview and comparison of various elastography technologies.

Modality/features	**Manual palpation**	**USE**	**MRE**	**OCE**	**PAE**
Interrogating mechanism	External assessment by hand	Acoustic waves	Acoustic waves	Usually optical or acoustic waves	Optical waves (near infrared laser)
Detection	Sense of touch	Acoustic waves	Magnetic field gradients	Optical waves (near infrared)	Acoustic waves
Tissue property	Mechanical strain	Acoustic impedance	Tissue nuclear property	Optical absorption	Optical absorption/acoustic impedance
Spatial resolution	Not deterministic	≈ 500 µm	≈ 1 mm (clinical 3 T machine) - 500 µm(preclinical machine)	≈ µm	≈ 50 µm
Imaging depth	Not deterministic	≈ cm(s) (whole body)	≈ cm(s) (whole body)	≈ 1 mm	≈ cm(s)

USE, ultrasound elastography; MRE, magnetic resonance elastography; OCE, optical coherence elastography; PAE, photoacoustic elastography.